Synthesis of Molecular Species for Supramolecular Assembly

Nassiba Taleb, MSci

Thesis submitted to the University of Nottingham for the degree of
Doctor of Philosophy

January 2011

Abstract

This thesis details the synthesis and study of molecular species designed to form supramolecular assemblies, in particular for surface deposition purposes.

The first chapter gives a brief introduction to supramolecular chemistry concepts and the basis on which this project is built. The importance of non-covalent bonding interactions to form complex architectures capable of self-assembly is discussed, in particular hydrogen bonds and π-π interactions with a series of examples from the literature to illustrate the work that has been accomplished over the past few years in various fields of supramolecular chemistry and nanotechnology in particular. The present project aims at the design, the synthesis and the characterisation of two different groups of compounds, namely *p*-terphenyl tetracarboxylic acid derivatives and manganese based single molecule magnets.

The former are dealt with in the second chapter of the present thesis. The scientific background and the recent results obtained following the surface deposition of *p*-terphenyl-3,5,3',5'-tetracarboxylic acid are explained and discussed in the introduction. The focus of the research is to design and synthesise similar derivatives, i.e capable of self-assembling to produce similar ordered arrays on surfaces as observed for the parent molecule, but bearing some specific functional groups that are anticipated to either induce a change in the observed assembly process or even impart the molecular functionality upon the assembly.

The third chapter of the thesis describes the synthesis and functionalisation of manganese-based single molecule magnets, which are believed to be promising candidates for future applications such as high-density data storage. The crystal structures of some derivatives are discussed and a crystallographic comparative study between the as-synthesised derivatives and literature examples is detailed. In addition,

the magnetic properties of selected complexes are discussed and compared. Finally, the results resulting from surface deposition studies that have been carried out in collaboration with the School of Physics and Astronomy at the University of Nottingham are presented in the last section of this chapter.

Acknowledgments

Symbols & Abbreviations

°	degrees
~	about
χ	susceptibility
Å	angstroms
ΔE	effective energy barrier
cm^3	cubic centimetres
AC	alternating current
Au	gold
bipy	bipyridine
C	Celsius
Cg	centroid
d	days
d	doublet (NMR)
dd	doublet of doublet (NMR)
ddd	doublet of doublet of doublet (NMR)
D	axial zero-field splitting parameter
DC	direct current
DMF	dimethylformamide
DMSO	dimethylsulfoxide
EA	elemental analysis
EI	electron impact
ESI	electrospray ionisation
Et_2O	diethyl ether
FT-IR	Fourier transform infrared
g	gram
h	hour(s)
Hg	mercury
HOPG	highly orientated pyrolitic graphite
IR	infrared
K	Kelvin
K_B	Boltzmann constant

M	molar
m	multiplet (NMR)
m (IR)	medium
MALDI	Matrix-Assisted laser desorption ionisation
MeOH	methanol
MeCN	acetonitrile
Me	methyl
mg	milligram
MHz	megahertz
min.	minute(s)
mL	millilitres
MLCT	metal to ligand charge transfer
mm	millimeters
mmol	millimole
mol	mole
MOF	metal organic framework
MS	mass spectrometry
m/z	mass/charge ratio
nm	nanometres
NMR	nuclear magnetic resonance
Oe	Oersted
p	para
Ph	phenyl
ppm	parts per million
q	quartet (NMR)
QTM	quantum tunnelling of magnetisation
s	second
s (IR)	strong
S	spin ground state
SCE	saturated calomel electrode
SMMs	single molecule magnets
SPM	scanning probe microscopy
STM	scanning tunelling microscopy
t	triplet (NMR)

T	temperature
ToF-SIMs	time-of-flight secondary ion mass spectrometry
UHV	ultra high vacuum
UV-vis	ultraviolet visible
vdW	van der Waals
vs (IR)	very strong
vs	versus
w (IR)	weak
XAS	X-ray absorption spectroscopy
XMCD	X-ray magnetic circular dichroism
XRD	X-ray diffraction
XPS	X-ray photoelectron spectroscopy

Contents

Chapter 1:

Introduction

1.1 Supramolecular chemistry

Supramolecular chemistry was first described by J.M Lehn as "the chemistry beyond the molecule".[1] As molecular chemistry has been the focus for more than a hundred years and concerns the covalent bond, we have witnessed the design and formation of more and more complex molecules through elaborated strategies aiming at breaking and creating covalent bonds in a controllable and accurate manner. As for supramolecular chemistry, this is an area of chemistry that focuses on the reversible "intermolecular bond"[2] and aims at controlling the non-covalent intermolecular forces responsible for the "association of two or more chemical species"[2] in view of constructing complex and organised large architectures. These non-covalent interactions include several types of interactions, such as metal-ligand (M-L) coordination, hydrogen-bonding, π-donor-π-acceptor interactions and van der Waals (vdW) interactions, differing in strength and directionality ranging from a few hundred kilojoules per mole for the strongest interactions (typically ~200 kJ.mol^{-1} for M-L coordination bonds) to a few kilojoules per mole for the weakest ones (2-25 kJ.mol^{-1} for hydrogen bonds or π-π interactions). The fact that these interactions are reversible makes it challenging and difficult to gain control over the forces responsible for the formation of these complex systems. However, because they are under thermodynamic control, supramolecular entities possess the capability of "self-correction".[3]

Historically, supramolecular architectures found inspiration from nature with especially the examples of biological species such as the DNA double helix and the structures of proteins.[4] Since then, the field has evolved considerably with the development of a wide number of sub-branches including molecular recognition, host-guest chemistry, self-assembly and molecular machines to name a few. This chapter

will essentially relate to self-assembly concepts and examples based on hydrogen-bonding and π-π interactions.

1.2 Self-assembly

Molecular self-assembly is the spontaneous self-organisation of building blocks into ordered functional structures resulting from weak intermolecular forces that maximise favourable interactions. Therefore this implies that the tectons that self-assemble must be cautiously designed and capable to do so without any external assistance.

There are several strategies to design molecules with complementary binding groups capable to self-assemble. Two of them consist of incorporating groups capable of hydrogen-bonding and/or π-π stacking.

1.2.1   H-bonding

Hydrogen bonds are among the most widespread fundamental supramolecular forces encountered in nature. They are formed when a hydrogen atom attached to a relatively electronegative one, termed the hydrogen-bond donor D, is attracted by means of electrostatic interactions, towards another electronegative atom or groups of atoms from a different molecule (intermolecular H-bond) or even belonging to the same molecule (intramolecular H-bonds) which becomes the hydrogen-bond acceptor A (Scheme 1.1). Although stronger than most other intermolecular forces, the bond energy associated with H-bonds, is fairly weak compared to covalent bonds. However, the bond strength depends on several factors such as the electronegativities of the donor and acceptor atoms, the temperature, the pressure, the bond angle and the overall chemical environment. The energy of hydrogen bonds ranges from very weak

with values comprised between 2-40 kJ.mol^{-1} to strong with bond energies up to 155 kJ.mol^{-1} in the bifluoride ion HF$_2^-$.[5] As seen in the latter example, the hydrogen bond can be highly directional and has some features of covalent bonding which explains the strong value for the bond energy. The distance and the angle formed between the acceptor and the hydrogen atom are a good indicator of the strength of the bond. The shorter the hydrogen-acceptor (H-A) distance is, the stronger the bond is. As the D-H…A angle deviates from ideal conditions (it tends towards 180˚ and should be over 110˚), the interaction becomes weaker.[6] This is anticipated for weak hydrogen bonds like in C-H···O where smaller angles, as low as 120˚, are commonly observed.
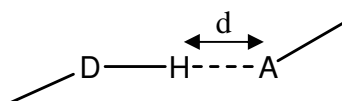
Scheme 1.1. Schematic representation of a hydrogen bond between an acceptor atom A and the hydrogen atom of a donor atom D. The hydrogen bond length d is a good indicator of the strength of the bond.

The use of multiple hydrogen bonding is a powerful strategy to enhance the strength of the interaction and the directionality and hence stabilise the formation of the desired complex array. In addition, it is possible to increase the selectivity of the association by increasing the number of sites capable of hydrogen-bonding by designing more complex tectons or building blocks. For example, 2-pyridinones are compounds that are capable of self-organisation into cyclic dimers or chains in solution and in the solid state (Figure 1.1) through the use of double hydrogen-bonding. However, the motif that will be observed is quite hard to anticipate and therefore to control. To overcome this situation, it was demonstrated that by

incorporating an acetylenic linker in between two pyrimidone units, it was possible to control the type of supramolecular self-assembled motif observed (Figures 1.2 and 1.3).[7] The dipyrimidone compound shown on the left in Figure 1.2 is self-complementary and therefore self-assemble into a cyclic dimer by means of quadruple hydrogen-bonds, while the compound in Figure 1.3 which displays a pattern of the type of acceptor-donor-donor-acceptor (ADDA) is not self-complementary and therefore results in the formation of oligomeric chains.
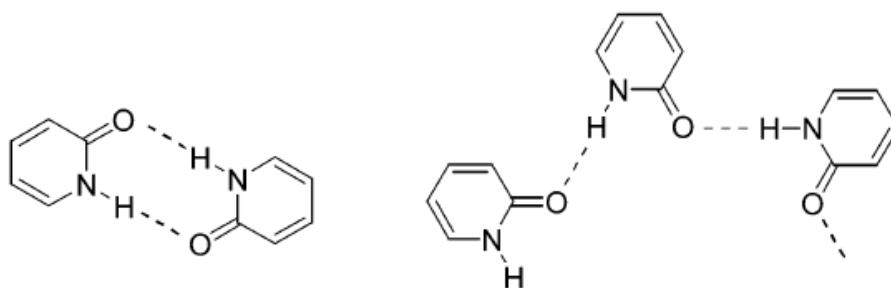
Figure 1.1. Cyclic dimers (left) or chains (right) resulting from the self-association of two pyridinone compounds.
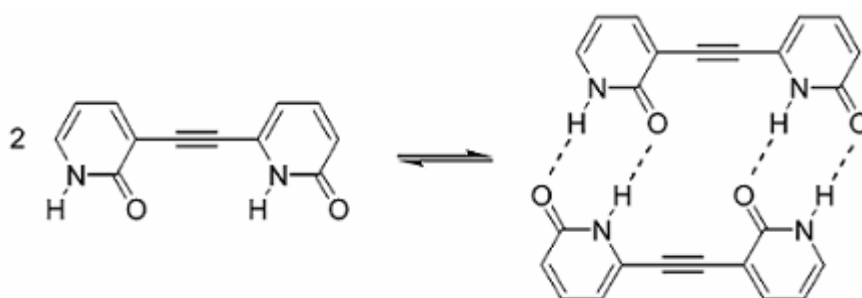
Figure 1.2. The self-complementary of the dipyridinone compound enable the formation of cyclic dimers in solution and in the solid-state.
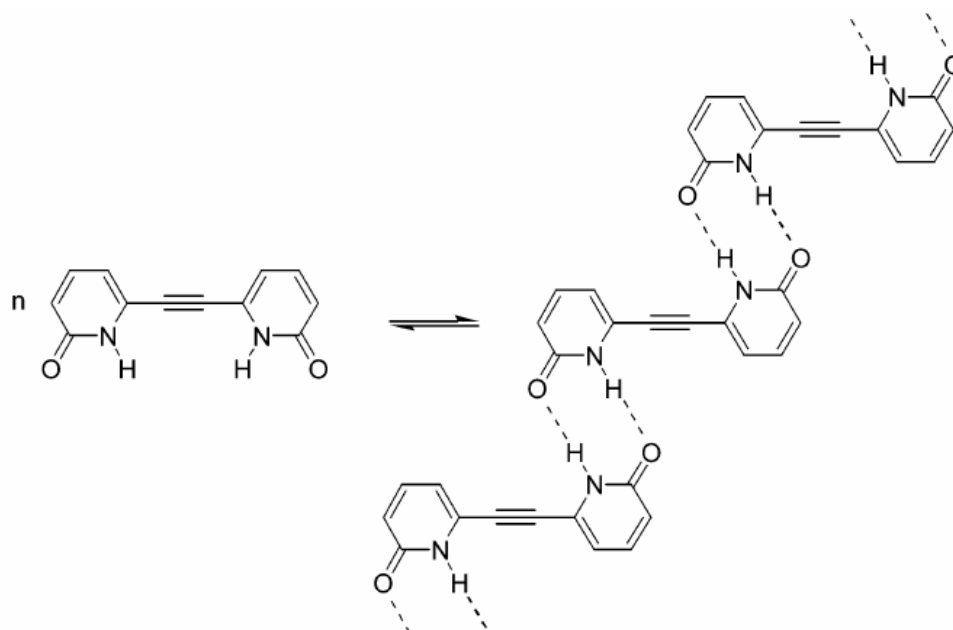
Figure 1.3. The quadruple pattern of hydrogen-bonding sites is not self-complementary yielding the formation of oligomeric chains.

1.2.2   π-π interactions

π-π interactions, or also termed π-π stacking, refers to the intermolecular overlapping of p-orbitals in π-conjugated systems. Several conformations have been described, namely parallel displaced and T-shaped π-π stacking (Scheme 1.2).[8,9] The latter is also referred to as a weak C-H···π interaction where the electron deficient hydrogen atom of an aromatic molecule interacts with the delocalised π-electron cloud of a second aromatic system.

Scheme 1.2. Representation of π-π interactions: off-centred parallel displaced conformation on the left and T-shaped motif on the right.

An electrostatic model has been proposed to explain this phenomenon, whereby the π-system of an aromatic molecule attracts more strongly the σ-system of another aromatic molecule so that the π-π repulsion supposedly destabilising the complex is disfavoured.[8]

These types of non-covalent interactions are quite important in biological systems as illustrated by the stabilisation of the double helical structure of DNA through vertical π-stacked base-base interactions, tertiary structure of proteins and much more.[10,11,12,13] More recently, the influence of these interactions in organometallic compounds have been established when π-π interactions have been shown to alter the coordination geometry and stabilize different geometries for Pd complexes.[14] Using these non covalent forces, functional supramolecular assemblies have been achieved both in solution and in the solid state.

1.3 Self-assembly in solution

The self-assembly process is normally carried out in solution or at smooth interfaces as it allows the mobility of the different components required for self-assembly to occur. In solution, thermal motion is responsible for the steering of the components and is therefore the main contribution for bringing molecules in contact. Examples of solution-based self-assembly are numerous in the literature and a few were selected and illustrated here.

Molecular switches are molecules that can be switched between several states in a reversible manner by applying one or several relevant stimuli such as temperature, light, pH, etc. Some of the most advanced molecular switches are based on self-

assembled mechanically-interlocked or intertwined molecular architectures such as catenanes and rotaxanes by exploiting the molecular recognition between π-electron rich and π-electron deficient aromatic systems.[15]

It has been demonstrated that it is possible to perturb non-covalent interactions in rotaxanes and pseudo-rotaxanes to generate molecular switches in solution.[16] A [2]-rotaxane constituted by two hydroquinone rings and a tetrathiafulvalene (TTF) unit as the π-electron rich recognition sites displayed solvent-dependent molecular switching properties (Figure 1.4).[17] ^{1}H NMR spectroscopy was used to probe the molecular motion of the architecture. It was established that in CD_3COCD_3, the tetracationic cyclophane resides exclusively on the two degenerate hydroquinone rings, whilst in CD_3SOCD_3 the macrocycle occupies solely the TTF unit.
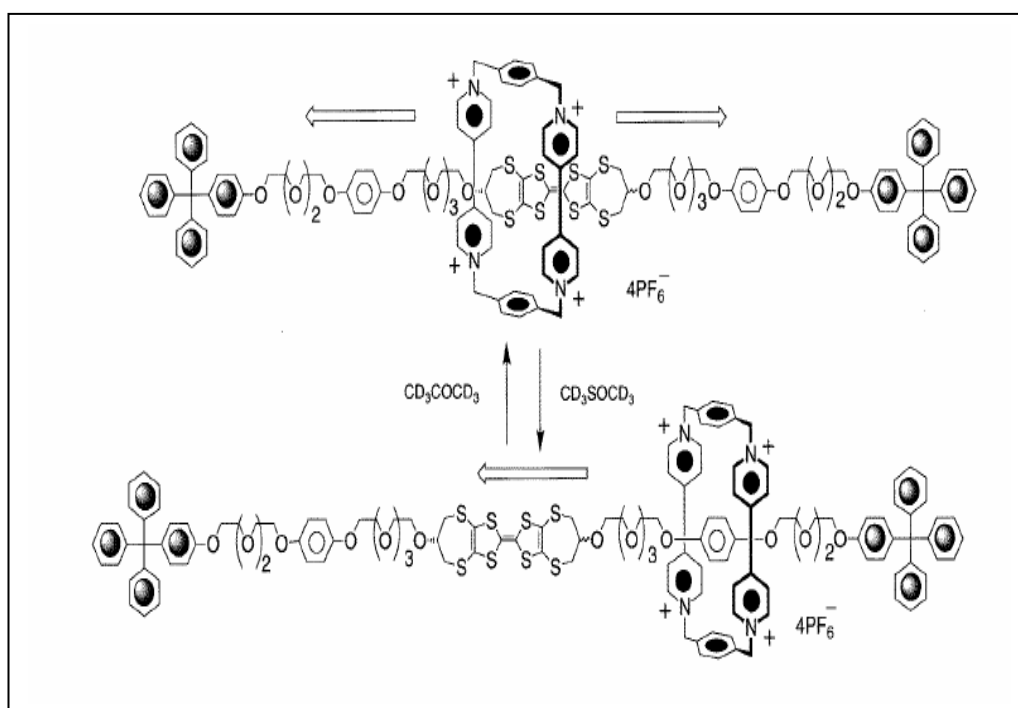
Figure 1.4. Representation of the solvent-dependent molecular shuttle composed of a TTF unit sandwiched by two hydroquinone stations.[17]

Another example in the field of molecular machines was reported by Stoddart and co-workers in 2001.[18] It was shown that the threading-dethreading of a pseudo-rotaxane was achievable in solution by visible light irradiation. The pseudo-rotaxane is formed by the stable self-assembly of a thread-like species trans-**1** containing an electron-rich azobiphenoxy unit with the electron-acceptor macrocycle **2**$^{4+}$ in a solution of acetonitrile (Figure 1.5). When engaged in the pseudo-rotaxane superstructure, the intense fluorescence characteristic of the free macrocycle is completely quenched. When this solution is irradiated with a 365 nm light, the trans-cis photoisomerisation of **1** occurs leading to a dethreading process as **2**$^{4+}$ has less affinity for the cis isomeric form of compound **1**, as confirmed by the observed increase in the fluorescence intensity of the free **2**$^{4+}$. Upon irradiation at 436 nm, the trans-isomer is regenerated and is rethreaded back inside the macrocycle. Because the photoisomerisation of **1** is a fully reversible process, it was shown that the photo-induced threading-dethreading cycles can be repeated consecutively using the same solution.
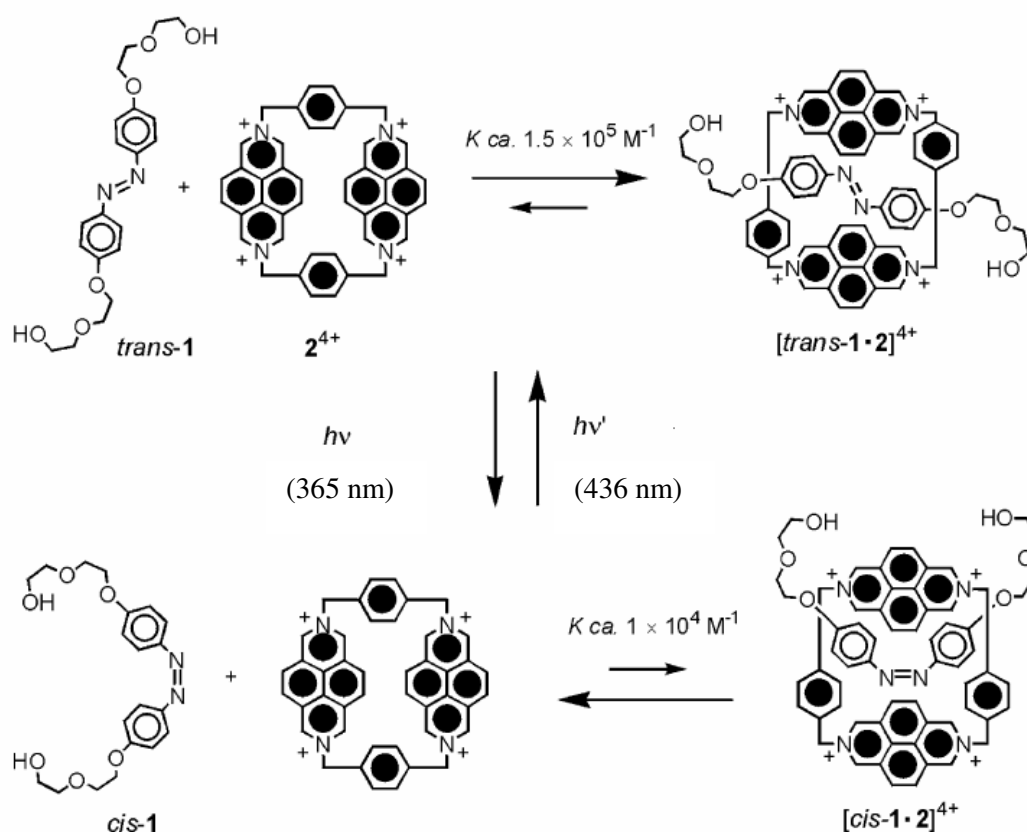
Figure 1.5. Light energy controlled threading-dethreading of a self-assembled pseudo-rotaxane [1.2]$^{4+}$ resulting form the cis-trans photoisomerisation of the azobenzene-type moiety contained in component 1.[18]

1.4 Solid-state self-assembly

Self-assembly is a concept that can also be applied to solid-state chemistry and can be referred to as crystal engineering. Crystal engineering can be regarded as the "design of crystal structures"[19] using non covalent forces. Initially, the research focus dealt with purely organic-based systems, exploiting supramolecular forces in particular hydrogen-bonding, to generate solid-state architectures.[20] This field of chemistry has developed significantly with the study of inorganic systems based on coordination complexes due to the great variety of geometries available for transition metal complexes.[21] Although these geometries are mainly governed by the

coordination properties of the transition metal and ligands, the use of non covalent interactions can considerably influence the structural motifs observed.[14] The supramolecular structures generated can, to a certain extent, be anticipated and topologies such as ladder,[21i-j] honeycomb[21k] and brick-walled[22] structures have been described.

In 1999, Ranganathan and co-workers reported the structure of the network formed by the co-crystallisation of melamine [1,3,5-triazine-2,4,6-triamine: (M)] and cyanuric acid (CA) using a hydrothermal synthesis because of the high tendency of these two molecules to hydrogen-bond which limits significantly their solubility in most organic solvents.[23] Crystals were anticipated to form a hexagonal network through triple hydrogen-bonds. The crystal packing study of the 1:1 (M)-(CA) adduct revealed, as predicted, the formation of rosette (hexamer) through triple hydrogen-bonds: two N…H-O and one N…H-N bonds as illustrated in Figure 1.6a. The hexamers arrange in two-dimensional planar sheets as predicted.[24] The observed motif presents a central cavity of mean diameter of 4Å. In addition, a remarkable feature of this network is the three-dimensional arrangement of these planar sheets into channels of approximately 4 Å diameter as they stack on one another (Figure 1.6b).
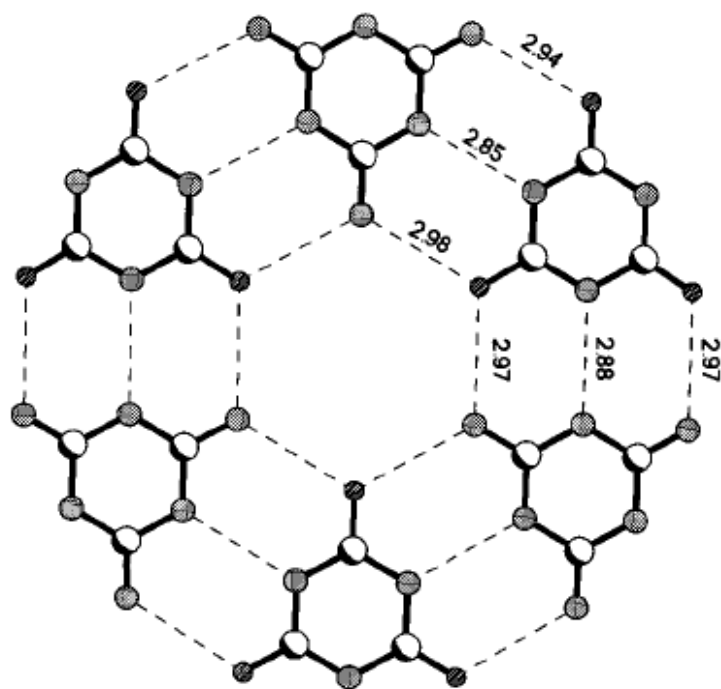
(a)
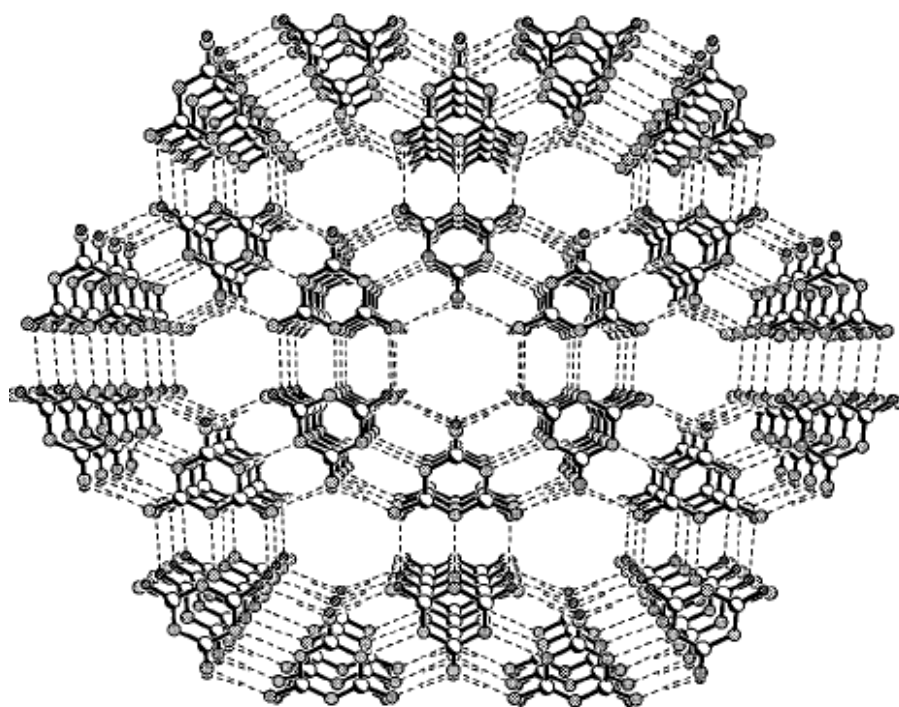
(b)

Figure 1.6. (a) Rosette formed by the 1:1 (M)-(CA) adduct through triple hydrogen-bonding. The hexamer presents a cavity diameter of approximately 4 Å. Dashed lines represent intermolecular hydrogen bonds. (b) Three-dimensional arrangement of the 1:1 (M)-(CA) adduct into channels. View along the crystallographic *c*-axis.[23]

1.5 Self-assembly on surfaces

The concept of supramolecular chemistry has been extensively studied and mainly applied in solution and in the solid-state as detailed above. However, little has been carried out to exploit the formation of supramolecular architectures on surfaces. This area of chemistry has received more and more interest since the development of scanning probe techniques such as scanning tunnelling microscopy (STM).[25] In addition to be able to predict or anticipate the network to be formed, one has to take into consideration the contributions of the substrate and the potential adsorbate-substrate interactions, hence the knowledge of supramolecular concepts valid for solutions or crystals cannot be directly translated to direct the assembly of adsorbed molecules into ordered arrays on surfaces. However, these concepts can be used as tools to promote the formation of complex architectures held by non covalent forces through the choice of judicious functional groups, surface patterns and templates with relevant geometry and symmetry.

π-conjugated aromatic molecules are fruitful compounds for surface deposition purposes as they tend to sit in a flat manner parallel to the surfaces thus allowing the peripheral functional groups to interact with each other making use of non-covalent interactions, provided that the molecules possess a certain mobility on the substrate. The design of the building blocks or tectons enables tuning of the supramolecular surface patterns. Numerous examples of supramolecular self-assembly on surfaces have been described in the literature over recent years.

The deposition of trimesic acid (1,3,5-benzenetricarboxylic acid) has been carried out using ultra-high vacuum conditions.[26,27] It is anticipated that the motif generated upon surface deposition would be a planar honeycomb network due to dimerisation of the carboxylic acid functionalities.[25] This was the case when trimesic

acid was adsorbed on a Cu surface at low temperature; however no long range order was observed. In addition to a honeycomb structure, a flowerlike motif has also been reported when trimesic acid was deposited on graphite under UHV conditions (Figure 1.7).[26] These two structures differ in the way the hexagons are connected to each other.
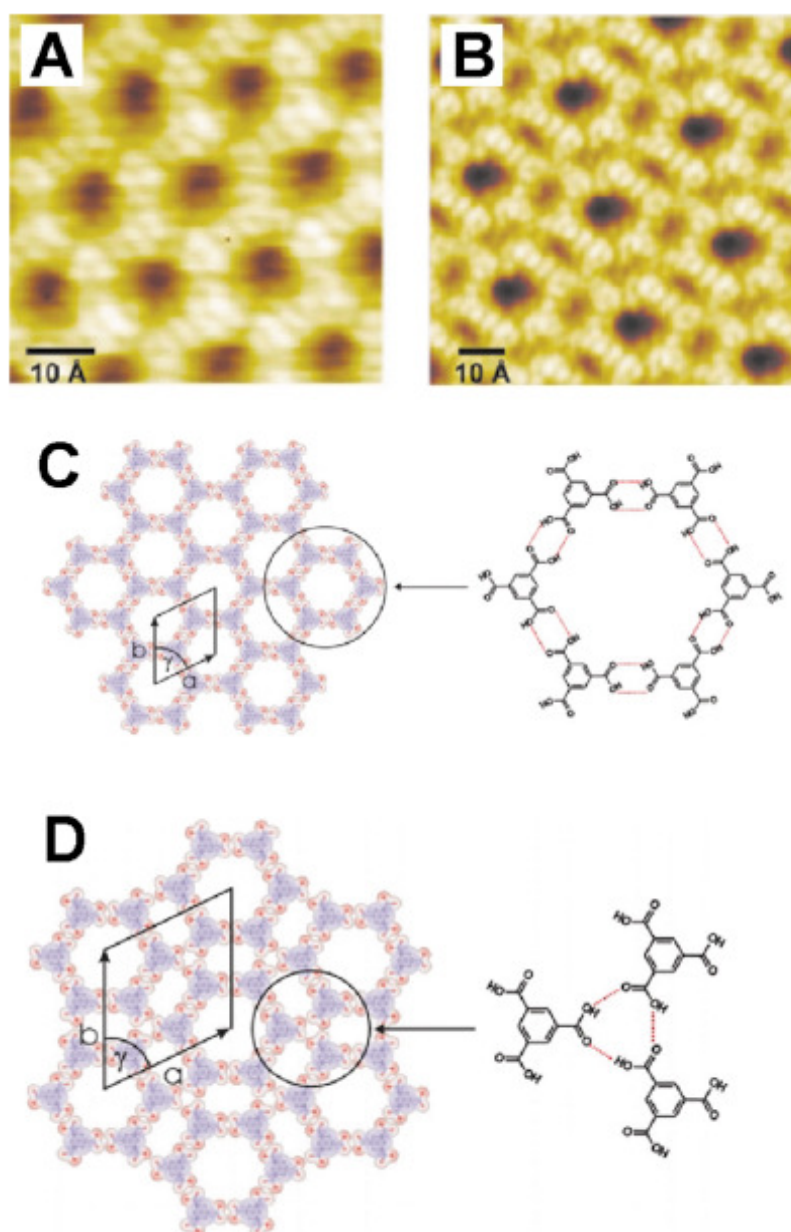
Figure 1.7. (A,B) STM images of trimesic acid adsorbed on graphite under UHV conditions. (A, C) honeycomb structure (B, D) flowerlike structure.[26]

Another appealing example is the self-assembly behaviour of 4-[trans-2-pyrid-4-yl-vinyl)benzoic acid (PVBA) on noble metal surfaces using UHV conditions studied by STM.[28] Isolated molecules were observed when deposited on a palladium substrate at room temperature due to strong adsorbate-substrate interactions which prevent the molecules from self-assembling through head-to-tail hydrogen-bonding.[27] However on closed-packed noble-metal surfaces, the molecules are able to diffuse more and the formation of meandering chains and twin chains has been observed on surfaces. This example illustrates the effect of factors like surface symmetry and chemical functionality on the fine balance between intermolecular forces and adsorbate-surface interactions which ultimately determines the network observed.

Another extended two-dimensional hydrogen-bonded honeycomb network with larges pores was achieved by co-depositing perylene tetra-carboxylic di-imide (PTCDI) with melamine (1,3,5-triazine-2,4,6-triamine) on a silver terminated silicon surface.[29] The network is stabilised by triple hydrogen-bonding between melamine, which as a trigonal connector forms the vertices of the network and the linear PTCDI linker which corresponds to the edges of the network (Figure 1.8a). This open network acts as a two-dimensional array of large pores of sufficient capacity to accommodate several large guest molecules, with the network itself also serving as a template for the subsequent formation of other layers, as it was demonstrated by the encapsulation of C_{60} heptamers within the network pores forming regular arrays on the two-dimensional bimolecular honeycomb arrangement (Figure 1.8c-d).
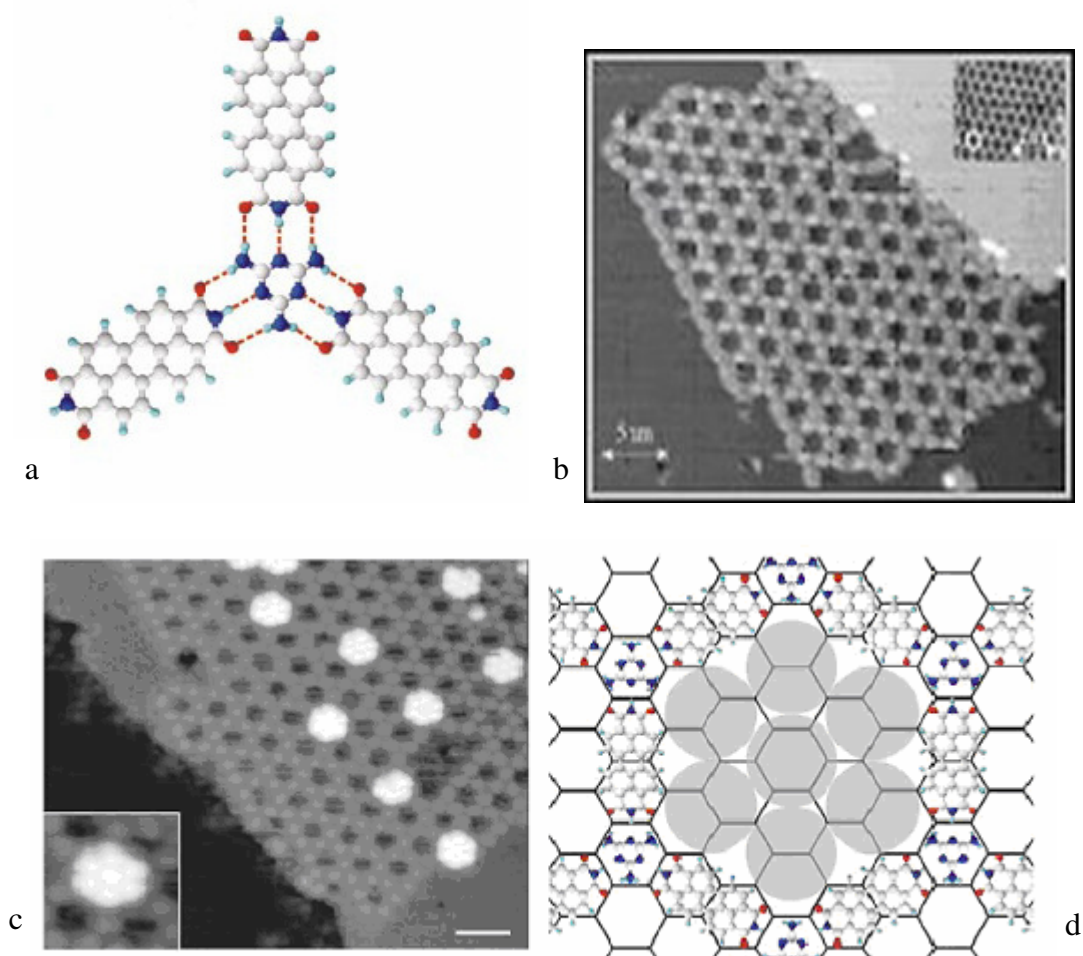
Figure 1.8. (a) Schematic diagram of a PTCDI–melamine trigonal motif showing the stabilized triple hydrogen-bonds (dotted lines) between the two tectons. (b) STM image of a PTCDI–melamine network formed on the Ag passivated Si(111) substrate Scale bars, 3 nm. (c) STM images of C_{60} heptamers trapped within the pores of the PTCDI–melamine network. Inset, high-resolution view showing an individual cluster. Scale bar, 5 nm. (d) Schematic representation of a C_{60} heptamer.[29]

Finally the last example to be mentioned in this section will be the deposition of cyanuric acid (CA) and melamine (M) on a silver terminated silicon substrate using UHV conditions.[30] As mentioned earlier, this structure has been the focus of numerous studies and the solid-state structure has only been recently elucidated[23] (see above). The co-deposition and the sequential deposition of (CA) followed by (M) both yielded the formation of a surface-based self-assembled (CA)-(M) network. It was shown that the resulting network was not contaminated by the presence of islands of

either individual tecton thus demonstrating the increased stability of the network phase over the precursors. This network is very similar to the PTCDI-melamine network described previously,[29] the replacement of PTCDI by CA molecules resulting in the decrease in the size of the network pores.

1.6 Self-assembly for nanotechnology

Nanotechnology is the engineering of functional systems at the molecular scale. It is a quite recent concept that has attracted great interest over the past decade or so, because of the vast variety of future potential applications that can emerge from this field. Usually, nanomaterials refer to materials made-up from few molecules with at least one dimension on the nanoscale *i.e.* comprised between 0.1 and 100 nm.

Owing to their very small sizes, novel properties different from those observed for the bulk materials have been observed such as the well-known blue-shift of absorption for semiconductor nanoparticles with decreasing size of the particles. The uniqueness of these properties make nanotechnology an inter-disciplinary area common to physics, chemistry, biology, material science, medicine, manufacturing and more.

Two main approaches have been developed to access nanoscopic materials: the first one, known as the "top-down" approach, utilises the techniques from microtechnology such as lithography to achieve nanostructured objects. The main limitations of this approach are practical, technological, economical and fundamental[31] as the race towards miniaturisation has not been predicted to stop anytime soon. The alternative strategy that has been developed is the so-called "bottom-up" approach which consists of building up materials or machines by assembling components at a molecular level (atom by atom, or molecule by

molecule). With the development of supramolecular chemistry, the bottom-up approach has opened many possibilities for the design and the construction of artificial molecular-level devices.

As discussed previously, solution-based self-assembly and crystal engineering have made considerable progress but for supramolecular entities to be able to display device-like properties, such architectures need to be spatially addressed at a molecular scale which is not possible with crystals or solutions. Therefore these nanomaterials, to be functional, need to be organised at interfaces,[32] deposited on surfaces,[33] immobilised inside membranes[34] or porous materials[35] so they can behave in a coherent manner. Hence, templating surfaces in a controllable way will prove to be extremely important.

In his renowned talk in 1959, Richard P. Feymann declared that "there is plenty of room at the bottom"[36] and predicted exciting times providing we could gain control over matter. Since then, nanomaterials with unprecedented properties have been discovered such as semiconductor quantum dots, carbon nanotubes and single molecule magnets for example. The development of techniques, such as scanning tunnelling microscopy (STM),[25] has enabled the imaging and manipulation of individual atoms or molecules. Because of the ever-decreasing size for nano-sized objects, several industries are about to face enormous difficulties to meet the requirements to keep up with this trend, especially branches of microelectronics and magnetic materials. As a consequence, new fields of research such as molecular spintronics[37] and molecular magnetism[38] have emerged. Molecular magnetism is an emerging field that aims at developing molecular approaches to create new classes of magnetic nanomaterials. Among the latter, single molecule magnets (SMMs) are nanomagnets[38,39] that find future potential applications for high-density magnetic

storage devices,[39] quantum computers,[40] molecular spin-valves,[37] and molecular spin-transistors.[37]

In this context, the present project aims at designing and synthesising molecular species capable of forming supramolecular architectures for surface deposition applications. As mentioned previously, templating surfaces is a possible way to obtain regular arrays of nanoscopic-sized objects. This approach can afford a great variety of topologies on surfaces depending on the subtle balance between the non-covalent interactions that pushes the different components to self-assemble and the adsorbate-substrate interactions as detailed above.

The first chapter of this thesis is dedicated to the synthesis of *p*-terphenyl-3,5,3',5'-tetracarboxylic acid derivatives that are anticipated to self-assemble on surfaces to form two-dimensional regular arrays that can serve as templates for the subsequent ordering of functional guest-molecules such as C_{60} fullerenes or even ultimately endohedral fullerenes. The design and challenging synthesis of derivatives that are capable of self-assembling into ordered arrays and directly incorporating functional components is presented in this chapter. This approach represents a one-pot strategy towards the ordering and the controlled spacing of functional supramolecular species on surfaces.

The second chapter describes the synthesis of functionalised single molecule magnets, their characterisations, and the efforts made towards growing crystals so as to gain deeper knowledge of the solid-state chemistry of these compounds and to establish the structure-property observed relationships, particularly their magnetic properties. For the reasons invoked previously, potential applications of SMMs would eventually require their organisation into ordered patterns on surfaces. Consequently,

the surface deposition of these functionalised nanomagnets on diverse substrates will also be the subject of this second chapter.

1.7 References

1. J-M. Lehn, *Angew. Chem. Int. Ed.*, 1990, **29**, 1304

2. J-M. Lehn, *Angew. Chem. Int. Ed.*, 1988, **27**, 89

3. L. F. Lindoy, I. M. Atkinson, *Self Assembly in Supramolecular Systems*, Cambridge, UK, 2000

4. (a) E.L. Shakhnovich, V. Abkevich, O. Ptitsyn, *Nature*, 1996, **379**, 96. (b) A. Klug, *Angew. Chem. Int. Ed. Engl.*, 1983, **22**, 565

5. J. Emsley, *Chemical Society Reviews*, 1980, **9**, 91

6. T. Steiner, *Angew.Chem .Int. Ed. Engl.*, 2002, **41**, 48

7. Y. Ducharme, J. D. Wuest, *J. Org. Chem.*,1988, **53**, 5787

8. C. A. Hunter, J. K. M. Sanders, *J. Am. Chem.Soc.*, 1990, **112**, 5525

9. C. A. Hunter, K. R. Lawson, J. Perkins, C. J. Urch, *J.Chem.Soc. Perkin. Trans.*, 2001, **2**, 651

10. W. Saenger, *Principles of Nucleic Acid Structures*, Springer-Verlag: New York, 1984, 132

11. S. K. Burley, G. A. Petsko, *Adv. Protein Chem.*, 1988, **39**, 125

12. L. P. G. Wakelin, *Med. Res. Rev.*, 1986, **6**, 275

13. D. Ranganathan, V. Haridas, R. Gilardi,I. L. Karle, *J. Am. Chem. Soc.*, 1998, **120**, 10793

14. A. Magistrato, P. S. Pregosin, A. Albinati, U. Rothlisberger, *Organometallics*, 2001, **20**, 4178

15. B. L. Allwood, N. Spencer, H. Shahriari-Zavareh, J. F. Stoddart, D. J. Williams, *J. Chem. Soc., Chem. Commun.*, 1987, 1064

16. M. Gomez-Lopez, J. A. Preece, J F. Stoddart, *Nanotechnology*, 1996, **7**, 183

17. P. R. Ashton, R. A. Bissell, N. Spencer, J. F. Stoddart, M. S. Tolley, *Synlett*, 1992, 923

18. V. Balzani, A. Credi, F. Marchioni, J. F. Stoddart, *Chem. Commun.*, 2001, 1861

19. D. Braga, F. Grepioni, *Coord. Chem. Rev.*, 1999, **183**, 19

20. (a) G.R. Desiraju, Crystal Engineering, Elsevier, Amsterdam, 1989. (b) G.R. Desiraju, *The Crystal as a Supramolecular Entity*, Wiley, New York, 1995. (c) G.R. Desiraju, *Angew. Chem.*, 1995, **107**, 2541. (d) G.R. Desiraju, *Angew. Chem. Int. Ed. Engl.*, 1995, **34**, 2311

21. (a) R. Robson, B. F. Abrahams, S. R. Batten, R. W. Gable, B. F. Hoskins, J. Liu, *Supramolecular Architecture*, ACS, Washington, DC, 1992, Ch. 19. (b) M. Fujita, Y. J. Kwon, S. Washizu, K. Ogura, *J. Am. Chem. Soc.*, 1994, **116**, 1151. (c) L. R. MacGillvary, S. Subramanian, M. J. Zaworotko, *J. Chem. Soc. Chem. Commun.*, 1994, 1325. (d) A. J. Blake, N. R. Champness, S. M. Chung, W.-S. Li, M. Schroder, *Chem. Commun.*, 1997, 1005. (e) L. Carlucci, G. Ciani, D. M. Proserpio, A. Sironi, *J. Chem. Soc. Chem. Commun.*, 1994, 2755. (f) A. J. Blake, N. R. Champness, A. N. Khlobystov, D. A. Lemenovski, W.-S. Li, M. Schroder, *Chem. Commun.*, 1997, 1339. (g) S. Subramanian, M.J. Zaworotko, *Angew. Chem.*, 1995, **107**, 2295. (h) S. Subramanian, M.J. Zaworotko, *Angew. Chem. Int. Ed. Engl.*, 1995, **34**, 2127.(i) A.J. Blake, N. R. Champness, A. N. Khlobystov, D. A. Lemenovskii, W.-S. Li, M. Schroder, *Chem. Commun.*, 1997, 2027.(j) P. Losier and M. J. Zaworotko, *Angew. Chem.*, 1996, **108**, 2957; *Angew. Chem. Int. Ed. Engl.*, 1996, **35**, 2779. (k) G. B. Gardner, D. Venkataraman, J. S. Moore, S. Lee, *Nature*, 1995, **374**, 792

22. M. Fujita, Y. J. Kwon, O. Sasaki, K. Yamaguchi, K. Ogura, *J. Am. Chem. Soc.*, 1995, **117**, 7287

23. A. Ranganathan, V. R. Pedireddi, C. N. R. Rao, *J. Am. Chem. Soc.*, 1999, **121**, 1752

24. (a) G. M. Whitesides, E. E. Simanek, J. P. Mathias, C. T. Seto, D. N. Chin, M. Mammen,D. M. Gordon, *Acc. Chem. Res*., 1995, **28**, 37. (b) G. M. Whitesides, J. P. Mathias, C. T. Seto, *Science*, 1991, **254**, 1312

25. G. Binnig, H. Rohrer, *Rev. Mod. Phys.*, 1987, **59**, 615

26. N. Dmitriev, N. Lin, J. Weckesser, J. V. Barth, K. Kern, *J. Phys. Chem. B*, 2002, **106**, 6907

27. S. Griessl, M. Lackinger, M. Edelwirth, M. Hietschold, W. M. Heckl, *Single Mol.*, 2002, **3**, 25

28. J. V. Barth, J. Weckesser, C. Cai, P. Günter, L. Bürgi, O. Jeandupeux, K. Kern, *Angew. Chem. Int. Ed.*, 2000, **39**, 1230. (b) J. V. Barth, J. Weckesser, G. Trimarchi, M. Vladimirova, A. De Vita, C. Cai, H. Brune, P. Günter, K. Kern, *J. Am. Chem. Soc.*, 2002, **124**, 7991

29. J. A. Theobald, N. S. Oxtoby, M. A. Phillips, N. R. Champness, P. H. Beton, *Nature*, 2003, **424**, 1029

30. L. M. A. Perdigao, N. R. Champness, P. H. Beton, *Chem. Commun.*, 2006, 538

31. (a) R. W. Keyes, Proc. IEEE, 2001, **89**, 227. (b) International Technology Roadmap for Semiconductors, ITRS, 2003

32. (a) D. E. Lynch, D. G. Hamilton, N. J Calos, B. Wood, J. K. M. Sanders, *Langmuir*, 1999, **15,** 5600. (b) C. L. Brown, U. Jonas, J. A. Preece, H. Ringsdorf, M. Seitz, J. F. Stoddart, *Langmuir*, 2000, **16,** 1924

33. (a) M. Cavallini, F. Biscarni, S. Leon, F. Zerbetto, G. Bottari, D. A. Leigh, *Science*, 2003, **299**, 531. (b) B. Long, K. Niktin, D. Fitzmaurice, *J. Am. Chem. Soc.*, 2003, **125**, 5152

34. (a) G. Steinberg-Yfrach, P. A. Lidell, S-C. Hung, A. L. Moore, D.Gust, T. A. Moore, *Nature*, 1997, **385**, 239. (b) I. M. Bennett, H. M. V. Farfano, F. Bogani, A. Primak, P. A. Liddel, L. Otero, L. Sereno, J. J. Silber, A. L. Moore, T. A. Moore, D. Gust, *Nature*, 2002, **420**, 398

35. (a) S. Chia, J. Cao, J. F. Stoddart, J. I. Zink, *Angew. Chem. Int. Ed.*, 2001, **40**, 2447. (b) M. Alvaro, B. Ferrer, H. Garcia, E. J. Palomares, V. Balzani, A. Credi, M. Venturi, J. F. Stoddart, S. Wenger, *J. Phys. Chem. B,* 2003, **107**, 14319

36. R. P. Feymann, *The pleasure of finding things out: The Best Short Works Of Richard Feymann,* Ed. J. Robbins, Penguin, London, 2001

37. L. Bogani, W. Wernsdorfer, *Nature Materials*, 2008, **7**, 179

38. E. Coronado, C. Marti-Gastaldo, S. Tatay, *Appl. Surf. Science*, 2007, **254**, 225

39. D. A. Thomson, J. S. Best, *J. Res. Dev.*, 2000, **3**, 311

40. M. Affronte, F. Troiani, A. Ghirri, A. Candini, M. Evangelisti, V. Corradini, S. Carretta, P. Santini, G. Amoretti, F. Tuna, G. Timco, R. E. P. Winpenny, *J. Phys D : Appl. Phys.*, 2007, **40**, 2999

Chapter 2:

Design, synthesis and characterisation of *p*-terphenyl-3,5,3',5'-tetracarboxylic acid derivatives for surface deposition studies

2.1 Introduction

As we discussed in the introduction of this thesis, supramolecular architectures can be readily formed in solution,[1-3] solid-state[4-9] or on surfaces,[10-14] provided the right tools are engaged/incorporated in the specifically designed tectons building these assemblies. Among the large variety of accessible tools are the relatively weak and reversible non-covalent interactions such as hydrogen bonding, π–π interactions, metal coordination and much more. We have seen the example of the co-deposition of PTCDI-melamine on a silver terminated silicon substrate yielding the formation of an open two dimensional extended honeycomb network.[14] This network, stabilised by triple hydrogen bonds, exhibits large regular pores in which heptameric C_{60} clusters have been encapsulated.[14] This study showed that it was possible to direct the formation of subsequent layers using a designed supramolecular arrangement as a template. A similar example was the deposition of *p*-tetraphenyl-3,5,3',5'-tetracarboxylic acid onto a graphite substrate. The use of coronene as guest template molecule induced the formation of a two dimensional Kagomé network rather than the parallel hydrogen-bonded arrangement observed when the tetraphenyl derivative was adsorbed directly onto the surface.[15]

p-Terphenyl-3,5,3',5'-tetracarboxylic acid has already been successfully synthesised within our group and deposited on HOPG with the collaboration of the Beton group from the School of Physics and Astronomy at the University of Nottingham. This molecule was chosen because the positions of the four carboxylic acid groups would promote directional intermolecular hydrogen bonding. Two possible relative configurations, stabilised by double hydrogen bonds (R^2_2 (8) graph set), termed as parallel or arrowhead (Figure 2.1b and 2.1c respectively), which differ in the placement of the neighbouring molecules, are observed.

A small amount of a saturated solution of *p*-terphenyl-3,5,3',5'-tetracarboxylic acid in nonanoic acid was deposited on freshly cleaved HOPG surface and the solution/substrate interface was imaged using scanning tunnelling microscopy (STM) technique.
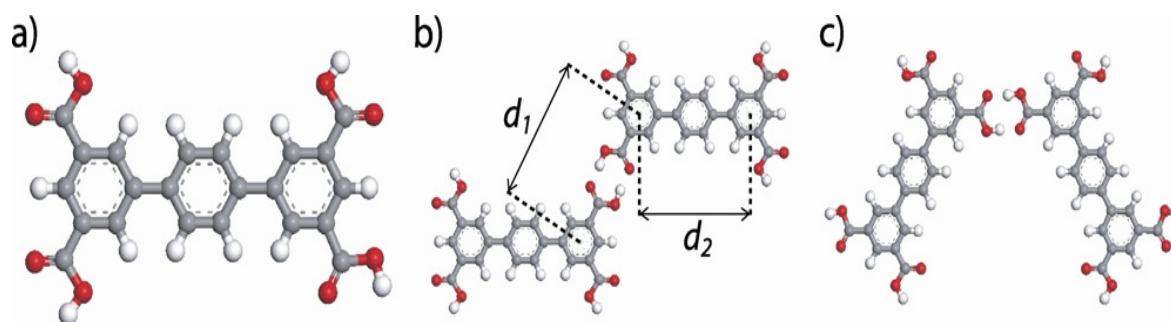
Figure 2.1 (A) Molecular structure of *p*-terphenyl-3,5,3',5'-tetracarboxylic acid (TPTC). Arrangements for a pair of molecules linked through a carboxylic acid-carboxylic acid hydrogen bond, (B) parallel: with the long axes of both molecules parallel to each other, and (C) arrowhead: with one molecule rotated by 60° with respect to the other. Marked on (B) are the calculated distances between two phenyl rings of different TPTC molecules taken across a carboxylic-carboxylic hydrogen-bond (d_1), and the distance between the two end phenyl rings of a single TPTC molecule (d_2).[16]

Figure 2.2a shows a characteristic region of the network formed on the HOPG substrate. The backbone of the terphenyl molecules appear as bright rod-like features on the STM image. A hexagonal orientational order can be noticed, however, the as-formed network displayed no translational symmetry. It was calculated that the hexagonal array has a period of 16.6 ± 0.8Å oriented at an angle of ± 6 ° towards the substrate.[16] For clarity, the blue dots overlaid on Figure 2.2a correspond to depressions or pores and not to as-mentioned hexagonal array. Although the pores of the network are regularly arranged, they are not all made up with the same arrangement of terphenyl molecules. Five types of different pores can be

distinguished, as described in Figure 2.2b to 2.2f, differing by the number and orientation of terphenyl molecules constituting the pores.

Figure 2.2b shows a hexagonal pore made up with three terphenyl molecules with edges alternating from a molecule backbone and a hydrogen-bond. In Figure 2.2c and 2.2d, four terphenyl molecules are making up the two different types of pores each one containing two terphenyl backbone edges.
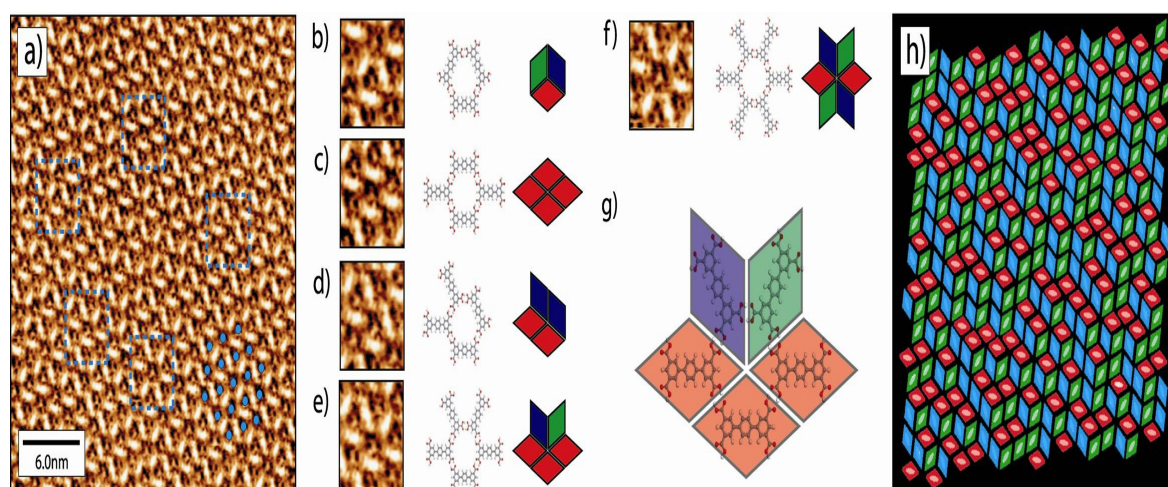
Figure 2.2 (a) STM image of a typical area of the terphenyl network at the nonanoic acid/HOPG interface. The group of three phenyl rings constituting the backbone of the molecules appear as bright rod like features in the image. The hexagonal orientational order of the structure is highlighted by the group of blue dots in the lower right hand corner of the image marking the location of dark contrast regions in the image (depressions/pores in the network). (b-f) Molecular diagrams and tiling representations for the five possible arrangements of the terphenyl molecules around a network pore. Also shown are magnified STM image examples of each pore type from (a), the locations of the magnified regions are marked in (a) by a blue dashed squares. Scanning conditions: (a), tunnelling current I_t = 0.015nA, tip voltage V_t = 1200mV. (g) Enlarged version of the molecular arrangement shown in (e). The equivalent tiling representation is shown as a transparent overlay which highlights the location of the carboxylic acid-carboxylic acid hydrogen-bonds at the midpoint of edges between tiles. (h) Corresponding tiling representation of (a), the colouration of (h) represents the three possible orientations of rhombi within the tiling (red, green, and blue). Idealised representations of the molecular positions are shown faintly in the tiling.[16]

The hexagonal arrangement in Figure 2.2e and 2.2f contains five and six terphenyl molecules respectively with only one terphenyl edge for the pore in Figure 2.2e while the pore in Figure 2.2f displays no terphenyl edge at all. The distances d_1 and d_2 depicted in Figure 2.1b corresponding to the lengths of the hydrogen-bonded edge and the terphenyl edge respectively were calculated to be 9.6 and 8.7 Å. Because the intermolecular binding energy for the parallel and arrowhead configurations is the same,[16] the pores were estimated to be between 15.8 Å (Figure 2.2b) and 16.6 Å (Figure 2.2f) wide which agreed with the measured periodicity. The network is therefore built up by combining these five types of different pores in such a manner that some orientational order exists but no translational symmetry.
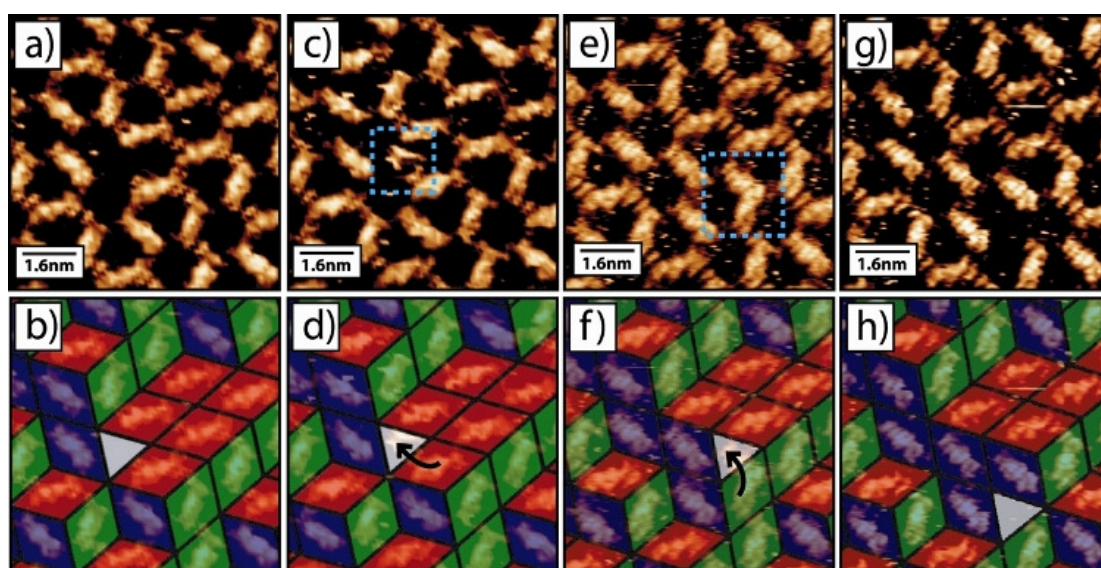
Figure 2.3. (A, C, E, and G) STM images showing two separate movements of a single defect through the network structure. (B, D, F, and H) Tiling representation of the network structure during the defect motion. The effective rearrangements of rhombi in the tiling are marked by the black arrows in (D) and (F). Transient image artefacts observed within the defect site prior to defect motion are highlighted by blue dashed squares (C and E). Scanning conditions: (all images) tunnelling current $I_t = 0.021$nA, tip voltage $V_t = 1200$mV.[16]

The molecular network can be represented as a rhombus tiling where each rhombus is virtually defining one molecule pointing in one of the three possible high-symmetry direction (each rhombus with the same orientation has been attributed the same colour). Also, it can be noticed that the midpoint of each rhombus edge corresponds to the hydrogen-bonds linking two terphenyl molecules (Figure 2.2g). Figure 2.2h shows the representation of the molecular network seen in Figure 2.2a using the rhombus tiling. The orientational order is conserved in this mapping and the lack of translational symmetry is highlighted by the fact that there is clearly no order in the rhombi arrangement.

Another interesting feature that has been observed in this network is the presence of tiling defects in the form of triangular voids which appear totally confined by the rhombi (Figure 2.3). The existence of such defects have been examined theoretically in numerous previous studied but never observed experimentally.[17-19] The occurrence of these topological defects was estimated to around 3×10^{-3} defects per adsorbed molecule. These defects have been shown to migrate through the network (Figure 2.3c to 2.3h) giving rise to a re-ordering of individual molecules within the network in view of, possibly, reducing transitions between local energy minima. This observed rhombus tiling system was also determined to be random through a complex analysis following theoretical studies[20-22] and described as dynamically arrested which makes it an effective model for the study of materials such as structural glasses.[23-26] It was thus demonstrated through the scope of this study that the *p*-terphenyl-3,5,3',5'-tetracarboxylic acid molecule does form a network too, when deposited on surfaces, presenting a hexagonal directional order with no sign of transitional symmetry. Therefore, one can ask the question of whether it is possible to modify the present

network by altering the molecule constitutive of this array with the tools accessible to chemists. This is the concept underlying the work presented in this chapter.

This chapter describes the efforts made towards the synthesis of *p*-terphenyl-3,5,3',5'-tetracarboxylic acid derivatives towards surface deposition purposes. The first target molecule we aim to synthesise is the *p*-terphenyl-3,5,3',5'-tetracarboxylic acid mentioned so far throughout the introduction. The objective is to investigate whether it is possible to guide the formation of another type of network on the surface using, for instance, a guest template molecule as it has been realised in the studies mentioned previously. Another fundamental but nonetheless interesting aspect and challenge is to gain insight into the solid-state chemistry of this molecule. Crystal structures have been described for metal-organic framework (MOF) compounds containing this molecule as a ligand,[27] but no single crystal constituted solely of this terphenyl tetracarboxylic acid has been reported so far to our knowledge.

The second direction we can give to this project is to work on the design and elaborate an improved version of this *p*-terphenyl-3,5,3',5'-tetracarboxylic acid trying to pre-consider what effects the chemical changes brought to the molecule would have on the network that will perhaps form on surfaces. With this perspective in view, the second target molecule to be synthesised will bear groups on the side of the central phenyl ring to distort somehow the network, perhaps modifying the size of the pores or even bring a certain topological dimensionality to the network as the benzyloxy groups to be introduced would potentially tilt the molecule and therefore render the molecule incapable of sitting flat on the surface.

Finally a new strategy was envisaged for the design of the third and last target compound of this chapter. So far, we have seen examples where molecules were designed to form a specific pattern on surfaces and once observed, this pattern acted as a template for the further deposition of a second type of guest molecule. Or even, the use of guest template molecules mediated the formation of a different, less stable network. What if it was possible to design a molecule that possessed the right tools to self-assemble when deposited on a substrate but also that possessed the relevant functionalities to induce an active chemical role within an ordered array? Such an approach would be a one pot procedure to deposit a certain type of functionality on a surface while controlling the regular spacing and the positioning of this functionality at a molecular scale. This can potentially be achieved with introducing ethynylferrocenyl groups on both sides of the central phenyl ring, the ferrocenyl moieties being chosen because of their advantageous redox properties. The exciting breakthrough would be to be able to control the position and the spacing of the ferrocenyl groups on the surface. Because of the potential applications we are envisaging, some electrochemical experiments will be performed on this molecule not only for the sake of studying its electrochemical behaviour but also to elucidate the question of electronic communication between the two metal centres.

The challenge in this project is far from being a synthetic challenge as the chemistry involved in the preparation of the target compounds should not pose any major issue. Having said that, the limitations we are likely to encounter concern the actual ability to grow crystals of these terphenyl derivatives as the solubility of these tetracarboxylic acids is expected to be very low in most organic solvents. The other difficulty will reside in the potential achievement of the desired ordered network or

even the observation of any network on surfaces, as in some cases even if all the tools

required for network formation are gathered, the network does not always form.

2.2 Results and Discussion

2.2.1 Molecular synthesis

a) Synthetic strategy to the desired molecules

For the three desired tetracarboxylic acid terphenyl ring derivatives, the same synthetic strategy has been employed. Namely the central phenyl ring (i.e. the spacer) was first synthesised, then coupled to both external phenyl rings using 3,5-di(ethoxycarbonyl)phenylboronic acid (or 3,5-dimethylphenylboronic acid) employing a Suzuki coupling methodology.[28] In the first case, a simple deprotection reaction of the carboxylic acid groups would lead to the desired tetracarboxylic acid terphenyl ring derivatives. In the second case, further oxidation of the four methyl groups would be required to access the corresponding tetracarboxylic acid terphenyl molecule, as depicted in Scheme 2.1.

It has been thought that it is much simpler and easier, in terms of synthetic routes and yields, to first design the spacer (and therefore introduce the desired functionality in the molecule) and then to couple it to the external phenyl rings, rather than preparing first the molecule backbone and then introducing the desirable substituents on the side. Therefore the latest approach has not been envisaged over the course of the present study. The Suzuki coupling conditions have been tailored for each target molecule to give the best yields possible in each case taking into account the solubility, stability and availability of the starting materials.
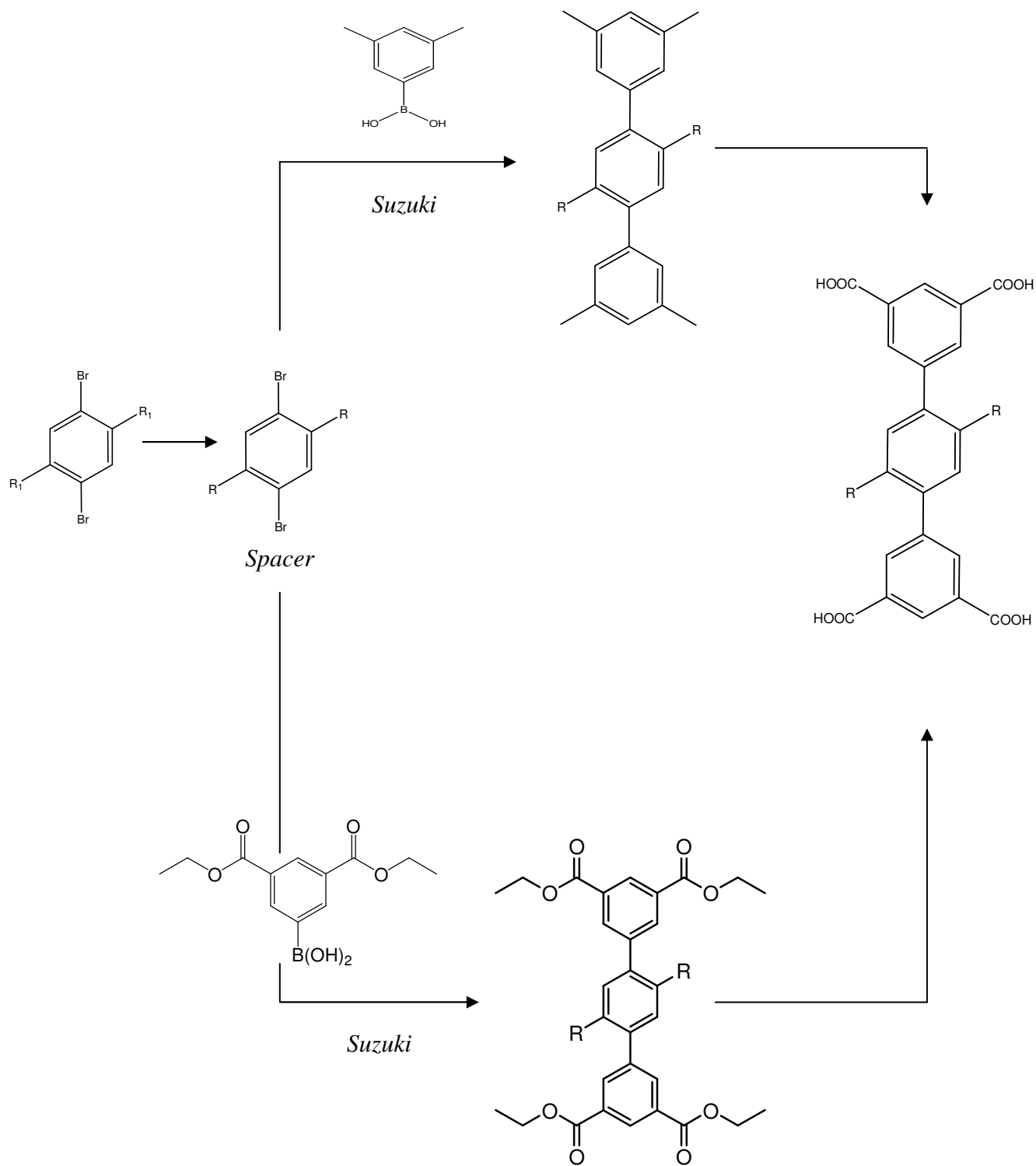
Scheme 2.1. Synthetic strategy used for the design of the target molecules.

The Suzuki coupling reaction is the coupling between organoboronic acids or boron-esters with organohalides or pseudohalides (such as triflates) catalysed by a palladium (0) complex. It is one of the most versatile reactions for the selective formation of carbon-carbon bonds, especially for the preparation of biaryl compounds.[29] Because of the stability and low toxicity of boronic acids and boronate esters, the Suzuki coupling reaction is commonly thought as a preferable alternative to the use of other coupling reactions such as for example the Stille coupling, which is considered less environmentally-friendly given the toxicity of tin-based intermediates and by-products formed during such reaction. The Suzuki reaction proceeds following the mechanism outlined in Figure 2.4.
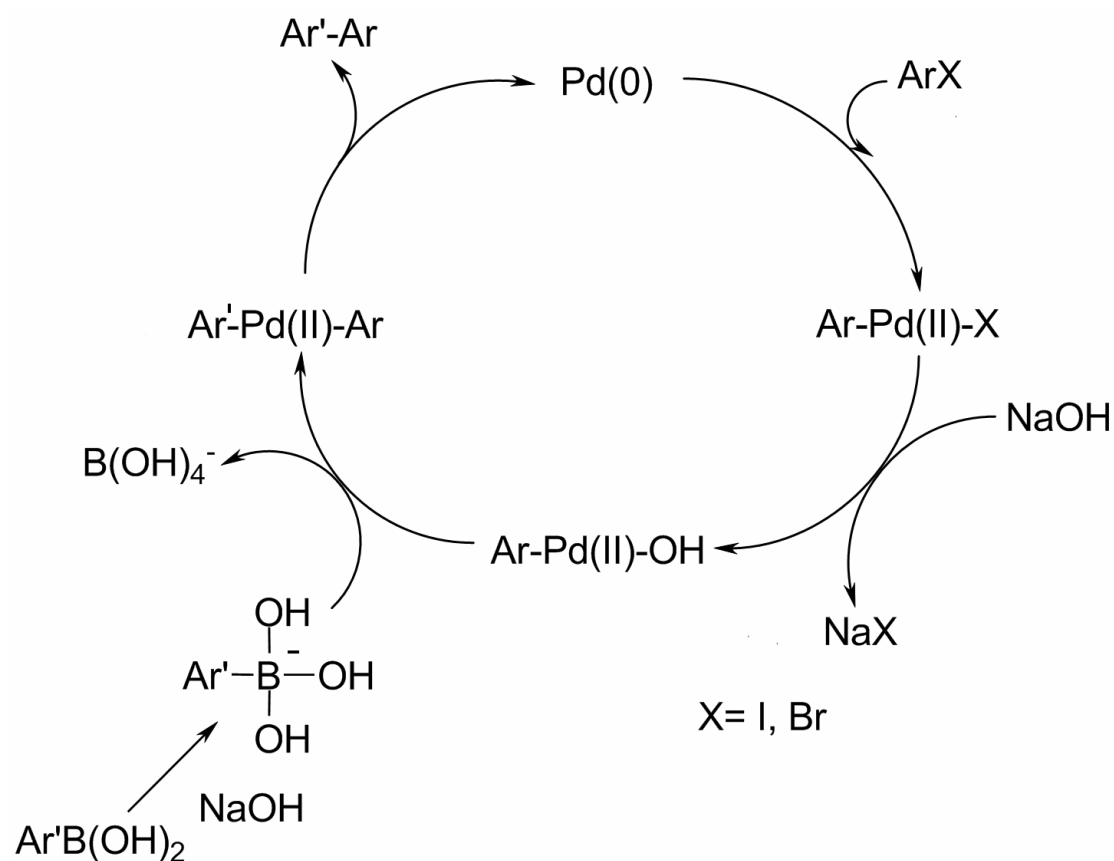
Figure 2.4. Catalytic cycle for the Suzuki reaction.

As depicted in Scheme 2.2, the boronic acid, either 3,5-dimethylphenylboronic acid or the corresponding ester 3,5-di(ethoxycarbonyl)phenylboronic acid, had to be synthesised. The synthesis was performed in situ in two steps for the first molecule, starting from 1-bromo-3,5-dimethylbenzene, making the Grignard reagent which was then treated with trimethyl borate to obtain the final boronic acid. Purification by recrystallisation in hot water yielded the white pure solid, in relatively low yield (35%). The carboxylate ester was prepared in good yield in two steps. The oxidation of the former 3,5-dimethylphenylboronic acid was followed by the esterification of 3,5-dicarboxylatephenylboronic acid.
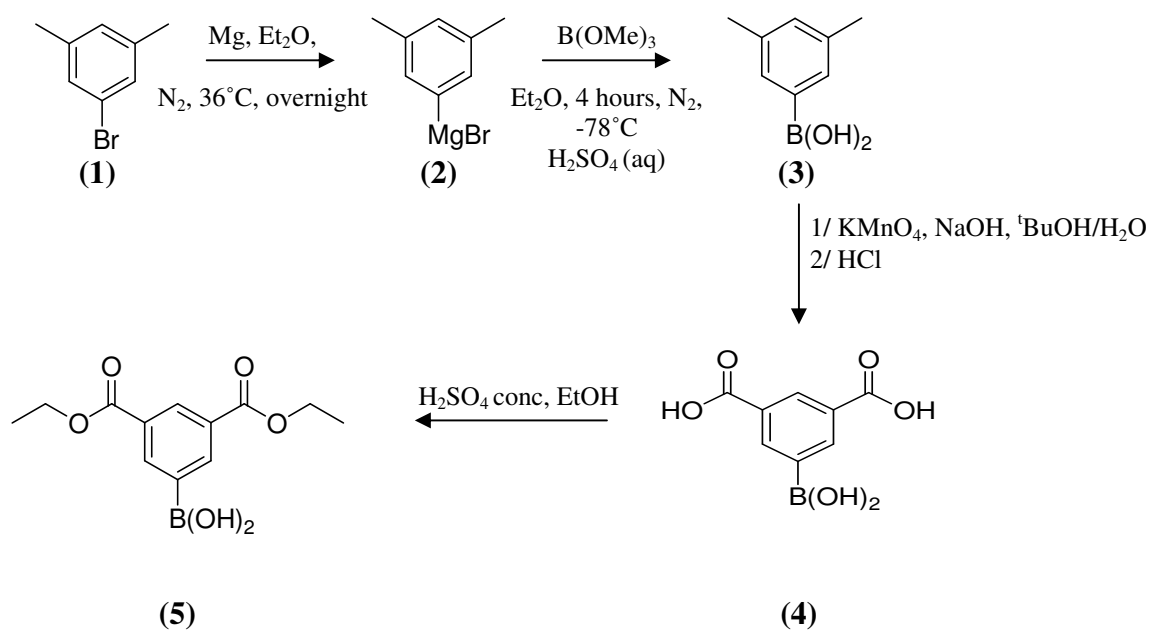
Scheme 2.2. Synthesis of the boronic acid (4) and corresponding carboxylate ester (5).

b) Synthesis of *p*-terphenyl-3,5,3',5'-tetracarboxylic acid

The first target molecule to be prepared was *p*-terphenyl-3,5,3',5'-tetracarboxylic acid. This molecule is the simplest version with no substituent on the side of the spacer and presents no added additional functionality. The four carboxylic acid groups are included in the molecular design as they have the ability to form strong hydrogen bonds and therefore potentially self-assemble on surfaces. *p*-Terphenyl-3,5,3',5'-tetracarboxylic acid has already been successfully synthesised within our group [15-16] using both strategies mentioned above, see Scheme 2.1. The aim of this synthesis here was twofold, firstly synthesising more compound to continue surface studies (with the collaboration of the University of Nottingham, School of Physics and Astronomy) and deepen our knowledge on the characteristics and properties of the molecular self-assembly previously observed on surfaces.[15-16] The second aim was to potentially grow, for the first time, crystals of this molecule to study the solid state chemistry of this compound which would in turn give more insight into its structure-property relationship.

For this first target molecule, there was no need to synthesise the spacer as 1,4-dibromobenzene **(6)** is commercially available. Therefore the Suzuki reaction could be directly performed, using the conditions previously utilised within the group, by reacting **(6)** with the previously synthesised boronate ester **(5)** (Scheme 2.2) and K_3PO_4 as a base in freshly degassed 1,4-dioxane at reflux under inert atmosphere for 3 days (Scheme 2.3). The ester protected molecule **(7)** was then purified by column chromatography and obtained with a relatively good yield.

The final step to access the first target molecule was the deprotection of the carboxylic acid groups.
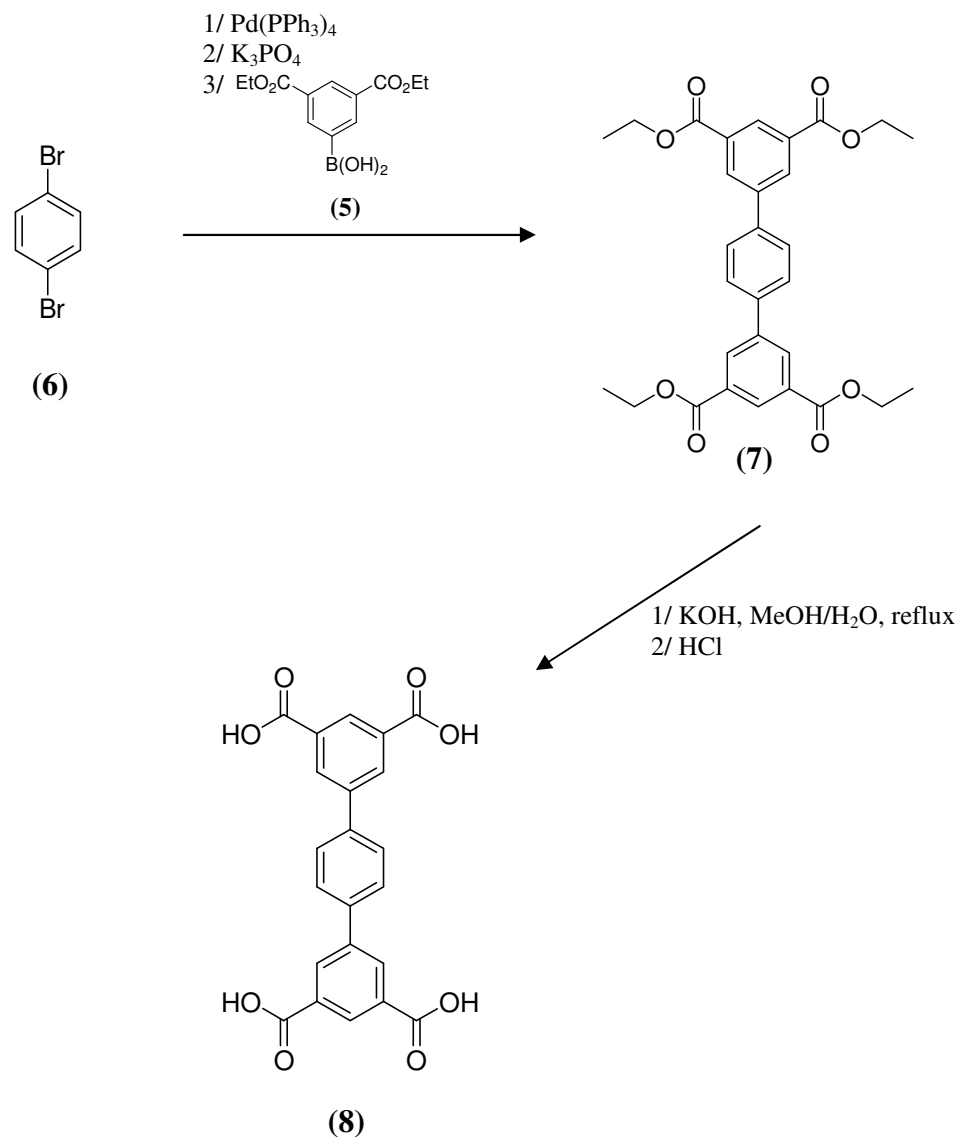
Scheme 2.3. Synthesis of *p*-terphenyl-3,5,3',5'-tetracarboxylic acid (8).

This was typically carried out using a large excess of base, here potassium hydroxide, in a mixture methanol/water at reflux overnight. *p*-Terphenyl-3,5,3',5'-tetracarboxylic acid **(8)** was obtained as a white solid (90%) and the purity of the compound was confirmed by ^{1}H and ^{13}C NMR spectroscopy and elemental analysis techniques. As

mentioned above, one of the aims of the present synthesis was to be able to grow single crystals. After several attempts, suitable crystals for X-ray diffraction studies were obtained by slowly diffusing a solution of MeOH into a DMF solution of the compound, see below for a discussion of the resulting structure.

c) **Synthesis of *p*-terphenyl-2'',5''-bis(benzyloxy)-3,5,3',5'-tetracarboxylic acid**

The second target molecule to be prepared was the *p*-terphenyl-2'',5''-bis(benzyloxy)-3,5,3',5'-tetracarboxylic acid. The addition of groups on both sides of the molecule was intended to introduce distortion into the molecular framework and therefore influence the configuration the molecule will adopt once deposited on a surface. This would also affect the solid-state behaviour of this new tetracarboxylic terphenyl derivative.

The first step towards this second target molecule was to prepare the spacer. This was done easily by reacting 3,5-dibromo-2,4-dihydroxyquinone with benzylbromide as depicted in Scheme 2.4. Purification by column chromatography yielded pure 1,4-bis(benzyloxy)-2,5-dibromobenzene **(10)** as confirmed by NMR and elemental analysis.

(9) **(10)**
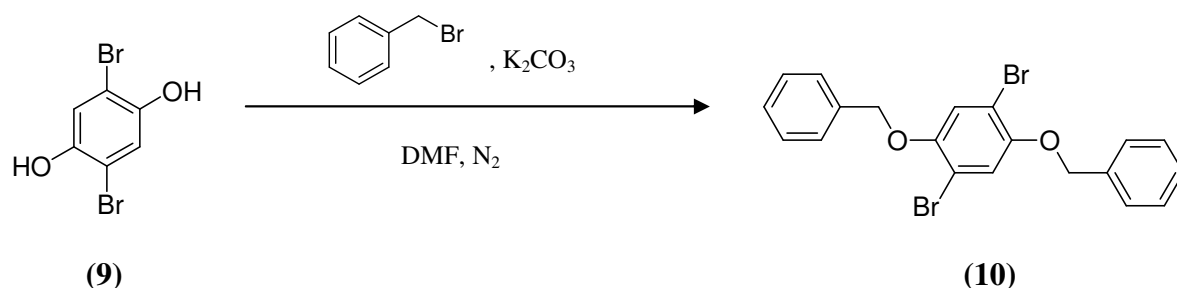
Scheme 2.4. Synthesis of 1,4-bis(benzyloxy)-2,5-dibromobenzene.

The second step is the Suzuki coupling reaction with either the 3,5-dimethylphenylboronic acid to obtain the tetramethyl terphenyl derivative, or directly with the boronate ester to follow the same route as previously described for **(8)** (Scheme 2.5). Both strategies were performed for the synthesis of the second target molecule. 2'',5''-Bis(benzyloxy)-3,5,3',5'-tetramethyl-p-terphenyl **(11)** was synthesised in a 40% yield (after purification) using EtOH and Cs_2CO_3 as solvent and base respectively (Scheme 2.5).
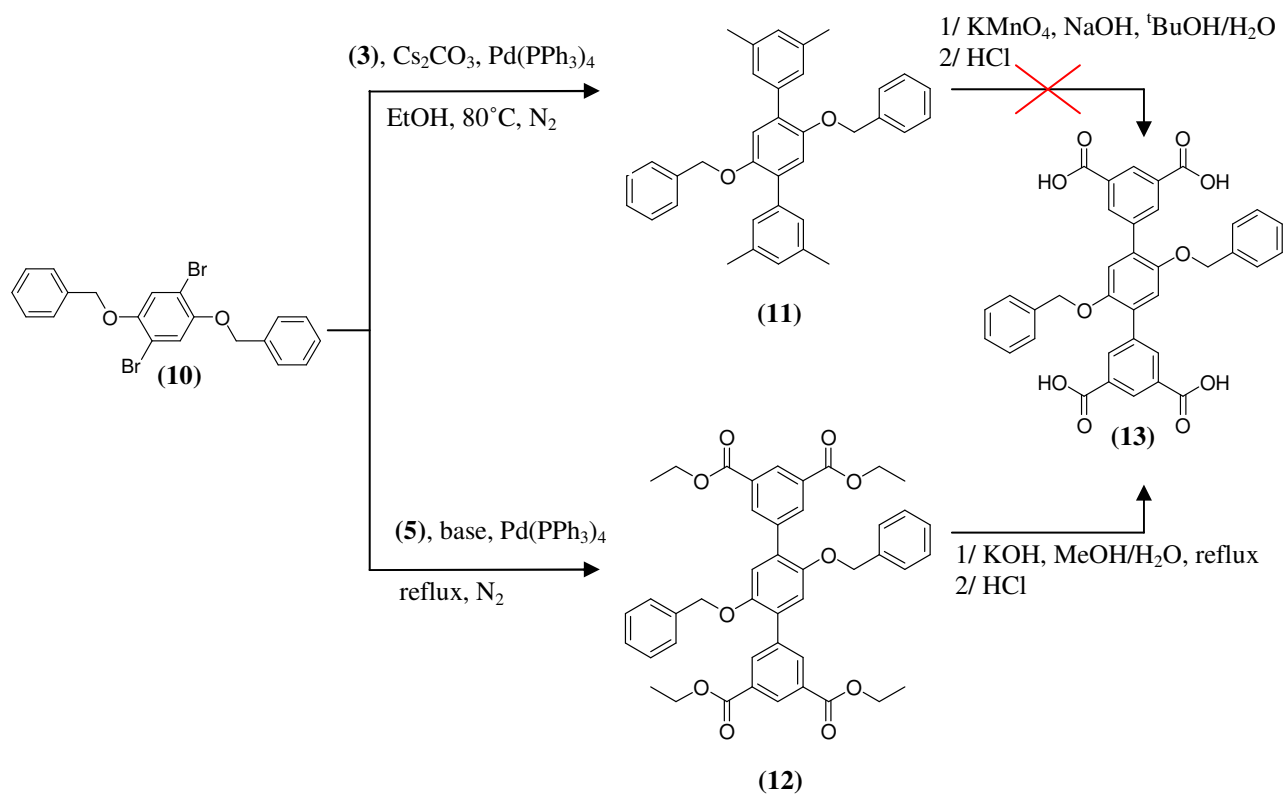
Scheme 2.5. Synthetic pathway to *p*-terphenyl-2'',5''-bis(benzyloxy)-3,5,3',5'-tetracarboxylic acid (13).

41

However the oxidation step proved to be unsuccessful despite many efforts. The suggested explanation is that KMnO$_4$ might perhaps cleave the benzyloxy groups on the side groups as well. As a matter of fact, alkyl-group side chains are readily attacked by oxidizing agents, being converted to carboxyl groups. However the mechanism requires a C-H bond at the position next to the aromatic ring to produce benzylic radicals. This requirement is clearly fulfilled by the four methyl groups situated on the external phenyl rings but it is also unfortunately the case for the benzyloxy groups of the spacer. Nevertheless no concrete evidence has been found to comfirm this theory.

Therefore, in order to successfully synthesise this target molecule, the second strategy previously described (and used for the first target compound (**8**)) was carried out. Several conditions were employed for the Suzuki coupling reactions to improve and obtain a decent yield. The data are summarized in Table 2.1.

Table 2.1. Suzuki reaction conditions used for the synthesis of (12).

	Base	Solvent	Tp (˚C)	Yield (%)
Conditions 1[a]	Na$_2$CO$_3$	toluene	110	22.5
Conditions 2[b]	K$_3$PO$_4$	1,4-dioxane	101	50
Conditions 3[c]	2M aq.Na$_2$CO$_3$	toluene	110	71

2.5 eq. of boronic ester[a,b], 3.5 eq. of boronic ester[c], 0.07eq. of Pd(PPh$_3$)$_4$[a,b,c].Yields are for products following purification.

In the first conditions employed, the poor yield obtained can be explained by the lack of solubility of the base in the medium whereas the starting material (**10**) would only partially dissolve in dioxane in the second set of conditions. However, an average 50 % yield (after purification) could still be reached. An interesting point to

be noted is that these same conditions were employed for the preparation of **(7)** and the molecule was obtained with a slightly higher yield (60%). Despite the lack of solubility of the 1,4-bis(benzyloxy)-2,5-dibromobenzene in dioxane, another possible explanation is that the reaction seems sensitive to the electronic effects of the substituents attached to the spacer. The electron donating benzyloxy groups may also be one cause of the poor coupling yield observed. As shown in Table 2.1, the best conversion was obtained when using a 2M aqueous solution of Na_2CO_3 in toluene at reflux. It appears that the relative solubility of the base is crucial for the coupling to take place, thus the use of a biphasic solvent system. A toluene/H_2O solvent system proved to be a better alternative.

Finally, the deprotection step (Scheme 2.5) led to the target molecule **(13)** as a white solid (91%). The purity was assessed by NMR and elemental analysis techniques. Suitable crystals for X-ray structure analysis were obtained by slow diffusion of a MeOH solution into a DMF solution of the compound, see below for a discussion of the resulting structure.

d) Synthesis of *p*-terphenyl-2'',5''-bis(ferrocenylethynyl)-3,5,3',5'-tetracarboxylic acid.

The third and final target molecule of this chapter is *p*-terphenyl-2'',5''-bis(ferrocenylethynyl)-3,5,3',5'-tetracarboxylic acid. This molecule represents, in terms of design, an advanced model of the two previous compounds **(8)** and **(13)**. While the first two molecules were about designing a network and altering its properties by introducing specific functionalities that would perhaps direct and therefore modify the self-assembly observed on surfaces, the third target compound is

a more elaborated version. The idea is not only to design a molecule capable of self-assembly on surfaces and forming a specific and tailored network, but also to design a molecule that possesses the desired functionality that we want to position within the network. In other words it can be viewed as a one pot procedure in order to direct the formation of a regular spacing of a certain functionality and control its positioning on a surface. The third target compound consists of the *p*-terphenyl-3,5,3',5'-tetracarboxylic acid backbone with ethynylferrocene groups on both sides of the spacer. The ferrocenyl moieties have been chosen because of their advantageous properties, namely their high stability and redox and/or spin activity. Here again, the spacer was synthesised first (Scheme 2.6) using a Sonogashira coupling.

The Sonogashira reaction is the coupling between terminal alkynes with aryl or vinyl halides.
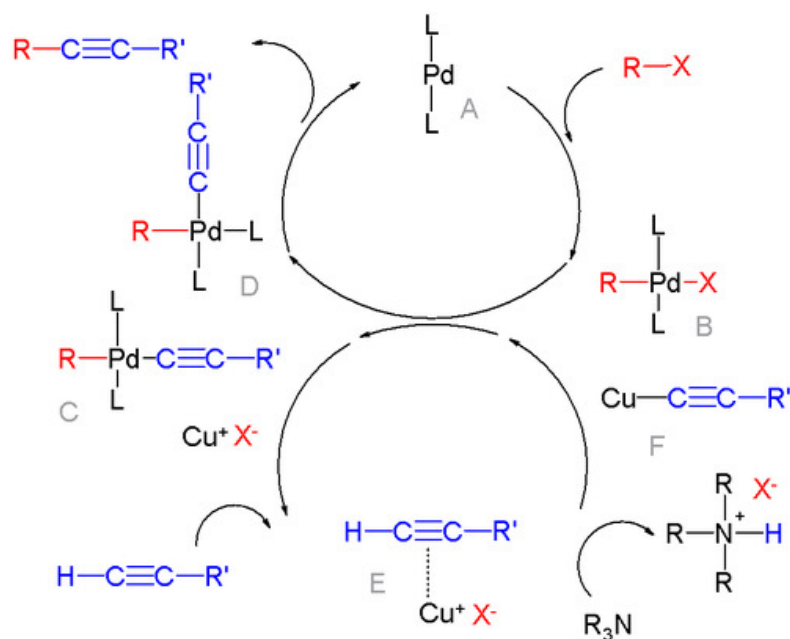
Figure 2.5. Sonogashira reaction mechanism as proposed in mechanism textbook.[30]

Typically the use of a palladium(0) complex and a halide salt of copper(I) as catalyst and co-catalyst respectively is required for this reaction. Moreover, the medium needs to be basic to neutralize the hydrogen halide released during the coupling, thus the use of amine compounds sometimes even used as solvents. Although the mechanism of this coupling reaction is not fully understood, a mechanism involving a palladium cycle and a copper cycle has been proposed (Figure 2.5).[30]

The starting materials for the Sonogashira coupling needed to be prepared, starting from 1,4-dibromobenzene to get the 1,4-dibromo-2,5-diiodobenzene (14) using slight modifications on the conditions reported in the literature.[31] Ethynylferrocene was prepared in two steps[32] reacting ferrocenecarboxaldehyde (15) with triphenylphosphine and carbon tetrachloride in acetonitrile to obtain 1,1-dichlorovinylferrrocene (16) as a red crystalline solid.
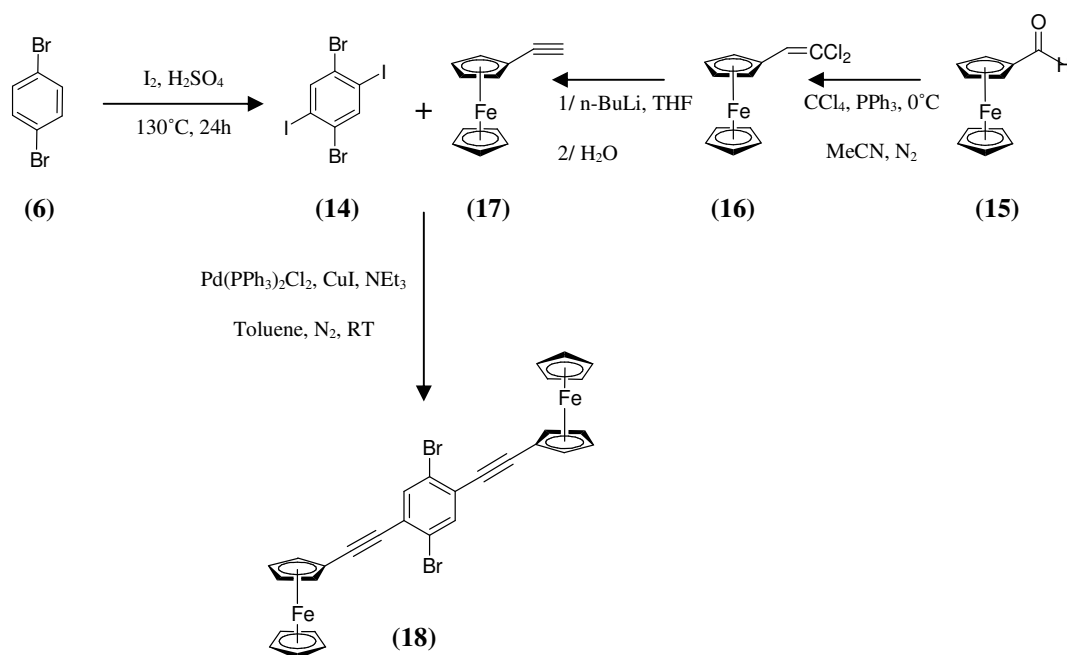
Scheme 2.6. Synthetic route employed to prepare (18).

The latter was then treated with n-Buli in THF to obtain the final product **(17)** which was purified by column chromatography. The following step was the Sonogashira coupling reaction which was found to be more difficult that anticipated. The major limitation encountered was the competitive homocoupling side reaction where two ethynylferrocene moieties couple together. The amount of side product generated was almost independent of the reaction conditions. Hence several parameters were adjusted to maximise the hetero-cross-coupling reaction. It was observed, as reported previously,[33-36] that the reaction needed drastic anaerobic conditions as oxygen was the predominant cause for acetylene-acetylene coupling. Adding the solution of ethynylferrocene dropwise into the solution of arylhalide **(14)** proved to be also quite useful to significantly diminish the yield of homo-coupling. With all these precautions, the desired compound **(18)** was successfully prepared with a relatively good yield (65%).

Once the spacer was designed, the next step was the Suzuki coupling reaction to get the terphenyl derivative **(19)** (Scheme 2.7). For solubility reasons, the reagent system Na_2CO_3/Pd(PPh$_3$)$_4$/toluene was used. However in the first attempted synthesis, only a poor yield (12%) could be obtained. This was probably due to the lack of solubility of the mineral base in toluene, as outlined previously in this chapter. Therefore the system was readjusted to the biphasic system Na_2CO_3/Pd(PPh$_3$)$_4$/toluene/H_2O employed previously, which led to a significant increase in the yield (60% after chromatographic purification). The orange solid was fully characterised with the usual techniques. The ^{1}H NMR spectrum showed two signals at 4.21 and 4.38 ppm corresponding to the protons on the substituted Cp rings. The characteristic $\nu(C \equiv C)$ stretching modes were observed distinctively at ~2200 cm^{-1} in the IR spectrum which

also confirmed the presence of the acetylene units. However, at this stage an extremely pure sample of the compound was needed for two reasons. Firstly, the tetracarboxylic target molecule was anticipated to be highly insoluble in most solvents making the purification highly difficult at the final synthetic step and a highly pure sample is a paramount requirement for the surface deposition studies.

The second reason, specific to this compound, is that we had to ensure no communication between the two ferrocenyl moieties in the molecule, prior to subsequent surface deposition studies. The electronic communication between two iron centres is considered, for the present purpose of this application, as an undesirable phenomenon. The electronic/redox properties of the compound would therefore have to be verified by electrochemistry experiments. Because of the anticipated solubility issues mentioned above, the electrochemistry work had to be performed on (19), rather than (20). Hence this compound had to be extremely pure. Attempts to grow crystals were thus carried out, and single crystals suitable for X-ray diffraction studies were obtained by carefully layering an equal volume of hexane on top of a saturated solution of the compound in CH_2Cl_2.
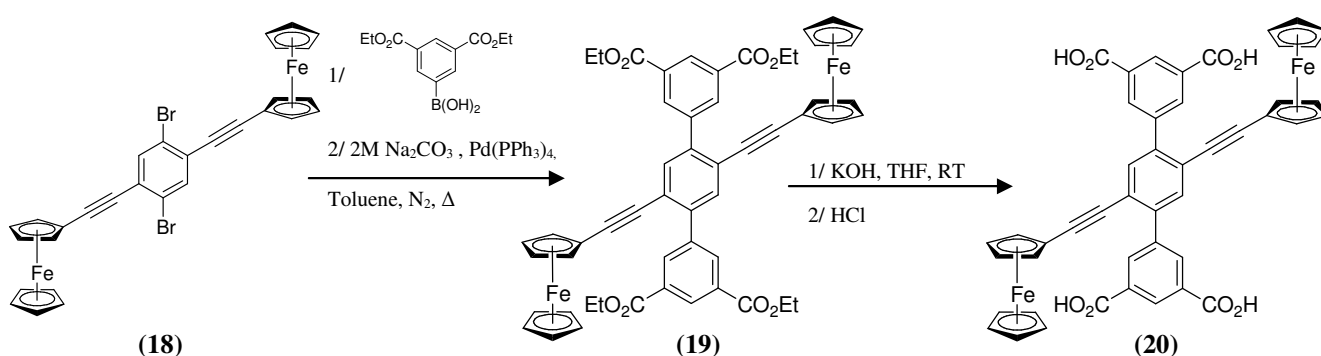
Scheme 2.7. Synthetic route to (20).

47

The deprotection step of **(19)** was not as trivial as it was for the first two target molecules, compounds **(8)** and **(13)**. The reaction did not proceed using the previous deprotection conditions. **(19)** was not sufficiently soluble in the usual MeOH/H$_2$O solvent mixture and it was decided that heating the reaction mixture was undesirable as this may have lead to polymerisation or degradation of the compound. New mild conditions were adopted[37] to deprotect the ester compound (Scheme 2.7). This worked with a relatively good yield (63%) of the final target molecule **(20)**. Elemental analysis and ^{1}H and ^{13}C NMR confirmed that the compound obtained was sufficiently pure to proceed with surface deposition. However, despite recurrent efforts to grow crystals using different types of crystallisation techniques (layering and vapour diffusion) and different solvent systems (DMF/MeOH, DMF/Toluene, DMF/Et$_2$O, etc...), all the attempts failed.

2.2.2 X-ray Crystallographic Analysis

a) Crystal structure of *p*-terphenyl-3,5,3',5'-tetracarboxylic acid (8)

Single crystals of **(8)** suitable for X-ray structure analysis were obtained by slow diffusion of methanol into a saturated DMF solution of the compound. Figure 2.6 shows a representation and the atom-labeling scheme adopted for **(8).** The complex crystallises in the monoclinic space group *P*2(1)*/c* (Table 2.2). The molecule lies on a crystallographic centre of symmetry with the asymmetric unit containing half of the tetracarboxylic acid terphenyl molecule and one dimethylformamide (DMF) solvent molecule. Full lists of bond lengths and angles are given in tables in Appendix A.1.

The phenyl ring in the centre is orientated at a dihedral angle of 31.5 (2)° with respect to the terminal phenyl rings and all three rings are essentially planar with the carboxyl groups only deviating slightly from co-planarity with the aromatic ring (the dihedral angles between the ring C11-C16 and the planes C21/O22/O23 and C31/O32/O33 are 3.0 (2) and 2.1 (2) respectively). The bond lengths and angles are within the range of values commonly reported for similar phenyl esters.

The molecules interact with one another *via* a series of CO-H···OC hydrogen bonds between carboxylic acid moieties to form a one-dimensional infinite chain (Figure 2.7).

The molecules in the chain are arranged alongside each other lengthways connected to each neighbouring molecule by two hydrogen bonds (one donated and one accepted) (Table 2.3). Each molecule has an OH group (O33) at each end not involved in propagating the chain which donates a hydrogen bond to the carbonyl oxygen of a dimethylformamide molecule. In addition, each molecule has two carbonyl groups (O22) directed into the space between neighbouring molecules which are only involved in weak hydrogen bonds to a pair C-H donors (the central phenyl ring of a neighbour in the chain and a methyl group of a dimethylformamide molecule below the chain). All molecules in the chain are approximately coplanar with an offset of only 0.36 Å. The centroid-centroid distance between neighbouring molecules in the chain is *ca* 8.8 Å.

Molecules in adjacent layers are orientated in a direction so that π-π interactions between the terminal isophthalic acid rings of molecules from different planes (below and above) are maximised, to form a two-dimensional layered structure (Figure 2.8).

Table 2.2. Crystal data and structure refinement parameters for compound (8).

Compound	$\mathbf{8}.2(C_3H_7NO)$
Empirical formula	$C_{22}H_{14}O_8.2(C_3H_7NO)$
Formula weight	552.52
Temperature	90(2) K
Wavelength	0.71073 Å
Crystal system	Monoclinic
Space group	P 21/c
a, Å	a = 10.9751(12)
b, Å	b = 8.8065(10)
c, Å	c = 13.1616(15)
β, ˚	93.686(2)
Volume, Å^3	1269.5(2)
Z	2
Density (calculated) Mg/m^3	1.445
Absorption coefficient	0.111 mm^{-1}
F(000)	580
Crystal size (mm^3)	0.13 x 0.09 x 0.07
Theta range for data collection	2.78-27.51°
Index ranges	-14<=h<=11, -10<=k<=11, -16<=l<=17
Reflections collected	7734
Independent reflections	2915 [R(int) = 0.030]
Completeness to theta = 27.50°	99.40%
Absorption correction	Semi-empirical from equivalents
Max. and min. transmission	0.746 and 0.642
Refinement method	Full-matrix least-squares on F^2
Data / restraints / parameters	2915 / 0 / 189
Goodness-of-fit on F^2	1.02
Final R indices [I>2sigma(I)]	R1 = 0.0464, wR2 = 0.111
R indices (all data)	R1 = 0.0556, wR2 = 0.116
Largest diff. peak and hole	0.51 and -0.23 e.Å^{-3}
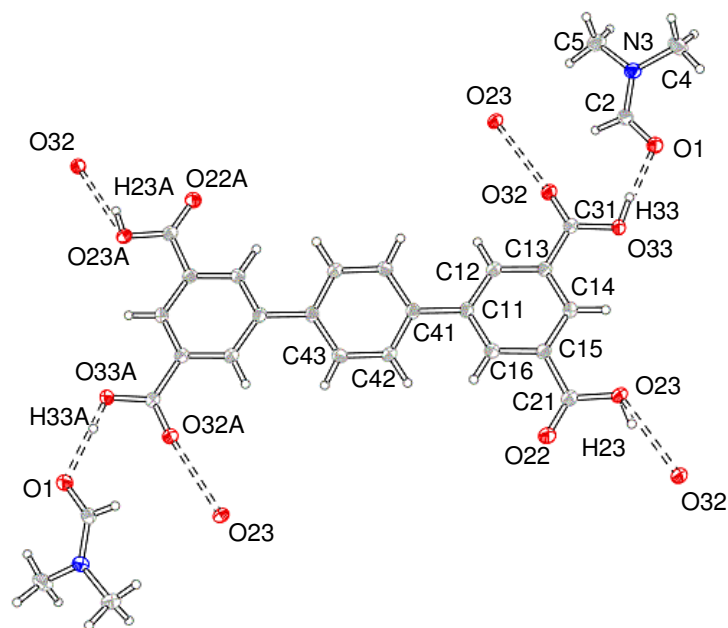
Figure 2.6. A view of molecule (8), showing the atom-labelling scheme. Displacement ellipsoids are drawn at the 50% probability level, hydrogen bonds are shown as dotted lines.
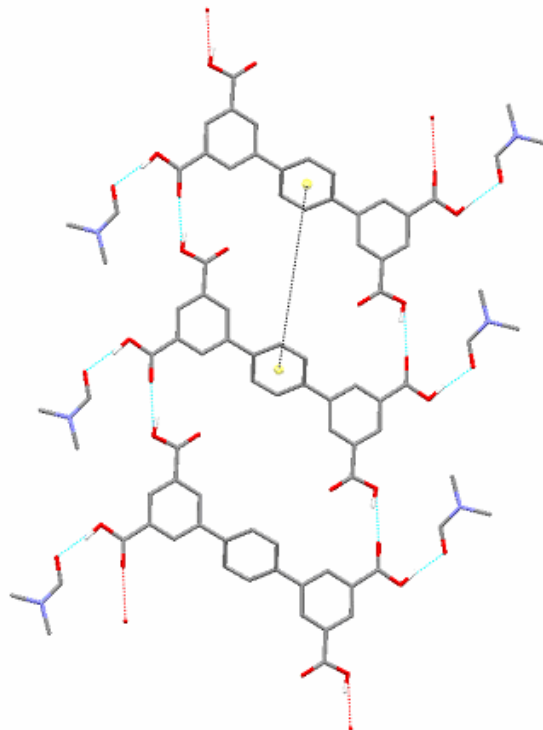
Figure 2.7. 1D infinite chain-type structure. Hydrogen bonds are shown as blue dotted lines. The distance separating two adjacent molecules is *ca* 8.8 Å. H atoms not involved in hydrogen bonding have been omitted for clarity.
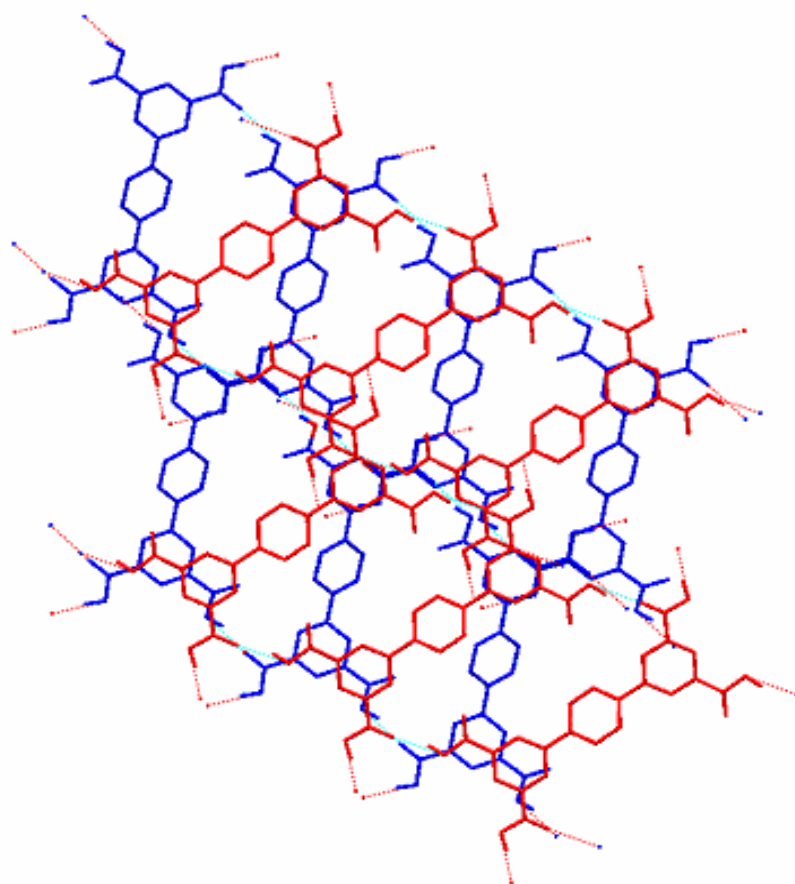
Figure 2.8. 2D structure of (8) showing the relative orientation of adjacent layers towards one another. Hydrogen bonds are shown as blue dotted lines. H atoms not involved in hydrogen bonding and DMF molecules have been omitted for clarity. The blue molecules are located on the plane below the red ones.

Table 2.3. Hydrogen bonding geometries (Å, ˚) for (8).

D-H...A	D-H	H...A	D...A	D-H...A
O33-H33...O1	0.94(2)	1.66(2)	2.6016(16)	171.6(2)
O23-H23...O32^i	0.85(2)	1.82(2)	2.6307(16)	159(2)

Symmetry code: (i) x, y+1, z.

b) Crystal structure of molecule (13)

Single crystals of (**13**) suitable for X-ray structure analysis were obtained by slow diffusion of methanol into a saturated DMF solution of the compound. Figure 2.9 shows the crystal structure of (**13**) as well as the atom-labeling scheme adopted**.** The complex crystallises in the triclinic space group *P*-1 (Table 2.4). The molecule lies on a crystallographic centre of symmetry with the asymmetric unit containing half of the tetracarboxylic acid terphenyl molecule and one dimethylformamide (DMF) solvent molecule.
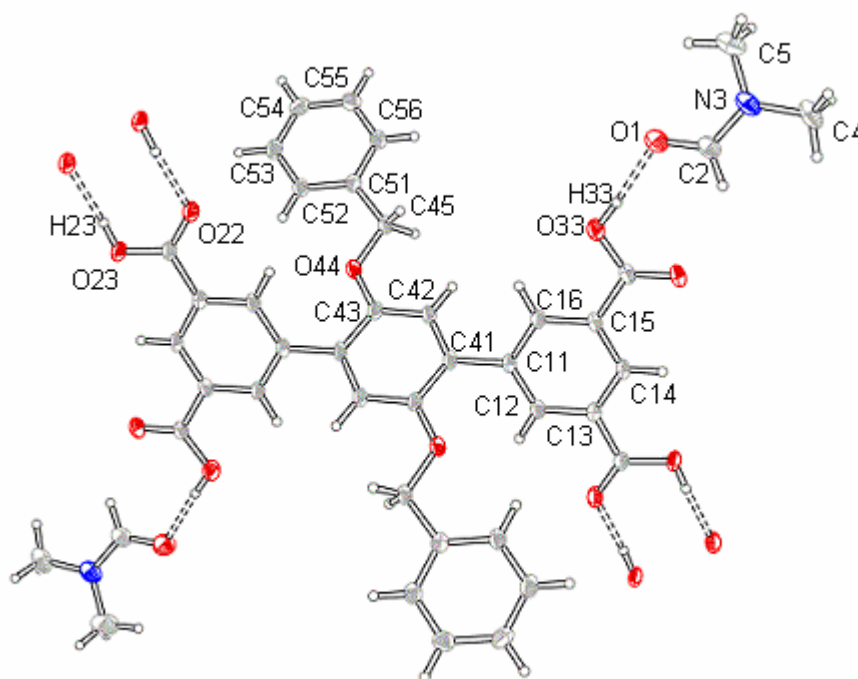
Figure 2.9. A view of molecule (13), showing the atom-labelling scheme. Displacement ellipsoids are drawn at the 50% probability level, hydrogen bonds are shown as dotted lines.

Table 2.4. Crystal data and structure refinement parameters for compound (13).

Compound	**13**.2(C_3H_7NO)
Empirical formula	$C_{42} H_{40} N_2 O_{12}$
Formula weight	764.76
Temperature	90(2) K
Wavelength	0.71073 Å
Crystal system	Triclinic
Space group	P -1
a, Å	8.8842(10)
b, Å	10.6117(12)
c, Å	11.0545(13)
α, °	97.073(2)°
β, °	102.099(2)°
γ, °	109.701(2)°
Volume	937.88(19) $Å^3$
Z	1
Density (calculated) Mg/m^3	1.354 Mg/m^3
Absorption coefficient	0.100 mm^{-1}
F(000)	402
Crystal size (mm^3)	0.24 x 0.11 x 0.08 mm^3
Theta range for data collection	2.09 to 27.50°
Index ranges	-11<=h<=11, -13<=k<=13, -14<=l<=14
Reflections collected	8341
Independent reflections	4237 [R(int) = 0.027]
Completeness to theta = 27.50°	98.10%
Absorption correction	Semi-empirical from equivalents
Max. and min. transmission	0.862 and 0.776
Refinement method	Full-matrix least-squares on F^2
Data / restraints / parameters	4237 / 0 / 257
Goodness-of-fit on F^2	1.03
Final R indices [I>2sigma(I)]	R1 = 0.0465, wR2 = 0.122
R indices (all data)	R1 = 0.0534, wR2 = 0.127
Largest diff. peak and hole	0.43 and -0.23 e.$Å^{-3}$
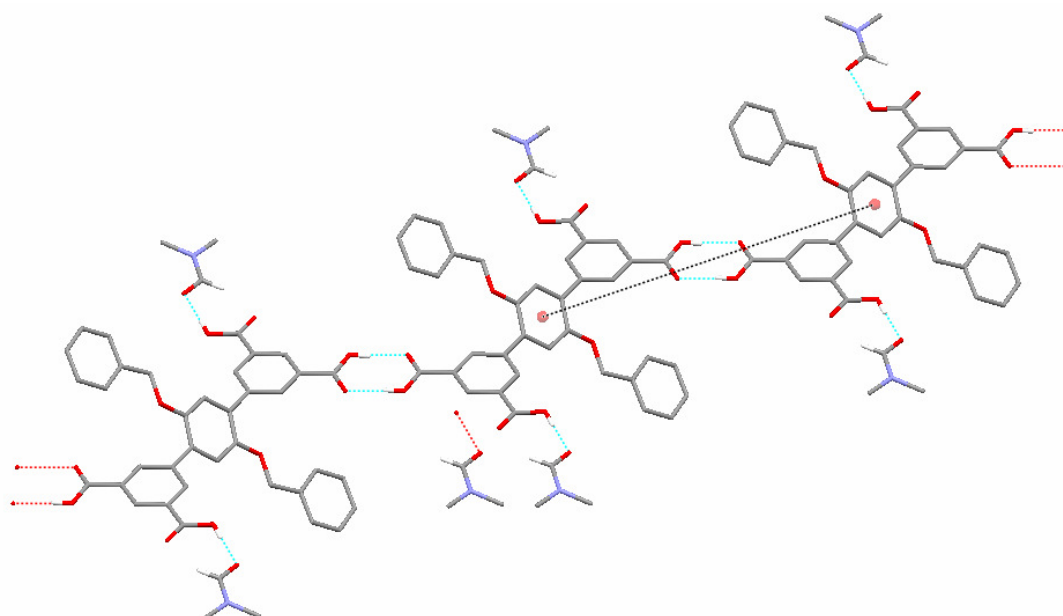
Figure 2.10. 1D infinite chain-type structure. Hydrogen bonds are shown as blue dotted lines. The distance separating two adjacent molecules is *ca* 15.6 Å. H atoms not involved in hydrogen bonding have been omitted for clarity.

The molecule is found to adopt a non planar conformation with the central phenyl ring orientated at a dihedral angle of 47.7˚ with respect to both terminal phenyl rings and all three rings are essentially planar. This confirms that introducing benzyloxy groups on both sides of the molecule leads to a considerable increase in the twisting of the molecule as compared to compound **(8)** (the dihedral angle measured was 31.5 (2) ˚). The bond lengths and angles do not show atypical features and are within the range of values observed for similar compounds.[38-40] (A full list of bond lengths and angles is given in Appendix A.1).

In this case as well, the molecules are linked into one-dimensional infinite chain through their carboxylic acid moieties via pairs of CO-H···OC hydrogen bonds (one donated and one accepted) adopting an $R_2^2(8)$ arrangement (Figure 2.10). In addition, the OH group O33 of each molecule is not involved in propagating the chain but donates a hydrogen bond to the carbonyl oxygen of a dimethylformamide molecule.

As a result of the increased twist of the molecule, the calculated centroid-centroid distance between neighbouring molecules in the chain is also increased (15.6 Å).

Table 2.5. Hydrogen bonding geometries (Å, ˚) for (13).

D-H...A	D-H	H...A	D...A	D-H...A
O33-H33...O1[i]	0.84	1.73	2.5711(14)	174
O23-H23...O22[ii]	0.84	1.77	2.6098(14)	175

Symmetry codes: (i) x, y+1, z, (ii) -x+2,-y+2,-z+1.

c) Crystal structure of molecule (19)

Single crystals of **(19)** suitable for X-ray structure analysis were obtained by layering carefully an equal volume of hexane on a saturated solution of the compound in CH_2Cl_2. A perspective view of the molecular structure of **(19)** and the atom-numbering scheme is illustrated in Figure 2.11. The complex crystallises in the monoclinic space group C2/c (Table 2.6). A full list of bond lengths and angles is given in Appendix A.1. Because the molecule lies on an inversion centre, the asymmetric unit contains only one-half of the centrosymmetric organic molecule. As detailed in the experimental section, the carbonyl group C21=O22 is disordered unequally (87/13) over two orientations. The minor component has been refined isotropically and, in the following, only dimensions associated with the major conformer will be discussed.

All three phenyl rings being fairly planar, the functionalised phenyl ring is tilted at an angle of 59.9 (3)˚ (C43-C41-C11-C12) towards the terminal phenyl rings. The two

terminal phenyl rings do not have the same orientations but are making an angle of 120.4 (2)°. The spacer has an extended conformation, the two ethynyl linkages being essentially linear (the angles being 177.4 (2)° and 176.2 (2)° at C51 and C52 respectively) with a C(52)…C(52') separation of *ca* 8.066 (3) Å which is in good agreement with values reported in the literature for similar derivatives.[41-46] Both cyclopentadienyl rings (Cp) have similar C–C and C–Fe bond distances; the iron atom lies at 1.645 (3) and 1.642 (3) Å respectively from the Cp planes, the slightly longer distance being the distance to the non substituted Cp ring (Fe(1)-Cg distance Cg is the centroid of the Cp ring). Similarly, the bond lengths of the ethynyl linkages C–C≡C–C show no unusual features and are in the range of those observed for similar compounds.[41-46]
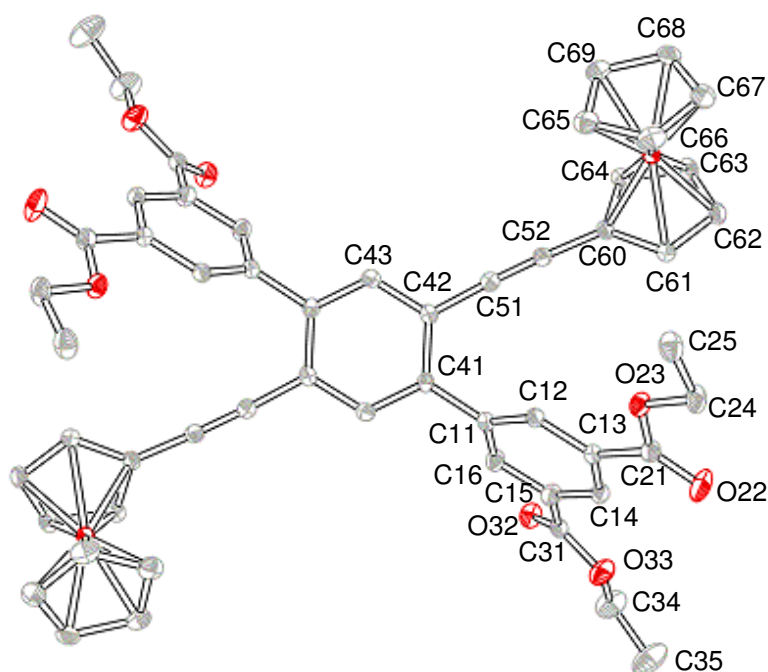
Figure 2.11. A view of molecule (19), showing the atom numbering scheme. Displacement ellipsoids are drawn at the 50% probability level. For more clarity hydrogen atoms have been omitted and only atoms of the major disordered components of the disordered carbonyl group are shown.

Table 2.6. Crystal data and structure refinement parameters for compound (19).

Compound	19
Empirical formula	$C_{54} H_{46} Fe_2 O_8$
Formula weight	934.61
Temperature	90(2) K
Wavelength	0.71073 Å
Crystal system	Monoclinic
Space group	C 2/c
a, Å	34.6730(9)
b, Å	7.3148(2)
c, Å	17.8248(5)
β, °	109.961(2)
Volume, Å^3	4249.2(2)
Z	4
Density (calculated) Mg/m^3	1.461
Absorption coefficient	0.743 mm^{-1}
F(000)	1944
Crystal size (mm^3)	0.11 x 0.06 x 0.04
Theta range for data collection	2.32-27.51°
Index ranges	-44<=h<=44, -9<=k<=9, -23<=l<=23
Reflections collected	16636
Independent reflections	4878 [R(int) = 0.033]
Completeness to theta = 27.50°	99.80%
Absorption correction	Semi-empirical from equivalents
Max. and min. transmission	0.746 and 0.656
Refinement method	Full-matrix least-squares on F^2
Data / restraints / parameters	4878 / 3 / 300
Goodness-of-fit on F^2	1.06
Final R indices [I>2sigma(I)]	R1 = 0.0429, wR2 = 0.113
R indices (all data)	R1 = 0.0484, wR2 = 0.117
Largest diff. peak and hole	0.98 and -0.31 e.Å^{-3}

The Cp rings of each of the ferrocene moieties are approximately eclipsed and almost parallel with an interplanar angle of 1.92˚.

Also an important aspect to describe in this structure is the relative orientation of the ferrocenyl units towards the aromatic ring C41-C43'. The cyclopentadienyl plane is orientated at an angle of 40.1 ˚ from the plane of the central phenyl ring which in turn means that the two ferrocenyl moieties are almost orthogonal, the angle between their respective planes being 80.1˚. This conformation is stabilised by the presence of some weak C–H…π interactions (between C68-H68 of a Cp ring and the Cp plane C65-C69 of a molecule at the symmetry position x-1/2, y-1/2, z with a H…centroid distance of 3.005 Å (Figure 2.11) and also π-π stacking (between the phenyl ring C11-C16 of a molecule and the phenyl ring C11'-C16' of another molecule at a symmetry position x, y, z+1/2) that links the molecules into zigzag chains down the crystallographic *b*-axis.
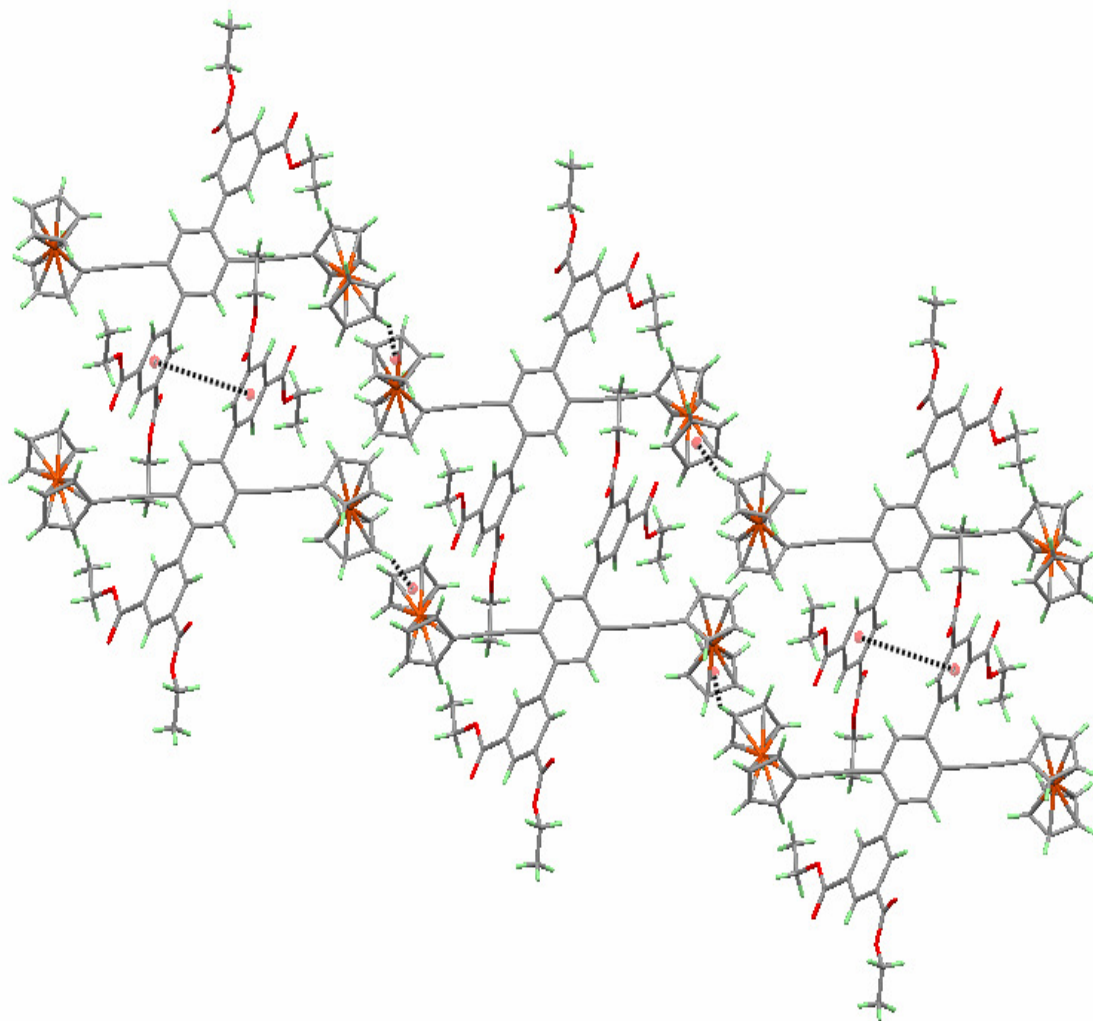
Figure 2.11. Crystal packing of (19) showing the π-π stacking and C–H…π interactions involved, represented as dashed black lines, giving rise to zigzag chains down the crystallographic *b*-axis. For clarity, hydrogen atoms are represented in light green.

2.2.3 Spectroelectrochemistry results

a) Cyclic Voltammetry

As discussed earlier, electrochemical experiments were performed on **(19)** to ensure that no electronic communication was occurring between the two iron centres present in the molecule. Electronic communication is, here, an unwanted phenomenon since it would not permit the addressing and perhaps eventually manipulating each ferrocenyl group individually which is one of the requirements for information storage and/or quantum computing applications.[47-52]

Cyclic voltammetry (CV) measurements were carried out on **(19)** at different scan rates (100, 200, 300, 50 and 20 mV) in dichloromethane containing [NBu$_4$][BF$_4$] salt as supporting electrolyte using a three electrode system with a glassy carbon working electrode, a Pt electrode as a secondary electrode and a saturated calomel electrode as a reference. In all cases, the ethynylferrocene complex showed, as expected, a unique reversible oxidation wave (Figure 2.12) due to the oxidation of the ferrocene tethers. This suggests that the two metal centres do not interact with each other through the conjugated aryl ethynyl bridges.
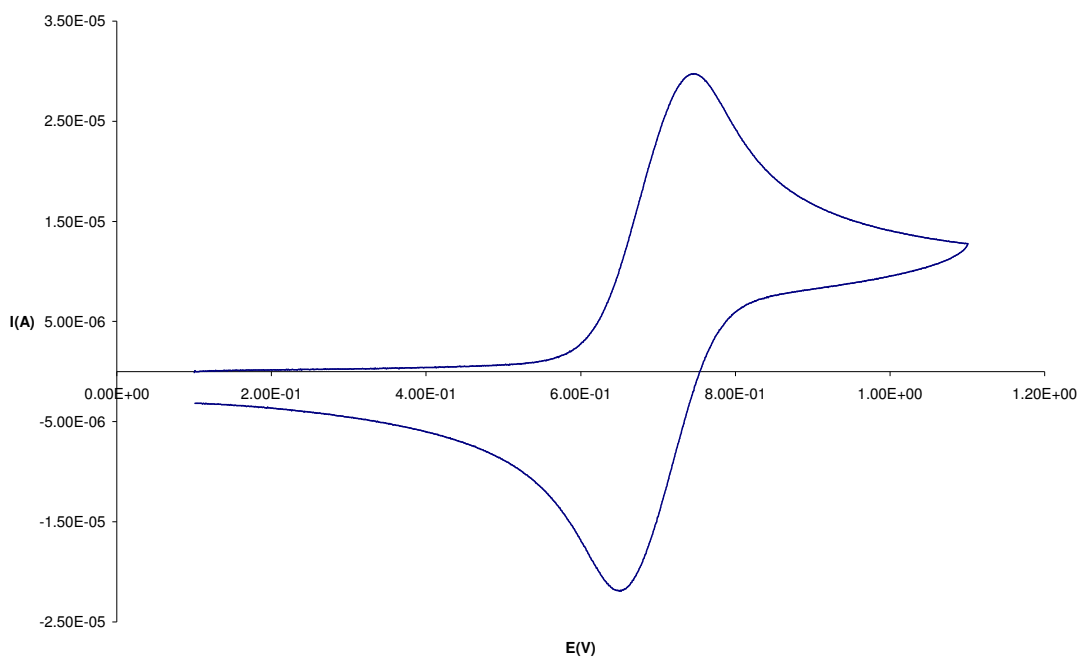
Figure 2.12. Cyclic voltammogramm of compound (19) recorded in CH$_2$Cl$_2$ using [NBu$_4$][BF$_4$] as a supporting electrolyte at 100mV/s scan rate.

As seen in Figure 2.13, the ratio I$_{pa}$/I$_{pc}$ is proportional to the square root of the scan rate confirming that the process is purely reversible and diffusion controlled. The CVs of compounds **(17)**, **(18)** were also recorded using the same conditions. Furthermore in order to build up a full comparison data set, the synthesis of 1,4-bis(ferrocenylethynyl)benzene[53] **(21)** and [phenyl(ethynyl)]ferrocene[41] **(22)** was undertaken using the Sonogashira coupling conditions employed previously (Scheme 2.8). The data are summarised in Table 2.7.
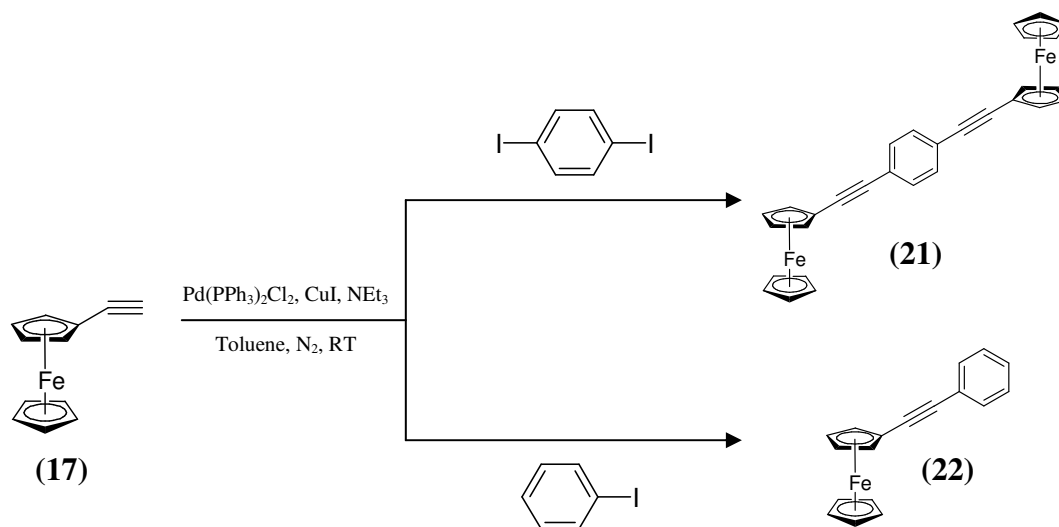
Scheme 2.8. Synthetic route employed to prepare compounds (21) and (22).
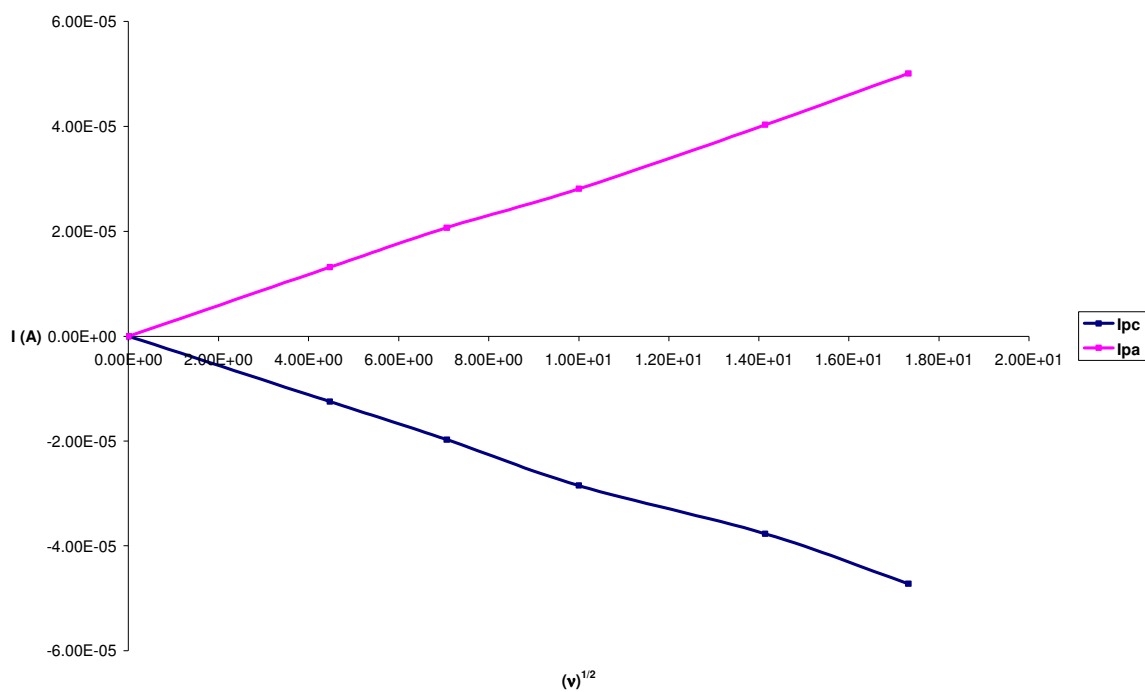
Figure 2.13. Plot of the variation of peak current (Ip$_a$/Ip$_c$) with square root of scan rate for (19).

All compounds exhibited the normal expected behaviour of a chemically, reversible one electron $[Fc]^{+/0}$ couple as observed previously for (19). It has been established[44,53] that the central phenyl ring in these types of compounds does not allow the peripheral ferrocenyl subunits to communicate electronically with each other whereas two well separated (130mV) one electron oxidation waves are observed when the molecule lacks the benzene bridge as seen for Fc–C≡C–Fc.[54] (17), (21) and (22) have been studied previously by cyclic voltammetry and showed a unique reversible oxidation wave.[41,44,53]

$E_{1/2}$ values, for all compounds, are very similar to one another (ranging from 0.13 to 0.18V) and to the values reported in the literature.[41-46,53] The potentials are slightly more anodic compared to ferrocene ($E^{1/2}_{[FcH]}$=0.55V vs $[FeCp*_2]^{0/+}$)[41,45] which can be explained by the fact that an ethynyl substituent on a ferrocenyl ring is electron withdrawing. And for the same reason, this is why compound (18) has the most anodic potential (0.18V) due to the presence of the two extra bromide groups reinforcing the electron withdrawing effect.

Table 2.7. Electrochemical data of iron complexes[a].

	$E_{1/2}{}^b$	ΔE^c	I_{pa}/I_{pc}
(19)	0.16	100	0.986
(18)	0.18	80	1.033
(21)	0.13	80	1.077
(22)	0.13	70	1.105
(17)	0.16	70	1.107

[a]From cyclic voltammetry in CH_2Cl_2/ $[NBu_4][BF_4]$ solutions at 100mV/s scan rate.
[b]Potentials $E_{1/2}$ are in V vs $[FeCp_2]^{0/+}$, [c]peak potential differences ΔE are in mV.

However while having a closer look at the data, a larger peak separation can be noticed for the bis-ferrocenyl compounds **(18)**, **(19)**, **(21)** with a quite large peak to peak separation (ΔE =100mV) for compound **(19)**. Similar trends have been reported in the literature for compounds where no electronic communication was occurring.[41-46] This phenomenon has been interpreted as the effect of superimposed one electron waves.[44,54-55] Yet, a large peak to peak separation usually reflects a certain degree of electronic communication, which in our case would be a feasible explanation. For compounds **(17)**, **(22)** bearing just one ferrocenyl unit, the peak to peak separation is the same as the one observed for the internal reference ($\Delta E = \Delta E_{decamethylferrocene}$ =70mV) whereas ΔE becomes larger for **(18)** and **(21)** (80mV) and significantly larger for **(19)** (100mV) suggesting an increase of the electronic communication for the ester derivative. To investigate further, it was decided to also perform UV-Vis and IR spectroelectrochemistry on some of these compounds.

b) Spectroscopy of neutral species

The electronic spectra of the neutral species **(17)**, **(18)**, **(19)**, **(21)** and **(22)** are very similar and display two different groups of absorption bands between 230-900 nm (Figure 2.14). The more intense band A lies between 230 and 430nm. This can be assigned to the $\pi \rightarrow \pi^*$ transition arising from the arylethynyl group.[41,45] An increase in conjugation shifts the band towards lower energies.
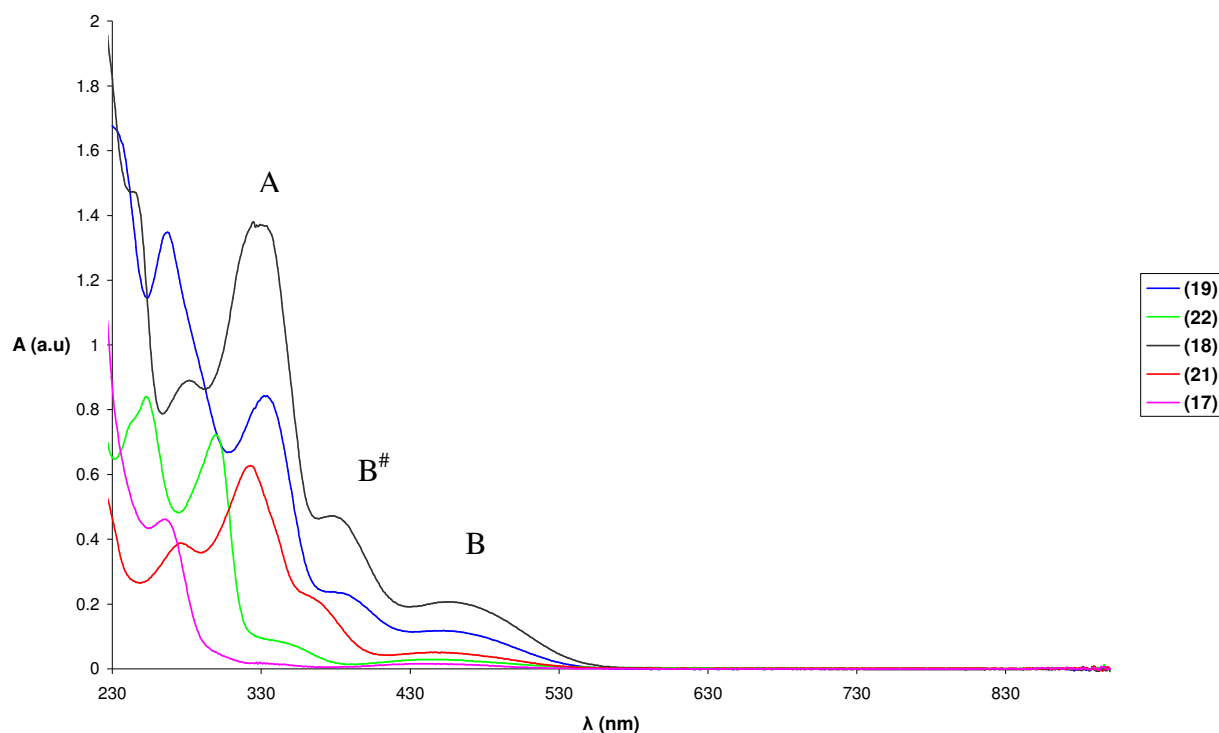
Figure 2.14. UV-Vis spectra of compounds (17), (18), (19), (21) and (22).

This effect can, indeed, be observed in Figure 2.14 where the longer wavelength for the absorption band A has been recorded for the ester compound **(19)**. The intensity and shape of band A also depends on the degree of conjugation.

Two weak low energy bands at about 325 and 440 nm attributable to d-d transitions arising from the ferrocene moiety can be seen, which correspond to bands B[#] and B respectively. These bands, especially B[#], can sometimes be slightly masked by the red shifted band A.

c) UV-Vis and IR Spectroelectrochemistry

▪ *Uv-vis Spectroelectrochemistry*

To ensure the redox process was purely chemically reversible, UV-Vis spectroelectrochemistry were performed on compounds (**17**), (**18**), (**19**), (**21**) and (**22**). The compounds were oxidised in situ at the appropriate potential in an optically transparent electrode (OTE) UV-vis cell in CH_2Cl_2.

Spectra showed complete reversibility when the potential was cycled which attested to the chemical reversibility of all the redox processes studied. Spectroelectrochemical oxidation showed, for all complexes, the development of new absorption bands C and D at about 780 nm and 580 nm respectively (Figure 2.15a). Band C has been previously observed and described as the LMCT transition band.[41,45] Bands B# and B in the neutral compounds are increasing in intensity and mixing to give a more complex and wider transition band B' for the oxidised species. Finally the more intense band A observed for the neutral compounds is slightly shifted towards smaller wavelengths (blue-shift) upon oxidation.

For compounds (**17**) and (**22**), consistent isosbestic points were observed in the spectra which attested of the stability of the cations (**17**)$^+$ and (**22**)$^+$. However, this was not the case for bis-ferrocenyl complexes where upon oxidation the intensity of band D increases first before depleting yielding inconsistent isobestic points (Figure 2.15b).
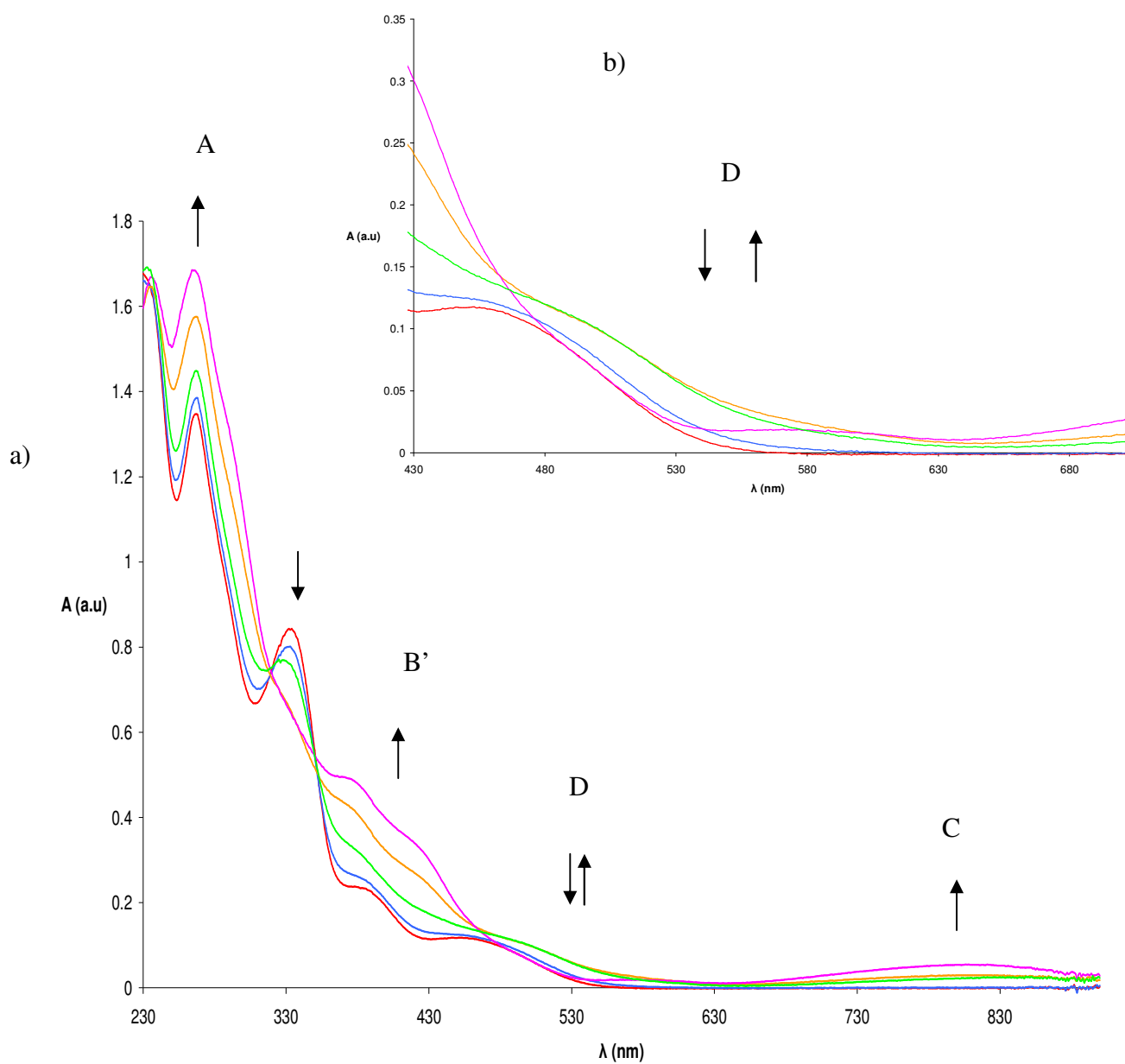
Figure 2.15. UV-Vis OTE spectra of (19) (0˚C, CH₂Cl₂, Pt electrode, 0-1.1V). The arrows indicate the direction of change of the spectral features during the gradual oxidation of the compound.

The occurrence of isosbestic points in the course of a spectrophotometric event means that only two species are in equilibrium. Therefore, this behaviour is normally indicative of the formation of an intermediate mixed valence species during the process, corresponding to the following equation:

$$(FeII) \leftrightarrows (FeIII)(FeII) \leftrightarrows (FeIII)$$
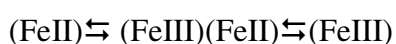
which would suggest that the two ferrocene moieties do not behave totally independently. These observations are in good agreement with the larger peak to peak separations obtained for (18), (19) and (21) and described earlier during the CV experiments. Surprisingly, this phenomenon has not been described for compound (21) where it was established that no communication between the ferrocene moieties was occurring through the ethynylbenzene bridge and that the oxidation was rather more metal-centered.[44,56,57] Thus, it would in turn mean that the two ferrocenyl subunits do communicate electronically but that the extent of communication is rather too weak to be observed on the timescale of a CV experiment and therefore induce two separate waves but strong enough to give rise to a rather large peak to peak separation.

- ■ *IR spectroelectrochemistry*

IR spectroelectrochemistry was carried out in the range of 2300 to 1600 cm^{-1} for compounds (19) and (18) to probe for vibrational changes upon electrochemical oxidation. The potential was adjusted to record separately the first oxidation (corresponding to the one electron process) and then the second oxidation. Both neutral species exhibit bands of medium intensity at about 2220 cm^{-1} which

corresponds to the symmetric $\nu(C{\equiv}C)$ stretch characteristic of ethynyl derivatives (Figures 2.16 and 2.17). Therefore it can be noted that the frequency does not depend much on the aryl group present in the molecule. Furthermore compound **(19)** shows a very strong absorption band at 1720 cm^{-1} characteristic of a $\nu(C{=}O)$ stretch of the ester groups.

Upon oxidation the $\nu(C{\equiv}C)$ band decreases for both fully oxidised complexes and a new band of weak intensity at 2100 cm^{-1} can be observed. It is noteworthy that for compound **(19)**, this new band is much more pronounced for the 1st oxidation species before decreasing during the second oxidation. In addition, the development of a band of medium intensity for **(19)** and **(18)** respectively, is observed at about 1820 cm^{-1} in both the one and two oxidation processes (for **(18)** the band is already present in the neutral compound but notably increases during oxidation).
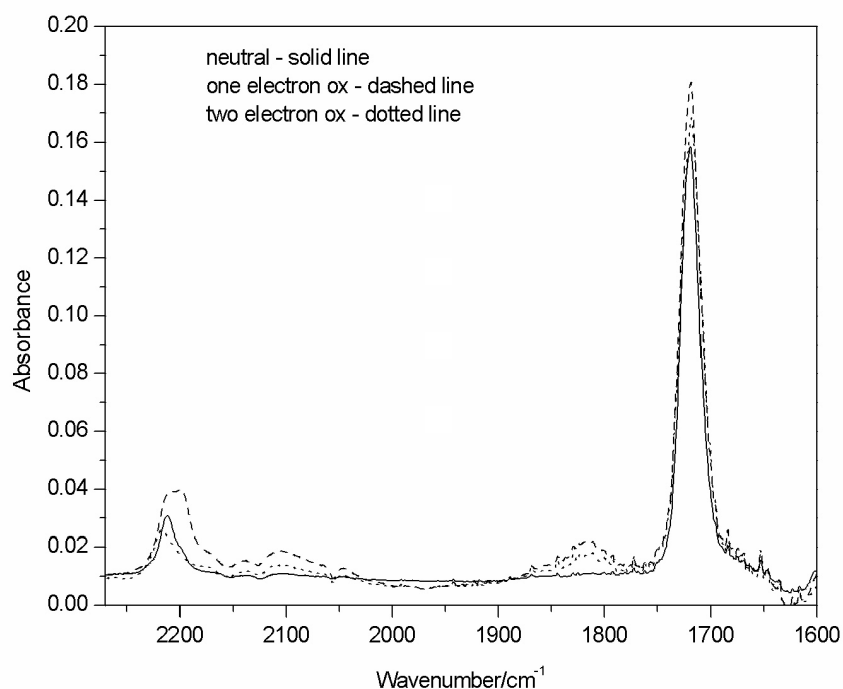
Figure 2.16. IR spectra of (19), (19)$^{+}$ and (19)$^{2+}$.
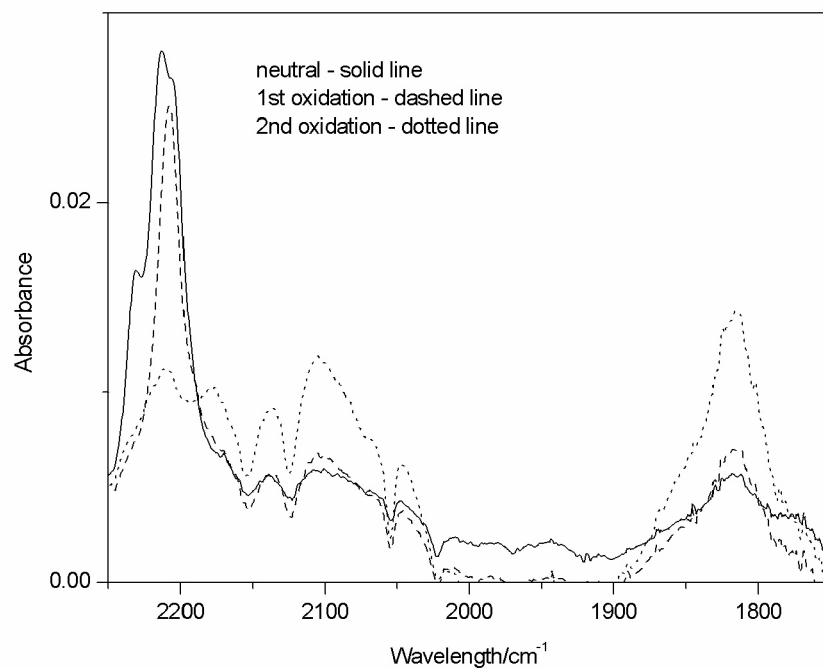
Figure 2.17. IR spectra of (18), (18)⁺ and (18)²⁺.

The depletion of the $\nu(C\equiv C)$ band and the development of the new bands at 2100 cm⁻¹ and 1820 cm⁻¹ are in agreement with what have been described previously for similar compounds,[45b] where an allenylic type of structure would replace the arylethynyl arrangement upon oxidation (Scheme 2.9).
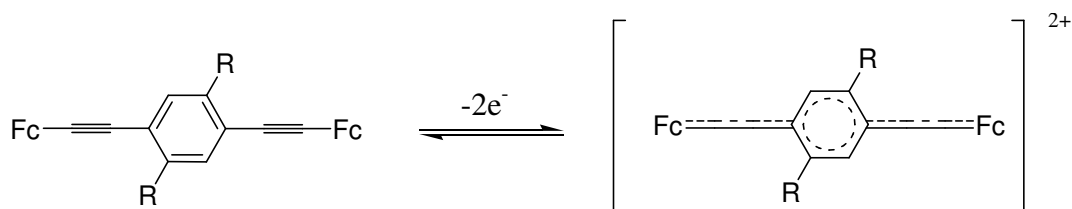
Scheme 2.9. Delocalised allenylic structure suggested for the oxidised arylferrocenyl complexes.

In summary, the CV experiments have shown that, for the series of the studied complexes, reversible one electron oxidation waves were obtained with values of the potentials similar to the ones reported in the literature.[41-46,53] However, for the bisferrocenyl compounds large peak to peak separations were recorded, which revealed a degree of communication between the two metal centres through the ethynylbenzene bridge, as an intermediate mixed valence species was observed for (18), (19) and (21) during UV-vis spectroelectrochemistry experiments. The changes in vibrational frequencies recorded upon electrochemical oxidation of (18) and (19) tend to confirm the formation of oxidised species with a delocalised allenylic type of structure described before for similar compounds.

2.2.4 Surface deposition studies

a) Deposition of *p*-terphenyl-3,5,3',5'-tetracarboxylic acid (8) on HOPG

It has been shown in previous studies that it was possible to direct the formation of a less stable network by co-depositing the molecule in the presence of a guest template molecule.[14,15,58-65] This has been realised within our group with *p*-tetraphenyl-3,5,3',5'-tetracarboxylic acid. As mentioned in the introduction, the co-deposition of this tetracarboxylic acid and coronene yielded the formation of a less stable 2D Kagomé network on a HOPG surface with the coronene guest molecule being encapsulated within the hexa-isophthalate node formed by the framework.[15] Furthermore, the addition of more coronene did not modify or alter the network arrangement previously described. Therefore it was demonstrated that the planar coronene guest template

molecule was playing an active role in the formation of the network rather than filling

passively the pre-existing voids.[15]

The deposition of *p*-terphenyl-3,5,3',5'-tetracarboxylic acid on a HOPG surface led to the formation of an extended monolayer array of hexagonal pores stabilised by hydrogen bonds and distant of 16.6 Å from each other, as discussed earlier in the introduction[16] (Figure 2.18). These pores could act as potential host sites for the further deposition of guest molecules. It has to be reminded that the pores formed by the present network are not all equivalent but possess approximately equal dimensions. The guest molecule chosen, here, was the fullerene C_{60}. Firstly, *p*-terphenyl-3,5,3',5'-tetracarboxylic acid **(8)** was adsorbed on freshly cleaved HOPG as detailed in the experimental section to form a monolayer.
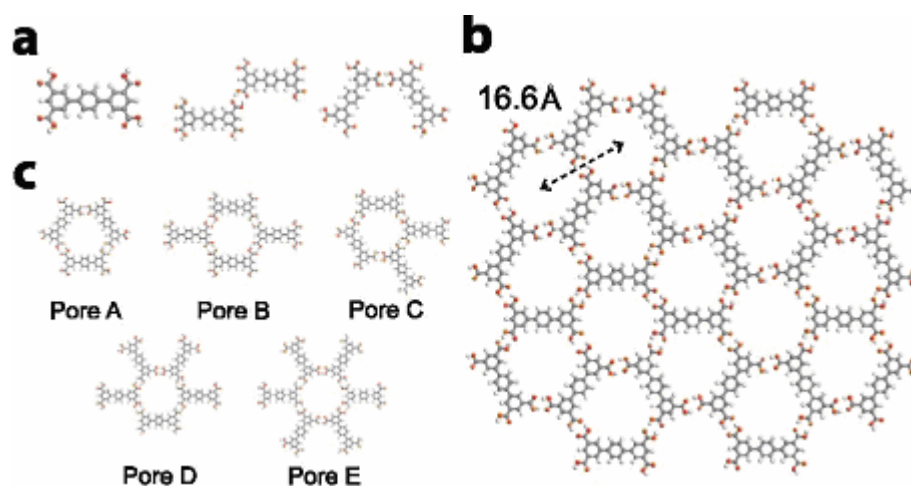
Figure 2.18. Molecular structure of the network formed by (8): A) Molecular structure and arrangements for hydrogen-bonded dimers with either the long axes of molecules mutually parallel, or with one molecule rotated by 60°. B) Molecular schematic of a section of the network highlighting the hexagonally-ordered network of pores. The pore-pore separation (16.6 Å) is labelled. C) Five possible arrangements of molecules which surround each pore within the network. The arrangements contain either three (Pore A), four (Pore B and C), five (Pore D) or six (Pore E) molecules. Examples of each of these pore types can be seen in B).[67]

Then the deposition of a small amount of a saturated solution of C_{60} in nonanoic acid was undertaken and the graphite/solution interface was imaged using Scanning Tunnelling Microscopy (STM) about 24 hours after the C_{60} solution deposition. Figure 2.19 shows the structure of the network obtained. The bright spots in the STM image correspond to the adsorbed C_{60} molecules sitting within the pores of the underlying network. The distance as measured between each individual spot is around 16.5 Å which is consistent with the hexagonal pore-pore separation of the *p*-terphenyl-3,5,3',5'-tetracarboxylic acid network described earlier. As shown in Figure 2.19, about 53% of the network pores are filled with C_{60} after approximately 24 hours. To get more insight of the becoming of the network in proximity of the C_{60} molecules adsorbed, the growth of a small area C_{60}/*p*-terphenyl-3,5,3',5'-tetracarboxylic acid network on a HOPG nucleation site (which is effectively a defect of the substrate) was followed by sequential STM.
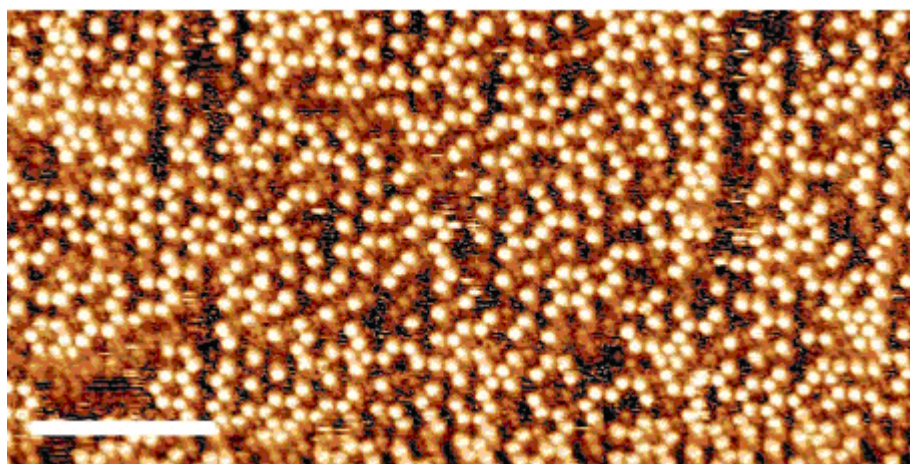
Figure 2.19. STM image of a local area of the network formed by (8) on HOPG at about 24 hours after the C_{60} deposition. The bright features in the image correspond to the C_{60} molecules; the underlying network structure is not visible. Scale bar: 160 Å.[67]

Figure 2.20 shows a large intense bright line which corresponds to the nucleation site on the substrate (defect). An area growing outside this defect can be identified as C_{60} molecules closely encircled by the *p*-terphenyl-3,5,3',5'-tetracarboxylic acid network.
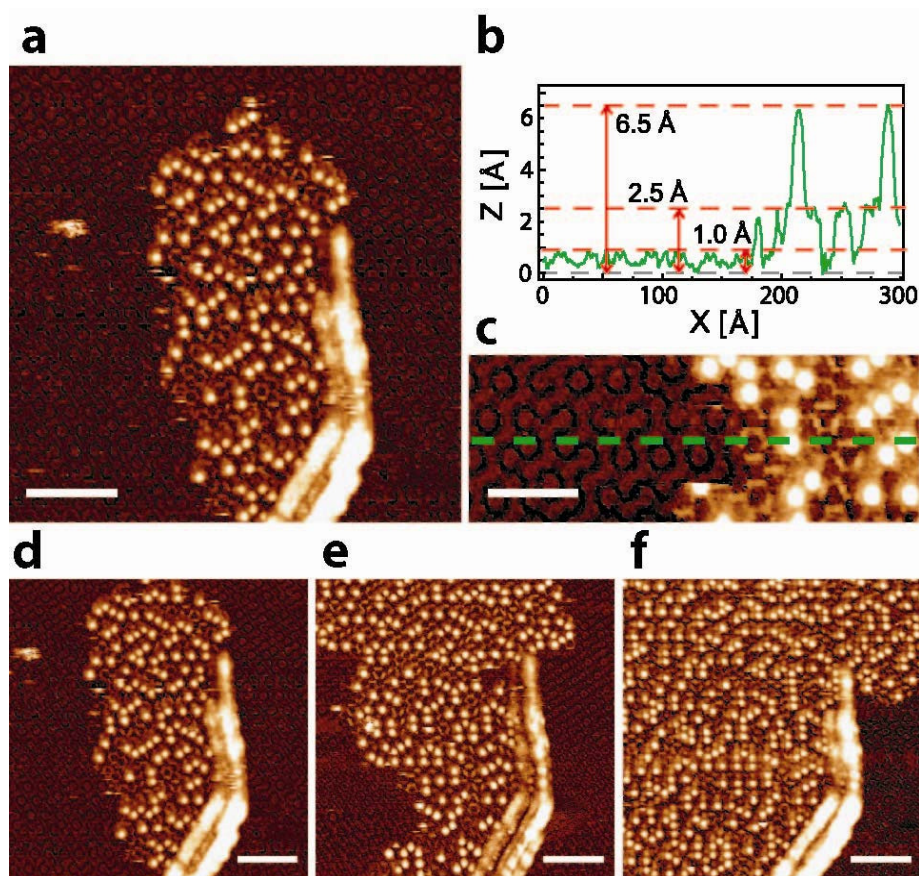
Figure 2.20. Images showing the growth of the TPTC/C_{60} bilayer: A) STM image of the network immediately after the C_{60} deposition. An island of C_{60} and bi-layer network is growing outwards from a surface defect. The initial monolayer of the network is visible with an altered contrast while the network second layer molecules as bright rod–like features. Scale bar: 110 Å. B) Height profile taken through the edge of the bi-layer/C_{60} island. The location of the height profile is marked on the magnified STM image shown in C). Scale bar: 60 Å. D-F) STM images showing the growth of the bi-layer/C_{60} island; the images were taken approximately every 5 mins.. All images were acquired with tunnelling current of 20pA and tip bias of +1.2V. Scale bars: 100 Å.[67]

The molecules constituting the network in this region appear as bright rod-like features since they are in fact in an upper layer of what corresponds to a *p*-terphenyl-3,5,3',5'-tetracarboxylic acid bilayer structure, the lower layer (monolayer directly adsorbed on graphite) appearing, here, with lower contrast. This bilayer proved to be rather fragile as it could be removed with the STM tip with, however, potential subsequent re-growth. The molecules that constitute the bilayer, which immediately surround the adsorbed C_{60} molecules, appear to be at about 2.5Å height while the apparent height of the ones forming the monolayer (i.e. directly adsorbed onto the graphite) is much lower (~1Å), as shown in the cross-section depicted in Figure 2.20b. The green line in Figure 2.20c shows where the cross-section has been realised within the network. It is noteworthy that the C_{60} peak height (~6.5Å) is consistent with formerly reported C_{60} values recorded by STM.[68] To avoid any misunderstanding, it has to be clarified that the heights given above do not correspond to estimated molecular dimensions. However, this indicates that the molecules of *p*-terphenyl-3,5,3',5'-tetracarboxylic acid constituting the network in an area close to the adsorbed C_{60} molecules, as seen in the STM images, are part of an overlayer. This confirms thus the formation of a *p*-terphenyl-3,5,3',5'-tetracarboxylic acid bilayered structure upon addition of C_{60} guest molecules. Another interesting feature to be noted is that this second layer network growth is not observed without the addition of C_{60} molecules which testifies on the co-dependent nature of these two processes making this example quite different from previously related surface bilayer growth.[69] STM images in Figure 2.20d, e and f show the extent of the bilayer/C_{60} island growth over time. Once adsorbed, the C_{60} molecules become encapsulated within the *p*-terphenyl-3,5,3',5'-tetracarboxylic acid bilayer and remain sited, for the vast majority, in the same pores.

Table 2.8. Occupancy and trapping energies for C_{60} guest in different pores.[67]

	A	B	C	D	E
TPTC monolayer pore distribution	40%	2.9%	27%	19%	9.2%
Pores in initial TPTC layer which trap a C_{60}	76%	1.6%	15%	6.2%	1.1%
Calculated trapping energy of C_{60} guest in pores in a single layer TPTC on HOPG	-2.20 eV	-2.10 eV	-2.11 eV	-2.05 eV	-1.98 eV

Therefore they can be regarded as labels for determining which network pore type in the monolayer will preferentially trap C_{60} in the bilayer structure. The different pore types encountered in the monolayer were determined by using the outermost region of the STM image in Figure 2.20a. The data are summarised in Table 2.8. A direct result from this table is that there is a strong preference for C_{60} molecules to be trapped in pores of type A (76%) which represent 40% of the total pores in the initial layer. The other parameter to be taken into account was the trapping energy for C_{60} molecules in each pore type calculated following a recent study using molecular dynamics.[67b] The most stable configuration is for C_{60} molecules trapped in a pore of type A with a trapping energy of -2.2eV while the most unstable one is recorded for C_{60} molecules being trapped in a pore of type E (-1.98eV) which corresponds to the network pore type that captures the least C_{60} molecules. Therefore one can strongly correlate the encapsulation probability of C_{60} molecules and the calculated binding energy. But additionally one can wonder why there is such a preference for C_{60} molecules to be trapped in pores A. This can be explained in terms of internal pore dimensions. The backbone of molecule (**8**) constitutes the edge of the pores which slightly stand inside the pores giving rise to increased van der Waals interactions. Because pores of type A exhibit the configuration that displays the more edges, these pores have the smallest

internal size and therefore the highest binding energy. Because the fullerene is a spherical molecule, its footprint onto the substrate will be smaller than its diameter. In addition, the interactions between the C_{60} molecules and the network molecules of the first and second layer respectively are expected to be different since the cross-sectional area of intersection between C_{60} and terphenyl molecules are different for the first and second layer molecules, as shown in Figure 2.21a and b for a fullerene encapsulated in a pore of type A. Molecular dynamics simulations were carried out to calculate the stabilisation energy of a C_{60} guest molecule within the different pore type. These calculations showed that the C_{60} molecule is stabilised at a position distant from a displacement r from a hydrogen bond type edge within the hexagonal pore of the network, and therefore is not located in a central position. The parameter r is effectively dependent upon the distance d of the considered layer from the graphite surface. Figure 2.21c shows the variation of both the calculated interaction energy E between the fullerene and the pore and the distance r in function of d for a pore of type A (it should be noted that the interactions with the graphite surface are not included for the calculation of E). It is found that the displacement r is equal approximately to 0.8Å for d=3.4Å which corresponds to the height of the first monolayer, while for the overlying terphenyl layer (d=7.1Å) r is equal to about 0.1Å. Similar calculations have been carried out for the other types of pores (pores B to E [67b]) and demonstrate that as the internal pore dimension increases (decrease in the number of terphenyl edges), the binding energy diminishes and the displacement, r, increases. Consequently, a relative lateral displacement between molecules of two consecutive layers of the network exists and is estimated to be about 0.6Å if the interaction fullerene/terphenyl molecules are maximised in both layers simultaneously.
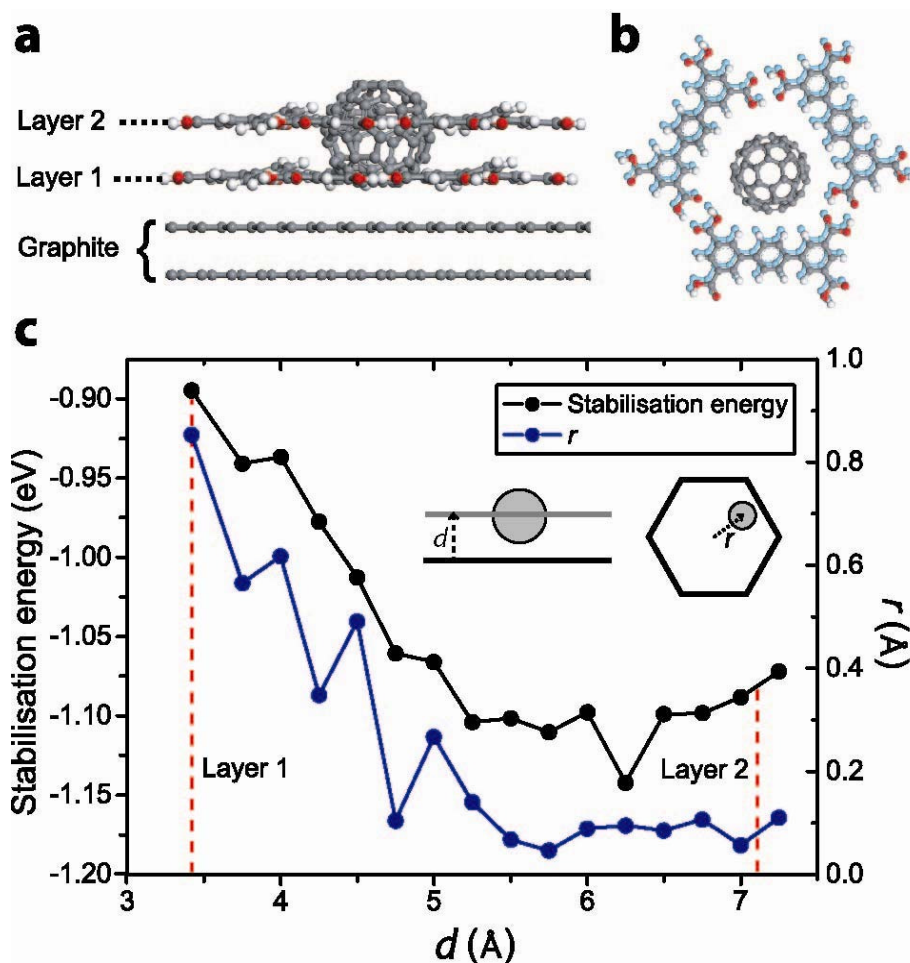
Figure 2.21. Structure of a terphenyl/C_{60} bilayer. A) Side-view C_{60}/bilayer network consisting of two overlying pores of type A. B) Top view of this arrangement with the C_{60} placed in its minimum energy position for both the first (light blue) and second layer pores (grey). The two layers are slightly displaced with respect to each other which aid clarity. C) Variation in stabilisation energy and position for a C_{60} in a single layer pore of type A when the vertical position of the pore is varied from the equilibrium position for a first layer pore (3.4 Å) up to just above that for an equilibrium second layer pore (7.25 Å). The equilibrium vertical positions for layer 1 and layer 2 are marked by red dashed lines.[67]

However, such a small displacement cannot be outlined specifically in the present STM images mainly due to resolution limitations. Another alternative is to study the growth of the bilayer over time as shown in Figures 2.20 d-f to elucidate the question of the preferential orientation of the second layer with respect to the first monolayer or in other words if a terphenyl molecule of layer 2 will be preferentially adsorbed onto another molecule rather than on top of a hydrogen-bonded edge. The answer to

this question is that there is no preference whatsoever and the placement is considered to be purely at random.

Finally to evaluate the stability and robustness of the bi-layered structure, another experiment consisting of the addition of coronene as a second guest molecule was performed. STM images were taken respectively at 20, 40 and 60 mins. following the addition of 10 μL of a coronene solution in nonanoic acid (0.0015mg/mL) to the sample (Figures 2.22a-c). The formation of the bi-layer fullerene/terphenyl molecule network is, indeed, reversible as the formation of a monolayer of p-terphenyl-3,5,3',5'-tetracarboxylic acid network is observed with coronene molecules being trapped within the network pores (preferentially pores of type E as reported previously[70]). It seems that the removal of C_{60} is an activated process as it can be observed in Figure 2.22a, b and c. Between the first two STM images which correspond to a time interval of 20 mins., the process is slowly starting with the number of C_{60} molecules decreasing of about 10%. However, Figure 2.22c shows a unique monolayer of p-terphenyl-3,5,3',5'-tetracarboxylic acid molecules with coronene adsorbed onto the network. More than a temporal evolving process, the reversal of the bilayered structure has also a spatial coordinate/dimension (Figure 2.22d). The blue spots in Figure 2.22d correspond to the locations of the removed fullerene molecules during the 20 mins. interval of STM images a and b, while the green one are the positions of the fullerene molecules that remained in the same locations and the red ones represent the small number of C_{60} molecules newly trapped. The analysis of this schematic view shows that, initially, the fullerenes are essentially adsorbed in concentrated small isolated islands of lateral dimensions of about 250 Å which is in good agreement with the idea of individual and well separated nucleation sites (defects) mentioned earlier in this study.
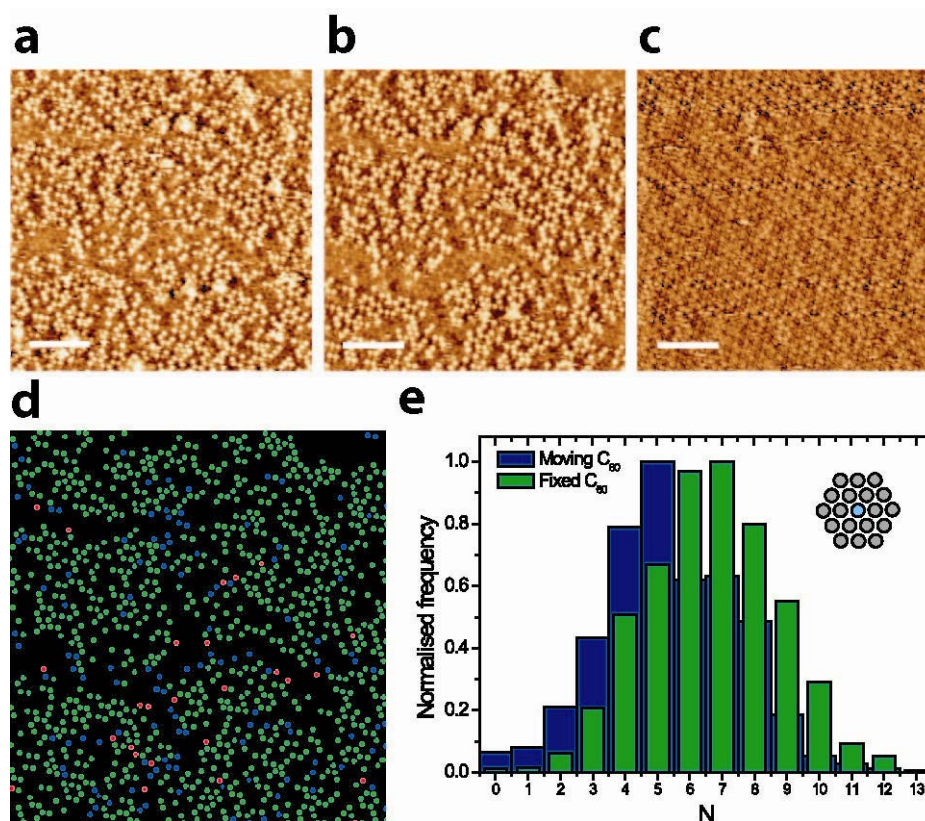
Figure 2.22. Reversal of bilayer formation by addition of coronene. A) – C) Removal of the bi-layer by coronene. Image A was taken approximately 20 mins. after the addition of the coronene solution, and B and C at 20 minute intervals following this. Scale bars: 160 Å. D) Schematic view showing C_{60} locations in A and B. C_{60} molecules which remain fixed in place between A and B are coloured green, removed C_{60} (those present in A but not B) are coloured blue and recaptured C_{60} (those present in B but not A are coloured red). E) Histograms detailing the distribution of co-ordination number, N (number of occupied nearest neighbour and next nearest-neighbour sites, see inset) for fixed C_{60} (green) and moving C_{60} (blue).[67]

The blue spots are in fact mainly located at the edges of those islands suggesting that the removal of the bilayer is the antagonist process compared to the bilayer growth. This is confirmed by the histogram displayed in Figure 2.22e which shows the co-ordination number N (corresponding to the number of nearest-neighbour, and next nearest neighbour sites occupied by a C_{60}) for fixed (green) or removed (blue) C_{60}. The removed C_{60} molecules have a lower value peak (N=5) as compared with the fixed ones (N=7) which in turn means that the removed fullerenes have the least number of nearest neighbours and therefore are located on the edges of the growing

domains. Another interesting feature is that a growing domain is not going to necessarily join another growing domain emerging from another nucleating site which is in accordance with the idea of a certain lateral displacement of the overlying terphenyl growing layer mentioned previously.

This work demonstrates that the use of a non planar guest molecule can direct the development of three-dimensional supramolecular bilayers which can be reversed while playing subtly with the interactions necessary to the growth of such a bilayer. This represents a primary example of a molecular switching system based on guest molecules exchange to induce a shift in its dimensionality.

b) Case of compounds (13) and (20)

After the encouraging and exciting results obtained for the *p*-terphenyl-3,5,3',5'-tetracarboxylic acid molecule, the situation proved to be different for the two other target molecules. Compound **(13)** has also been deposited on highly orientated pyrolitic graphite (HOPG) substrate. Several deposition attempts from nonanoic acid solutions were performed. However in this case, no adsorption of the molecule was observed despite the recurrent efforts. One possible postulated explanation is that the benzyloxy groups added on the side could be relatively too flexible and induce a significant twist of the molecule. The crystal structure of **(13)** revealed that the molecule is indeed more twisted than compound **(8),** due to the presence of the side groups, which could therefore inhibit surface adsorption.

Regarding compound **(20)**, sadly no deposition was attempted given the fact that it was synthesised towards the end of the project and that we did not have the time necessary to perform the desired experiments.

2.3   Conclusion

The synthesis of the three p-terphenyl target compounds have been successfully achieved throughout the present project. The three compounds have been prepared using a similar synthetic route, starting from the synthesis of the spacer (central phenyl ring) then coupling the former with the relevant boronate phenylesters (terminal phenyl rings) *via* Suzuki coupling reactions.

For the *p*-terphenyl-3,5,3',5'-tetracarboxylic acid molecule **(8)**, a significant breakthrough has been realised. The molecule was successfully crystallised and the crystal structure and packing were studied. It was shown that the molecules are interacting with each other through a series of hydrogen-bonds to form 1D infinite chains. In addition, the adsorption of compound **(8)** on a HOPG substrate led to the formation of an extended monolayer array of hexagonal pores (five different types of pores were identified) stabilised by hydrogen bonds. The further deposition of C_{60} molecules, as a non planar guest template molecule, proved to direct the formation of a C_{60}/*p*-terphenyl-3,5,3',5'-tetracarboxylic acid bilayer in which the fullerenes sit preferably in one type of pore. Furthermore, it was demonstrated that this bilayered structure could be completely reversed by the subsequent adsorption of coronene molecules as the formation of a monolayer of **(8)**, encapsulating coronene molecules within its pores, was observed.

The initial plan for molecule **(13)** was that it would perhaps distort the network slightly or even completely modify it when deposited on surface. Despite several attempts to deposit **(13)** from nonanoic solutions on HOPG, the molecule could not be adsorb onto the substrate. It is postulated that the adjunction of relatively flexible

benzyloxy groups to the molecule inhibited the capacity of the latter to be adsorbed onto the substrate. However, single crystals have been successfully grown and the crystal structure of compound **(13)** revealed that the molecules are linked into one-dimensional infinite chain through their carboxylic acid moieties via pairs of CO-H···OC hydrogen bonds (one donated and one accepted) adopting an $R_2^2(8)$ arrangement. It has also confirmed that the molecular twist of **(13)** induced by the presence of the side groups was greater as compared to compound **(8)**.

Finally, compound **(20)**, which represents an elaborate version in terms of design among the present three target molecules, has been successfully prepared and characterised towards the end of the project. However, due to lack of time no surface deposition could be attempted for this molecule. Also, attempts to grow crystals of **(20)** using different crystallisation techniques and different solvent systems failed. Nevertheless, suitable crystals of **(19)** (the terphenylester derivative) for XRD were obtained and the crystal structure has been reported here. The electronic behaviour of compound **(19)** has also been studied by electrochemistry. It was found that the molecule showed a unique reversible oxidation wave due to the oxidation of the ferrocene moieties with, however, a large peak to peak separation which suggested the occurrence of a certain degree of communication between the two metal centres through the ethynylbenzene bridge. This hypothesis was confirmed by a series of spectroelectrochemistry experiments during which an intermediate mixed valence species was observed for **(19)**.

2.4 Experimental

All reagents and solvents were purchased from Sigma Aldrich, Alfa Aesar, Fischer Scientific UK, and used without further purification unless otherwise stated. Elemental microanalyses were carried out by Stephen Boyer at the Microanalysis Service, London Metropolitan University, UK. Infrared spectra were measured as KBr discs using a Bruker Tensor 27 FT-IR spectrometer over the range 400-4000cm^{-1}. ^{1}H and ^{13}C NMR spectra were measured using either a Jeol 270 MHz, Bruker 300 MHz, Bruker 400 MHz, DPX 300 MHz, DPX 400 MHz or Bruker 500 MHz spectrometer. MALDI-TOF mass spectra were obtained using a Bruker Ultraflex MALDI-TOF mass spectrometer. MALDI-TOF-MS samples were prepared by dissolution of the compounds in CH_2Cl_2 (10 μL) and then mixing this solution with a solution of the matrix DCTB (Trans-2-[3-(4-tert-butylphenyl)-2-methyl-2-propenylidone]-malononitrile) in MeCN (20 μL). A sample of the resulting solution (5 μL) was loaded onto a plate, the solvent was removed in air, and the sample transferred to the mass spectrometer for analysis. Electrospray ionisation mass spectra were collected using a microTOF mass spectrometer. UV-vis spectra were obtained on a Unicam UV/Vis 2 spectrometer.

Cyclic voltammetric studies were carried out using an Autolab PGSTAT20 potentiostat, using a three-electrode arrangement in a single compartment cell. A glassy carbon working electrode, a Pt secondary electrode and a saturated calomel reference electrode (chemically isolated for the test solution *via* a bridge tube containing electrolyte solution and fitted with a porous vycor frit) were used in the cell. Experiments were performed under an atmosphere of argon. Sample solutions

were prepared under an argon atmosphere using Schlenk line techniques. The supporting electrolyte employed was a 0.4M [NBu$_4$][BF$_4$] solution. Redox potentials were referenced vs the Fc/Fc$^+$ couple. Decamethylferrocene was used as the internal standard. Compensation for internal resistance was not applied.

UV/Vis spectroelectrochemical experiments were carried out with an optically transparent electrochemical (OTE) cell (modified quartz cuvette, optical pathlength 0.5mm). A three electrode configuration, consisting of a Pt/Rh gauze working electrode, a Pt wire secondary electrode (in a fritted PTFE sleeve) and a saturated calomel electrode, (chemically isolated from the test solution via a bridge tube containing electrolyte solution and terminated in a porous frit) were used in the cell. The potential at the working electrode was controlled by a Sycopel Scientific Ltd. DD10M potentiostat. UV/Vis data were recorded on a Perkin Elmer Lambda 16 spectrophotometer. The cavity was purged with N$_2$ gas and temperature control at the sample was achieved by flowing cooled N$_2$ gas across the surface of the cell.

Sample solutions were prepared under an atmosphere of argon using Schlenk line techniques and consisted of a 0.4M [NBu$_4$][BF$_4$] solution as the supporting electrolyte and a 10^{-4}M solution of the test compound. The test species in solution was oxidised at constant potential and the redox process was considered complete when consecutive spectra were identical. The reversibility of the process was investigated by applying a potential at the working electrode to re-reduce the electrogenerated product. The process was considered to be reversible, under the conditions of the experiment, if the spectral profile of the starting material was reproduced.

Crystallography

All single crystal X-ray experiments were performed on a Bruker SMART 1000 CCD or a Bruker SMART APEX CCD equipped with an Oxford Cryosystems open flow cryostat, [graphite monochromated Mo-Kα radiation (λ=0.71073 Å), ω scans]. Absorption corrections, if necessary, were applied by a semi-empirical approach. All of the single crystal structures were solved by direct methods using SHELXS-97[71], all non-H atoms were located using subsequent difference-Fourier methods.[72] Unless otherwise stated, hydrogen atoms were placed in calculated positions and thereafter allow to ride on their parent atoms.

For compound (**8**), the two carboxylic acid hydrogens atoms were located in difference Fourier maps and their positions refined with their isotropic atomic displacement parameters fixed at 1.5 times that of their parent oxygen atoms.

For compound (**19**), the carbonyl group C21=O22 is disordered over two possible positions with occupancies of 0.87 and 0.13; the minor component was refined isotropically and its geometry restrained to approximate that of the major component with a standard deviation of 0.02Å.

Additional restraints were placed on thermal and geometric parameters as required and appropriate. All graphical representations were generated using Mercury 1.4.1 (copyright CCDC 2001-2005).

Surface deposition studies

The experiments were carried out by the Beton group from the School of Physics and Astronomy at the University of Nottingham. STM experiments were carried out on an Agilent Technologies 4500 PicoPlus STM using a PicoScan controller. STM tips were formed from mechanically cut 80:20 PtIr wire and substrates were freshly cleaved highly oriented pyrolytic graphite (HOPG). Nonanoic acid (>95%), C_{60} (fullerene powder sublimed 99.92%) and coronene (>99%) were used as purchased from Fluka, Alfa Aesar and Sigma-Aldrich, respectively.

Saturated solutions of C_{60} and *p*-terphenyl-3,5,3',5'-tetracarboxylic acid both in nonanoic acid were prepared by placing an excess of solid in the solvent and using ultrasonic agitation to ensure complete saturation of the solution. HOPG surfaces were mechanically cleaved prior to each experiment to ensure a clean substrate. In order to form *p*-terphenyl-3,5,3',5'-tetracarboxylic acid networks, a 10μL droplet of compound **(8)** in nonanoic solution was deposited on to an HOPG surface with imaging commencing immediately using the STM tip. Once imaging of the *p*-terphenyl-3,5,3',5'-tetracarboxylic acid network was complete, the tip was withdrawn and a further 10μL droplet of C_{60} in nonanoic acid solution was added to the liquid cell. The tip was then re-engaged and imaging commenced. After imaging the bilayer network structure the tip was withdrawn again and 10μL of coronene in nonanoic acid solution (0.0015mg/mL) was added to the liquid cell, and this was followed by further imaging.

Compound Synthesis

Synthesis of 1,3-dimethylbenzyl-5-boronic acid (3)

A solution of 1,3-dimethyl-5-bromobenzene (8.2mL, 58.5mmol) in dry diethyl ether was added dropwise under N_2 to an excess of magnesium (3g, 117mmol). The mixture was reacted overnight under N_2 at 36°C. This solution was then added dropwise at -78 °C to 6.5mL of $B(OMe)_3$ (58.5mmol) in dry diethyl ether and further reacted for 4 h under N_2 to yield a white precipitate. The suspension was then allowed to gain room temperature and poured into a 100mL solution of 10% sulfuric acid, extracted with Et_2O and dried over $MgSO_4$. The resulting solid was purified by recrystallisation from water (3.1g, 20.5mmol, 35%). ^{1}H NMR (270 MHz, CD_3OD): δ ppm 2.29 (s, 6 H), 7.03 (s, 1 H), 7.18 (s, 2 H). ^{13}C NMR (101 MHz, CD_3OD): δ ppm 21.6, 132.2, 132.7, 138.1.

Synthesis of benzene-1,3-dicarboxylic-5-boronic acid (4)

1,3-Dimethylbenzyl-5-boronic acid (1.5g, 10mmol) and sodium hydroxide (3.2g, 80mmol) were dissolved in a mixture of $^tBuOH/H_2O$. The temperature was set to 55°C and $KMnO_4$ (9.5g, 60mmol) was added in small portion over 3 d. The resulting solution was filtered off, concentrated under reduced pressure and acidified with hydrochloric acid to get a white precipitate which was then washed with water, acetone and dried in air (1.5g, 7.1mmol, 71.3%). ^{1}H NMR (400 MHz, DMSO-d_6): δ ppm 8.50 (t, J=1.88 Hz, 1 H), 8.52 (d, J=1.63 Hz, 2 H). ^{13}C NMR (101 MHz, DMSO-d_6): δ ppm 130.4, 131.6, 139.1, 167.0. ESI-MS m/z: 209.0266 [M-H]$^-$.

Synthesis of benzene-1,3-dicarboxyethylester-5-boronic acid (5)

A solution of benzene-1,3-dicarboxylic-5-boronic acid (1.8g, 8.8mmol) in ethanol containing 1% of sulfuric acid was refluxed overnight. The mixture was cooled down to room temperature and concentrated under reduced pressure. After addition of water a white precipitate formed which was filtered, washed with water and dried in air (2.2g, 8.3mmol, 94%). ^{1}H NMR (400 MHz, CD$_3$OD): δ ppm 1.42 (t, J=7.16 Hz, 6 H), 4.41 (q, J=7.16 Hz, 4 H), 8.59 (d, J=1.51 Hz, 2 H), 8.61 - 8.65 (t, J =1.8 Hz, 1 H). ^{13}C NMR (101 MHz, CD$_3$OD): δ ppm 14.74, 62.64, 131.60, 132.68, 139.89, 139.99, 167.49. ESI-MS m/z: 267.1028 [M+H]$^+$; 284.1288 [M+H$_4$N]$^+$; 289.0844 [M+Na]$^+$.

Synthesis of *p*-terphenyl-1,3,1',3'-tetracarboxyethylester (7)

1,4-Dibromobenzene (650mg, 2.75mmol), benzene-1,3-dicarboxyethylester-5-boronic acid (1.8g, 6.9mmol) and K$_3$PO$_4$ (2.9g, 13.8mmol) were suspended in 100 mL of 1,4-dioxane under N$_2$. Pd(PPh$_3$)$_4$ (446mg, 0.38mmol) was then added and the reaction mixture was heated at 80˚C under N$_2$ for 4 d. The product was extracted with CHCl$_3$ and water and purified by column chromatography using chloroform as eluent to afford a white solid (1.2g, 1.6mmol, 60%). ^{1}H NMR (400 MHz, CDCl$_3$): δ ppm 1.46 (t, J=7.15 Hz, 12 H), 4.47 (q, J=7.11 Hz, 8 H), 7.81 (s, 4 H), 8.52 (d, J=1.63 Hz, 4 H), 8.69 (t, J=1.51 Hz, 2 H). ^{13}C NMR (75 MHz, CDCl$_3$): δ ppm 14.38, 61.53, 127.84, 129.51, 131.62, 132.10, 139.00, 141.06, 165.79. ESI-MS m/z: 519.2018 [M+H]$^+$, 541.1830 [M+Na]$^+$, 536.2274 [M+H$_4$N]$^+$. Elemental Analysis (%) Calculated for C$_{30}$H$_{30}$O$_8$: C, 69.49; H, 5.83; Found: C, 69.47; H, 5.83.

Synthesis of *p*-terphenyl-3,5,3',5'-tetracarboxylic acid (8)

An aqueous solution H_2O/MeOH (20mL/80mL) of compound (**7**) (452 mg, 0.9mmol) and KOH (7.3g, 130.8mmol) were refluxed for 12h. After evaporation of the solvents, the residue was acidified with HCl until a pH of 1 was reached inducing product precipitation. The white powder was filtered off and washed with water and dried in air (501mg, 0.8mmol, 90%). Suitable crystals for XRD were obtained by slowly diffusing a solution of MeOH into a DMF solution of the compound. ^{1}H NMR (400 MHz, DMSO-d_6): δ ppm 7.93 (s, 4 H), 8.46 (d, *J*=1.61 Hz, 4 H), 8.50 (t, *J*=1.61 Hz, 2 H). ^{13}C NMR (101 MHz, DMSO-d_6): δ ppm 127.74, 129.51, 131.16, 132.21, 138.15, 140.28, 166.46. ESI-MS m/z: 405.0628 [M-H]$^-$. FT-IR (KBr, cm^{-1}): 3075m (br), 1853w, 1699s, 1600m, 1520m, 1458w, 1420m, 1274s (br), 920m, 757s. Elemental Analysis (%) Calculated for $C_{22}H_{14}O_8$: C, 65.03; H, 3.47; Found: C, 64.93; H, 3.47.

Synthesis of 1,4-bis(benzyloxy)-2,5-dibromobenzene (10)

3,5-Dibromo2,4-dihydroxyquinone (2.7g, 10mmol), benzylbromide (7.2mL, 60mmol) and K_2CO_3 (7.5g, 108.5mmol) were dissolved in 40mL of dry DMF under N_2. The mixture was reacted at room temperature under N_2 for 48h. 200mL of water was then added and the white precipitate formed was filtered, extracted with CH_2Cl_2, washed with a 5% solution of sodium hydroxide and dried over $MgSO_4$. The resulting solid was purified by column chromatography (Silica, hexane/ $CHCl_3$:1/1) to yield a white powder (3.4g, 7.5mmol, 75%). ^{1}H NMR (400 MHz, CDCl$_3$): δ ppm 5.09 (s, 4 H), 7.20 (s, 2 H), 7.30 - 7.54 (m, 10 H). ^{13}C NMR (101 MHz, CDCl$_3$): δ ppm 71.95, 111.52, 119.24, 127.22, 128.11, 128.60, 136.13, 150.02. ESI-MS m/z: 468.9428 [M+Na]$^+$; 463.9860 [M+H$_4$N]$^+$. FT-IR (KBr, cm^{-1}): 3090m, 3064m, 2963m, 2875w, 1942w, 1872w, 1750m, 1667m, 1607m, 1492s, 1451s, 1387s, 1451s, 1387s, 1364s, 1262s,

1223m, 1207m, 1064-1013s (br), 910m, 856m, 796s (br), 736m, 691s, 628m, 596m, 522s, 452s, 437s. Elemental Analysis (%) calculated for $C_{20}H_{16}Br_2O_2$: C, 53.60; H, 3.59; Found: C, 53.66; H, 3.67.

Synthesis of 2'',5''-bis(benzyloxy)-3,5,3',5'-tetramethyl-p-terphenyl (11)

- Conditions 1:

1,4-Bis(benzyloxy)-2,5-dibromobenzene (450mg, 1mmol), 3,5-dimethylphenylboronic acid (380mg, 2.5mmol) and Cs_2CO_3 (890mg, 2.5mmol) were dissolved in 10 mL of degassed EtOH under N_2. $Pd(PPh_3)_4$ (12mg, 0.01mmol) was then added and the reaction mixture was refluxed under N_2 for 4 d. The product was extracted with $CHCl_3$ and water and purified by column chromatography (silica, hexane/CH_2Cl_2: 1/0.4) to afford a white solid (200mg, 0.4mmol, 40%). ^1H NMR (400 MHz, $(CD_3)_2CO$): δ ppm 2.33 (s, 12 H), 5.12 (s, 4 H), 6.98 (s, 2 H), 7.17 (s, 2 H), 7.27 (t, J=0.73Hz, 4 H), 7.28 - 7.45 (m, 10 H). ^{13}C NMR (101MHz, $(CD_3)_2CO$): δ ppm 21.5, 72.0, 117.7, 128.3, 128.4, 128.5, 129.2, 129.4, 132.0, 138.0, 138.8, 139.1, 151.1. ESI-MS m/z: 499.3638 [M+H]$^+$; 516.2900 [M+H$_4$N]$^+$; 521.2459 [M+Na]$^+$. Elemental Analysis (%) Calculated for $C_{36}H_{34}O_2$: C, 86.7; H, 6.9; Found: C, 86.9; H, 6.6.

- Conditions 2:

1,4-Bis(benzyloxy)-2,5-dibromobenzene (300mg, 0.67mmol), 3,5-dimethylphenylboronic acid (354mg, 2.35mmol) and Na_2CO_3 2M (3.4mL, 6.72mmol) were dissolved in 40 mL of degassed toluene under N_2. The temperature was set to 110°C and $Pd(PPh_3)_4$ (109 mg, 0.09mmol) was then added. The reaction mixture was

further refluxed under N_2 for 3 d. The product was extracted with $CHCl_3$ and water and purified by column chromatography (silica, hexane/CH_2Cl_2: 1/0.4) to afford a white solid (230mg, 0.46mmol, 46%). ^1H NMR (400 MHz, $(CD_3)_2CO$): δ ppm 2.33 (s, 12 H), 5.12 (s, 4 H), 6.98 (s, 2 H), 7.17 (s, 2 H), 7.27 (s, 4 H), 7.28 - 7.45 (m, 10 H). ^{13}C NMR (101 MHz, $CD_3)_2CO$): δ ppm 21.5, 72.0, 117.7, 128.3, 128.4, 128.2, 129.2, 129.4, 132.0, 138.0, 138.8, 139.1, 151.1. ESI-MS m/z: 499.2644 $[M+H]^+$; 516.2898 $[M+H_4N]^+$; 521.2453 $[M+Na]^+$. Elemental Analysis (%) Calculated for $C_{36}H_{34}O_2$: C, 86.7; H, 6.9; Found: C, 86.8; H, 6.7.

Attempted Synthesis of *p*-terphenyl-2'',5''-bis(benzyloxy)-3,5,3',5'-tetracarboxylic acid (13)

2'',5''-Bis(benzyloxy)-3,5,3',5'-tetramethyl-p-terphenyl (64mg, 0.13mmol) and sodium hydroxide (85mg, 2.14mmol) were dissolved in a mixture of $^tBuOH/H_2O$. The temperature was set to 55°C and $KMnO_4$ (254mg, 1.6mmol) was added in small portion over 3 d. The mixture was then heated at 90°C for several minutes and a few drops of ethanol were added to destroy the excess of $KMnO_4$. The resulting solution was filtered off to remove MnO_2, concentrated under reduced pressure and acidified with hydrochloric acid (ph=2) to afford a white precipitate which was washed with water, acetone and dried in air. However, all attempts to characterise the product failed.

Synthesis of (12)

- Conditions 1

1,4-Bis(benzyloxy)-2,5-dibromobenzene (500mg, 1.1mmol), benzene-1,3-dicarboxyethylester-5-boronic acid (731mg, 2.75mmol) and Na_2CO_3 (1.17g, 11.1mmol) were dissolved in 20 mL of degassed toluene under N_2. $Pd(PPh_3)_4$ (127mg, 0.11mmol) was then added and the reaction mixture was refluxed under N_2 for 4 d. The product was extracted with $CHCl_3$ and water and purified by column chromatography using chloroform as eluent to afford a white solid (180mg, 0.25mmol, 22.5%). ^{1}H NMR (400 MHz, $CDCl_3$): δ ppm 1.43 (t, J=7.16 Hz, 12 H), 4.45 (q, J=7.16 Hz, 8 H), 5.08 (s, 4 H), 7.15 (s, 2 H), 7.27 - 7.39 (m, 10 H), 8.50 (d, J=1.46 Hz, 4 H), 8.69 (s, 2 H). ^{13}C NMR (101 MHz, $CDCl_3$): δ ppm 14.36, 61.37, 71.57, 127.25, 127.80, 128.41, 130.83, 134.74, 150.07, 165.86. FT-IR (KBr, cm^{-1}): 3112m, 2974m, 2881m, 1729s, 1607m, 1588w, 1513s, 1450s, 1233s (br), 1002s, 864m, 755s. ESI-MS m/z: 753.2664 $[M+Na]^+$, 748.3110 $[M+H_4N]^+$. Elemental Analysis (%) Calculated for $C_{44}H_{42}O_{10}$: C, 72.31; H, 5.79; Found: C, 72.26; H, 5.73.

- Conditions 2

1,4-Bis(benzyloxy)-2,5-dibromobenzene (2g, 4.5mmol), benzene-1,3-dicarboxyethylester-5-boronic acid (2.9g, 11.15mmol) and K_3PO_4 (4.7g, 22.3mmol) were suspended in 100 mL of degassed 1,4-dioxane under N_2. $Pd(PPh_3)_4$ (728mg, 0.63mmol) was then added and the reaction mixture was heated at 80˚C under N_2 for 4 d. The product was extracted with $CHCl_3$ and water and purified by column chromatography using chloroform as eluent to afford a white solid (1.6g, 2.25mmol, 50%). ^{1}H NMR (400 MHz, $CDCl_3$): δ ppm 1.42 (t, J=7.1 Hz, 12 H), 4.44 (q, J=7.16 Hz, 8 H), 5.08 (s, 4 H), 7.15 (s, 2 H), 7.27 - 7.36 (m, 10 H), 8.49 (d, J=1.46 Hz, 4 H),

8.68 (s, 2 H). ^{13}C NMR (101 MHz, CDCl$_3$): δ ppm 14.36, 61.37, 71.57, 127.25, 127.80, 128.41, 130.83, 134.74, 150.07, 165.86.ESI-MS m/z: 753.2677 [M+Na]$^+$, 748.3119 [M+H$_4$N]$^+$. FT-IR (KBr, cm^{-1}): 3112m, 2974m, 2881m, 1729s, 1607m, 1588w, 1513s, 1450s, 1233s (br), 1002s, 864m, 755s. Elemental Analysis (%) Calculated for C$_{44}$H$_{42}$O$_{10}$: C, 72.31; H, 5.79; Found: C, 72.28; H, 5.81.

- Conditions 3

1,4-Bis(benzyloxy)-2,5-dibromobenzene (800mg, 1.8mmol), benzene-1,3-dicarboxyethylester-5-boronic acid (1.7g, 6.25mmol) and a 2M aqueous solution of Na$_2$CO$_3$ (1.9g, 17.85mmol, 8.9mL) were dissolved in 80 mL of degassed toluene under N$_2$. Pd(PPh$_3$)$_4$ (290mg, 0.25mmol) was then added and the reaction mixture was refluxed under N$_2$ for 4 d. The product was extracted with CHCl$_3$ and water and purified by column chromatography using chloroform as eluent to afford a white solid (924mg, 1.3mmol, 71%). ^{1}H NMR (400 MHz, CDCl$_3$): δ ppm 1.43 (t, *J*=7.16 Hz, 12 H), 4.45 (q, *J*=7.16 Hz, 8 H), 5.08 (s, 4 H), 7.15 (s, 2 H), 7.27 - 7.39 (m, 10 H), 8.50 (d, *J*=1.46 Hz, 4 H), 8.68 (t, *J*=1.63 Hz, 2 H). ^{13}C NMR (101 MHz, CDCl$_3$): δ ppm 14.36, 61.37, 71.57, 127.25, 127.80, 128.41, 130.83, 134.74, 150.07, 165.86. FT-IR (KBr, cm^{-1}): 3112m, 2974m, 2881m, 1729s, 1607m, 1588w, 1513s, 1450s, 1233s (br), 1002s, 864m, 755s. ESI-MS m/z: 731.2872 [M+H]$^+$; 753.2663 [M+Na]$^+$, 748.3109 [M+H$_4$N]$^+$. Elemental Analysis (%) Calculated for C$_{44}$H$_{42}$O$_{10}$: C, 72.31; H, 5.79; Found: C, 72.24; H, 5.69.

Synthesis of molecule *p*-terphenyl-2'',5''-bis(benzyloxy)-3,5,3',5'-tetracarboxylic acid (13)

An aqueous solution H_2O/MeOH (10mL/60mL) of compound **(12)** (180mg, 0.24mmol) and KOH (2g, 36.9mmol) were refluxed for 12h. After evaporation of the volatiles, the residue was acidified with HCl to a pH of 1 and cooled down in ice to make the product precipitate. The white powder was filtered off and washed with water and dried in air (135mg, 0.22mmol, 91%). Suitable crystals for XRD were obtained by slowly diffusing a solution of MeOH into a DMF solution of the compound. ^{1}H NMR (400 MHz, DMSO-d_6): δ ppm 5.20 (s, 4 H), 7.22 - 7.44 (m, 12 H), 8.42 (d, *J*=1.38 Hz, 4 H), 8.45 - 8.47 (t, *J*=1.51 Hz, 2 H). ^{13}C NMR (101 MHz, DMSO-d_6): δ ppm 70.85, 116.49, 127.96, 128.12, 128.70, 129.42, 131.71, 134.72, 137.43, 138.70, 149.82, 167.05. ESI-MS m/z: 617.1432 [M-H]$^-$. FT-IR (KBr, cm^{-1}): 3065m (br), 2647m, 1714s, 1600m, 1509m, 1455m, 1278s, 1022m, 919m, 691m. Elemental Analysis (%) Calculated for $C_{36}H_{26}O_{10}$: C, 69.90; H, 4.24; Found: C, 69.86; H, 4.19.

Synthesis of 1,1-dichlorovinylferrrocene (16)

The compound was synthesised as described previously[32] using slight modifications. 2.3mL of CCl_4 was added into a solution of ferrocenecarboxaldehyde (2,5g, 11.7 mmol) and triphenylphosphine (12.25g, 46.7mmol) in anhydrous acetonitrile (20mL) at 0°C under N_2. The reaction mixture was allowed to regain room temperature and was reacted overnight under N_2 at room temperature. Water was then added to the mixture and the product was extracted using diethyl ether, washed with brine and dried over $MgSO_4$. The resulting solid was purified by column chromatography (silica, hexane) to yield a red crystalline solid (2.6g, 9.36mmol, 80%). ^{1}H NMR (400

MHz, CDCl$_3$) δ ppm: 4.20 (s, 5 H), 4.30 (t, J=1.90 Hz, 2 H), 4.59 (t, J=1.83 Hz, 2 H), 6.54 (s, 1 H).

Synthesis of ethynylferrocene (17)

The compound was synthesised as described previously[32] using slight modifications. 1,1-dichlorovinylferrrocene **(16)** (1.2g, 4.2mmol) was dissolved in 10mL of anhydrous THF under N$_2$ and n-BuLi 1.6M (8.4mmol, 5.2mL) was added in one portion under N$_2$ at 0˚C. The reaction mixture was allowed to regain room temperature and was further reacted under nitrogen for 3 h. After the addition of 10mL of H$_2$O, the solid was extracted with diethyl ether, dried over MgSO$_4$, and purified by column chromatography (silica, chloroform) to afford a red solid (776mg, 3.7mmol, 88%). ^{1}H NMR (400 MHz, CDCl$_3$): δ ppm 2.73 (s, 1 H), 4.21 (t, J=1.83 Hz, 2 H), 4.23 (s, 5 H), 4.47 (t, J=1.83 Hz, 2 H). ^{13}C NMR (101 MHz, CDCl$_3$): δ ppm 63.84, 68.66, 68.70, 70.03, 71.73, 73.49, 82.59. MALDI-TOF-MS (RP-m/z): 209.877 [M]$^+$. FT-IR (KBr, cm^{-1}): 3280s, 3103m, 3087m, 2102s, 1406m, 1103s, 815s, 478s. Elemental Analysis (%) Calculated for C$_{12}$H$_{10}$Fe: C, 68.62; H, 4.80; Found: C, 68.69; H, 4.81. E$_{1/2}$ (V, CH$_2$Cl$_2$, vs [FeCp$_2$]$^{0/+}$): 0.16.

Synthesis of 1,4-dibromo2,5-diiodobenzene (14)

The compound was synthesised as described previously[31] using slight modifications. Iodine (24g, 94.5mmol) was added in small portions to a solution of 1,4-dibromobenzene (5.8g, 24.6mmol) in sulfuric acid (80mL) at 125-135˚C. The reaction was further reacted for 24 h at 125-135˚C. The mixture was then cooled down to room temperature and poured into a beaker of ice and water, filtered off, washed with a saturated solution of sodium thiosulfate and then with a saturated solution of sodium

hydrogen carbonate. The resulting residue was then purified by recrystallisation from benzene (6.8g, 14mmol, 57%). ^{1}H NMR (400 MHz, CDCl$_3$): δ ppm 8.06 (s, 2 H). ^{13}C NMR (101 MHz, CDCl$_3$): δ ppm 101.30, 129.19, 142.31. Elemental Analysis (%) Calculated for C$_6$H$_2$Br$_2$I$_2$ C, 14.78; H, 0.41; Found: C, 14.89; H, 0.42.

Synthesis of 2,4-dibromo-bis(ethynylferrocenyl)benzene (18)

1,4-Dibromo-2,5-diiodobenzene (1.05g, 2.2mmol), CuI (8.2mg, 4.3.10^{-3}mmol), Pd(PPh$_3$)$_2$Cl$_2$ (30.5mg, 4.3.10^{-3}mmol) and 6mL of NEt$_3$ were dissolved in 20 mL of toluene under N$_2$. A solution of ethynlferrocene (1g, 4.8mmol) in 100 mL of toluene was then added dropwise to the former solution and further reacted at room temperature overnight under N$_2$. Toluene was evaporated to yield an orange solid which was washed with plenty of hexane and then purified by column chromatography (silica, hexane/ethylacetate:9/1).Yield: 932mg, 65%. ^{1}H NMR (400 MHz, CDCl$_3$): δ ppm 4.29 (s, 10 H), 4.31 (t, J=1.88 Hz, 4 H), 4.56 (t, J=1.82 Hz, 4 H) 7.72 (s, 2 H). ^{13}C NMR (101 MHz, CDCl$_3$) δ ppm 63.92, 69.07, 69.39, 70.17, 71.70, 83.25, 96.48, 123.21, 126.35, 135.72. MALDI-TOF-MS (RP-m/z): 652.072 [M]$^+$. FT-IR (KBr, cm^{-1}): 3106w, 2230m, 1493m, 1436m, 1341m, 1105m, 1065m, 1001m, 895s, 811s, 490s, 475s. Elemental Analysis (%) calculated for C$_{30}$H$_{20}$Br$_2$Fe$_2$: C, 55.26; H, 3.09; Found C, 55.28; H, 3.13. E$_{1/2}$ (V, CH$_2$Cl$_2$, vs [FeCp$_2$]$^{0/+}$): 0.18.

Synthesis of compound (19)

- Conditions 1

Benzene-1,3-dicarboxyethylester-5-boronic acid (752mg, 2.8mmol) and Na$_2$CO$_3$ (1.2g, 11mmol) were dissolved in 25mL of degassed toluene under N$_2.$ The reaction

mixture was heated at reflux under N_2 and Pd(PPh$_3$)$_4$ (105mg, 0.09mmol) was added. A solution of 2,4-dibromo-bis(ethynylferrocenyl)benzene (424mg, 0.65mmol) in degassed toluene (60mL) was added dropwise to the previous mixture under N_2 and further reacted for 2-3 d. Toluene was evaporated to yield an orange solid which purified with column chromatography (silica, hexane/ethylacetate: 9/1). Yield: 112mg, 12%. Suitable crystals for XRD were obtained by layering carefully an equal volume of hexane on top of a saturated solution of the compound in CH_2Cl_2. ^{1}H NMR (400 MHz, CDCl$_3$): δppm 1.45 (t, J=7.03 Hz, 12 H), 4.12 (br. s., 10 H), 4.26 (br. s., 4 H), 4.35 - 4.64 (m, 12 H), 7.68 (s, 2 H), 8.59 (s, 4 H), 8.77 (s, 2H). ^{13}C NMR (101 MHz, CDCl$_3$): δ ppm 14.08, 61.22, 64.44, 69.05, 69.94, 71.30, 83.00, 94.46, 122.03, 129.87, 130.88, 133.32, 134.48, 137.87, 140.29, 165.79. MALDI-TOF-MS (RP-m/z): 934.2 [M]$^+$. FT-IR (KBr, cm^{-1}): 2980w, 2927w, 2214m, 1719s, 1440w, 1385w, 1338m, 1237s, 1106m, 1026m, 805m, 761m, 497m. $E_{1/2}$ (V, CH_2Cl_2, vs [FeCp$_2$]$^{0/+}$): 0.16.

- Conditions 2

Benzene-1,3-dicarboxyethylester-5-boronic acid (1.035g, 3.9mmol) and a 2M aqueous solution of Na$_2$CO$_3$ (1,2g, 11.1 mmol, 5.55mL) were dissolved in 30 mL of degassed toluene under N_2. The reaction mixture was heated at reflux under N_2 and Pd(PPh$_3$)$_4$ (180mg, 0.155mmol) was added. A solution of 2,4-dibromo-bis(ethynylferrocenyl)benzene (1.1mmol, 725mg) in degassed toluene (50mL) was added dropwise to the previous mixture under N_2 and further reacted for 2-3 d. Toluene was evaporated to yield an orange solid which was washed with plenty of hexane and then purified with column chromatography (silica, hexane/ethylacetate: 9/1). Yield: 605mg, 60%. Suitable crystals for XRD were obtained by layering

carefully an equal volume of hexane on a saturated solution of the compound in CH_2Cl_2. ^{1}H NMR (500 MHz, $CDCl_3$): δ ppm 1.45 (t, J=7.09 Hz, 12 H), 4.07 (s, 10 H), 4.21 (s, 4 H), 4.38 (s, 4 H), 4.48 (q, J=7.09 Hz, 8 H), 7.70 (s, 2 H), 8.61 (d, J=1.58 Hz, 4 H), 8.78 (t, J=1.58 Hz, 2 H). ^{13}C NMR (126 MHz, $CDCl_3$): δ ppm 14.40, 61.53, 64.44, 69.16, 70.06, 71.37, 84.32, 94.74, 122.04, 129.87, 130.89, 133.32, 134.48, 140.29, 140.85, 165.78. MALDI-TOF-MS (RP-m/z): 934.3 [M]$^+$. FT-IR (KBr, cm^{-1}): 2980w, 2927w, 2214m, 1719s, 1440w, 1385w, 1338m, 1237s, 1106m, 1026m, 805m, 761m, 497m. Elemental Analysis (%) calculated for $C_{54}H_{46}O_8Fe_2$: C, 69.39; H, 4.96; Found C, 69.31; H, 4.86. $E_{1/2}$ (V, CH_2Cl_2): 0.16.

Synthesis of *p*-terphenyl-2'',5''-bis(ferrocenylethynyl)-3,5,3',5'-tetracarboxylic acid (20)

Compound (**19**) (100mg, 0.11mmol) was suspended in 30 mL of THF, to which a 2M KOH aqueous solution (5.8mL, 11.6mmol) was added. The mixture was stirred at room temperature overnight. THF was evaporated under reduced pressure and diluted HCl was added to the remaining aqueous solution until it became acidic. The orange solid was filtered off, washed several times with water and dried in air to yield the corresponding tetracarboxylic acid (55mg, 0.067mmol, 63%). ^{1}H NMR (400 MHz, DMSO-d_6): δ ppm 4.03 (s, 10 H), 4.31 (br. s., 4 H), 4.44 (br. s, 4 H), 7.78 (s, 2 H), 8.53 (br. s, 4 H), 8.59 (br. s, 2 H). ^{13}C NMR (126 MHz, DMSO-d_6): δ 63.5, 69.2, 69.7, 71.0, 83.9, 94.6, 121.4, 129.3, 131.4, 132.9, 133.8, 139.3, 140.5, 166.5. MALDI-TOF-MS (m/z): RP 822.2 [M]$^+$; RN 821.2 [M]$^-$. FT-IR (KBr, cm^{-1}): 3436m (br), 3091m (br), 2640w, 2200m, 1709s, 1600m, 1506m, 1449w, 1413m, 1276s, 1107m, 895m, 820m, 762, 686m, 495m. Elemental Analysis (%) calculated for $C_{46}H_{30}Fe_2O_8$: C, 67.18, H, 3.68; Found: C, 67.26, H, 3.72.

Synthesis of 1,4-Bis(ferrocenylethynyl)benzene (21)

1,4-diiodobenzene (178.5mg, 0.54mmol), CuI (2mg, 0.01mmol), $Pd(PPh_3)_2Cl_2$ (78mg, 0.01mmol) and 2.5mL of NEt_3 were dissolved in 10 mL of degassed toluene under N_2. A solution of ethynylferrocene (250mg, 1.2mmol) in 40 mL of degassed toluene was then added dropwise to the former solution and further reacted at room temperature overnight under N_2. Toluene was evaporated to yield an orange solid which was washed with pentane and recrystallised from CH_2Cl_2/hexane (202mg, 0.41mmol, 75%). ^1H NMR (400 MHz, C_6D_6): δ ppm 3.95 (t, J=1.88 Hz, 4 H), 4.08 (s, 10 H), 4.47 (t, J=1.88 Hz, 4 H), 7.37 (s, 4 H). ^{13}C NMR (101 MHz, $CDCl_3$): δ ppm 65.0, 69.0, 70.0, 71.4, 85.7, 90.1, 123.1, 131.2. MALDI-TOF-MS (RP-m/z): 494.1 $[M]^+$. FT-IR (KBr, cm^{-1}): 3079w, 2934w, 2201m, 1518m, 1408m, 1202m, 1103m, 1030m, 1004m, 924m, 828s, 812vs, 539m, 491vs. Elemental Analysis (%) calculated for $C_{30}H_{22}Fe_2$: C, 72.91, H, 4.49; Found: C, 73.04, H, 4.41. $E_{1/2}$ (V, CH_2Cl_2, vs $[FeCp_2]^{0/+}$): 0.13.

Synthesis of [Phenyl(ethynyl)]ferrocene (22)

Iodobenzene (221mg, 1.1mmol, 0.12mL), CuI (4.1mg, 0.022mmol), $Pd(PPh_3)_2Cl_2$ (15.2mg, 0.022mmol) and 2.5mL of NEt_3 were suspended in 10 mL of toluene and carefully degassed. A solution of ethynylferrocene (250mg, 1.2mmol) in 40 mL of degassed toluene was then added dropwise to the former solution and further reacted at room temperature overnight under N_2. Toluene and the excess amine were evaporated under reduced pressure. The orange residue was chromatographed on a silica column using 20% (v/v) CH_2Cl_2 in hexane as the eluent. Evaporation of the first coloured band afforded the orange product (277mg, 0.97mmol, 90%). ^1H NMR (400 MHz, $CDCl_3$): δ ppm 4.21 - 4.29 (m, 7 H), 4.52 (t, J=1.83 Hz, 2 H), 7.29 - 7.37 (m, 3

H), 7.46 - 7.53 (m, 2 H). ^{13}C NMR (101 MHz, CDCl$_3$): δ ppm 65.57, 69.10, 70.26, 71.71, 86.01, 88.58, 124.25, 127.95, 128.57, 131.70. MALDI-TOF-MS (RP-m/z): 285.96 [M]$^+$. FT-IR (KBr, cm^{-1}): 3090w, 3027w, 2223m, 1586w, 1492m, 1438s, 1407w, 1204w, 1101m, 1068m, 1023m, 998s, 921m, 834vs, 821s, 756vs, 692s, 543s, 514m, 495vs, 482vs. Elemental Analysis (%) calculated for C$_{18}$H$_{14}$Fe: C, 75.55, H, 4.93; Found: C, 75.59; H, 4.83. E$_{1/2}$ (V, CH$_2$Cl$_2$, vs [FeCp$_2$]$^{0/+}$): 0.13.

2.5 References

1. M. Gomez-Lopez, J. A. Preece, J F. Stoddart, *Nanotechnology*, 1996, **7**, 183

2. P. R. Ashton, R. A. Bissell, N. Spencer, J. F. Stoddart, M. S. Tolley, *Synlett*, 1992, 923

3. V. Balzani, A. Credi, F. Marchioni, J. F. Stoddart, *Chem. Commun.*, 2001, 1861

4. (a) G.R. Desiraju, Crystal Engineering, Elsevier, Amsterdam, 1989. (b) G.R. Desiraju, The Crystal as a Supramolecular Entity, Wiley, New York, 1995. (c) G.R. Desiraju, *Angew. Chem.*, 1995, **107**, 2541. (d) G.R. Desiraju, *Angew. Chem. Int. Ed. Engl.*, 1995, **34**, 2311

5. (a) R. Robson, B. F. Abrahams, S. R. Batten, R. W. Gable, B. F. Hoskins, J. Liu, Supramolecular Architecture, ACS, Washington, DC, 1992, Ch. 19. (b) M. Fujita, Y. J. Kwon, S. Washizu, K. Ogura, *J. Am. Chem. Soc.*, 1994, **116**, 1151. (c) L. R. MacGillvary, S. Subramanian, M. J. Zaworotko, *J. Chem. Soc. Chem. Commun.*, 1994, 1325. (d) A. J. Blake, N. R. Champness, S. M. Chung, W.-S. Li, M. Schroder, *Chem. Commun.*, 1997, 1005. (e) L. Carlucci, G. Ciani, D. M. Proserpio, A. Sironi, *J. Chem. Soc. Chem. Commun.*, 1994, 2755. (f) A. J. Blake, N. R. Champness, A. N. Khlobystov, D. A. Lemenovski, W.-S. Li, M. Schroder, *Chem. Commun.*, 1997, 1339. (g) S. Subramanian, M.J. Zaworotko, *Angew. Chem.*, 1995, **107**, 2295. (h) S. Subramanian, M.J. Zaworotko, *Angew. Chem. Int. Ed. Engl.*, 1995, **34**, 2127.(i) A.J. Blake, N. R. Champness, A. N. Khlobystov, D. A. Lemenovskii, W.-S. Li, M. Schroder, *Chem. Commun.*, 1997, 2027.(j) P. Losier and M. J. Zaworotko, *Angew. Chem.*, 1996, **108**, 2957; *Angew. Chem. Int. Ed. Engl.*, 1996, **35**, 2779. (k) G. B. Gardner, D. Venkataraman, J. S. Moore, S. Lee, *Nature*, 1995, **374**, 792

6. M. Fujita, Y. J. Kwon, O. Sasaki, K. Yamaguchi, K. Ogura, *J. Am. Chem. Soc.*, 1995, **117**, 7287

7. A. Ranganathan, V. R. Pedireddi, C. N. R. Rao, *J. Am. Chem. Soc.*, 1999, **121**, 1752

8. (a) G. M. Whitesides, E. E. Simanek, J. P. Mathias, C. T. Seto, D. N. Chin, M. Mammen,D. M. Gordon, *Acc. Chem. Res*., 1995, **28**, 37. (b) G. M. Whitesides, J. P. Mathias, C. T. Seto, *Science*, 1991, **254**, 1312

9. A. Magistrato, P. S. Pregosin, A. Albinati, U. Rothlisberger, *Organometallics*, 2001, **20**, 4178

10. G. Binnig, H. Rohrer, *Rev. Mod. Phys.*, 1987, **59**, 615

11. N. Dmitriev, N. Lin, J. Weckesser, J. V. Barth, K. Kern, *J. Phys. Chem. B*, 2002, **106**, 6907

12. S. Griessl, M. Lackinger, M. Edelwirth, M. Hietschold, W. M. Heckl, *Single Mol.*, 2002, **3**, 25

13. J. V. Barth, J. Weckesser, C. Cai, P. Günter, L. Bürgi, O. Jeandupeux, K. Kern, *Angew. Chem. Int. Ed.*, 2000, **39**, 1230. (b) J. V. Barth, J. Weckesser, G. Trimarchi, M. Vladimirova, A. De Vita, C. Cai, H. Brune, P. Günter, K. Kern, *J. Am. Chem. Soc.*, 2002, **124**, 7991

14. J. A. Theobald, N. S. Oxtoby, M. A. Phillips, N. R. Champness, P. H. Beton, *Nature*, 2003, **424**, 1029

15. M. Blunt, X. Lin, M. del C. Gimenez-Lopez, M. Schroder, N. R. Champness, P. H. Beton, *Chem. Commun.*, 2008, 2304

16. M. O. Blunt, J. C. Russell, M. del C. Giménez-López, J. P. Garrahan, X. Lin, M. Schröder, N. R. Champness, P. H. Beton, *Science*, **322**, 2008, 1077. See Sup. Info. for details of the calculations.

17. M. E. Fisher, J. Stephenson, *Phys. Rev.*, 1963, 132, 1411

18. J. Linde, C. Moore, M. G. Nordahl, *Discrete Mathematics and Theoritical Computer Science Proceedings AA* (DM-CCG), 2001, **23**

19. W. Krauth, R. Moessner, *Phys. Rev. B*, 2003, **67**, 064503

20. H. W. J. Blote, H. J. Hilborst, *J. Phys. A*, 1982, **15**, L631

21. C. L. Henley, in Quasicrystals, *the State of the Art*, D. P. Di Vincenzo, P. J. Steinhardt, Eds. World Scientific, Singapore, 1999, 459

22. R. Moessner, S. L. Sandhi, E. Fradkin, *Phys. Rev. B*, 2002, **65**, 024504

23. G. H. Fredrickson, H. C. Andersen, *Phys. Rev. Lett.*, 1984, **53**, 12441247

24. J. Garrahan, D. Chandler, *Phys. Rev. Lett.*, 2002, **89**, 035704

25. R. Otero, M. Lukas, R. E. A. Kelly, W. Xu, E. Laegsgaard, I. Stensgaard, L. N. Kan-torovich, F. Besenbacher,, *Science*, 2008, **319**, 312

26. D. B. Wilson, *Ann. Appl. Probab.*, 2004, **14**, 274

27. X. Lin, I. Teepeni, A. J. Blake, A. Dailly, C. M. Brown, J. M Simmons, N. Zoppi, G. S. Walker, K. M. Thomas, T. J. Mays, P. Hubberstey, N. R. Champness, M. Schroder, *J. Am. Chem. Soc.*, 2009, **131**, 2159

28. N. Miyaura, A. Suzuki, *Chem. Comm.*, 1979, 866

29. D. Milstein, J. K. Stille, *J. Am. Chem. Soc.*, 1978, **100**, 3636

30. C. Amatore, A. Jutand, *J. Organomet. Chem.*, 1999, **576**, 254

31. H. Hart, K. Harada, C-J. F. Du, *J. Org. Chem.*, 1985, **50**, 3104

32. S.-J. Luo, Y.-H. Liu, C-M. Liu, Y-M. Liang, Y-X. Ma, *Synth. Comm.*, 2000, **30**, 1569

33. (a) C. Glaser, *Ber. Dtsch. Chem. Ges.*, 1869, **2**, 422. (b) C. Glaser, *Ann. Chem. Pharm.*, 1870, **154**, 137. (c) P. Siemsen, R. C. Livingston, F. Diederich, *Angew. Chem.*, *Int. Ed.*, 2000, **39**, 2632(d) A. S. J. Hay, *J. Org. Chem.*, 1962, **27**, 3320. (e) R.

Rossi, A. Carpita, C. Bigelli, *Tetrahedron Lett.*, 1985, **26**, 523 (f) Q. Liu, D. J. Burton, *Tetrahedron Lett.*, 1997, **38,** 4371

34. S. Thorand, N. Krause, *J. Org. Chem.*, 1998, **63**, 8551

35. H-F. Chow, C-W. Wan, K-H. Low, Y-Y. Yeung, *J. Org. Chem.*, 2001, **66**, 1910

36. A. Elangovan, Y-H. Wang, T-I. Ho, *Org. Lett.,* 2003, 5, 1841

37. S. Ma, D. Sun, J. M. Simmons, C. D. Collier, D. Yuan, H-. Zhou, *J. Am. Chem. Soc.*, 2008, **130**, 1012

38. S. J. Coles, R. Holmes, M. B. Hurtshouse, D. J. Price, *Acta. Cryst. E*, 2002, **58**, o626

39. P. Holy, P. Sehnal, M. Tichy, J. Zavada, I. Cisarova, *Tetrahedron*, 2004, **15**, 3805

40. R. S. Wright, T. K. Vinod, *Tetrahedron Lett.*, 2003, **44**, 7129

41. L. Cuffe, R. D. A. Hudson, J. F. Gallagher, S. Jennings, C. J. McAdam, R. B. T. Connelly, A. R. Manning, B. H. Robinson, J. Simpson, *Organomettalics*, 2005, **24**, 2051

43. J. Tiburcio, V. M. Ugalde-Salvidar, S. J. Loeb, H. Torrens, *Inorg. Chemi. Acta*, 2009, **362**, 4241

44. H. Fink, N. J. Long, A. J. Martin, G. Opromolla, A. J. P. White, D. J. Williams, P. Zanello, *Organomettalics*, 1997, **16**, 2646

45. a) E. McGale, B. H. Robinson, J. Simpson, *Organomettalics*, 2003, **22**, 931. b) A. Klein, O. Lavastre, J. Fiedler, *Organometallics*, 2006, **25**, 635

46. N. Chawdhury, N. J. Long, M. F. Mahon, L-L. Ooi, P. R. Raithby, S. Rooke, A. J. P. White, D. J. Williams, M. Younus, *J. Org. Chem.*, 2004, **689**, 840

47. D. T. Win, *Au. J. T.*, 2010, **13**, 151

48. A. Cornia, A. C. Fabretti, M. Pacchioni, L. Zobbi, D. Bonacchi, A. Caneschi, D. Gatteschi, R. Biagi, U. Del Pennino, V. De Renzi, L. Gurevisch, H. S. J. Van der Zant, *Angew. Chem. Int. Ed.*, 2003, **42**, 1645

49. L. Bogani, W. Wernsdorfer, *Nature Materials*, 2008, **7**, 179

50. E. Coronado, C. Marti-Gastaldo, S. Tatay, *Appl. Surf. Science*, 2007, **254**, 225

51. D. A. Thomson, J. S. Best, *J. Res. Dev.*, 2000, **3**, 311

52. M. Affronte, F. Troiani, A. Ghirri, A. Candini, M. Evangelisti, V. Corradini, S. Carretta, P. Santini, G. Amoretti, F. Tuna, G. Timco, R. E. P. Winpenny, *J. Phys D : Appl. Phys.*, 2007, **40**, 2999

53. O. Lavastre, J. Plass, P. Bachmann, S. Guesmi, C. Moinet, P. H. Dixneuf, *Organomettalics*, 1997, **16**, 184

54. C. Levanda, K. Bechgaard, D. O. Cowan, *J. Org. Chem.*, 1976, **41**, 2700

55. J. A. Kramer, D. N. Hendrickson, *Inorg. Chem.*, 1980, **19**, 3330

56. A. Klein, O. Lavastre, J. Fiedler, *Organometallics*, 2006, **25**, 635

57. A. K. Diallo, J-C. Daran, F. Varret, J. Ruiz, D. Astruc, *Angew. Int. Ed.*, 2009, **48**, 3141

58. S. J. H. Griessl, *J. Phys. Chem. B,* 2004, **26**, 11556

59. R. Madueno, M. T. Raisanen, C. Silien, M. Buck, *Nature*, 2008, **454**, 618

60. O. Ivasenko, *Chem. Commun.*, 2009, **10**, 1192

61. G. Schull, *Adv. Mater.*, 2006, **18**, 2954

62. M. Wahl, M. Stohr, H. Spillmann, T. A. Jung, L. H. Gade, *Chem. Commun.*, 2007, 1349

63. S. Stepanow, *Nat. Mater.,* 2004, **3**, 229

64. K. Tahara, S. Furukawa, H. Uji-i, T. Uchino, T. Ichikawa, J. Zhang, W. Mamdouh, M. Sonoda, F. C. De Schryver, S. De Feyter, Y. Tobe, *J. Am. Chem. Soc.*, 2006, **128**, 16613

65. D. Wu, K. Deng, M. He, Q. Zeng, C. Wang, *Chem. Phys. Chem.*, 2007, **8**, 1519

66. M. Li, *Angew. Chem. Int. Ed.*, 2008, **120**, 6819

67. M. O. Blunt, J. C. Russell, M. del C. Gimenez-Lopez, N. Taleb, X. Lin, M. Schröder, N. R. Champness, P. H. Beton, *Nature Chemistry*, 2011, **3**, 74

68. D. L. Keeling, M. J. Humphry, P. Moriarty, P. H. Beton, *Chem. Phys. Lett.*, 2002, **366**, 300

69. P. Samorì, N. Severin, C. D. Simpson, K. Müllen, J.P Rabe, *J. Am. Chem. Soc.*, 2002, **124**, 9454

70. S. J. H. Griessl, *Langmuir*, 2004, **20**, 9403

71. G. M. Sheldrick, *Acta. Crystallogr. Sect. A*, 1990, **46**, 467

72. G. M. Sheldrick, University of Göttingen, 1997

Chapter 3: Synthesis, characterisation and surface deposition of Mn$_{12}$ single molecule magnets

3.1 Introduction

The advance in magnetic storage technology has increased considerably over the last decade leading to the miniaturisation of magnetic materials. One way employed to keep up with this trend is to squeeze more data onto storage devices by making the currently used magnetic nanoparticles even smaller. However, it now approaches its limit. For example, in a hard disk data is stored magnetically and each bit is a tiny area in which the material's crystals have all their magnetic fields aligned in the same direction. But as the bit gets smaller, the crystals do not have enough energy to keep the magnetic fields aligned and ambient temperature can reverse their magnetic orientation. As a consequence the bit is erased and therefore data is lost. Another important drawback of the traditional so-called top-down approaches is the distribution of particle size, anisotropy and shapes exhibited by the resulting fragmented ferro- or ferri-magnetic material obtained during the process of miniaturisation which leads to an undesirable distribution of the barrier heights for the inter-conversion of spins within the domains.[1]

The challenge is to find alternative ways to store and process information. This is where the idea of molecular magnetism (bottom-up approach) emerged. Rather than using solids consisting of extended lattices such as in oxides, the aim is to design and synthesise a solid lattice made up of discrete molecular building blocks (molecular magnets).

Molecular nanomagnets are large molecules comprising a large but finite number of magnetic centres (organic radicals, rare-earth ions or transition-metals) that exhibit magnetic properties intermediate between classical (magnetic hysteresis) and quantum nature.

Among the different molecular magnets studied, single molecule magnets (SMMs) are a class of major interest.[2] SMMs are transition metal clusters that individually exhibit the classical properties of a magnet below a critical temperature known as the blocking temperature T_B. They combine a large spin ground state (S) and a negative (easy axis) magnetoanisotropy as measured by the axial zero-field splitting parameter D, leading to a potential energy barrier for magnetisation reversal, whose upper limit is given by $S^2*|D|$ or $(S^2-1/4)*|D|$ for integer and half-integer spins respectively.

As a consequence, they display slow relaxation of magnetisation at low temperature which is of purely molecular origin.[3] In other words, the magnetic moment of a SMM can be magnetised with its spin "up" or "down" along the axial magnetic anisotropy axis when subjected to an external magnetic field and can retain the magnetisation on the removal of the magnetic field below T_B (the relaxation process following an Arrhenius law) rendering the system trapped in one of the high spin energy wells (Figure 3.1). This gives rise to magnetic hysteresis, as seen in classical magnets which is a requirement for information storage applications, but because of SMMs molecular dimensions quantum phenomena such as quantum tunnelling of magnetisation (QTM) through the anisotropy barrier have also been observed[4] opening the path towards quantum computing and spintronics applications (Figure 3.2).

Further experimental evidence for the slow magnetic relaxation of a SMM lies in the observation of frequency-dependent out-of-phase ac signals in magnetic ac susceptibility experiments (Figure 3.3).[3a,4,5] As well as allowing the calculation of the effective anisotropy potential energy barrier (ΔE),[6] these measurements also serve as important indicator as to whether a molecule functions as a SMM.

Besides their molecular dimensions, SMMs display numerous advantages over classical magnets including high monodispersity, solubility in organics solvents, low costs, high processabilty and tunability of their affinity towards the environment namely by altering the peripheral ligation crown which also provides protection to the inner magnetic core preventing close interactions with those of neighbouring molecules.
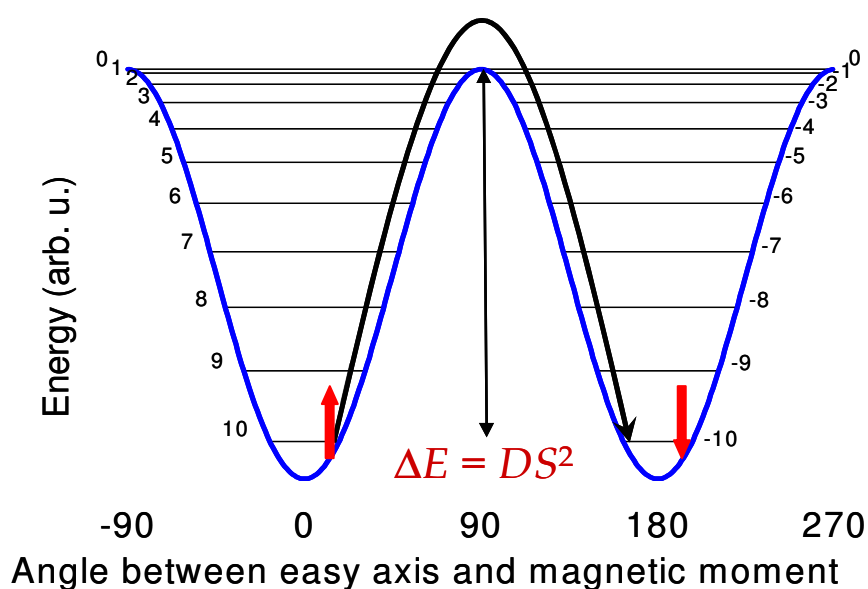
Figure 3.1. Schematic representation of the potential energy barrier of a SMM with a spin ground state $S = 10$. The magnetisation reversal between the spin up and down orientations is a process that follows a thermally activated law.
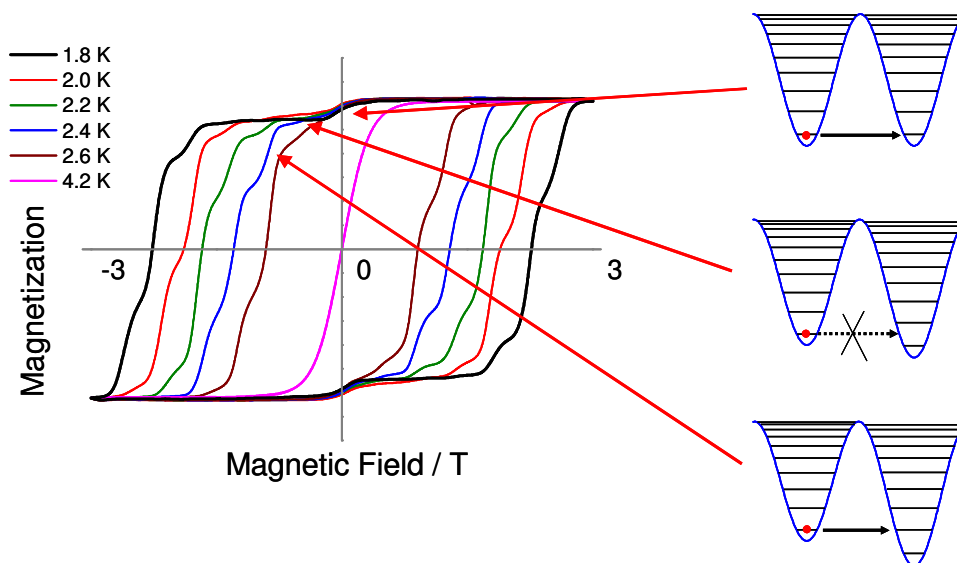
Figure 3.2. Hysteresis loops of $Mn_{12}O_{12}(CH_3COO)_{16}(H_2O)_4.2CH_3COOH.4H_2O$ at different temperatures. The loops exhibit a series of steps, which are due to resonant quantum tunnelling between energy levels.[7]
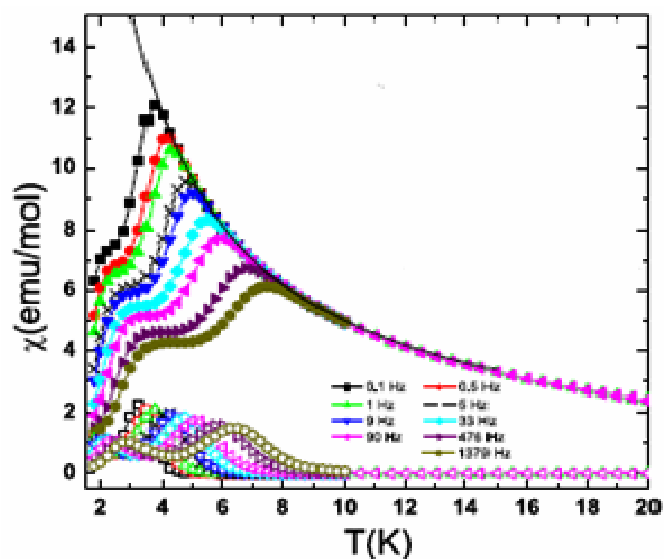
Figure 3.3. Magnetic ac-susceptibility data for $Mn_{12}O_{12}(CH_3COO)_{16}(H_2O)_4.2CH_3COOH.4H_2O$ as a function of temperature.[8]

In 1980, Lis[9] reported the structure of a dodecanuclear manganese cluster of formula $Mn_{12}O_{12}(CH_3COO)_{16}(H_2O)_4 \cdot 2CH_3COOH \cdot 4H_2O$ in short $Mn_{12}ac$ (Figure 3.4).

The molecule consists of twelve manganese ions: eight of the Mn in a non-planar external ring are in the +3 oxidation state ($3d^4$, S=2) and four in a central cubane structure in the +4 state ($3d^3$, S=3/2) linked through oxo bridges. The Mn^{+3} crown is antiferromagnetically coupled to the inner Mn^{+4} cubane yielding a total net spin S=10 in the ground state. The molecule crystallises in the tetragonal space group I-4 and has S_4 crystallographic symmetry.
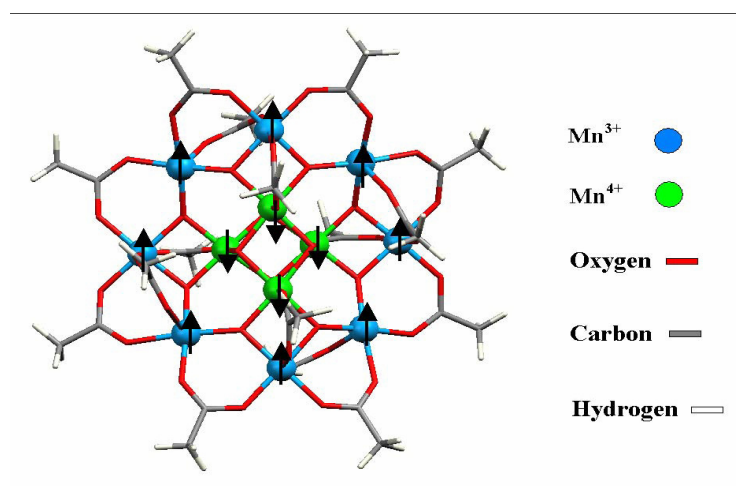
Figure 3.4. Schematic structure of $Mn_{12}O_{12}(CH_3COO)_{16}(H_2O)_4$. The coupling between the Mn ions is described by the arrows. The four Mn^{+4} are ferromagnetically coupled to each other (S=6) and so the eight Mn^{+3} are (S=16). The crown is antiferromagnetically coupled to the inner cubane yielding a spin ground state S=10.[10]

The main advantages of the SMMs from the manganese family are that they exhibit high thermal and chemical stabilities. They possess one of the highest blocking temperatures reported so far (4-6 K).[2] The easiness of preparation of these compounds and their rich synthetic behaviour enable the functionalisation of the peripheral organic ligands.[11] Indeed several new manganese SMMs derivatives have been

synthesised by simply carrying out ligand-exchange substitution reactions starting from the precursor Mn$_{12}$ac (Figure 3.5).
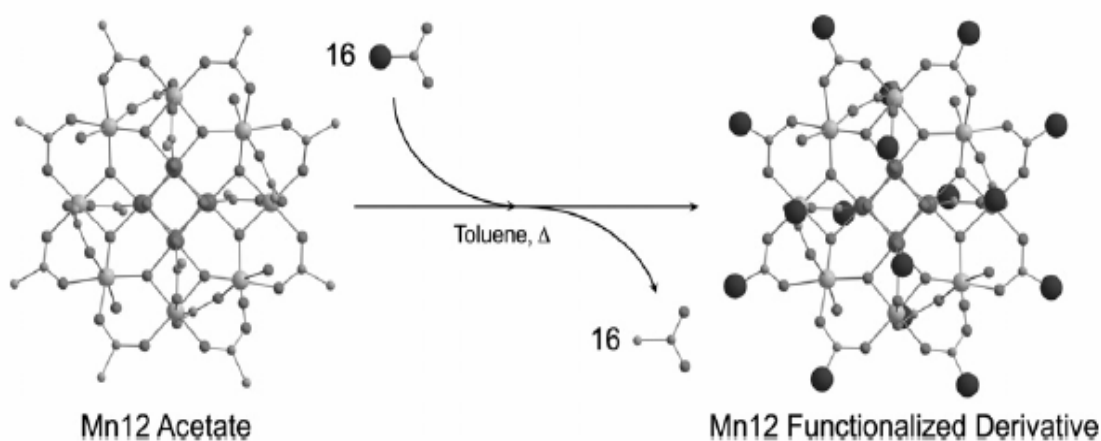
Figure 3.5. Schematics of the Mn$_{12}$ ligand-exchange reaction used for the preparation of functionalised derivatives.[12]

This simple procedure allows the variation and the control of the molecular dimensions of the SMMs synthesised, according to the use of different peripheral ligands. This approach afforded new species such as Mn$_{12}$O$_{12}$(R)$_{16}$(H$_2$O)$_4$ where R=benzoate,[3b] 4-methylthiolbenzoate[13] (Figure 3.6b), stearate,[14] tert-butylacetate[15] (Figure 3.6a), 2,2-dimethylbutyrate,[16] 4-chlorobutyrate,[17] ethanoate,[8] 16-(acetylthio)hexadecanoate[18] (Figure 3.6d), etc.

Mixed ligand derivatives have also been successfully prepared. Recently site-specific functionalisation of Mn$_{12}$ clusters has been achieved yielding [Mn$_{12}$O$_{12}$(O$_2$CC$_6$H$_5$)$_8$(10-(4-acetylsulfanylmethyl-phenyl)-anthracene-1,8 dicarboxyl)$_4$(H$_2$O)$_4$].8CH$_2$Cl$_2$[19] (Figure 3.6c) for example.

Changes in the nuclearity have also been achieved and Mn$_2$,[20] Mn$_4$,[21-29] Mn$_6$,[30,31] Mn$_9$,[32] Mn$_{16}$,[31,33,34] Mn$_{22}$,[35] Mn$_{25}$,[36], Mn$_{26}$,[37], Mn$_{30}$[38,39] and Mn$_{84}$[40] clusters have been reported. The latter is the largest SMM synthesised to date. The structure comprises a

giant Mn_{84} torus with a diameter of about 4.3nm and a thickness of about 1.2nm. It orders in nanotubular stacks parallel to the crystal c axis and to their neighbours displaying thus extensive cylindrical channel formation along one dimension (Figure 3.7). It has been therefore demonstrated that using the bottom-up approach enables to reach the same dimensions as conventional magnets (top-down approach)[40] (Figure 3.8).
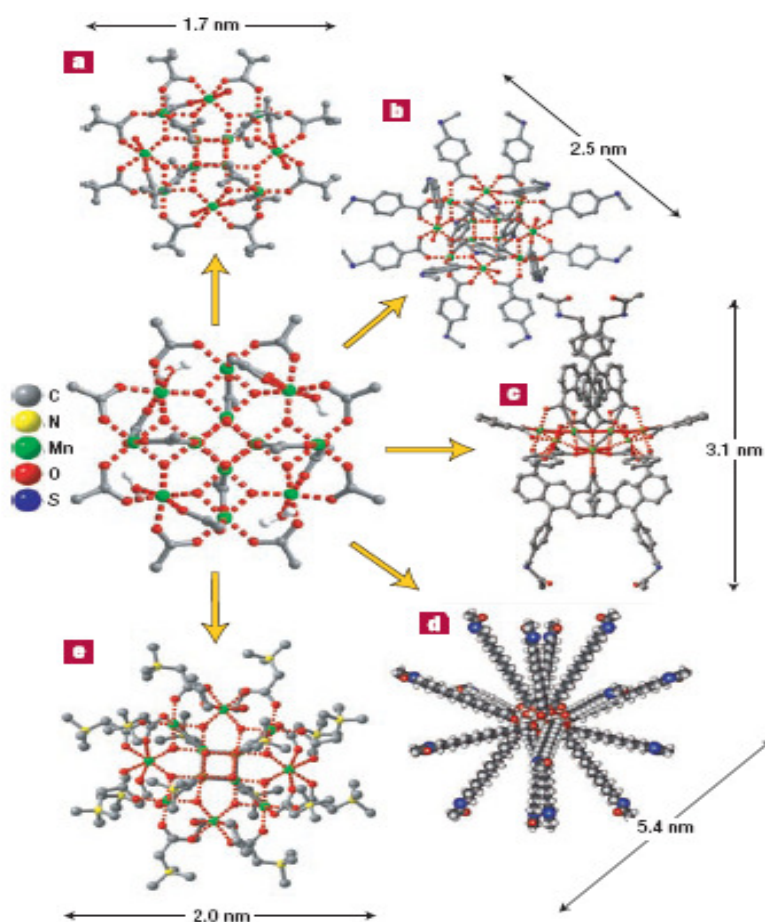
Figure 3.6. Representation of the different functionalisations of $Mn_{12}ac$ in the centre. a. $Mn_{12}O_{12}(C(CH_3)_3COO)_{16}(H_2O)_4$ b. $Mn_{12}O_{12}(p\text{-}CH_3S\text{-}C_6H_4\text{-}COO)_{16}(H_2O)_4$ c. $[Mn_{12}O_{12}(O_2CC_6H_5)_8(10\text{-}(4\text{-acetylsulfanylmethyl-phenyl)-}anthracene\text{-}1,8\text{-dicarboxyl})_4(H_2O)_4]$ d.$Mn_{12}O_{12}(CH_3OS(CH_2)_{15}COO)_{16}(H_2O)_4$ e. $[Mn_{12}O_{12}((CH_3)3NCH_2COO)_{16}(H_2O)_4]^{16+}$. All structures were determined by X-ray crystallography except for d which is a model. All solvents molecules have been omitted.[41]
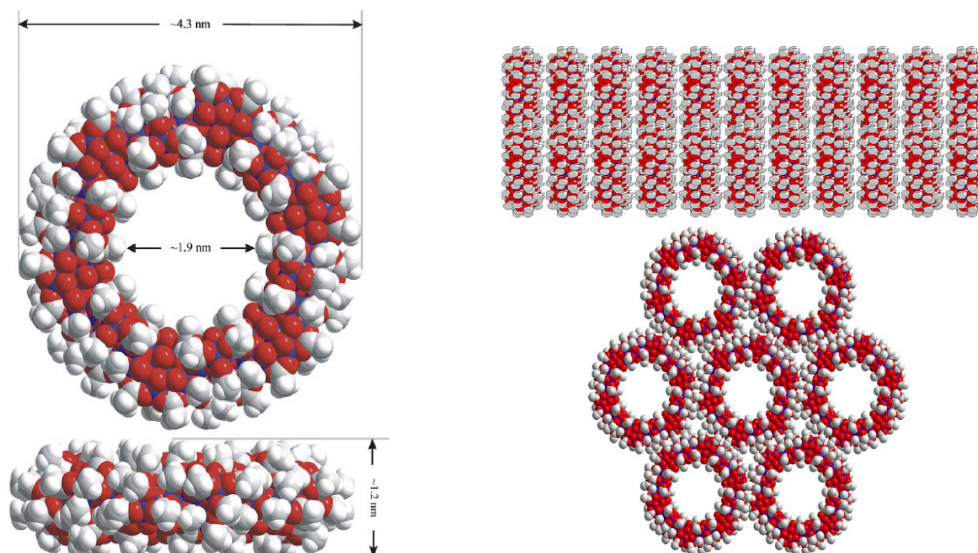
Figure 3.7. Wreath-shaped Mn$_{84}$ cluster, the largest SMM synthesized to date, crystallizes in hexagonal arrays. Multiple layers align to form nanotubular stacks which have potential for a wide range of future applications.[40]
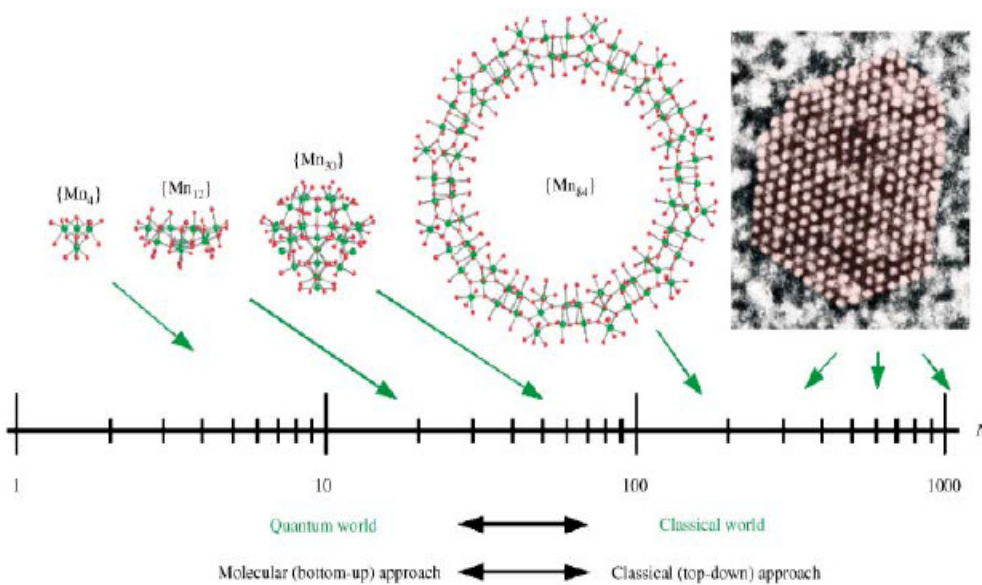
Figure 3.8. On the very right is a high-resolution TEM view along a [110] direction of a typical cobalt nanoparticle containing about 1000 Co atoms. The Mn$_{84}$ cluster has a diameter of ~4.2nm. Smaller SMMs, drawn to scale, have also been included for size comparison purposes.[40]

Most of the examples detailed above focused on preparing modified Mn_{12} derivatives with increased molecular dimensions, larger-spin ground state S or/and higher blocking temperatures. Overall, the Mn_{12} core is found to remain unchanged in these derivatives and studies have shown that the ground state spin (S=9-10) and characteristic hysteresis and frequency-dependent out-of-phase ac signals are still observed for these species.[3b,12-14,16,17,19,42,43]

One of the most attractive and challenging perspectives for information storage or "qbits" for quantum computing using molecular magnets require the addressing of individual magnetic molecules, that is, imaging, probing, and eventually manipulating individual molecules. The simplest strategy to do so is to organise SMMs in ordered arrays on a substrate and use the modern techniques such as scanning probe microscopy (SPM) for addressing single molecules.[18]

The first attempts to deposit Mn_{12} clusters on surfaces were reported by Coronado et al. in 1998 using a Langmuir-Blodgett technique[44] (Figure 3.12b). A surfactant molecular film was created at the air-water interface where the clusters were arranged into both isolated molecules and well-defined monolayers. Several experimental routes have been employed thereafter to deposit SMMs on surfaces. Among others, three main strategies have been employed: (1) modification of the clusters introducing surface-binding functional groups, (2) functionalisation of the substrate to encourage the formation of adsorbed monolayers and (3) a combination of both approaches (Figures 3.9 and 3.10).[45]

Various sulfur functionalised Mn_{12} complexes were synthesised, and deposited on gold surfaces. Nanostructuration of $Mn_{12}O_{12}(R)_{16}(H_2O)_4$ where R= 4-

(methylthio)benzoate, by direct soaking of Au (111) substrates into a solution of the cluster, has also been reported[13] (Figures 3.11 and 3.12a).

The presence of the intact clusters was observed from X-ray photoelectron spectroscopy (XPS), Scanning Tunnelling Microscopy (STM) (Figure 3.11) and time-of-flight secondary ion mass spectrometry (ToF-SIMs) studies. XPS experiments revealed a complete surface coverage for long exposition times.
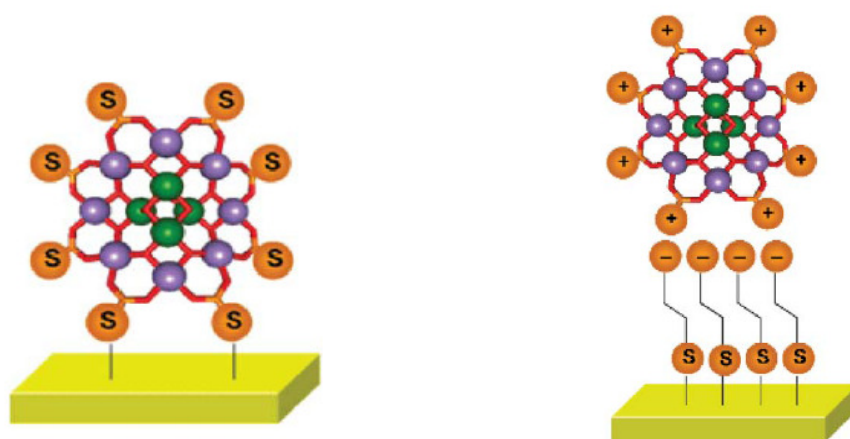
Figure 3.9. Schematics representing the direct anchoring of a thiol-modified Mn$_{12}$ on a gold surface on the left and a polycationic Mn$_{12}$ derivative deposited onto a gold surface functionalised with an anionic self-assembled monolayer on the right.[45]
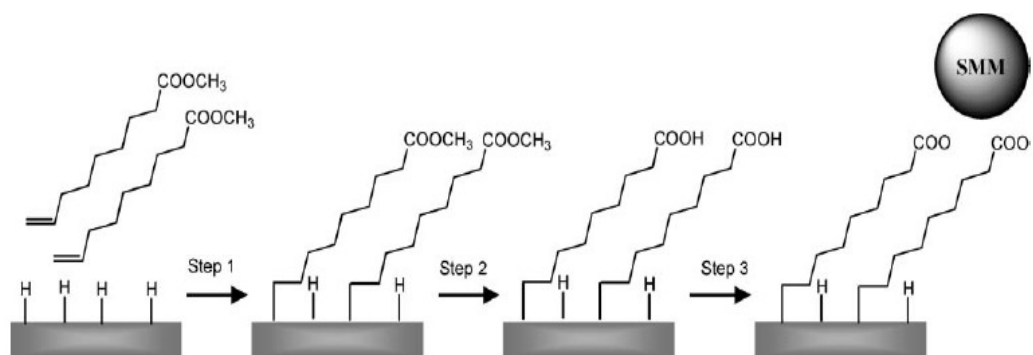
Figure 3.10. Functionalisation of a Si (100) substrate in three steps to promote the grafting of SMMs. *Reagents and conditions: step 1: mesitylene, 200˚C; step 2: H$^+$, H$_2$O, 100˚C; step 3: Mn$_{12}$ac, toluene, 60˚C, 100 mm Hg.[46]*
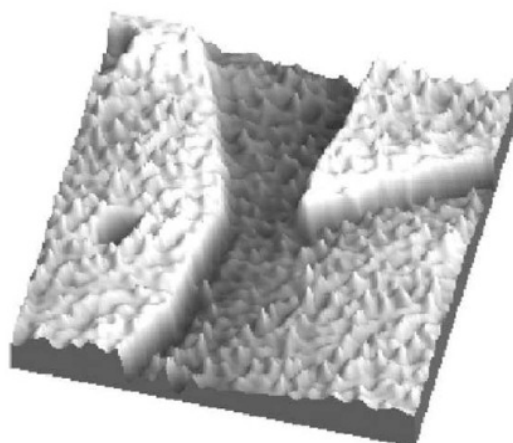
Figure 3.11. 3-D representation of a constant-current STM image (200x200 nm^2) of Mn$_{12}$O$_{12}$(p-CH$_3$S-C$_6$H$_4$-COO)$_{16}$(H$_2$O)$_4$ assembled on gold.[13]
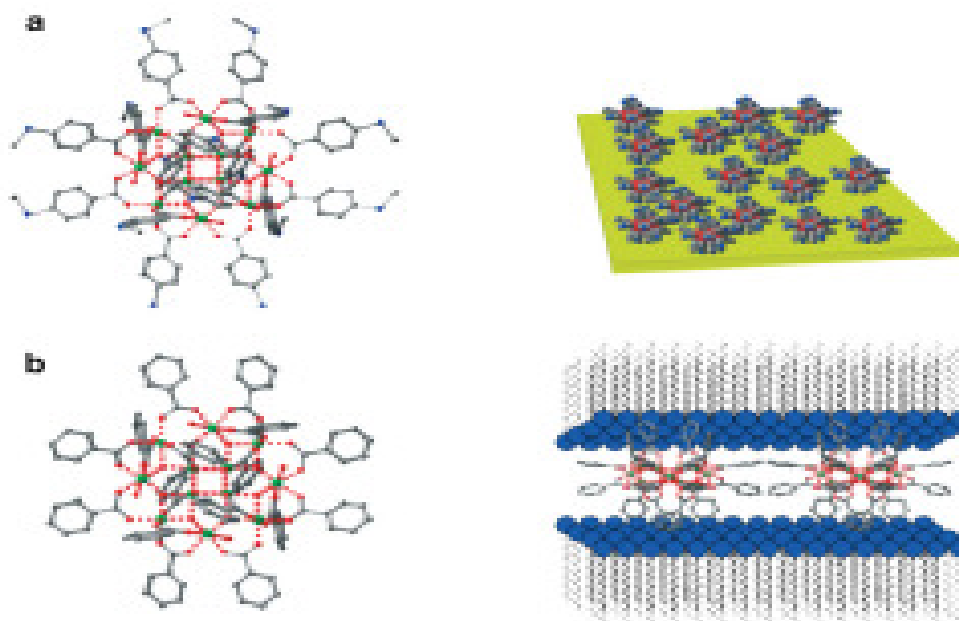
Figure 3.12. Organisations of adequately functionalised Mn$_{12}$ derivatives. a. deposited on gold surface; b. in Langmuir-Blodgett films; The corresponding molecular structure of the used Mn$_{12}$ derivatives is shown on the left.[46]

The deposition of the pristine Mn$_{12}$ac on different surfaces has also been investigated. However, it has been established that the cluster does not adhere to non functionalised surfaces in a stable manner.[47] For this reason, Cavallini et al.[48] have chosen to

investigate the deposition of the biphenyl derivative on HOPG. The biphenyl groups were expected to greatly improve the intermolecular interactions and the interactions with the substrate. The first attempt consisted on simply depositing a solution of the complex in chlorobenzene by drop casting. It resulted in the formation of an inhomogeneous layer of molecules on the surface. A stamp assisted deposition, the so-called lithographically controlled wetting (LCT), was then successfully used to overcome this situation (Figure 3.13).
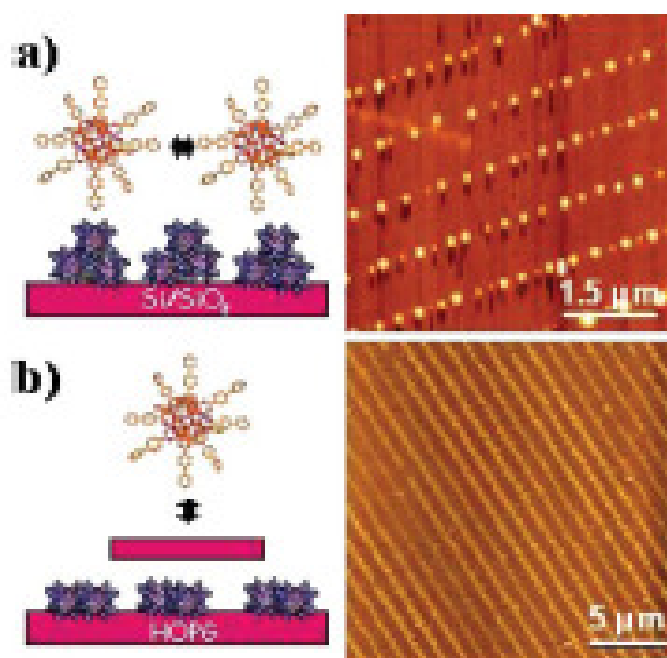
Figure 3.13. AFM images showing the spatially distributed arrays of Mn$_{12}$O$_{12}$(PhC$_6$H$_4$COO)$_{16}$(H$_2$O)$_4$. a. spherically-capped droplets on Si/SiO$_2$. b. monolayer stripes on an HOPG substrate.[48]

Spatially distributed droplets of the complex aligned along the stretching direction were obtained on the hydrophilic Si/SiO$_2$ surface while the deposition onto HOPG led to the formation of monolayer stripes due to enhanced adsorbate-substrate interactions.

However for all these examples no direct study of the magnetic properties was feasible due to the lack of sensitivity of the techniques available. Recently, the deposition of Mn_{12} SMMs on gold surfaces was studied for the first time using X-ray absorption spectroscopy (XAS) and X-ray magnetic circular dichroism (XMCD) using synchrotron radiation.[49,50] XAS spectra provided detailed information on the oxidation states of manganese ions in the adsorbates whilst XMCD spectra provided information on the magnetic polarisation of these ions. A large Mn^{II} signal was clearly detected for 16-sulfanylhexadecanoate and 4-(methylthio)benzoate Mn_{12} clusters adsorbed onto Au(111) surfaces, outlining a redox instability of Mn_{12} complexes at gold surfaces. In turn, the local magnetic polarizations were found to be significantly decreased with respect to the bulk Mn_{12} samples. Preliminary results have also suggested that magnetic hysteresis of these clusters is not retained upon surface deposition.[49] Use of these techniques for the study of Mn_{12} adsorbates on pre-functionalized gold surfaces as well as the aforementioned pre-functionalized silicon surface afforded similar results.[51,52,53] Therefore, although STM and XPS have previously suggested the presence of intact Mn_{12} clusters in monolayers on gold and silicon surfaces, recent use of highly-sensitive techniques has indicated otherwise.

This chapter describes the synthesis of the archetypal Mn_{12}ac and several other derivatives (including novel clusters), their characterisations using Infrared spectroscopy, matrix assisted laser desorption/ionization time-of-flight mass spectrometry (MALDI-TOF MS), elemental analysis as well as X-Ray diffraction studies whenever single crystals of good quality could be successfully grown.

The idea lying behind the varied functionalisations of the pristine $Mn_{12}ac$ is manifold: the solid-state chemistry of the clusters as well as their magnetic properties are of primary interest, although the ultimate goal remains surface deposition applications. As discussed previously, it is of great interest to obtain ordered arrays of SMMs on surfaces which can be directed by playing with several factors such as intramolecular interactions, molecule-surface interactions and lateral intermolecular interactions. All these features mainly depend on the molecular structure of the clusters. For this reason introducing functional carboxylate ligands that will increase the molecular dimensions of the cluster, but also capable of enhancing the adsorbate/surface interactions as well as increasing intermolecular interactions, is highly desirable. The replacement carboxylic acids have therefore been chosen with all these parameters in mind.

A comparative study has also been drawn between the structures of the complexes described herein and those reported in the literature trying to outline the effect that the modification of the peripheral ligand shell has on several criteria such as the $Mn_{12}O_{12}$ core structure, the crystal packing, the space group adopted, the molecular dimensions, the intermolecular separations, the intra and intermolecular interactions involved, etc.

The magnetic behaviour of the different complexes is expected to remain unchanged as the magnetic core should not be altered by modifying the peripheral organic ligation shell. However a series of alternating current (AC) magnetic susceptibility measurements will be carried out on relevant complexes to ensure this is effectively the case.

Finally the last part of the present chapter will deal with the surface deposition attempts. Au(111), HOPG and the PTCDI-melamine network mentioned in the primary introduction of this thesis, were the surfaces of choice for this project. However, due to lack of time, the deposition of only $Mn_{12}ac$ on gold and the PTCDI-melamine network has been carried out using ultra-high vacuum electrospray deposition (UHV-ESD) with the collaboration of the Beton and O'Shea groups from the School of Physics and Astronomy at the University of Nottingham, and the results will be detailed in the last part of this chapter.

3.2 Results and discussion

3.2.1 Choice of Synthetic route

As outlined in the introduction, the aim of this project is the synthesis of SMMs of the form $[Mn_{12}O_{12}(R)_{16}(H_2O)_4]$ where R is a carboxylate group containing functionalities specifically chosen to encourage deposition onto chosen surfaces.

The synthesis of these Mn_{12} clusters can be achieved in two ways. The first, a comproportionation reaction between a Mn^{II} source and Mn^{VII} from MnO_4^- in the presence of the desired carboxylic acid, the original method employed by Lis in the synthesis of Mn_{12}ac.[9]

$$44Mn^{2+} + 16Mn^{7+} \rightarrow 5[Mn_{12}]^{40+}$$
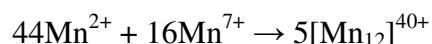
The second, a ligand substitution reaction with Mn_{12}ac where its sixteen peripheral acetate ligands are replaced by the desired functionalised carboxylate groups (Figure 3.5 and Scheme 3.1).[3b,12,14,16,42,43,54] Because the substitution reaction is reversible, the reaction is driven to completion by the removal of acetic acid, a large excess of the carboxylic acid and the repetition of the substitution process to ensure full substitution.

$$[Mn_{12}O_{12}(CH_3CO_2)_{16}(H_2O)_4] + 32\ RCO_2H \rightleftharpoons [Mn_{12}O_{12}(RCO_2)_{16}(H_2O)_4] + 16\ CH_3CO_2H$$
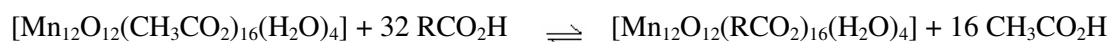
The latter of these two methods is reported to be significantly higher yielding[54] and consequently has been employed for the synthesis of functionalised Mn_{12} derivatives throughout the course of the present project.

3.2.2 Synthesis of Mn₁₂ac (1)

For the purpose of use as starting material in ligand substitution reactions with functionalised carboxylic acids, the synthesis of $[Mn_{12}O_{12}(CH_3CO_2)_{16}(H_2O)_4].2CH_3CO_2H.4H_2O$ **(1)** was here performed through a comproportionation reaction using a reported procedure[10] differing slightly from the original one described by Lis.[9]

$$Mn(CH_3CO_2)_2.4H_2O + KMnO_4 \xrightarrow{\quad CH_3CO_2H_{(aq)} \quad} [Mn_{12}O_{12}(CH_3CO_2)_{16}(H_2O)_4].2CH_3CO_2H.4H_2O$$
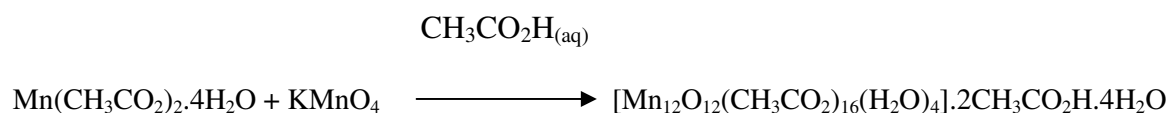
Manganese (II) acetate tetrahydrate was dissolved in a 60% acetic acid solution and potassium permanganate was added in small aliquots to this solution, ensuring no violent exothermic reaction occurred, and stirred until full dissolution. The resulting solution was then left to stand undisturbed for 3 days to allow for precipitation of Mn₁₂ac crystals which were characterised by infrared (FT-IR) spectroscopy, matrix assisted laser desorption/ionization time-of-flight mass spectrometry (MALDI-TOF MS) and elemental analysis. The unit cell was also measured by single crystal X-ray diffraction experiments for purposes of comparison to confirm the data were matching those reported in the literature.[55]

The IR spectrum exhibited a broad peak at 3426 cm^{-1} characteristic of the νO-H stretching band arising from the peripheral water molecules bound to the manganese ions.[14] Peaks at 2961 cm^{-1}, 2926 cm^{-1} and 2855 cm^{-1} correspond to the νC_{sp}^{3}-H stretching within the acetate groups whilst peaks at 1418 cm^{-1} and 1384 cm^{-1} are

characteristic of the νC-O stretching mode of the carboxylate groups bound to the Mn_{12} core.[14,56]

MALDI-TOF MS is a soft ionisation technique which has emerged as a particularly useful tool for characterisation of high mass molecules and metal clusters.[57] It has been employed throughout this research project in both positive and negative reflector modes and proven to greatly aid in successful identifications of Mn_{12} clusters.

MALDI-TOF MS spectrum of **(1)**, in the negative mode, displays the molecular ion peak corresponding to $[Mn_{12}O_{12}(CH_3CO_2)_{16}]^-$ at 1795.6 *m/z*. Molecular ion fragments corresponding to $[Mn_{12}O_{12}(CH_3CO_2)_{16-n}]^-$ where n=1-3 are also observed indicating the sequential loss of the acetate ligands under experimental conditions providing evidence for the formation of the desired complex (Figure 3.14). In the positive mode the molecular ion peak is not seen, however a longer progression of molecular ion fragments corresponding to $[Mn_{12}O_{12}(CH_3CO_2)_{16-n}]^+$ where n=1-7 is observed, proving each mode to be complementary to the other. The water molecules coordinated to the Mn_{12} core are lost under experimental conditions and this is found to be common to both previous experiments reported in the literature and later experiments performed in this project.[57] Elemental analysis also confirmed the successful synthesis of Mn_{12}ac and the unit cell was found to correspond to that reported in the literature.[9,55]
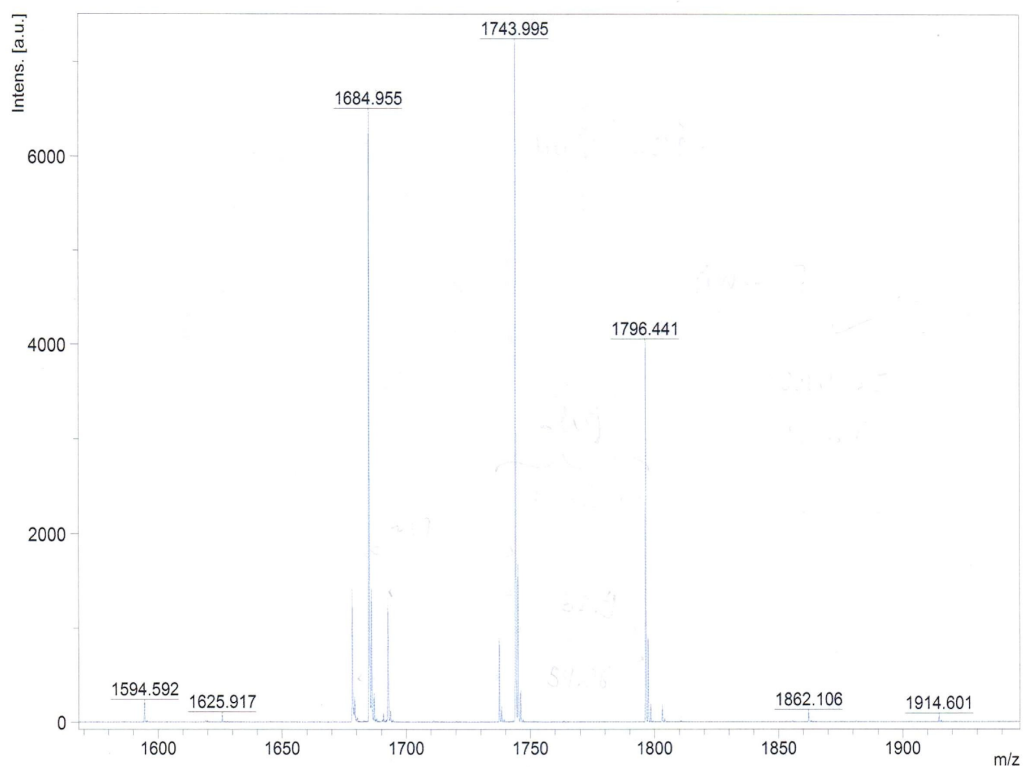
Figure 3.14. MALDI-TOF spectrum of (1) in negative reflector mode showing peaks corresponding to the molecular ion and fragments after the sequential loss of the acetate ligands.

3.2.3 Ligand substitution reactions

All the new complexes were synthesised from $Mn_{12}ac$ (**1**) by a ligand substitution reaction with the corresponding carboxylic acid as shown in Scheme 3.1. As mentioned earlier, the ligand exchange reaction is an equilibrium due to the similar ligand strength of the replacement carboxylate and acetate. Therefore, to drive the reaction to completion simple precautions have been employed: i) a large excess of the desired carboxylic acid was employed; ii) removal of the released acetic acid by vacuum distillation as its toluene azeotrope; iii) repeating the reaction twice.

$$[Mn_{12}O_{12}(CH_3CO_2)_{16}(H_2O)_4] \ + \ HL^i \ \xrightarrow[\substack{RT,\ overnight \\ x\ 2}]{DCM} \ [Mn_{12}O_{12}(L^i)_{16}] \ + \ CH_3CO_2H$$

(1)

$L^1 = $ (phenyl)–COO⁻ $\qquad$ $L^6 = $ (3,5-dimethylphenyl)–COO⁻ $\qquad$ $L^{11} = $ (anthracenyl with COO⁻)

$L^2 = $ (4-methylphenyl)–COO⁻ $\qquad$ $L^7 = $ (naphthyl)–COO⁻ $\qquad$ $L^{12} = $ (tert-butyl)–COO⁻

$L^3 = $ (4-ethylphenyl)–COO⁻ $\qquad$ $L^8 = $ (biphenyl)–COO⁻ $\qquad$ $L^{13} = $ (adamantyl)–COO⁻

$L^4 = $ (4-propylphenyl)–COO⁻ $\qquad$ $L^9 = $ (alkyl chain)–COO⁻ $\qquad$ $L^{14} = $ (bipyridyl)–COO⁻

$L^5 = $ (4-butylphenyl)–COO⁻ $\qquad$ $L^{10} = $ (alkyl)–COO⁻ $\qquad$ $L^{15} = $ (pyridyl)–COO⁻
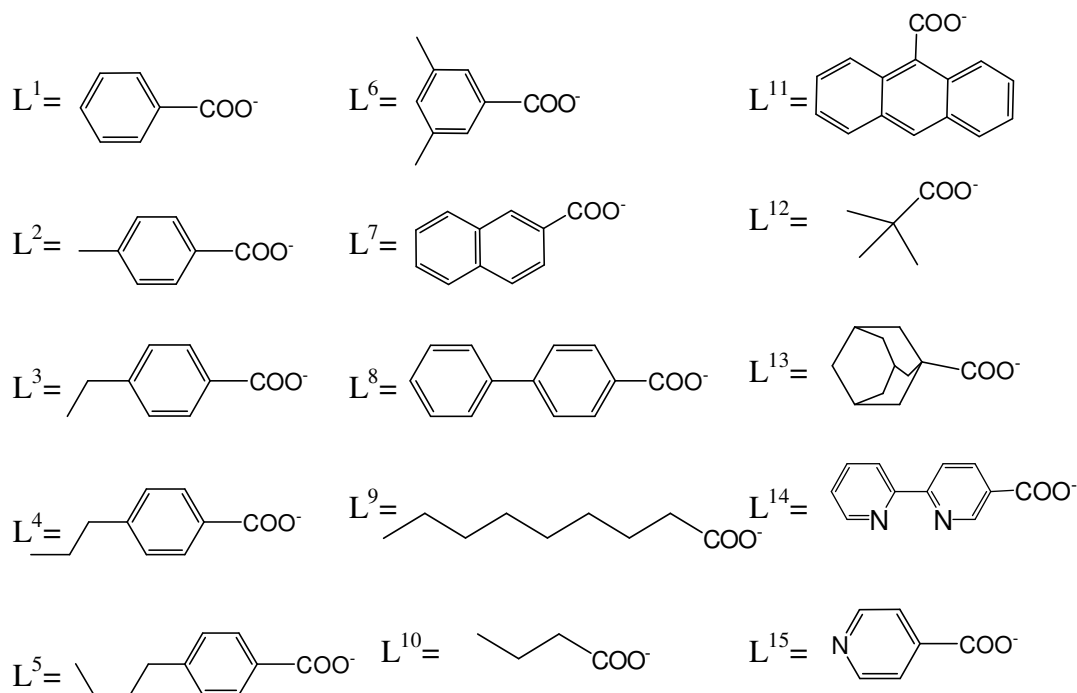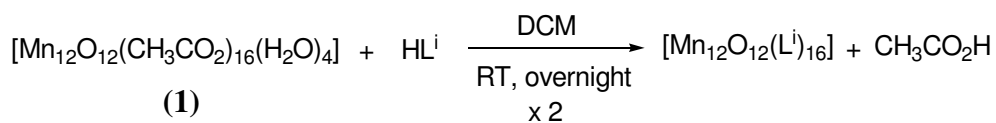
Scheme 3.1. Ligand-substitution reaction scheme between Mn$_{12}$ac (1) and various HL^i ligands in the aim of synthesising [Mn$_{12}$(L^i)$_{16}$] complexes.

The replacement carboxylic acids were all commercially available except for HL^{14} **(17)** which had to be synthesised using slight modifications to a reported route[58,59] (Scheme 3.2).

Purification of all the resulting powders was carried out by various crystallisation techniques mainly layering methods using for most cases DCM/*n*-hexane or DCM/MeOH. It can be noted that the four water molecules bound to the clusters can be exchanged with some solvent molecules during the crystallisation process [compound **(4)** and **(7)**].
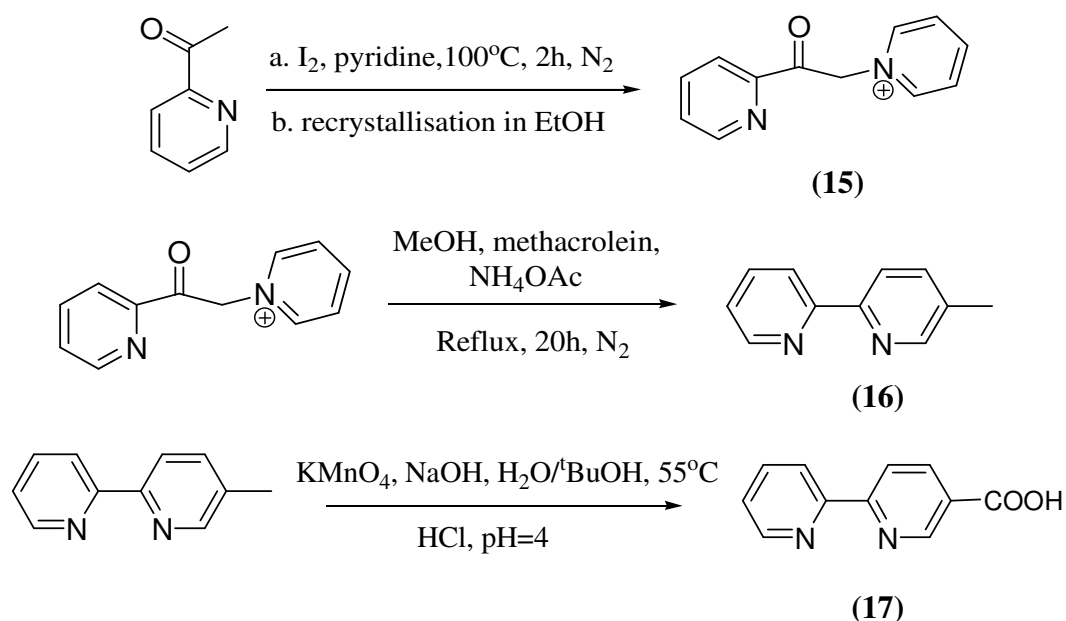
Scheme 3.2. Three step reaction scheme for synthesis of 2,2-bipyridinyl-5-carboxylic acid (17).

The characterisation of the final compounds relied mainly on Infrared spectroscopy and MALDI-TOF MS to identify the complexes and on elemental analysis to assess the purity of the samples, as NMR spectroscopy was not suitable mainly on account of paramagnetic clusters.

Attempts to grow crystals were performed for all clusters. Single crystals suitable for X-ray structure analysis have been obtained for clusters (2), (3), (4), (7), (9), and (12), see below for a detailed discussion of the resulting structures.

$[Mn_{12}O_{12}(C_6H_5CO_2)_{16}(H_2O)_4]$ (2) was first reported by Sessoli et al.[3b] in 1993 and later by Takeda et al.[60,61] Each of these authors prepared the desired cluster in a typical ligand substitution reaction starting from $Mn_{12}ac$. However, the complex was reported to crystallise in different space groups. While the former was obtained with no solvent molecule present in the unit cell and crystallised in the triclinic space group

P-1, the latter crystallised in the orthorhombic space group *Fdd*2 with the asymmetric unit comprising half of the cluster molecule and one benzoic acid molecule of crystallisation. Both crystal structures revealed that the cluster has molecular dimensions (approximately 2.10 nm in diameter, see Table 3) compatible for its deposition onto the PTCDI-melamine network, hence the synthesis of this cluster. Dark brown crystals were submitted for X-ray analysis and the measured unit cell suggested that the crystals obtained were crystallised in the same space group as those described by Takeda and co-workers[60,61] but with a slightly different unit cell. MALDI-TOF MS confirmed the identity of the desired product through observation of the molecular ion peak $[Mn_{12}O_{12}(C_6H_5CO_2)_{16}]^-$ at 2788.9 *m/z* in the negative mode as well as molecular fragments corresponding to $[Mn_{12}O_{12}(C_6H_5CO_2)_{16-n}]^+$ where n = 1-3 in the positive mode (Figure 3.15).
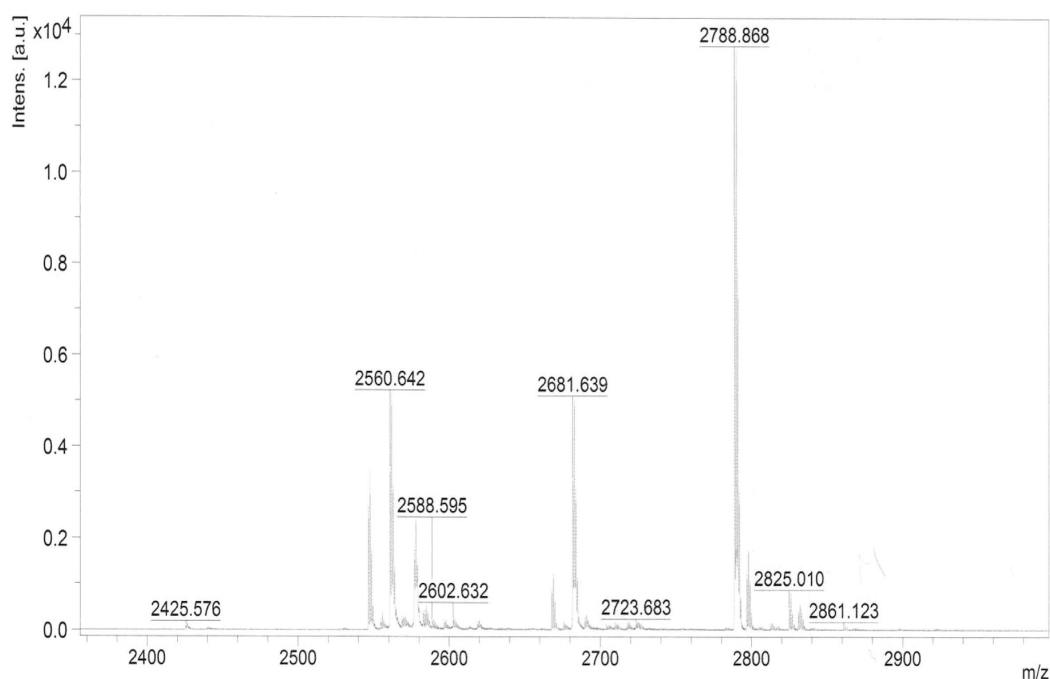
Figure 3.15. MALDI-TOF spectrum of (2) in negative reflector mode.

The synthesis of $[Mn_{12}O_{12}(CH_3\text{-p-}C_6H_4CO_2)_{16}(H_2O)_4]$ **(3)** has also already been reported by Aubin et al.[11] in 2001 with the description of two structures corresponding to two different crystallographic forms, solvates, of the complex namely $[Mn_{12}O_{12}(CH_3\text{-p-}C_6H_4CO_2)_{16}(H_2O)_4].CH_3C_6H_4CO_2H$ and $[Mn_{12}O_{12}(CH_3\text{-p-}C_6H_4CO_2)_{16}(H_2O)_4].3H_2O$. The former crystallises in the *C*2/*c* space group whilst the latter crystallises in the *I*2/*a* space group. Yet, in this case the SMMs were both prepared in a comproportionation reaction between $Mn(ClO_4)_2$ and p-methylbenzoic acid. In our case, a ligand exchange reaction with **(1)** as starting material was carried out. The complex was found to crystallise in the triclinic space group *P*-1 (see below for the description of the crystal structure).

The idea lying behind the synthesis of the new complex $[Mn_{12}O_{12}(C_2H_5C_6H_4CO_2)_{16}(MeOH)_4]$ **(4)** was its deposition onto chosen surfaces. The larger dimensions that this cluster possesses would potentially allow for a good 'fit' with respect to the pores of the PTCDI-melamine network, discussed above. Additionally, its organic framework comprising both a phenyl group and an alkyl chain would potentially allow for strong vdW bonding between this cluster and a HOPG surface, promoting its binding and thus its adsorption onto the substrate.
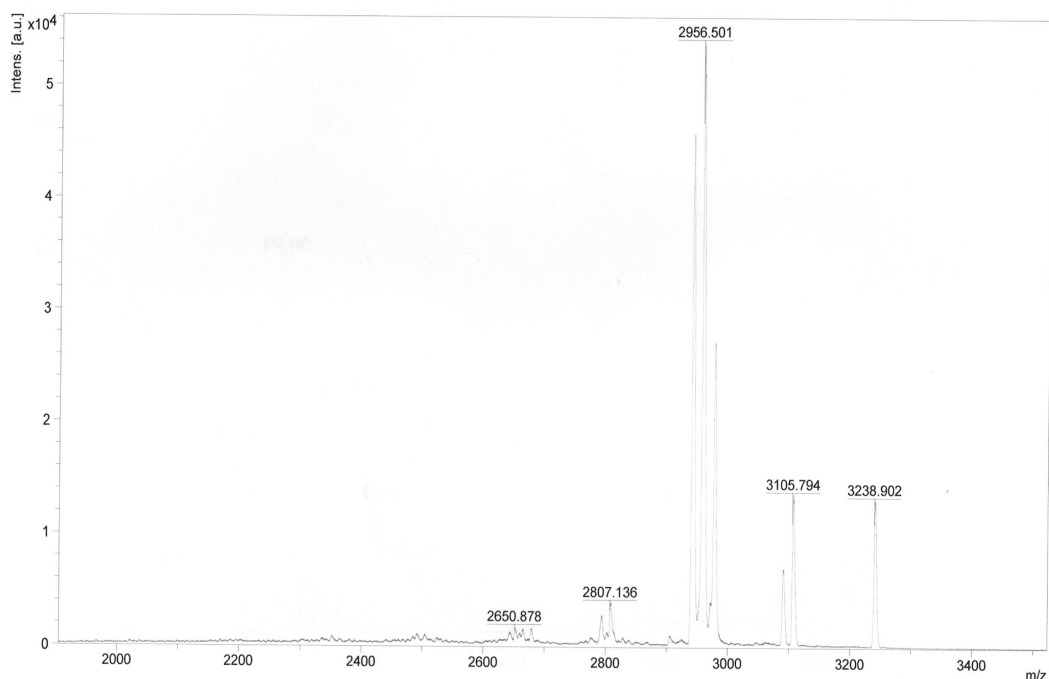
Figure 3.16. MALDI-TOF spectrum of (4) in negative reflector mode showing peaks corresponding to the molecular ion and fragments after the sequential loss of the ligands.

MALDI-TOF MS confirmed the identity of the obtained product through observation of the molecular ion peak $[Mn_{12}O_{12}(C_2H_5C_6H_4CO_2)_{16}]^-$ at 3238.9 *m/z* and a progression of molecular fragments corresponding to $[Mn_{12}O_{12}(C_2H_5C_6H_4CO_2)_{16-n}]^-$ where n=1-3, indicating the sequential loss of the ethylbenzoate ligands (Figure 3.16). Thereafter, it was also decided to study the influence of increasing the length of the ligand alkyl chains. Consequently the synthesis of $[Mn_{12}O_{12}(R_1C_6H_4CO_2)_{16}(R)_4]$ (with R=H$_2$O or MeOH) derivatives have been attempted where R_1 is a propyl group for compound (**5**) and a butyl group for compound (**6**) respectively. It is thought that the presence of a longer alkyl chain in the peripheral ligation would allow for an additional increase in the intermolecular separation as well as an increase in the strength of potential vdW bonding with the graphite surface. Purification of the resultant products was attempted *via* crystallisation.

134

For complex **(5)**, the resulting dark brown crystals obtained (by layering a solution of n-hexane on top of a saturated solution of the complex in dichloromethane) were found to exhibit poor diffraction, likely due to large poorly crystalline regions between the ordered Mn_{12} cores, and thus no data were collected. The layering process was repeated replacing dichloromethane with dibromomethane hoping the resulting diffraction would be much stronger. However again, the quality of the large single crystals obtained remained unsatisfactory for XRD data collection.

For Mn_{12}butylbenzoate **(6)**, no crystals could be obtained in spite of the numerous attempts of crystallisation including layering methods using various anti-solvents, vapour diffusion and evaporation.

This is consistent with disorder caused by the long alkyl chains of the ligands strongly disturbing the crystallisation of Mn_{12} clusters. However, characterisation of both samples confirmed the clusters had been successfully synthesised.

The next SMM to be synthesised was the new complex $[Mn_{12}O_{12}((CH_3)_2C_6H_3CO_2)_{16}(CH_3OH)_4]$ **(7)**. The brown crystalline powder obtained was characterised by FT-IR and MALDI-TOF MS. The peak corresponding to the molecular ion $[Mn_{12}O_{12}((CH_3)_2C_6H_3CO_2)_{16}]^-$ at m/z=3238 and fragments of it resulting from the stepwise loss of several $(CH_3)_2C_6H_3CO_2$ units (m/z=149) are observed in the mass spectrum recorded in the negative mode, confirming the synthesis of this new SMM had been successful.

$[Mn_{12}O_{12}(C_{10}H_7CO_2)_{16}(H_2O)_4]$ **(8)** was first reported by Kuroda-Sowa et al.[62] in 2005. It was the first example of a SMM that self-assembled in a two-dimensional manner because of intermolecular π–π interactions occurring between neighbouring

molecules (Figure 3.17). The extended π-conjugated system possessed by these naphtoate ligands made **(8)** a good candidate for our quest for increased molecular dimensions and for ordered self-assembled arrays upon surface deposition. Additionally, the large organic frameworks of this functionalised carboxylate may allow for strong vdW bonding with a HOPG surface, promoting the binding and thus deposition of this cluster.
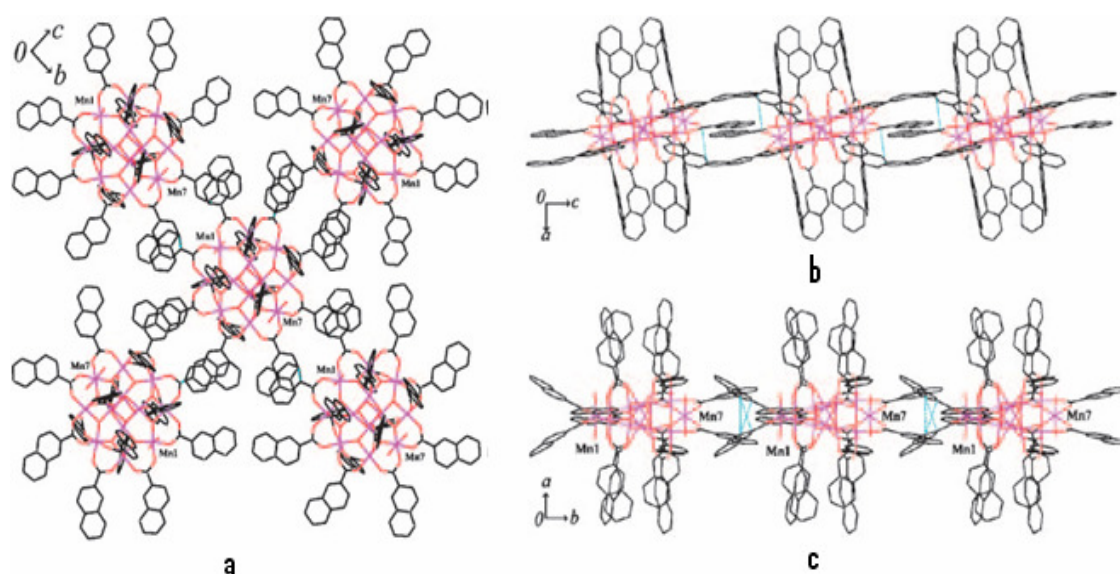
Figure 3.17. [Mn$_{12}$O$_{12}$(C$_{10}$H$_7$CO$_2$)$_{16}$(H$_2$O)$_4$] clusters demonstrating π-π stacking interactions between equatorial naphthalene rings residing on neighbouring molecules. a. a top view from the *a*-axis, b. a side view from the *b*-axis c. a side view from the *c*-axis.[62]

The resulting crystals, issued from varied layering systems, were however found to exhibit poor diffraction, likely due to regions of diffuse solvent molecules between the Mn$_{12}$ clusters, and thus no data could be collected. The molecular ion peak [Mn$_{12}$O$_{12}$(C$_{10}$H$_7$CO$_2$)$_{16}$]$^-$ at 3589.3 *m/z* as well as peaks corresponding to fragments [Mn$_{12}$O$_{12}$(C$_{10}$H$_7$CO$_2$)$_{16-n}$]$^-$ where n= 1,2 were observed in the MALDI-TOF MS spectrum recorded in negative mode (Figure 3.18).
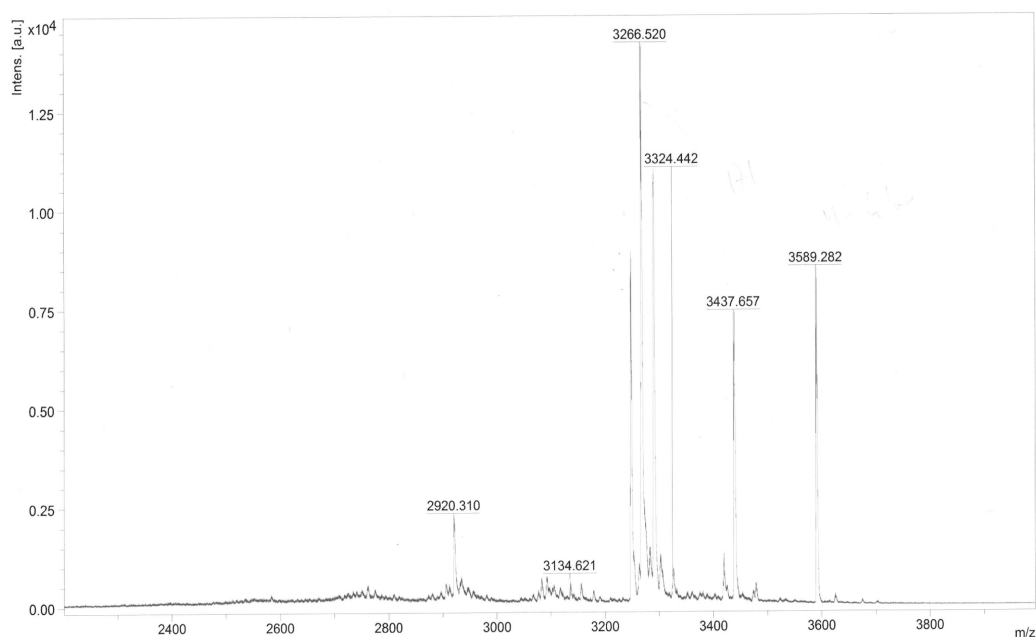
Figure 3.18. MALDI-TOF spectrum of (8) in negative reflector mode.

The synthesis of $[Mn_{12}O_{12}(C_6H_5C_6H_4CO_2)_{16}(H_2O)_4]$ **(9)** was first performed by Christou et al.[57] in 2002 and this cluster was later deposited onto diverse surfaces including native silicon oxide deposited onto Si(100), hexamethyldisiloxane (HMDS), and HOPG[48] using lithographically controlled wetting methods. It has been demonstrated that the use of these techniques allowed nanometre-sized ordered arrays of SMMs to be obtained on these surfaces. However, no crystal structure for this complex has been reported to date. The preparation of this cluster was carried out to try to exploit the potential intermolecular π-π stacking interactions as described for **(9)** due to the extended π-conjugated system of the ligands which could in turn lead the molecule to self-assemble on surfaces. MALDI-TOF MS performed on the dark brown crystals obtained confirmed the formation of the desired product through the observation of the molecular ion peak $[Mn_{12}O_{12}(C_{12}H_9CO_2)_{16}]^-$ at 4005.4 *m/z* as well as fragments $[Mn_{12}O_{12}(C_{12}H_9CO_2)_{16-n}]^-$ where n=1-3 corresponding to the sequential

loss of the ligands (Figure 3.19). Elemental analysis was consistent with the synthesis of the pure target cluster.
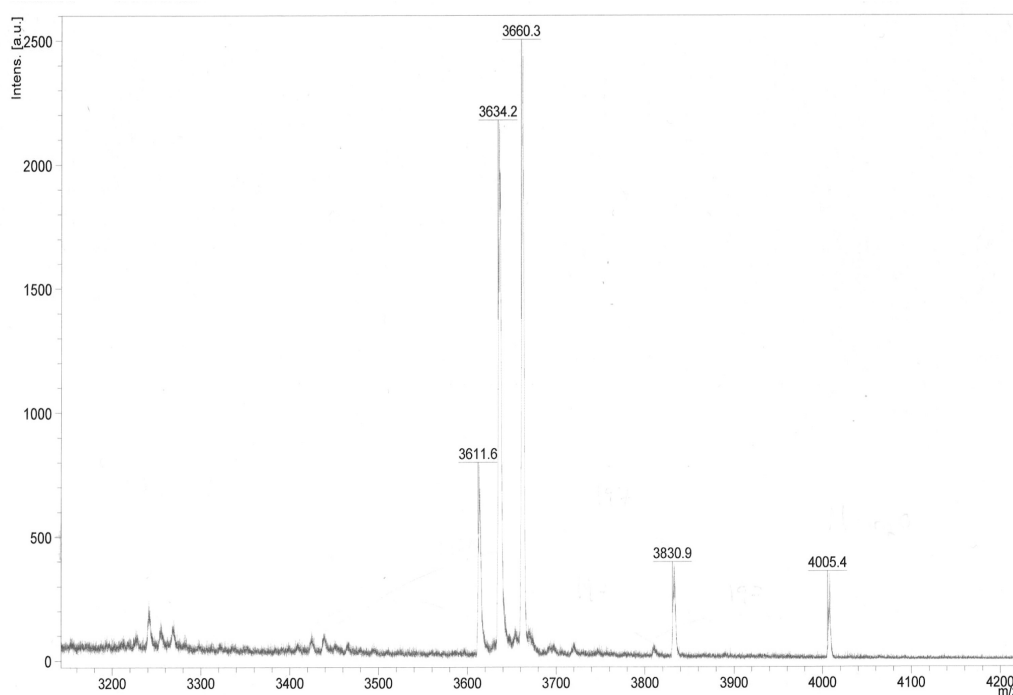
Figure 3.19. MALDI-TOF spectrum of (9) in negative reflector mode showing peaks corresponding to the molecular ion and fragments after the sequential loss of the biphenylcarboxylate ligands.

One way to deposit the functionalised SMMs onto surfaces will be from solution using n-nonanoic acid as the chosen solvent. Two major issues have, therefore, to be considered. Firstly the Mn_{12} derivatives have to be soluble in the chosen solvent, but more importantly the clusters have to be stable in n-nonanoic acid. The second point could lead to serious complications as ligand-exchange reactions with the solvent could potentially take place. Therefore the synthesis of $[Mn_{12}O_{12}(C_8H_{17}CO_2)_{16}(H_2O)_4]$ **(10)** has been carried out as it is hoped that the long alkyl chain will enhance its solubility in this solvent. In addition, the incorporation of peripheral ligands identical to that of the solvent used for surface deposition might also simplify the anticipated complications mentioned above. The long alkyl chains possessed by these

functionalised carboxylate groups are expected to enhance the potential vdW bonding with a HOPG substrate. The resultant product obtained was a dark brown oil which was purified by precipitation. Sadly, all the crystallisation attempts failed and no crystalline material could be obtained. This confirms the hypothesis drawn for clusters **(5)** and **(6)** where the longer and more mobile alkyl chains render the crystallisation of the clusters more difficult. However, the cluster was positively identified using the usual tools (IR spectroscopy, MALDI-TOF MS and elemental analysis).

The synthesis of $[Mn_{12}O_{12}(C_3H_7CO_2)_{16}(H_2O)_4]$ **(11)** was undertaken in hope that the shorter length of the peripheral alkyl chains, in comparison to compound **(10)**, would favour the crystallisation due to less flexibility and less disorder but will still display good solubility and potential for strong vdW bonding. The resultant dark brown oil was dried under vacuum to afford a microcrystalline solid on which subsequent characterisations were performed confirming the desired cluster had been obtained (see Figure 3.20). The attempts at growing crystals were in vain as well, which suggest that the length of this alkyl chain remains still too large, causing disorder and hindering crystallisation.
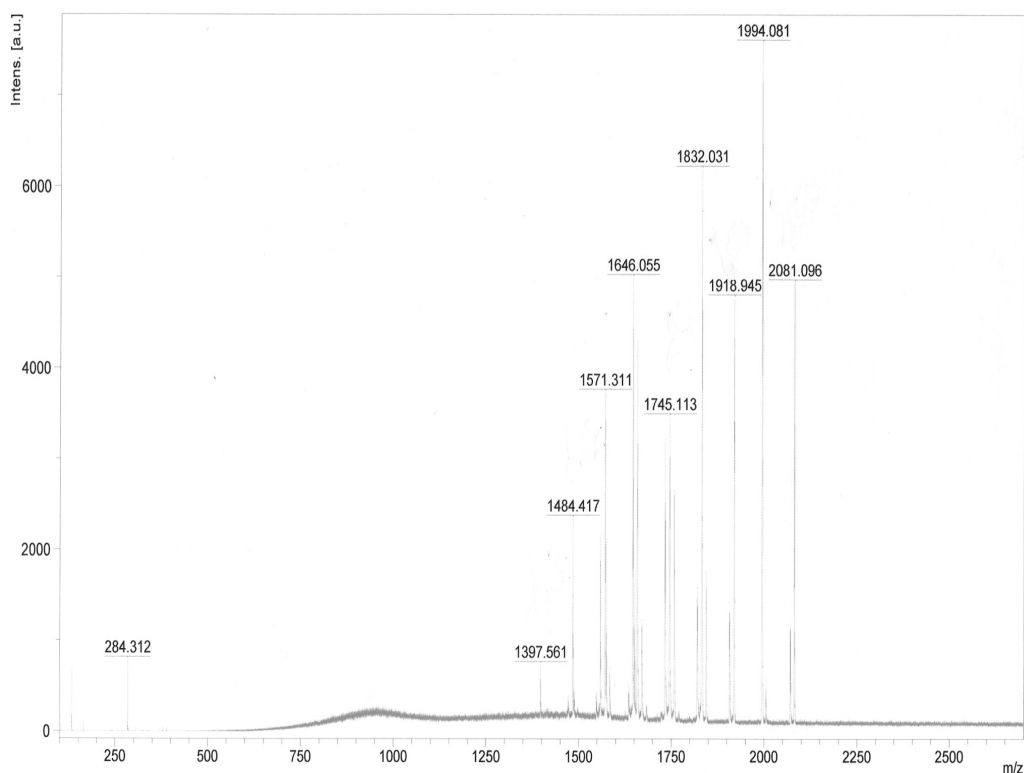
Figure 3.20. MALDI-TOF spectrum of (11) in positive reflector mode.

Similarly to compounds **(7)** and **(8)**, it is thought that the incorporation of anthracene groups within the organic ligation would, thanks to its extended π-conjugated system, allow for π-π stacking interactions between the equatorial ligands of neighbouring molecules. This could in turn provide a basis for ordered molecular self-assembly on surfaces. The challenge in the synthesis lies in the feasibility of introducing sixteen bulky groups like anthracene carboxylate ligands around the $Mn_{12}O_{12}$ core, which will be dependent upon several factors such as steric constraints as well as the ligand strength of 9-anthracenecarboxylic acid as compared to acetic acid.

The attempted synthesis of this new Mn_{12} cluster **(12)** was performed in a typical ligand substitution reaction. This afforded dark brown crystals which were used for characterisation purposes. MALDI-TOF mass spectra were suggestive of partial substitution of the starting material, though no fragment clearly indicative of

140

the extent of substitution was observed. IR spectroscopy revealed characteristic C-O carboxylate stretching, potentially as a result of either the acetate or anthracenecarboxylate groups, as well as both C_{sp}^{3}-H stretching, suggesting the presence of the former, and C_{sp}^{2}-H stretching, suggesting the presence of the latter. These observations could support the proposition of partial substitution. Elemental analysis values on the other hand did not correspond to that of the expected cluster.

Suitable single crystals for XRD were subsequently grown using a DCM/MeOH layering and maintained in their mother liquor for data collection. The resolution of the crystal structure enabled a definite answer on the identity of the cluster obtained. In fact the hypothesis of a partial substitution had to be rejected as a trinuclear μ_3-oxo-bridged manganese complex of general composition $[Mn_3O(O_2CC_{14}H_9)_6(HOCH_3)_3].2CH_3OH$ was obtained.

The syntheses of Mn_{12} clusters containing large organic functional groups, such as adamantane and anthracene, were attempted from simple ligand substitution reactions with Mn_{12}ac. These reactions however proved to be unsuccessful (ligand substitution was not achieved or resulted in formation of a complex of lower nuclearity) which is consistent with the unfavourable steric interactions which would occur upon accommodation of sixteen large organic ligands around the Mn_{12} core.

It is reported that the syntheses of particular Mn_{12} clusters previously found to be unattainable by ligand substitution reactions with Mn_{12}ac have been accomplished *via* ligand substitution reaction starting from $[Mn_{12}O_{12}(C(CH_3)_3CO_2)_{16}(H_2O)_4]^6$ **(13)**, a sterically crowded Mn_{12} complex whose peripheral ligation comprises sixteen *tert*-butanoate groups. It is plausible that for the syntheses of Mn_{12} clusters comprising large organic functional groups, substitution of sterically crowded *tert*-butanoate

groups would be favourable over that of direct substitution of acetate ligands as they are expected to be better leaving groups. In addition, complex **(13)** is also expected to be more soluble in organic solvents than compound **(1)**. Furthermore, the strong basicity of the *tert*-butanoate ligand, as reflected in the relatively high pK_a value of its conjugate acid (pK_a=5.01) combined with the bulkiness and hydrophobic nature of the tert-butyl groups may lead to interesting products.

For the purpose of use as starting material in ligand substitution reactions with large functionalised carboxylic acids, the synthesis of $[Mn_{12}O_{12}(C(CH_3)_3CO_2)_{16}(H_2O)_4]$ was performed using slight modifications to the reported procedure.[54]

MALDI-TOF MS revealed however that the desired compound was not obtained as the peaks observed did not correspond to any of the expected fragments. The reaction was repeated to ensure the full substitution of **(1)**. Characterisation of the resultant dark brown crystalline material by elemental analysis confirmed the purity of complex **(13)**. MALDI-TOF MS supported this finding with observation of the molecular fragments corresponding to $[Mn_{12}O_{12}(C_4H_9CO_2)_{16-n}]^-$ where n=2-3. The absence of a molecular ion peak can be explained by the fact that the cluster probably dissociates during ionisation due to the steric bulk of the *tert*-butyl groups. The infrared spectrum exhibited the characteristic functional group stretching frequencies (νC_{sp}^3-H, νO-H, νC-O).

The idea of preparing a sterically hindered cluster comprising of sixteen adamantanecarboxylic acid ligands has also been developed. $[Mn_{12}O_{12}(C_{10}H_{15}CO_2)_{16}(H_2O)_4]$ **(14)**, if successfully synthesised, would possess significantly increased molecular dimensions. As previously mentioned, the synthesis of this cluster was first attempted by simple ligand substitution between $Mn_{12}ac$ and

the required carboxylic acid. MALDI-TOF MS performed on the resultant powder suggested that the synthesis had unfortunately failed. Therefore, the synthesis has subsequently been attempted in a carboxylate exchange reaction starting with the previously prepared complex **(13)** and 1-adamantanecarboxylic acid hoping that the better *tert*-butyl leaving groups would favour the formation of the new complex.

MALDI-TOF MS carried out on the resulting dark brown powder did not give any suitable information as to the successful formation of the complex since no high-mass molecular fragments were observed. Numerous attempts to grow crystals were performed using several techniques and solvent systems but all proved to be ineffective.

The idea behind the synthesis of the new cluster of general formula $[Mn_{12}O_{12}(C_{10}H_7N_2CO_2)_{16}(H_2O)_4]$ **(18)** is the use of ligands suitable for metal coordination purposes. The accommodation of bidentate bipyridine (bipy) functional groups around the Mn_{12} core would potentially allow these peripheral ligands to bind to other metal ions, which represents a potential route for the formation of ordered assembly *via* coordination bonds.

The synthesis of this derivative was carried out using **(1)** as a starting material. Purification of the resultant dark brown powder was attempted by crystallisation using numerous layering methods with varying anti-solvents and crystallisation conditions but the crude powder proved to be insoluble in most common organic solvents. MALDI-TOF MS performed on the crude powder did not permit the identification of either the molecular ion peak or any other fragments. A possible explanation for the failure of the reaction is the lack of solubility of the ligand in DCM or any common organic solvent that would prevent the reaction from occurring. The observation of an

insoluble powder as product could be accounted for by coordination of the bidentate bipyridine groups to the manganese ions leading to the formation of a polymeric material.

To confirm the former hypothesis of undesired bipyridine ligand coordination to the manganese ions, it was decided to proceed to the synthesis of a similar cluster. The synthesis of $[Mn_{12}O_{12}(C_5H_4NCO_2)_{16}(H_2O)_4]$ **(19)** was attempted using the usual procedure starting from $Mn_{12}ac$. However the product could not be purified in any way and the characterisation techniques proved unable to determine the identity of the brown powder obtained.

Solubility tests were run to define the solvents in which isonicotinic acid was soluble. The starting material is insoluble in all common organic solvents. Therefore, the synthesis was attempted again using acetonitrile as a solvent as $Mn_{12}ac$ proved to be significantly more soluble in MeCN than in DCM. Unfortunately, the resulting brown powder was still insoluble in most organic solvents and consequently could not be purified by crystallisation or identified by the classic characterisation techniques leaving us with insufficient evidence to draw any definite conclusions of the nature of the product, however it seems likely that both **(18)** and **(19)** form coordination polymers.

3.2.4 Crystallography

Single crystals of complex **(2)** were obtained by layering a solution of *n*-hexane on a saturated solution of the compound in dichloromethane and left undisturbed for several days. The complex crystallises in the orthorhombic space group *Fdd*2 with the asymmetric unit comprising half of the cluster molecule and one benzoic acid

molecule of crystallisation (Figure 3.21). A very similar structure has already been reported in 1998 by Takeda and co-workers,[60-61] however it differs slightly in the unit cell parameters. The major difference in the present structure lies in the fact that the solvate benzoic acid molecule is disordered over two orientations. Half of the time it coordinates to Mn8 and acts as a capping ligand. A water molecule (O102) is filling the coordination site at Mn8 when the benzoic acid carboxylic group is pointing away from the cluster. Disorder was also observed in the position of the phenyl ring of a benzoate ligand (residue A). The occupancy of the major component was found to be 0.68(1). For the rest of the discussion, only the major component will be considered. A table corresponding to the crystal data and structure refinement for complex **(2)** is presented in Appendix A.2.
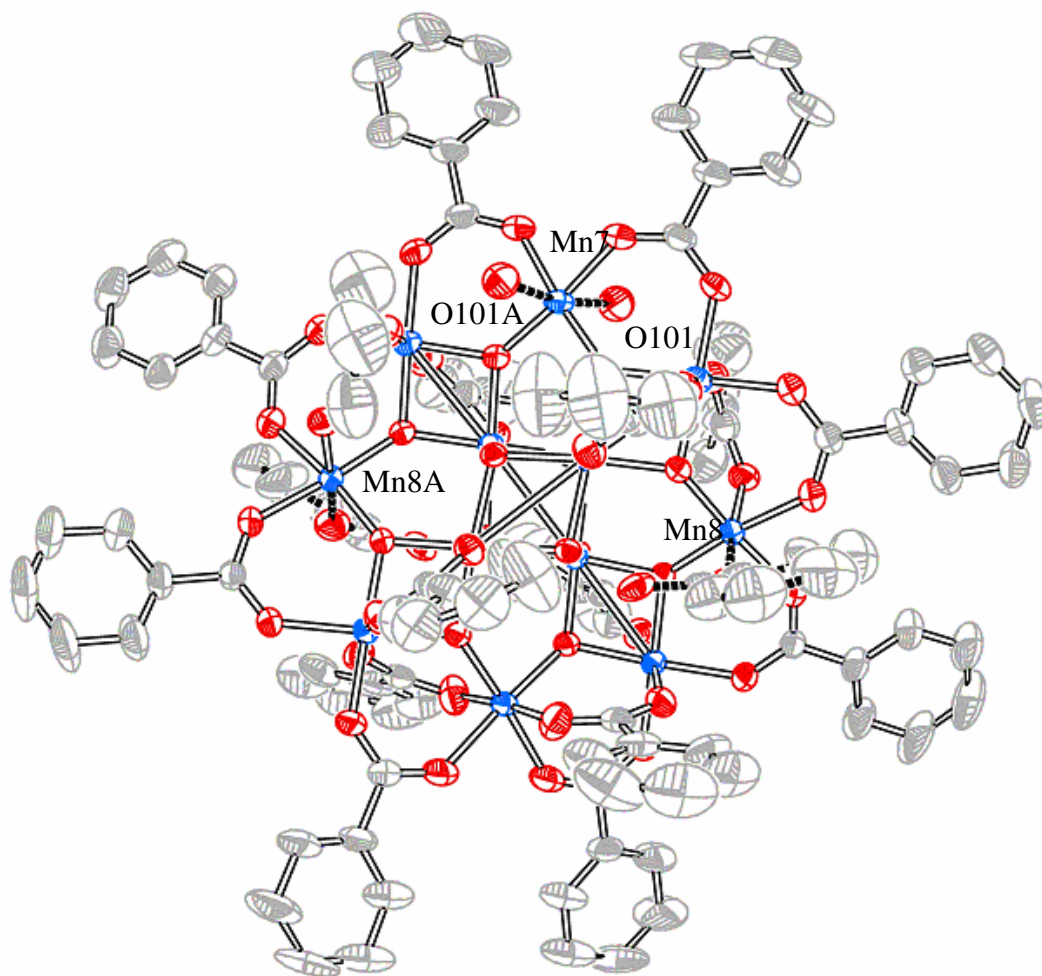
Figure 3.21. Representation of complex (2) showing the conformation with two capping ligands bound to Mn8 and Mn8A respectively and the two water ligands O101 and O101A coordinated to Mn7 (dashed lines). When the solvate benzoic acid moiety is pointing away from the cluster, water molecules (O102 and O102A) are bound to Mn8 and Mn8A, hence the 2:1:1 arrangement observed. Hydrogen atoms have been omitted for more clarity. Atoms are drawn at 50% probability level.

The cluster has the same overall structure as $Mn_{12}ac$ and other $[Mn_{12}O_{12}(O_2CR)_{16}]^{3b,11,60-61,63}$ derivatives consisting of a central $[Mn_4^{IV}O_4]$ cubane unit surrounded by a non-planar outer ring of eight Mn^{III} ions bridged and connected to the central cube by eight μ_3–O^{2-} ions. The oxidation states of the Mn ions were assigned on the basis of Mn-O bond distances. Peripheral ligation of the cluster is

provided by sixteen η^2-μ_2-benzoate groups, two water molecules bound to both Mn7 and two benzoic acid capping ligands coordinated to Mn8 and Mn8A (symmetry equivalent of Mn8). When the solvate benzoic acid moiety is pointing away from the cluster, then four molecules of water are present and are therefore bound in a 2:1:1 arrangement to Mn7, Mn8 and Mn8A respectively.

The eight Mn^{III} ions fall into two groups of four Mn^{III} ions. In the first group, each Mn^{III} ion is connected to only one Mn^{IV} by two oxo bridges whilst in the second group each Mn^{III} is bound to two Mn^{IV} by two oxo bridges. It is noteworthy that the H_2O ligands only coordinate to the four Mn^{III} ions of the second group. As expected for high-spin d^4 ions in near octahedral geometry, all the Mn^{III} exhibit Jahn-Teller (JT) distortions as indicated by the clear differences in Mn-O bond lengths among the six bond distances for each Mn^{III} ion. They can be divided into two groups: two long (in the range of 2.1-2.2 Å) and four short (in the range of 1.9 Å) Mn-O bonds. For seven of the Mn^{III} ions, the JT distortion takes the form of an axial elongation of two trans bonds and the JT axes are approximately parallel to each other and roughly perpendicular to the $Mn_{12}O_{12}$ core (Figure 3.22). However Mn5 has an abnormally oriented JT axis. Indeed the latter distortion is contained in the plane of the molecule (Mn_{12} core). This phenomenon has already been described in the literature for different complexes and has been termed Jahn-Teller isomerism.[11,60,61,63] Previously it has been identified and defined for $Mn_{12}O_{12}(O_2CC_6H_4$-p-Me$)_{16}(H_2O)_4$ in 2001[11] and more recently for $Mn_{12}O_{12}(O_2CCH_2Bu^t)_{16}(H_2O)_4$ in 2003 by Christou and co-workers.[63] It is also the case for the Mn_{12}benzoate complex synthesised by Takeda, mentioned above.[60-61] It has been demonstrated that this JT isomerism phenomenon results in important differences in the observed magnetic properties of the compounds[11,60-61,63] (see below for a description of the measured magnetic properties).

As a consequence of this abnormal Jahn-Teller elongation, Mn5 exhibit a compressed octahedral shape rather than an elongated one as observed for the seven others.
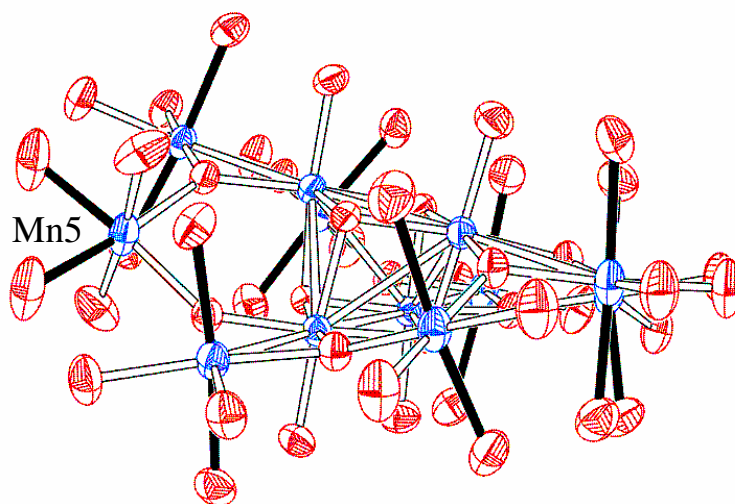
Figure 3.22. Representation of the Mn$_{12}$O$_{12}$ fragment for (2) showing the Jahn-Teller elongated bonds for all the Mn ions in thick black lines. Mn5 has its JT axis abnormally orientated. Atoms are drawn at 50% probability level.

Single crystals of **(3).3CH$_2$Cl$_2$** suitable for X-ray diffraction analysis were obtained by layering carefully an equal volume of *n*-hexane on a saturated solution of the compound in CH$_2$Cl$_2$. The complex crystallizes in the triclinic space group *P*-1 with the asymmetric unit consisting of the whole molecule and three CH$_2$Cl$_2$ molecules of crystallization. The cluster possesses the same overall structure as most derivatives (Figure 3.23). A table corresponding to the crystal data and structure refinement is presented in Appendix A.2. In here, the eight Mn^{III} centers display the usual axial JT distortion of two trans bonds with the axes being roughly parallel to one another and almost perpendicular to the Mn$_{12}$O$_{12}$ core. As is normally the case, the JT elongation axes normally avoid the Mn-O^{2-} bonds which are the shortest and therefore the strongest in the molecule. For this reason, they are commonly axially disposed. The four water molecules are connected in a 1:1:2 pattern to Mn10, Mn11 and Mn12

respectively. As mentioned previously, two other different crystallographic forms of this compound have been reported by Aubin et al. in 1991.[11] They all differ in the space groups they crystallize in, the positioning of the water ligands and the solvate molecules present in the unit cell. However, overall they possess the same core structure (see Table 2).
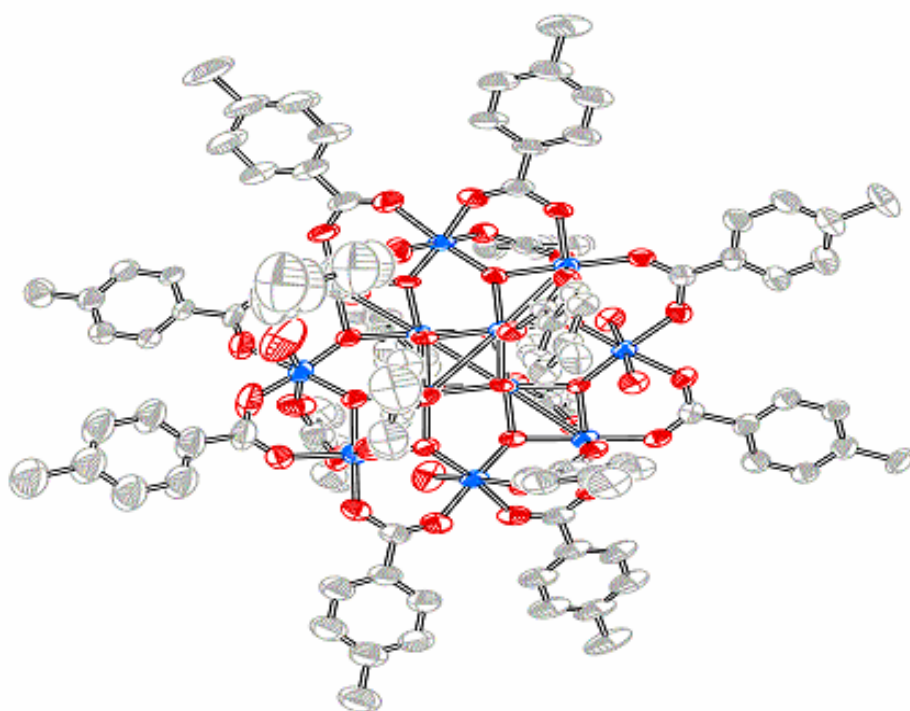
Figure 3.23. Representation of complex (3).3CH₂Cl₂. Hydrogen atoms and solvent molecules have been omitted for more clarity. Atoms are drawn at 50% probability level.

Single crystals of the novel complex **(4)** were obtained by layering a solution of methanol on a saturated solution of the compound in dichloromethane and left undisturbed for several days. The complex crystallizes in the monoclinic space group

*P*2/*c* with the asymmetric unit consisting of one half of the molecule. The structure of the cluster is similar to the ones described above (Figure 3.24). A table corresponding to the crystal data and structure refinement for the complex is presented in Appendix A.2. All the Mn^{III} ions in this structure exhibit an axial JT distortion as described previously. The water molecules being traditionally present in Mn$_{12}$ complexes were replaced here by four methanol ligands during the crystallisation process. The four terminal methanol groups coordinate to the four Mn^{III} ions belonging to the second group defined previously (Mn5, Mn5A, Mn7 and Mn7A in the present case) and sit, here, on the axial JT positions of these four Mn^{III} ions in a 1:1:1:1 fashion in an alternating up, down, up, down, up positions.
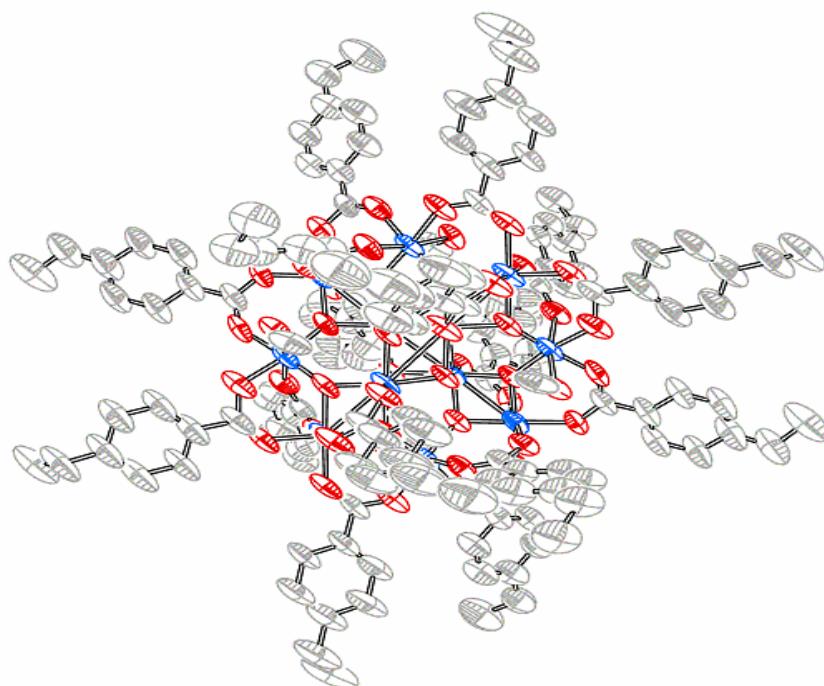
Figure 3.24. Representation of complex (4). Hydrogen atoms have been omitted for more clarity. Atoms are drawn at 50% probability level.

Single crystals of (**7**) were obtained after layering a solution of methanol on a saturated solution of the compound in dichloromethane and left undisturbed for

several days. Complex **(7)** crystallizes in the triclinic space group *P*-1 with the composition **(7).7CH₂Cl₂.4MeOH.H₂O**.

The asymmetric unit comprises one cluster molecule as well as seven dichloromethane, four methanol and one water molecules of crystallization. The $Mn_{12}O_{12}$ fragment structurally resembles the previous derivatives. Similarly to cluster **(4)**, the novel cluster possesses four methanol ligands coordinated in a 1:1:1:1 arrangement to Mn10, Mn9, Mn12 and Mn11 respectively which have been substituted to the usual water molecules during the crystallisation process (Figure 3.25). A table corresponding to the crystal data and structure refinement for complex **(7)** is presented in Appendix A.2.
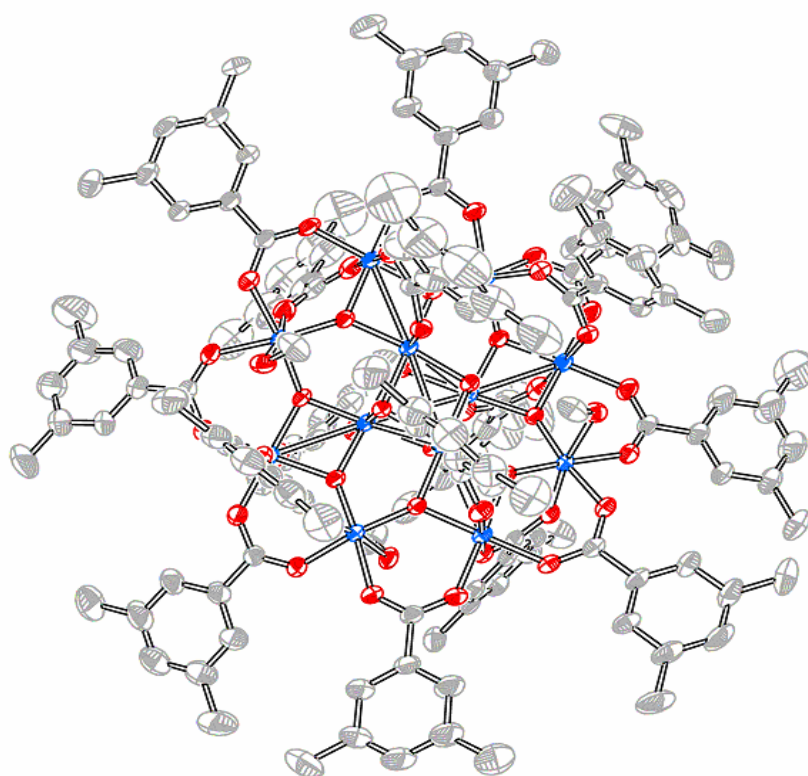
Figure 9.25. Representation of complex (7).7CH₂Cl₂.4MeOH.H₂O. Hydrogen atoms and solvent molecules have been omitted for more clarity. Atoms are drawn at 50% probability level.

Single crystals suitable for X-ray diffraction analysis were obtained for **(9).C$_6$H$_5$C$_6$H$_4$COOH** by layering carefully a solution of *n*-hexane on a saturated solution of the compound in dichloromethane and left undisturbed for several days. The complex crystallizes in the tetragonal space group *I*-42*d* with the asymmetric unit consisting of a quarter of the molecule and half of an uncoordinated biphenylcarboxylic acid molecule (Figure 3.26). A table corresponding to the crystal data and structure refinement for the complex is presented in Appendix A.2. Disorder was observed in the conformation of the phenyl rings for two of the ligands, namely ligand L and N. The occupancy of the major component for ligand N was found to be 0.57(1). The position of the carboxylate group of ligand L switches between bridging Mn6 and Mn9 or Mn6 and Mn9A (x+y, y-x+1, -z+2). The occupancies of the two positions were refined and found to have a value of 0.5. When the coordination sites on the two equivalent Mn9 and Mn9A atoms are not occupied by a carboxylate oxygen, the sites are occupied by water ligands (O102 and O101 respectively). Consequently, the water molecules adopt an arrangement of the type 1:1:1:1. An uncoordinated disordered biphenylcarboxylic acid molecule is also present in the unit cell and is centred on a special position so that the asymmetric unit contains one full occupancy phenyl ring and a half occupancy carboxylic acid group. The carboxylic acid group is set to point away when ligand L is bound to Mn9 so as not to clash with it. For the rest of the discussion, the disordered ligands were considered to exist in the conformations of ligands L and N. The Mn$_{12}$O$_{12}$ core structure of the cluster has the same features as described previously for the other derivatives. Here again, all the Mn^{III} ions show the axial JT elongation of two of their trans bonds.
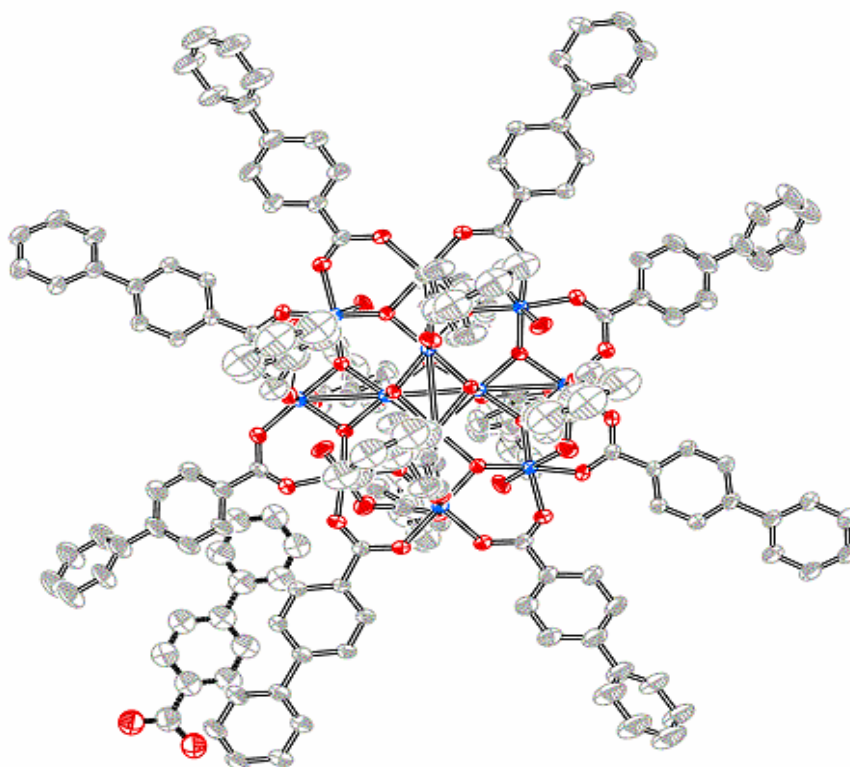
Figure 3.26. Representation of complex (9).C$_6$H$_5$C$_6$H$_4$COOH showing the disordered ligands in the major conformations. The uncoordinated disordered biphenylcarboxylic acid molecule is shown in thick dashed line and is represented in the conformation where it is pointing away from the cluster so as not to clash with ligand L. Hydrogen atoms have been omitted for more clarity. Atoms are drawn at 50% probability level.

3.2.5 Comparative study

A comparative study, between the complexes (**2**), (**3**), (**4**), (**7**), (**9**) synthesised during this project and the corresponding previously reported derivatives was undertaken to investigate and establish the influence of the peripheral ligation shell on the molecular dimensions, the intermolecular separations and the crystal packing of the clusters.

Firstly, the bond lengths of the different type of bonds involved in the structure were compared for each cluster (Table 1). The Mn^{IV}-Mn^{IV} bond lengths are all within the range of 2.8 to 3.0 Å and so are the Mn^{IV}-Mn^{III} distances with values comprised

between 2.7-2.8 Å which are very similar to the values reported for the pristine $Mn_{12}ac$. Except for complex **(2)**, longer Mn^{III}-O carboxylate bonds are observed and located in the axial positions confirming the Jahn-Teller distortion and indicating that these bonds are significantly weaker than the corresponding Mn^{III}-O carboxylate bonds in the equatorial sites since they are on average 0.2 to 0.4 Å longer. For **(2)** and examples taken from the literature[11,60-61] (shown in bold in Tables 1 and 2), one of the eight Mn^{III} ion in these structures has an abnormally orientated Jahn-Teller axis leading to the elongation of two Mn^{III}-O carboxylate bonds in the equatorial positions and to what has been described as a compressed octahedral environment for the corresponding Mn ion rather than an elongated one.

Table 1. Bond lengths of bonds involved in the $Mn_{12}O_{12}$ fragment for (1), (2), (3), (4), (7) and (9).

	$Mn_{12}ac^a$	2	3	4	7	9
Space group	*I-4*	*Fdd2*	*P-1*	*P2/c*	*P-1*	*I-42d*
Mn^{IV}-Mn^{IV} (Å)	2.81-2.82	**2.79-2.95**	2.84-2.97	2.83-2.94	2.81-2.95	2.82-2.99
Mn^{IV}-Mn^{III} (Å)	2.76-2.77	**2.77-2.78**	2.77-2.80	2.77-2.79	2..76-2.78	2.80-2.81
Mn^{IV}-O cubane (Å)	1.90-1.91	**1.86-1.94**	1.91-1.98	1.87-1.97	1.88-1.95	1.91-1.94
Mn^{IV}-Ooxo (Å)	1.88-1.89	**1.84-1.88**	1.87-1.91	1.84-1.92	1.86-1.88	1.86-1.89
Mn^{IV}-Oc [b] (Å)	1.911-1.913	**1.89-1.93**	1.91-1.94	1.91-1.96	1.89-1.91	1.94-1.95
Mn^{III}-Ooxo (Å)	1.88-1.90	**1.87-1.98**	1.87-1.97	1.82-1.95	1.87-1.92	1.88-1.90
Mn^{III}-Oc, eq [c] (Å)	1.93-2.01	**1.91-2.04**	1.91-2.10	1.9-2.0	1.92-2.06	1.91-1.97
Mn^{III}-Oc, ax [d] (Å)	2.13-2.25	**1.92-2.25**	2.01-2.28	2.09-2.29	2.08-2.25	2.16-2.20

[a] *as reported by T. Lis[9], [b] O_c=O carboxylate, [c] $O_{c, eq}$=O equatorial carboxylate, [d] $O_{c, ax}$=O axial carboxylate.*

Table 2. Comparison of the bond lengths of the Mn$_{12}$O$_{12}$ moiety for complexes (2) and (3) and their corresponding reported polymorphs.

	2	2	2	**3**	3	3
Author		Sessoli[3b]	Takeda[60-61]		Aubin[11]	Aubin[11]
Space group	**Fdd2**	P-1	**Fdd2**	P-1	I2/a	**C2/c**
Mn^{IV}-Mn^{IV} (Å)	**2.79-2.95**	2.81-3,00	**2.82-2.99**	2.84-2.97	2.82-2.97	**2.82-2.86**
Mn^{IV}-Mn^{III} (Å)	**2.77-2.78**	2.76-2.82	**2.80-2.82**	2.77-2.80	2.79-2.81	**2.78-2.79**
Mn^{IV}-O$_{cubane}$ (Å)	**1.86-1.94**	1.86-2.01	**1.88-1.95**	1.91-1.98	1.89-1.95	**1.90-1.95**
Mn^{IV}-O$_{oxo}$ (Å)	**1.84-1.88**	1.82-1.93	**1.84-1.89**	1.87-1.91	1.86-1.91	**1.84-1.90**
Mn^{IV}-Oc ^{b} (Å)	**1.89-1.93**	1.87-1.98	**1.92-1.94**	1.91-1.94	1.91-1.96	**1.89-1.96**
Mn^{III}-O$_{oxo}$ (Å)	**1.87-1.98**	1.85-1.95	**1.86-1.97**	1.87-1.97	1.86-1.93	**1.85-1.94**
Mn^{III}-Oc, eq ^{c} (Å)	**1.91-2.04**	1.88-2.03	**1.92-2.03**	1.91-2.10	1.93-1.95	**1.96-2.05**
Mn^{III}-Oc, ax ^{d} (Å)	**1.92-2.25**	2.07-2.27	**1.93-2.26**	2.01-2.28	2.21-2.26	**1.98-2.36**

$^{b}O_c$=O carboxylate , $^{c}O_{c,\,eq}$=O equatorial carboxylate , $^{d}O_{c,\,ax}$=O axial carboxylate .

The Mn$_{12}$O$_{12}$ moiety of all the complexes synthesised remains unchanged in terms of bond lengths and distances and is similar to the values reported for the pristine Mn$_{12}$ac and other derivatives. Overall, it is found and can be concluded that modifying the ligand organic shell does not alter the Mn$_{12}$O$_{12}$ core structure.

The molecular dimensions of all the complexes prepared as well those from the literature were measured and compared. A and B are the vertical and horizontal dimensions of the disk-shape core respectively when the complex is considered in a top down view, while C is the height from a side-on view (Figures 3.27). For all the derivatives, the dimensions of the clusters were measured without taking into account the hydrogen atoms.

(i) **(j)**

(k) **(l)**
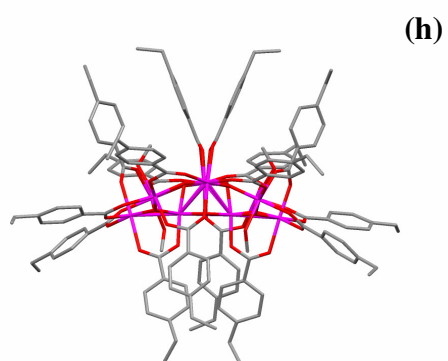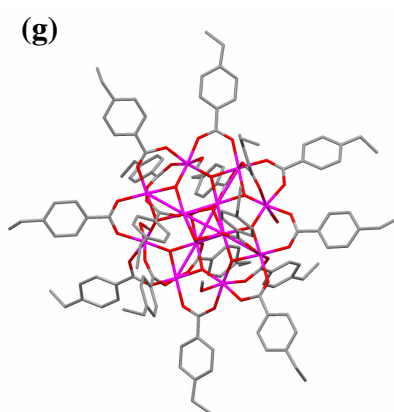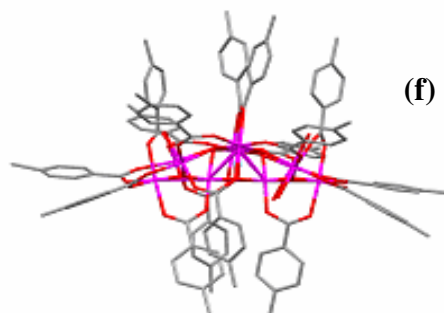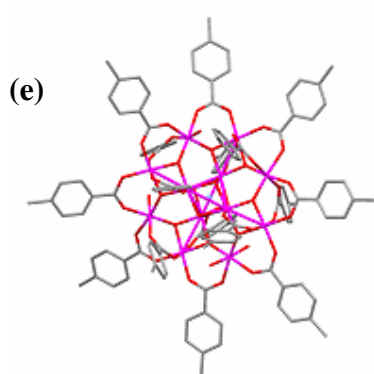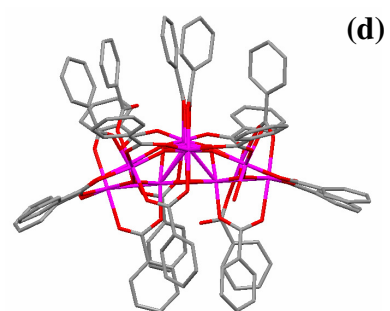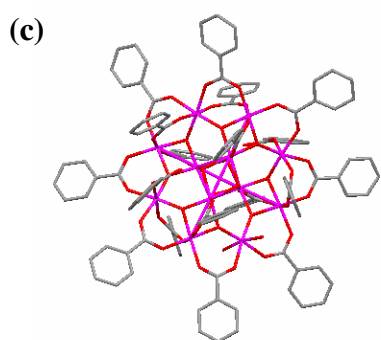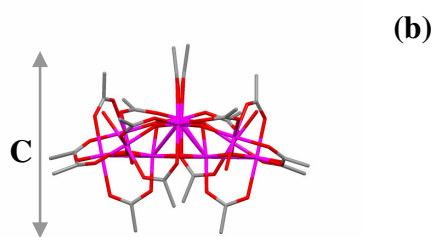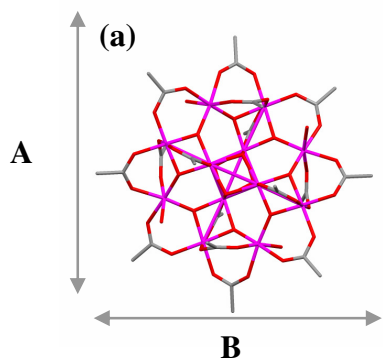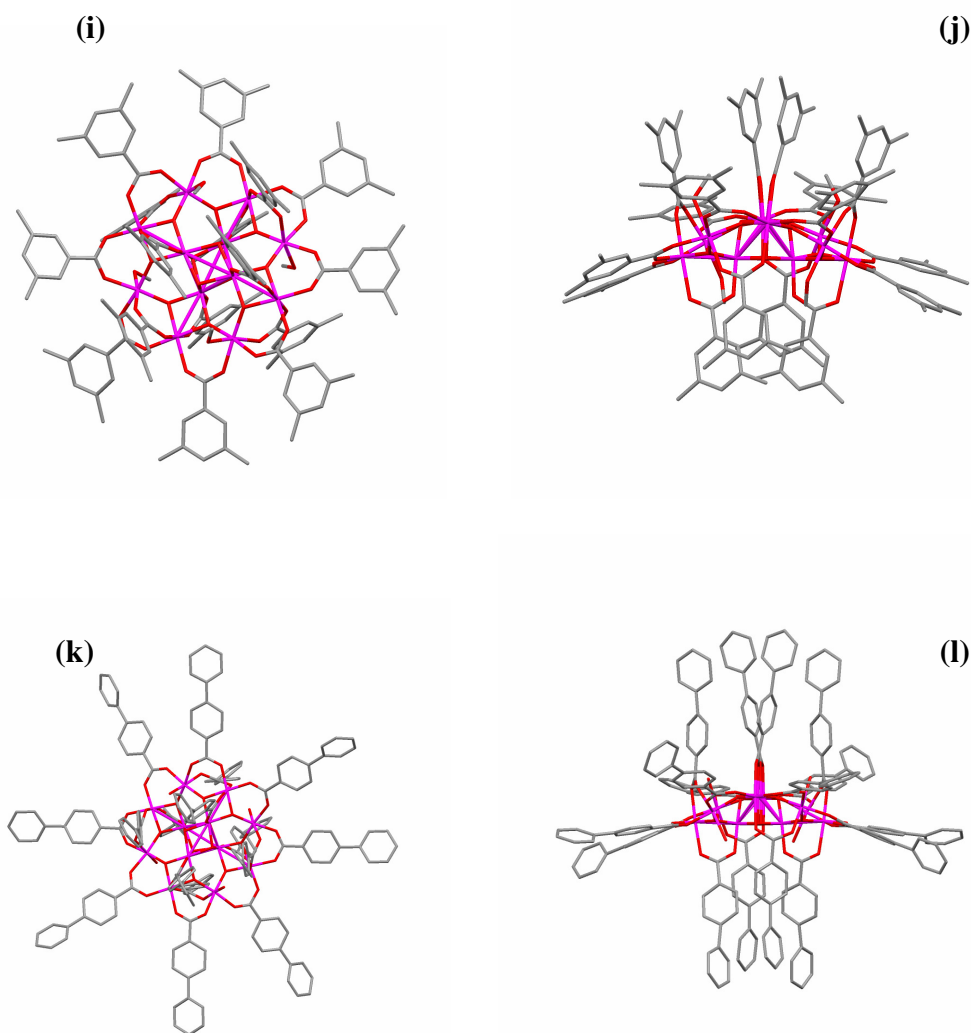
Figure 3.27. Representations of a top-down view on the left and a side-on view on the right for complexes: a-b (1), c-d (2), e-f (3), g-h (4), i-j (7) and k-l (9). The molecular dimensions A, B and C are illustrated for (1). Hydrogen atoms have been omitted for clarity.

The intermolecular separation between adjacent molecules was calculated by measuring the centroid-centroid distance, the centroid being placed in the centre of the inner $Mn^{IV}_4O_4$ cubane. As expected, the data summarised in Table 3 clearly demonstrate that increasing the size of the ligand increase the molecular dimensions of the cluster as well as the intermolecular separation between neighbouring molecules. $Mn_{12}ac$ has a mean diameter of 15.5 Å and a height of approximately 8.7 Å. The diameter of complex **(2)** averages 20.5 Å simply by replacing acetate by

benzoate ligands while the height is almost doubled (14.1-15.2 Å). Adding a methyl group to the benzoate derivative to yield the methylbenzoate complex (**3**) increase the molecular dimensions by about 3 Å, while the biphenylcarboxylate cluster (**7**) reaches dimensions as big as 29.5 Å for both A and B and 22.5 Å for C. It can also be noted that the molecular dimensions for (**2**) and (**3**) are similar to those measured for the versions reported by Takeda,[60-61] Sessoli[3b] and Aubin[11] respectively.

Table 3. Molecular dimensions and intermolecular separations measured for the different complexes.

	Space group	A (Å)	B (Å)	C (Å)	Intermolecular distance (Å)
Mn$_{12}$ac[a]	*I*-4	15.53	15.53	8.774	12.38-13.72
(**2**)	*Fdd*2	20.49	20.35	14.14-15.23	15.99-17.83
2[b]	*P*-1	20.74	20.72	14.0-14.3	14.25-17.51
2.2PhCO$_2$H[c]	*Fdd*2	21.04	20.88	13.98-14.32	16.00-16.97
(**3**)	*P*-1	23.93	23.46	17.14-17.53	15.785-20.00
3.3(H$_2$O)[d]	*I*2/*a*	23.55	23.45	16.9-17.25	15.19-17.60
3.(HO$_2$CC$_6$H$_4$CH$_3$)[d]	*C*2/*c*	23.8	23.63	17.35-17.47	15.97-18.23
(**4**)	*P*2/*c*	25.63	25.43	18.05-19.89	16.29-20.18
(**7**)	*P*-1	20.81	20.42	14.24-14.31	15.44-24.53
(**9**)	*I*-42*d*	29.52	29.52	22.53-22.58	19.15-20.59

[a] as reported by T. Lis[9], [b] reported by R.Sessoli[3b], [c] reported by Takeda[60-61], [d] reported by Aubin[11].

The crystal packing has been studied and another interesting feature that has been considered is the presence of intermolecular interactions such as π-π stacking or CH-π interactions that can modulate the intermolecular separation and also direct the alignment of the cluster along preferential directions.

For complex (2), the introduction of phenyl rings in the peripheral ligation shell was anticipated to yield π-π interactions between adjacent molecules. Figure 3.28 shows a partial crystal packing diagram adopted by (2). Intermolecular face-to-face π-π stacking interactions (4.324 Å) between ligands in the equatorial positions are observed leading the cluster to arrange into a one dimensional chain along the c-axis. The ($Mn^{IV}_4O_4$ cubane)centroid-($Mn^{IV}_4O_4$ cubane)centroid distance between adjacent molecules in the chain is *ca.* 17.42 Å.
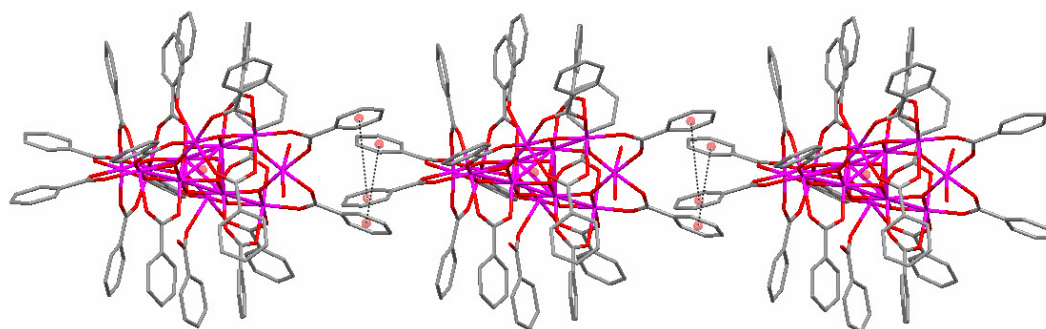
Figure 3.28. Intermolecular π-π interactions between equatorial benzoate ligands for (2) yielding the formation of one dimensional chain along the crystallographic c-axis. Hydrogen atoms have been omitted for clarity.

Similarly, the complexes reported by Sessoli[3b] and Takeda[60-61] respectively also exhibit some π-π stacking interactions between ligands in the equatorial positions (Figure 3.29 and 3.30). The former orders into a one dimensional zigzag chain while the latter adopts the same conformation as described for (2) with shorter distances for both the lateral π-π stacking (3.680 Å) and the intermolecular separation of two adjacent molecules within the chain (16.970 Å).
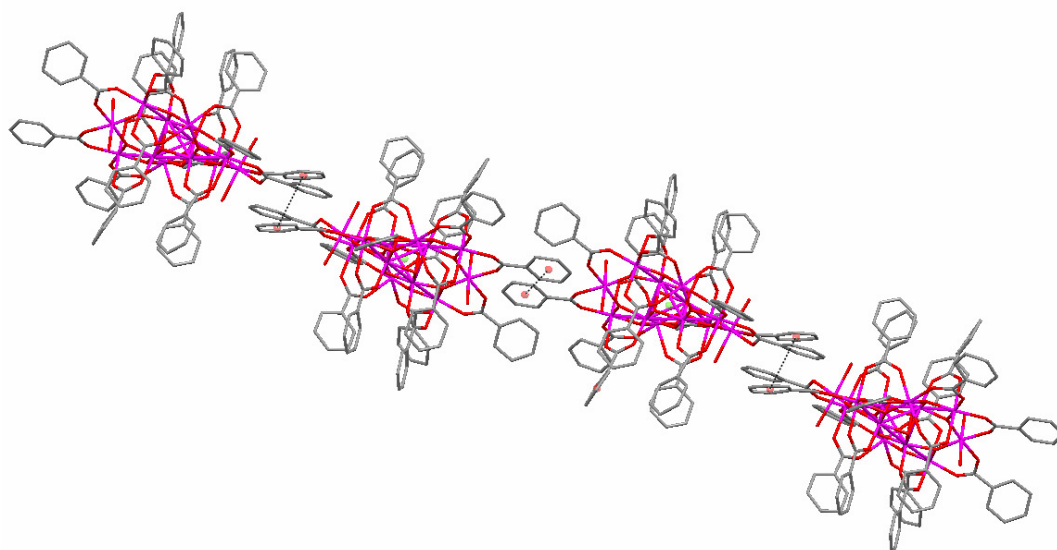
Figure 3.29. One-dimensional zigzag chain obtained for the Mn$_{12}$benzoate derivative reported by Sessoli and co-workers[3b] resulting from π-π interactions of benzoate groups in the equatorial positions. Hydrogen atoms have been omitted for clarity.
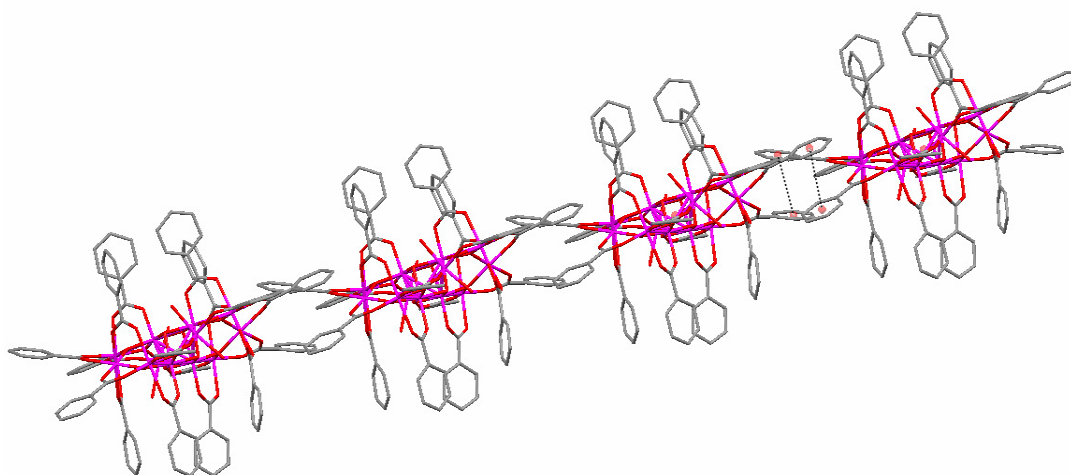
Figure 3.30. Intermolecular π-π interactions between equatorially located benzoate ligands for the Mn$_{12}$ benzoate complex reported by Takeda[60-61] yielding the formation of one-dimensional chain along the crystallographic c-axis. Hydrogen atoms have been omitted for clarity.

For complex (3), π-π interactions of similar strength in different directions are observed. The phenyl rings of neighbouring molecules in the equatorial positions stack to one another (3.748 Å and 3.959Å) resulting in a one dimensional chain arrangement of the cluster while the stacking of ligands in the axial sites (3.711 Å and 3.856 Å) leads to the formation of one dimensional zigzag chain (see Figure 3.31). The intermolecular centroid-centroid distance for the first chain is *ca.* 19.031 Å, while the corresponding distance between neighbouring molecules within the zigzag chain is *ca.* 15.788 Å.
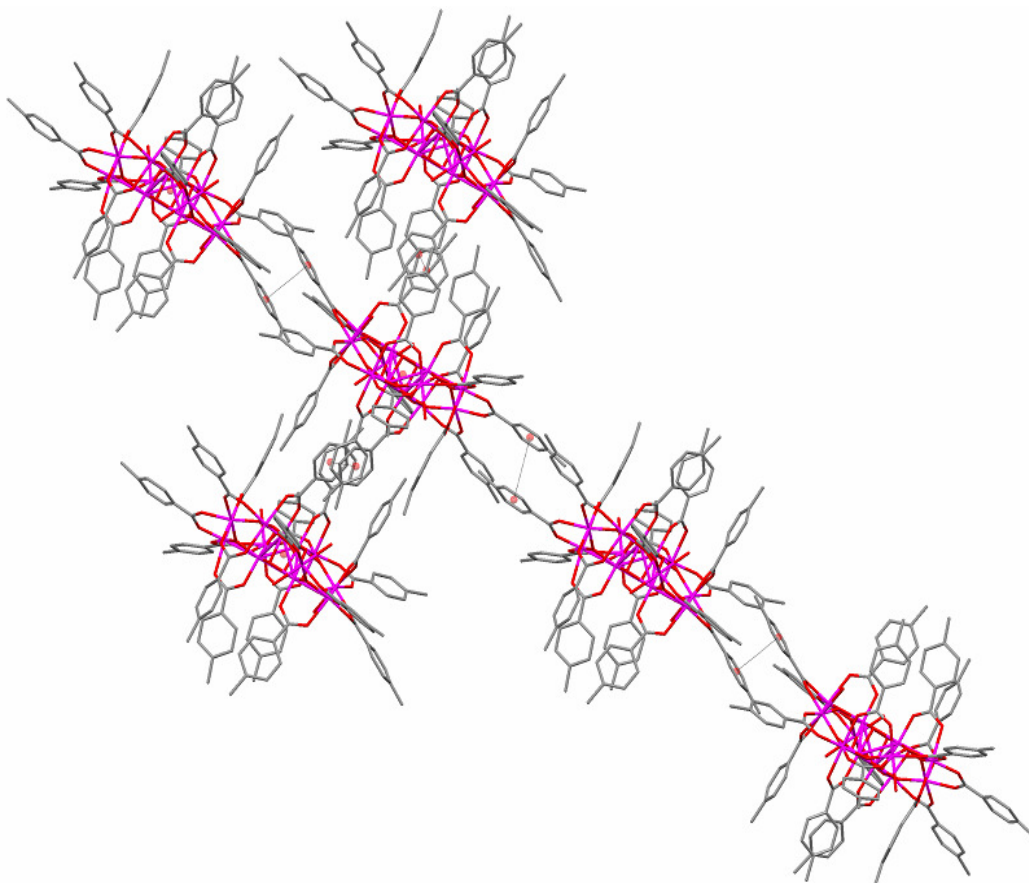
Figure 3.31. Intermolecular face-to-face π-π stacking interactions between equatorial and axial methyl-p-benzoate groups respectively of complex (3) leading the cluster to align into one-dimensional chains along two preferential directions. Hydrogen atoms have been omitted for clarity. View down the crystallographic a-axis.

The same phenomenon is observed for complex **(4)** with two of the phenyl rings of the equatorial ligands stacking (3.536 Å) with their counterparts from neighbouring molecules on both sides causing the cluster to align in one dimensional zigzag chain down the crystallographic c-axis (Figure 3.32). The intermolecular centroid-centroid distance in this direction is *ca.* 17.294 Å.
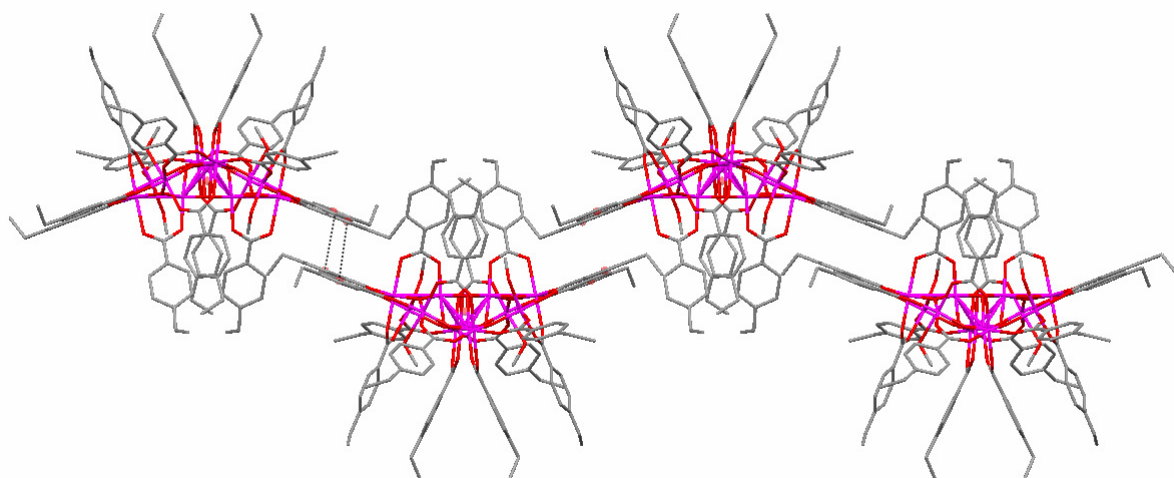
Figure 3.32. Intermolecular face-to-face π-π stacking interactions of typical distances (3.536 Å) between equatorial 4-ethyl benzoate groups of complex (4) residing on neighbouring molecules. The intermolecular distance (centroid-centroid, the centroid being positioned in the centre of the cubane $Mn^{IV}_4O_4$) between adjacent molecules within the chain is *ca.* 17.294 Å. Hydrogen atoms have been omitted for clarity. View down the crystallographic c-axis.

Similarly, **(7)** aligns into one dimensional zigzag chain with π-π interactions alternating between ligands in equatorial (3.830 Å) and axial positions (3.603 Å). The first interactions result in two adjacent molecules being distant from *ca.* 18.268 Å, while the second ones yield an intermolecular distance of *ca.* 15.443 Å between two neighbouring molecules (Figure 3.33). It can also be noted that molecules belonging

to adjacent chains also interact with one another *via* π-π stacking (3.657 Å) between phenyl rings sitting on axial binding sites.
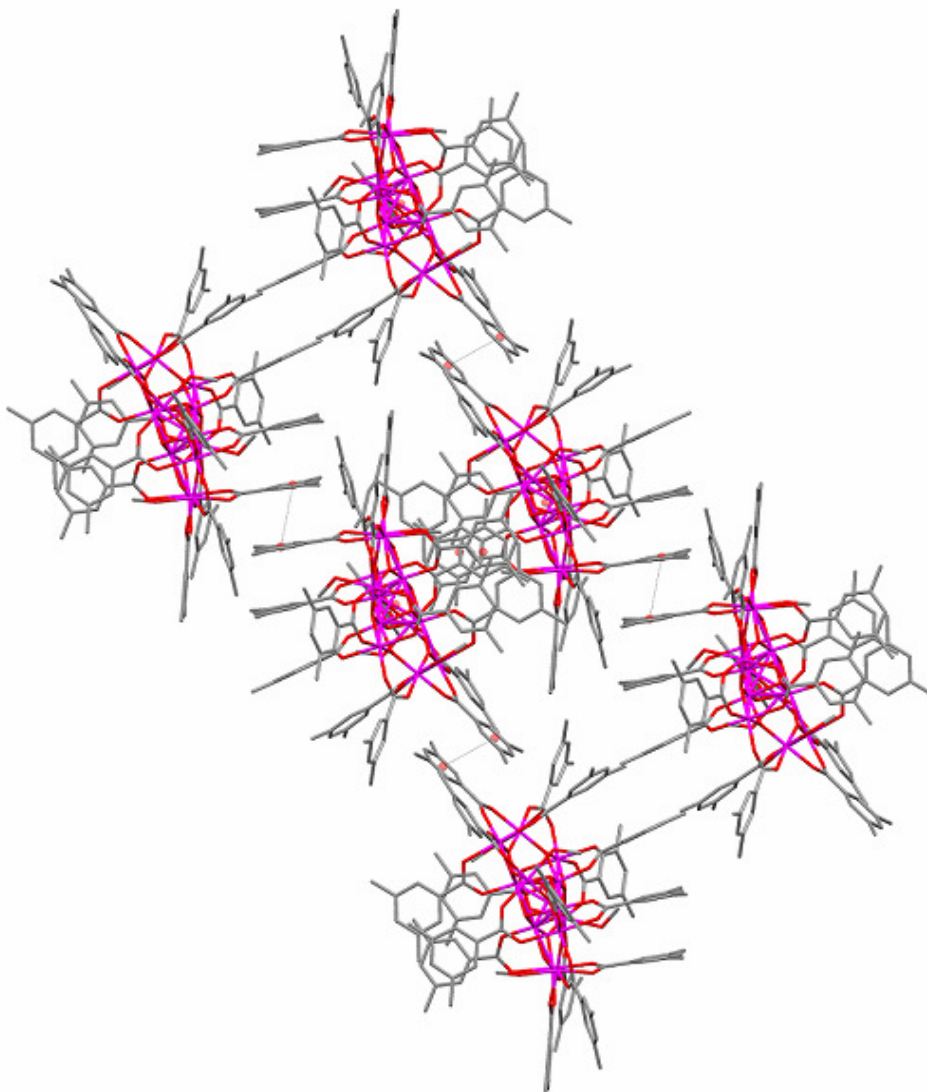
Figure 3.33. Partial packing for complex (7) showing the one-dimensional zigzag chain resulting from intermolecular π-π interactions alternating between equatorial and axial ligands. Molecules belonging to adjacent chains also interact with each other via π-π stacking. Hydrogen atoms have been omitted for clarity.

As far as complex **(9)** is concerned, all of the eight biphenylcarboxylic acid ligands situated in the equatorial positions are involved in both intermolecular π-π stacking (3.796 Å) as well as CH-π interactions (2.739 Å) with neighbouring molecules. These

series of interactions lead the cluster to align into one dimensional chains propagating

along the crystallographic a and b-axes respectively (Figure 3.34).
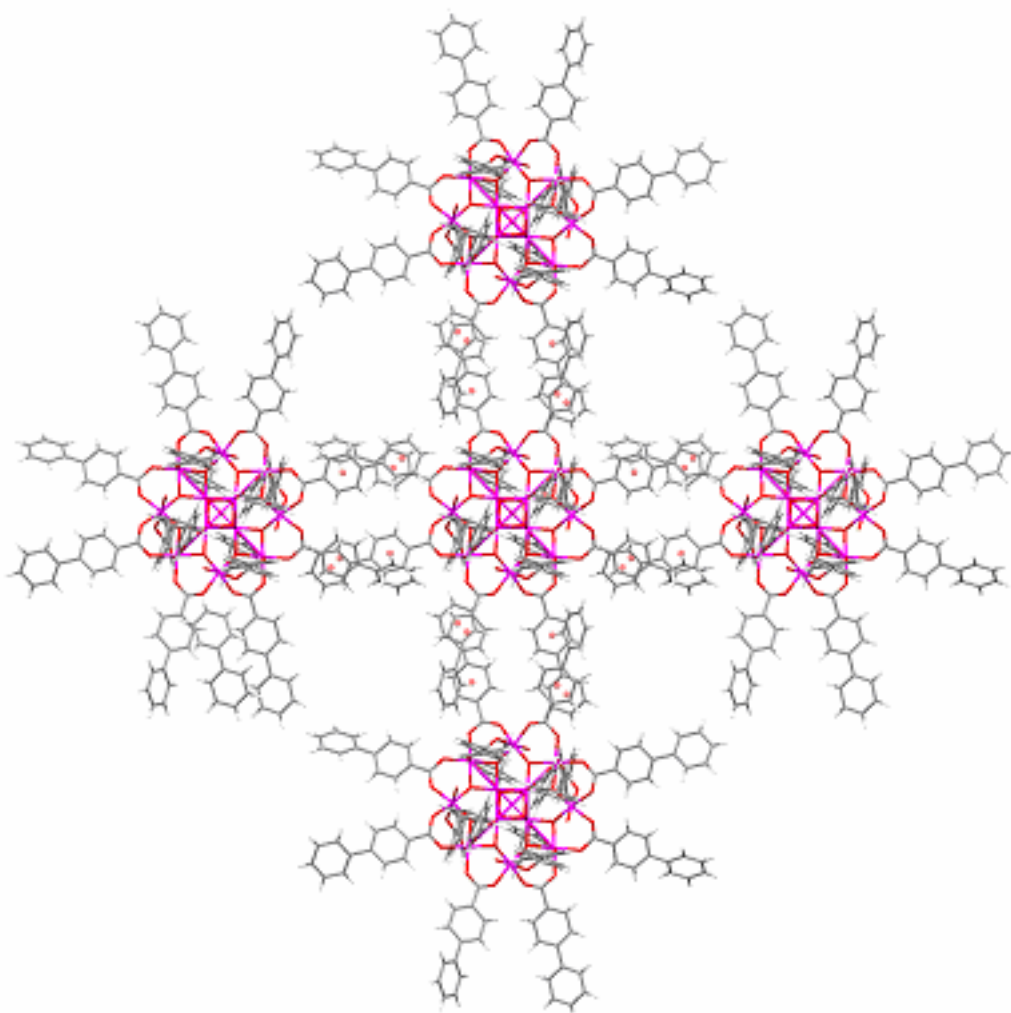
Figure 3.34. View down the crystallographic c-axis of complex (9) showing the intermolecular π-π interactions involving the eight equatorial biphenylcarboxylate ligands which lead the cluster to align into two 1-D chains along the a and b-crystallographic axes.

Overall, it has been demonstrated that modulating the organic ligand shell does not

alter the $Mn_{12}O_{12}$ core structure of the clusters as similar bond lengths are observed for

all the synthesised derivatives. As expected, the increase in the ligand size increases

the molecular dimensions of the metallic clusters so that eventually clusters can be tailored for subsequent surface depositions onto networks such as the PTCDI-melamine network mentioned previously. In addition, the incorporation of specific ligands can promote intermolecular interactions such as π-π stacking and CH-π interactions, as described in this study, which not only modulate the intermolecular separation between individual molecules but also can direct the alignment of the clusters into preferential directions. The latter phenomenon may turn out to be an interesting feature to observe a certain order on surfaces especially onto gold substrates. For other substrates such as HOPG, the alkyl groups present in complexes **(3)**, **(4)** and **(7)** may also enhance adsorbate-substrate affinity.

3.2.6 Alternating Current magnetic susceptibility

The magnetic properties of two clusters among the Mn_{12} derivatives prepared were measured in alternating current (AC) mode on polycrystalline samples.

The AC magnetic susceptibility data were collected for complexes **(2)** and **(4)** in the 1.8-10.0 K range in a 3.5 Oe AC field measured at frequencies of 99.9, 498.7 and 999.9 Hz. Plots of the in-phase component (χ'_M, plotted as $\chi'_M T$) and the out-of-phase component (χ''_M) versus T at the three different frequencies are shown in Figures 3.36, 3.35 and Figures 3.39, 3.38 for complex **(2)** and **(4)** respectively.
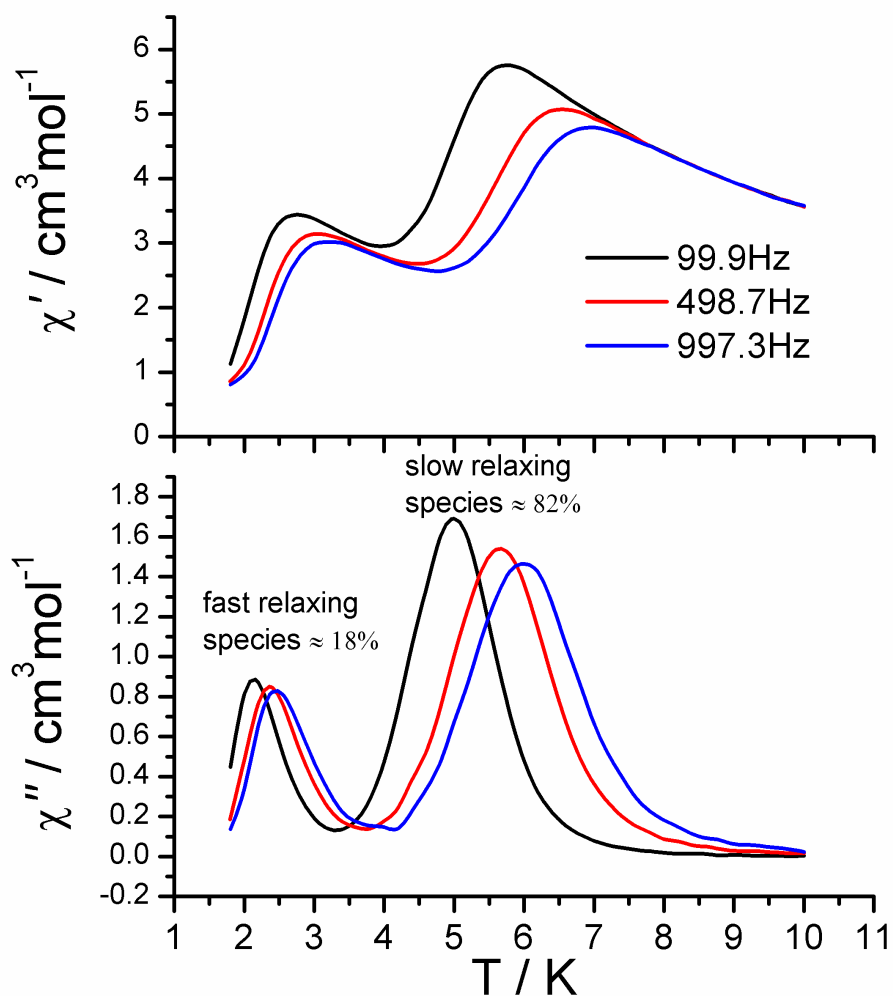
Figure 3.35. AC measurements performed on (2) reveal a frequency dependent out of phase component for T < 10 K in zero DC field due to the slow relaxation of the magnetisation. The two peaks found around 2.5 and 6K are ascribed to two different molecular species having different relaxation times [fast (A) and slow (B) relaxing species respectively]. The amount of these species has been estimated using the relations $A=(\chi''(B)T(B)/ \chi''(A)T(A))/(1+ \chi''(B)T(B)/ \chi''(A)T(A))$ and $B=1-A$.
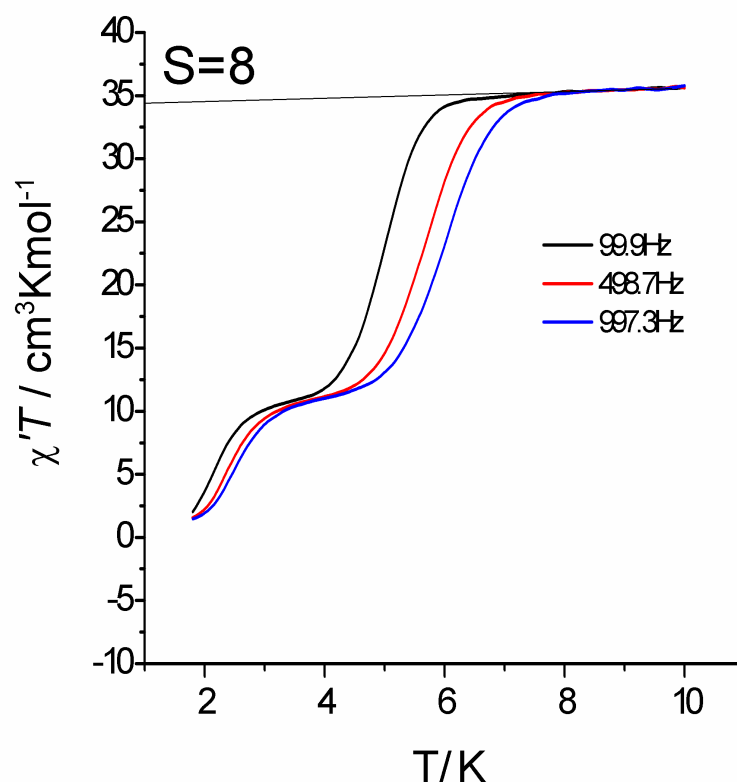
Figure 3.36. χ'T vs T plot at different frequencies for complex (2). Below 8K the curves are frequency dependent and deviate from the Curie law due to the blocking of the magnetisation. The extrapolated value of χ'T to 0K gives the molecular spin ground state S=8 assuming g=2.

For complex **(2)**, at 99.9 Hz the quantity $\chi'_M T$ remains relatively unchanged and equal to about 35 cm^3.K.mol^{-1} between 10 and 6.5 K. Below 6.5 K, the value of $\chi'_M T$ decreases rapidly to about 2.5 cm^3.K.mol^{-1} at 2 K. The decrease in $\chi'_M T$ occurs at even higher temperatures at higher frequencies.

Simultaneously with the abrupt drop in $\chi'_M T$, the presence of an out-of-phase signal χ''_M is observed indicating that at low temperatures the magnetization of the compound cannot keep in phase with the oscillating magnetic field. A frequency-dependent decrease in the in-phase $\chi'_M T$ component and an appearance of an out-of-phase χ''_M component of the AC magnetic susceptibility are the signature of SMM

behaviour. The χ''_M peak maximum is the temperature at which the frequency of the oscillating field equals the rate at which a single-molecule reverses its direction of magnetization. Complex **(2)** exhibits two χ''_M peaks in the temperature range of 2-2.5 K and 5-6 K with values of approximately 0.9 and 1.7cm^3.mol^{-1} at 99.9 Hz respectively.

It can also be noted that higher operating frequencies shift the χ''_M maxima to higher temperatures. The lower temperature peak was found to be therefore about half of the intensity of the higher temperature peak. These two maxima (at 2.5 and 6 K) are ascribed to the presence of two different Jahn-Teller isomers in the polycrystalline sample having different relaxing times (fast and slow relaxing species respectively). As mentioned during the description of the crystal structure, the single crystal obtained for complex **(2)** corresponds to the Jahn-Teller isomer for which one of the eight Mn^{III} ion has an abnormally orientated Jahn-Teller axis (the latter is contained in the plan of the molecule (Mn$_{12}$ core)), which correspond to the fast relaxing (FR) species based on similar results detailed in the literature for pairs of Jahn-Teller isomers of other derivatives.[11,60-61,63] The amount of the fast relaxing (FR) and slow relaxing (SR) species for the experimental batch used has been estimated to be 18% and 82% respectively.

At the temperature of the χ'' peak, the relaxation rate equals the AC frequency (ν), and thus the relaxation rate ($1/\tau$) can be obtained from the relationship $\omega\tau=1$, where $\omega=2\pi\nu$. AC magnetic susceptibility data were fit to the Arrhenius equation:

$$\tau = \tau_0 \exp(\Delta E / k_B T)$$

where k_B is the Boltzmann constant and ΔE the effective energy barrier.

Figure 3.37 gives the resulting Arrhenius plot of ln (1/τ) against (1/T). Analyzing the frequency dependence of χ'' by the Arrhenius law enables the determination of the energy barriers, the pre-exponential factors for both species:

$$\tau_0 \text{ (SR)} = 2.1 \times 10^{-9} \text{ s, } \Delta E(SR)/k_B = 69 \text{ K and for the SR process}$$

$$\tau_0 \text{ (FR)} = 6.9 \times 10^{-13} \text{ s and } \Delta E(FR)/k_B = 48 \text{ K for the FR process.}$$

Based on these parameters, the blocking temperatures for the SR and FR molecules were calculated as $T_B(SR) = 2.8$ K and T_B (FR) = 1.5 K respectively. Similar values were reported for a batch of sample containing a similar crystallographic form as (2)[60] (*i.e.* same Jahn-Teller isomer). Takeda and co-workers found a blocking temperature of 2.7 K for the SR species which was approximately double of that of the FR species (T_B=1.3 K). However, some differences are found for the values of the exponential prefactors τ_0 and the effective energy barriers. The most striking ones are for the FR process. An energy barrier of 38 K and a pre-exponential factor τ_0 of 3.2×10^{-11} s were reported. This non negligible gap could be related to the different ratio of FR and SR species present in the samples used for the measurements. Indeed, the FR species was found to be predominant and constituted about 70-75% of the sample used by Takeda et al.[61]

Furthermore, the extrapolation to 0 K of the $\chi'T$ plateau of the $\chi'T$ versus T plot provides a good indication of the spin ground state S of the system in zero applied field with the g value approximated to 2. For complex (2), the value deduced for the molecular spin ground state was S=8. The spin ground state value for the same complex (but with no solvent molecules present in the structure) has been reported to be S=9 at zero applied field by Sessoli et al. in 1993.[3b] However, it is important to

stress that it is difficult to estimate the ground state spin values S with a certainty less than +/- 1 with AC magnetic experiments. Further experiments such as high-field EPR measurements would be required to confirm these values.
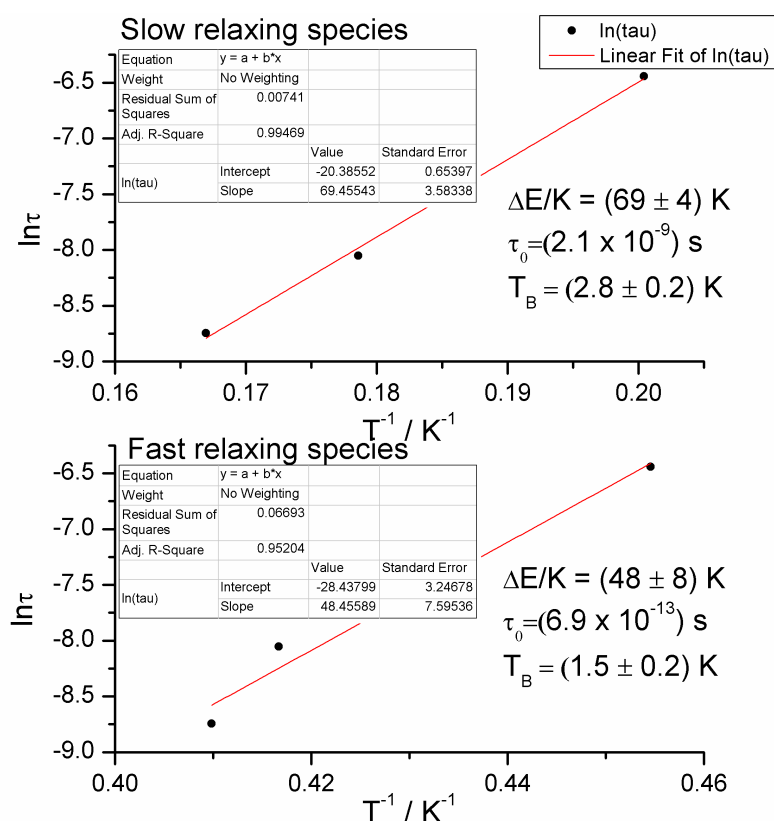
Figure 3.37. Arrhenius fit of the AC measurements of Figure 3.35. The energy barrier, the prefactor τ_0 and the blocking temperature have been estimated.

For the new complex (**4**), the variation of $\chi'_M T$ versus T follows the same trend as previously described for (**2**). $\chi'_M T$ remains constant and approximately equal to 48 $cm^3.mol^{-1}$ for temperatures above 8 K at the three frequencies studied (Figure 3.39). Below 8 K, the value of $\chi'_M T$ decreases rapidly to approximately 2 $cm^3.K.mol^{-1}$ at 2 K. At the same time, the presence of an out-of-phase signal χ''_M is observed. However, the main difference resides in the fact that (**4**) displays one single main χ''_M

peak at about 6 K corresponding to the SR species. A close look at the plot shows the presence of a significantly broad peak corresponding to the FR species.
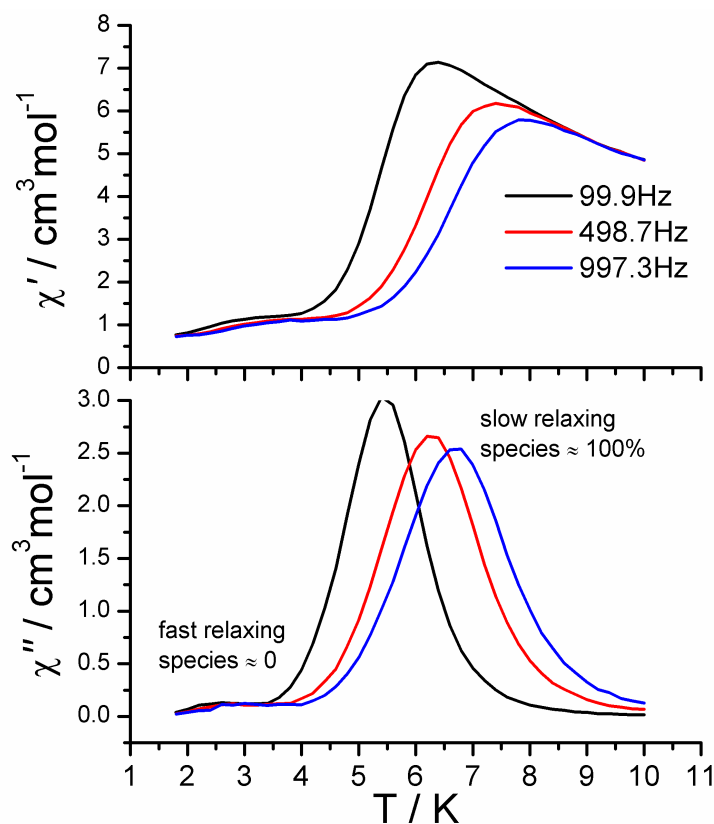
Figure 3.38. AC measurements carried out on complex (4) reveal a frequency dependent out of phase component for T < 10 K in zero DC field due to the slow relaxation of the magnetisation. The peak around 6K is ascribed to the relaxation process of SR species while the broad peak around 2.5K to the FR species. The amount of fast relaxing species is almost completely quenched and difficult to estimate.

Yet as the intensity of this peak is really low, the amount of FR species is almost completely quenched, and thus difficult to estimate and therefore considered quasi nil. This result is confirmed by the crystal structure of **(4)** where the normal JT isomer (corresponding to the SR species) is observed with all of the Mn^{III} centers displaying the usual axial JT distortion of two trans bonds with the axes being roughly parallel to one another and almost perpendicular to the Mn$_{12}$O$_{12}$ core.
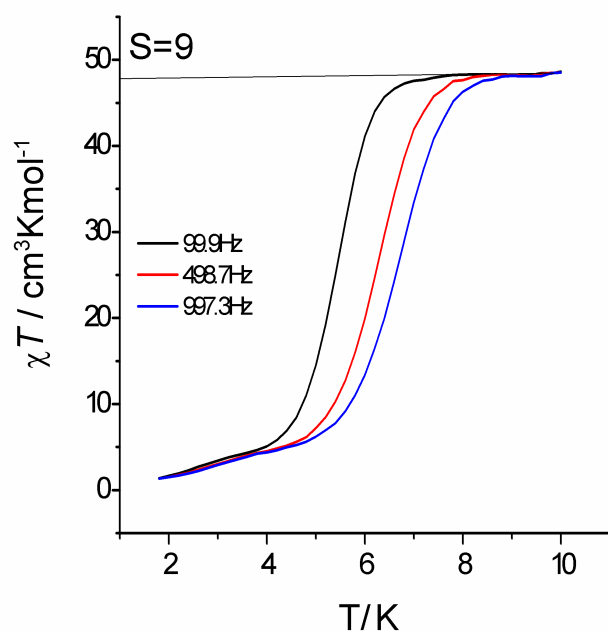
Figure 3.39. χ'T versus T plot for complex (4) at different frequencies. Below 8K the curves are frequency dependent and deviate from the Curie law due to the blocking of the magnetisation. The extrapolated value of χ'T to 0 K gives the molecular spin ground state S=9 assuming g=2.
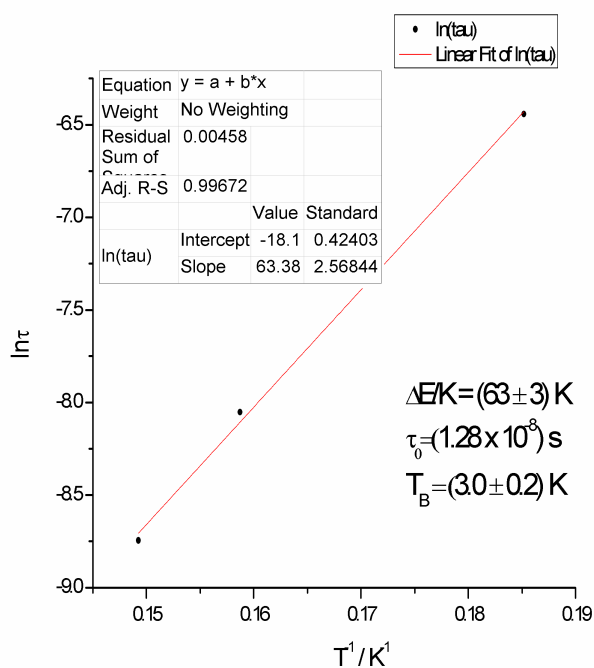
Figure 3.40. Arrhenius fit of the AC measurements in Figure 3.38. The energy barrier, the prefactor τ_0 and the blocking temperature have been estimated.

172

The AC measurements data were fit to the Arrhenius law using a least-squares approach (Figure 3.40) to give $\tau_0 = 1.28 \times 10^{-8}$ s ; $\Delta E = 63$ K and $T_B = 3$ K. The spin ground state S of complex **(4)** has been deduced from the extrapolation of the curve in Figure 3.39 to 0 K and estimated to be S=9-10. These values are of the same order of magnitude as those described for complex **(2)** and for other similar Mn_{12} derivatives.[3b,11,60-61,63]

Overall, complex (2) and complex (4) exhibit the expected magnetic properties commonly reported for SMMs belonging to the Mn_{12} family. The values found for the effective energy barriers, the blocking temperatures and the exponential pre-factors do not show unusual features. However, some discrepancies are still observed among the different clusters depending on the nature of the carboxylate ligands introduced around the magnetic core. It has been demonstrated that the differences in the observed magnetic properties are related to several factors such as the chemical and electronic structure of the ligands as well as the intramolecular exchange interactions between the metal centers within the complexes.[64] Dependence of the magnetic properties on the synthetic route employed, the solvents used, the type of sample studied (amorphous, crystalline, mixture of JT isomers, etc.) have also been established.[64,65, 66]

3.2.7 Case of the trinuclear complex (12)

- **Synthesis and X-ray structure**

A number of trinuclear $Mn_3(\mu_3-O)$ clusters with ancillary ligands are known[67] with a subset of those with the general formula $[Mn_3(\mu_3-O)(carboxylate)_6L_3]^{n+}$.[68-71] The

typical preparation of such compounds[68] involve the use of a variety of Mn starting materials, including mixtures of $Mn(O_2CMe).4H_2O$ and $[(^nBu)_4N]MnO_4$ to obtain the desired mixture of oxidation states in the final products.[68]

The title compound $[Mn_3O(O_2C-anth)_6(HOCH_3)_3].2(CH_3OH)$ **(12)** (where $O_2C-anth$ = 9-anthracenecarboxylate), was isolated from the reaction between $Mn_{12}ac$ **(1)** and 9-anthracene carboxylic acid. It was obtained during the course of our attempt to synthesise a new dodecanuclear mixed-valence manganese carboxylate complex comprising of sixteen anthracene carboxylate ligands. Indeed, the bulky anthracene based ligand $O_2C-anth$ has been used before in the preparation of Mn cluster compounds[72] but there are no previous reports of this ligand substituted onto a Mn_{12} cluster. This is presumably a result of steric interactions that prevents the accommodation of sixteen $O_2C-anth$ ligands around the $Mn_{12}O_{12}$ core.

Single crystals of complex **(12)** were grown by layering MeOH over a CH_2Cl_2 solution of the compound for a period of 5 days. It is also suggested that the methanol used during the crystallisation process may have played the role of reducing agent resulting in the reductive fragmentation of the $Mn_{12}O_{12}$ core as well as providing an additional source of alkoxide (*e.g.* MeO^-) bridging ligands yielding the oxo-centered trinuclear manganese cluster.

Complex (**12**) has an interesting C_3-symmetric structure in contrast to other related, less symmetrical, trinuclear manganese clusters impacting upon the compounds magnetic properties (see below). The X-ray diffraction analysis revealed the formation of a trinuclear $Mn_3(\mu_3-O)$ cluster decorated by 9-anthracenecarboxylate and methanol ligands (Figure 3.41). Thus, each Mn centre adopts a distorted octahedral O_6 coordination environment (Table 4) bound by four carboxylate ligands, a capping methanol ligand and the central μ_3-O oxygen atom. Adjacent Mn centres are bridged

by two carboxylate groups across each edge of the triangle defined by the three Mn centres. Thus, three 9-anthracenecarboxylate ligand sit above the $Mn_3(\mu_3$-O) plane and three below. The $Mn_3(\mu_3$-O) cluster is interesting in that the oxygen sits upon a threefold rotation axis resulting in the Mn centres and the corresponding Mn-O distances (Table 4) being crystallographically equivalent. The μ_3-O sits slightly [0.046(4) Å] out of the plane defined by the three Mn centres. The methanol ligands adopt positions within the Mn_3 plane with O_{oxo}-Mn-O_{meth} angles close to linearity [175.59(14) Å]. The Mn…Mn separation in the $Mn_3(\mu_3$-O) core is 3.3222(13) Å, in good agreement with other $Mn_3(\mu_3$-O) clusters.[67]
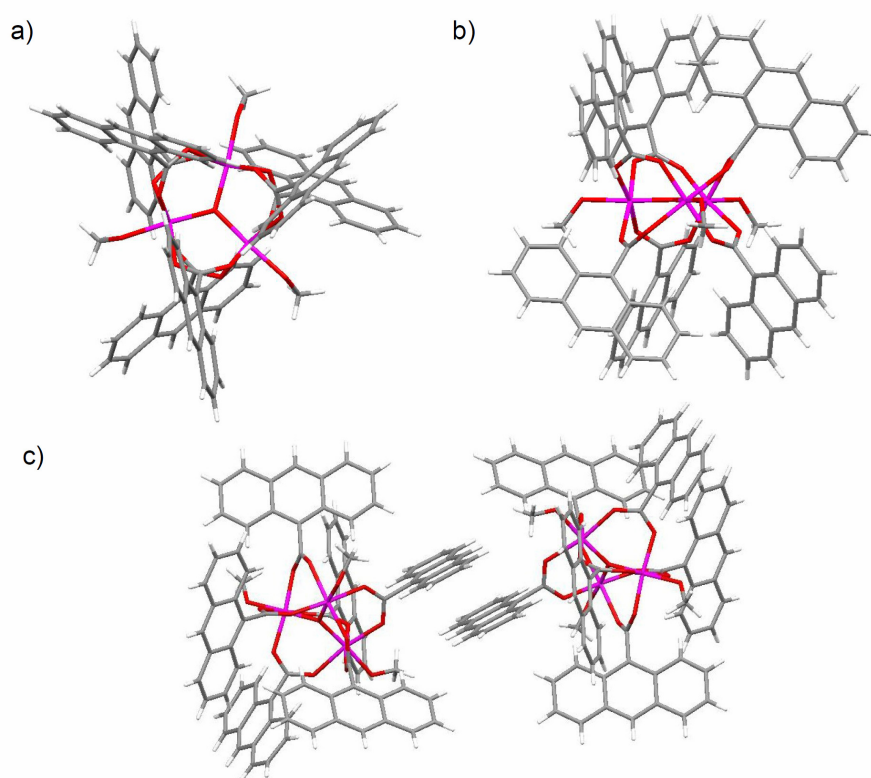
Figure 3.41. Views of the single crystal structures of (12). (a) along the crystallographic c-axis showing the trinuclear arrangement of the cluster; (b) view parallel to the Mn_3 plane, along the crystallographic a-axis; (c) view showing π-π interactions between adjacent molecules. Mn-$O_{carboxy}$ 2.007(4) - 2.196(5)Å; Mn-O_{meth} = 2.055(3) Å; Mn-O_{oxo} = 1.9187(7)Å; Mn-O_{oxo}-Mn = 119.94(3)°; O_{meth}-Mn-O_{oxo} 175.59(14)°; $O_{carboxy}$-Mn-O_{oxo} = 92.59(14) - 96.07(11)°; $O_{carboxy}$-Mn-O_{meth} 81.25(14) - 88.33(14)°; $O_{carboxy}$-Mn-$O_{carboxy}$ = 86.74(15) – 93.57(18)°; 169.49(13) ,173.81(14)°.

Table 4. Selected bond lengths (Å), angles and torsion angles (°) for (12).

Mn1-O1	2.026(3)	Mn1-O3	2.165(4)	Mn1-O5	2.055(3)
Mn1-O6	1.9187(7)	Mn1-O2^i	2.196(5)	Mn1-O4^i	2.007(4)

O1-Mn1-O3	91.33(13)	O1-Mn1-O5	87.04(14)	O1-Mn1-O6	92.59(14)
O1-Mn1-O2^i	86.74(15)	O1-Mn1-O4^i	173.81(14)	O3-Mn1-O5	88.33(14)
O3-Mn1-O6	96.07(11)	O2^i-Mn1-O3	169.49(13)	O3-Mn1-O4^i	87.24(17)
O5-Mn1-O6	175.59(14)	O2^i-Mn1-O5	81.25(14)	O4^i-Mn1-O5	86.90(14)
O2^i-Mn1-O6	94.34(12)	O4^i-Mn1-O6	93.55(15)	O2^i-Mn1-O4^i	93.57(18)
Mn1-O6-Mn1^i	119.94(3)				

^{i} = 1-x+y, 1-x, z.

Considering the extended aromatic structure of the anthracene moiety, it is perhaps unsurprising that face-to-face π-π stacking interactions are observed between adjacent molecules, with a centroid…centroid separation of 3.80 Å between central rings of anthracene moieties (Figure 3.41c). Close CH···C contacts between anthracene moieties on adjacent molecules are also observed, with the shortest contacts of 2.67 and 2.86 Å[73] leading to an arrangement reminiscent of phenyl embraces.[74] Similarly intramolecular CH···C interactions indicative of phenyl embraces are observed between the three anthracene groups above and below the Mn$_3$ plane (CH···C = 2.95 Å).

Some ambiguity arises from the single crystal structure over the assignment of the alcoholic ligand as either methanol, indicating a Mn^{II}.2Mn^{III} system or as methoxide giving a Mn^{III}.2Mn^{IV} cluster. The Mn-O distance is relatively short for such a bond, Mn-O = 2.055(3) Å, compared to values typically over 2.2 Å for Mn(II) and Mn(II)-HOMe Mn-O bond lengths.[75] Mn-O bond lengths for Mn(II)/(III)-methoxide complexes, are highly variable with some distances as short at 1.77 Å[76] but values as high as 2.3 Å have also been reported.[77] Bond valence sum analysis gives a valency of 2.74 for each Mn centre, all three Mn centres having the same calculated

value due to the symmetry of the system. This implies that the system has one Mn^{II} centre and two Mn^{III} centres the positions of which are averaged around the trinuclear cluster. The assignment of the cluster as a $Mn^{II}.2Mn^{III}$ system confirms the alcoholic ligand as coordinated methanol rather than methoxide. A table corresponding to the crystal data and structure refinement for **(12)** is presented in Appendix A.2.

- **Magnetism**

    The magnetic properties of such μ_3-oxide complexes have also been the centre of several investigations as they represent an ideal class of compounds for the study of intramolecular exchange interactions as well as electron transfer between metal centres.[68,78] Recently it has also been discovered that these clusters can function as SMMs and have been incorporated as building blocks for the preparation of new single-chain magnets (SCMs).[79,80] Most of the trinuclear Mn complexes described in the literature have $[Mn_3O(O_2CR)_6(L)_3]^{0/+}$ for general formula where L is a terminal ligand such as H_2O, MeCN, pyridine, etc.[68,81] When the manganese ions are antiferromagnetically coupled to one another in this type of structures with usually small S values, these compounds do not behave as SMMs. However it has been demonstrated that it was possible to convert these compounds into products possessing the same $[Mn_3(\mu_3\text{-}O)]$ core with the metal centers being ferromagnetically coupled to one another affording the first examples of triangular SMMs.[82]

    The oxidation state of the system was further probed by SQUID magnetometry measurements. The product of magnetic susceptibility and temperature as a function of temperature (Figure 3.42) has a value of $\chi T = 8.10\ cm^3.K.mol^{-1}$ at high temperatures, decreases monotonically with decreasing temperature and reaches a value of $\chi T = 0.76\ cm^3.K.mol^{-1}$ at the lowest measurement temperature of $T = 1.8$ K.

The decrease of χT suggests that the manganese ions in **(12)** are antiferromagnetically coupled, while the χT curve extrapolates to a nonzero value at 0 K, suggesting that the ground state of **(12)** has non-zero spin. The high temperature χT-value is lower than that expected for two independent Mn^{III} and one Mn^{II} ion ($\chi T = 10.38$ cm^3.K.mol^{-1}, assuming g=2), but higher than expected for two Mn^{IV} ions and a Mn^{III} ion ($\chi T = 6.75$ cm^3.K.mol^{-1}, assuming g=2). In view of the predominant antiferromagnetic exchange coupling and the fact that the single ion g values are expected to be g≤2 (less-than-half-filled d-shell), cluster χT-values that are larger than the independent-ion values are unlikely. Hence, the susceptibility measurements suggest that the correct assignments of the oxidation states of the manganese ions are $Mn^{II}.2Mn^{III}$, in agreement with what is obtained from the crystallographic and bond valence sum analyses (see above). The magnetization as a function of field (Figure 3.43) does not saturate even at the lowest temperature ($T = 1.8$ K) and highest field ($B = 5$ T), indicating the presence of low-lying excited spin states with higher spin than the ground state or significant magnetic anisotropy (zero-field splitting).
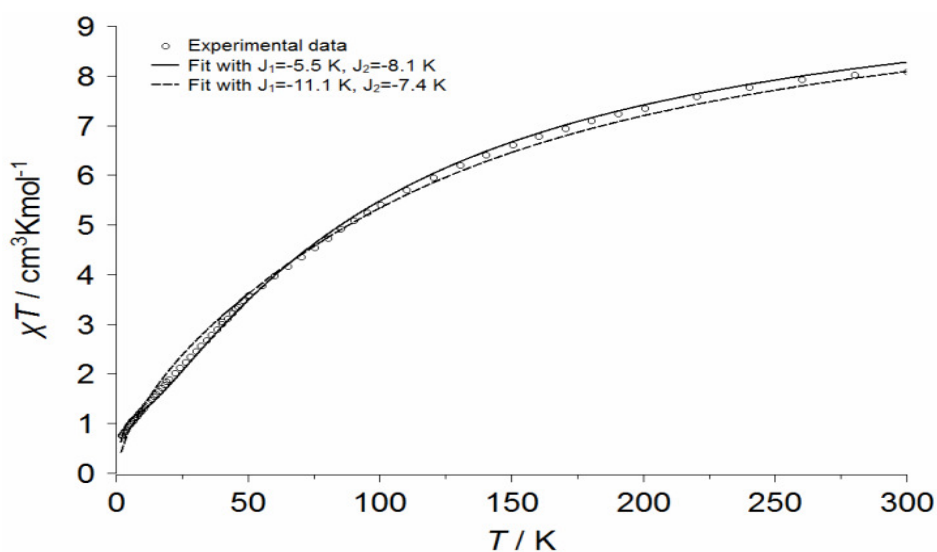
Figure 3.42. χT as a function of T recorded on a powder sample of (12) at applied fields of 1000 G ($T \le 50$ K) and 1 T ($T \ge 50$ K).
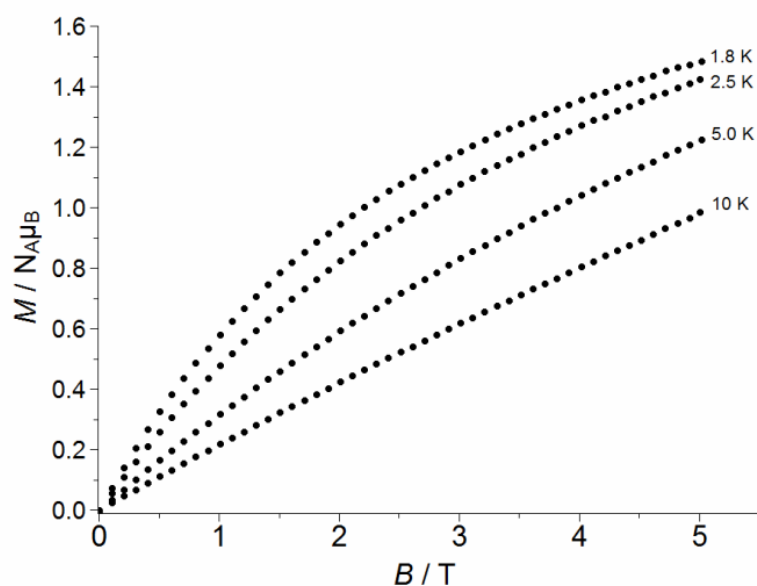
Figure 3.43. Magnetisation as a function of field recorded on a powder sample of (12) at different temperatures as indicated in the figure.

The magnetic susceptibility can be modelled by the Heisenberg spin Hamiltonian:

$$\mathcal{H} = -2J_1\hat{\mathbf{S}}_1 \cdot \hat{\mathbf{S}}_2 - 2J_2\left(\hat{\mathbf{S}}_1 \cdot \hat{\mathbf{S}}_3 + \hat{\mathbf{S}}_2 \cdot \hat{\mathbf{S}}_3\right),$$ (1)

where $\hat{\mathbf{S}}_1$ and $\hat{\mathbf{S}}_2$ denote the Mn^{III} ions and $\hat{\mathbf{S}}_3$ the Mn^{II} ion. A least squares fit using an equation described by Christou et al.[68] yields two possible parameter sets for J1 and J2. The slightly better fit is obtained for $J_1 = -5.55 \pm 0.04$ K and $J_2 = -8.07 \pm 0.04$ K (χ^2/d.o.f. $= 7 \times 10^{-3}$), while the fit for $J_1 = -11.1 \pm 0.16$ K and $J_2 = -7.37 \pm 0.07$ K (χ^2/d.o.f. $= 2 \times 10^{-2}$) is only slightly worse (Figure 3.42). Figure 3.44 displays the energies of the lowest spin states as a function of J_2/J_1. For both sets of parameters, the same ground state spin is obtained ($S_T = \frac{1}{2}$), with different intermediate spins S_{12}. In both cases, very low-lying excited $S = \frac{3}{2}$ excited states are predicted. The presence of excited states with higher spins can explain why the magnetisation does not

179

saturate to $M = gS = 1$ μ_B (for $S = \frac{1}{2}$ and $g = 2$) at low temperatures and high fields, but continues to increase: Excited states with higher spins will be stabilised in a field and correspondingly their energies will decrease and eventually these states with cross the zero-field ground state. No zero-field splitting is possible in a $S = \frac{1}{2}$ state. The obtained exchange interaction parameters are very similar to those obtained for other $[Mn^{II}Mn^{III}_2]$ clusters.[68] The low-spin state obtained is reminiscent of the coplanar spin arrangement found in equilateral homonuclear triangles.[67]
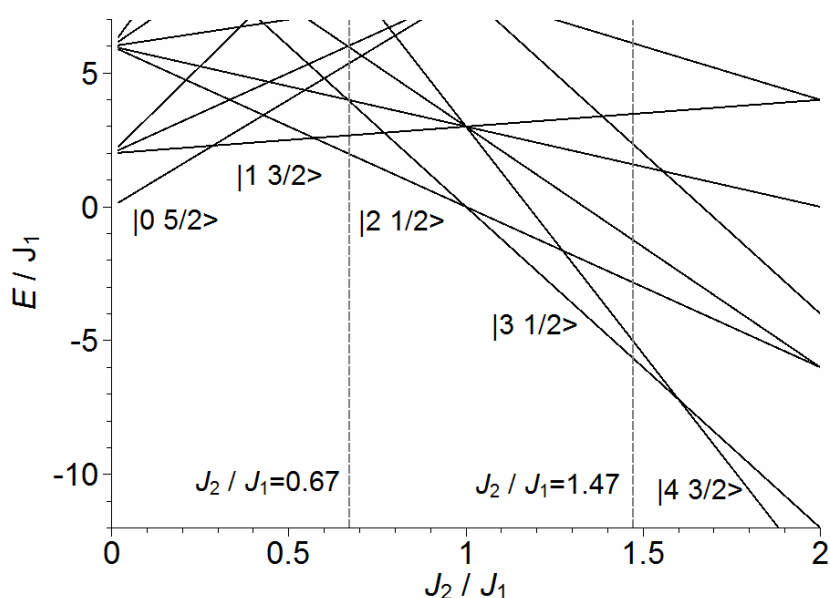
Figure 3.44. Energies E/J_1 of the low-lying spin states as a function of J_2/J_1. The grey vertical dashed lines indicate the J_2/J_1 ratios for the found parameter sets.

3.2.8 Surface deposition studies

Lateral organization of SMMs is highly desirable for exciting new technological applications such as high density magnetic data storage, quantum computing or even spintronic devices. However so far, there have been relatively few high resolution studies to determine the influence of intermolecular interactions on the packing and

ordering of molecules when deposited on surfaces. As outlined in the introduction of this chapter, a number of successful attempts to deposit various SMMs on surfaces using solution based deposition methods have been reported. This can be achieved either by functionalising the cluster so that it may be grafted onto a Au(111) surface,[13,18,83,85-87] or pre-functionalising both the substrate and the molecule to promote the formation of adsorbed layers.[88-90] Deposition in UHV using pulsed laser deposition (PLD),[91] matrix assisted pulsed laser evaporation (MAPLE),[92] a pulsed vacuum spray technique,[93] and a local mechanical method[94] have also been demonstrated. However when applied to the formation of $Mn_{12}ac$ films, fragmentation and possible damage to the manganese core[93,95] was reported. This is the result, in part, of the fragile nature of $Mn_{12}ac$ molecules which makes them unsuitable for sublimation and largely precludes the investigation of derived thin films using high resolution techniques such as ultra-high vacuum (UHV) scanning tunnelling microscopy (STM). Nevertheless, it has recently been shown that UHV-ESD, and related spray techniques, provide a viable method for the transfer of non-volatile/thermally labile species such as dye molecules, and polymers from solution onto surfaces held in UHV[96-102] and the development and application of this technique is crucial for the deposition of $Mn_{12}ac$.

Interestingly, $Mn_{12}ac$ exhibits a complex three-dimensional molecular shape with a complex intermolecular potential in which anisotropies arise from the asymmetric shape of the molecule. The structures resulting from the deposition of $Mn_{12}ac$ on a metallic surface under vacuum have been studied and are detailed in the following section. The anisotropic nature of the molecule leads directly to the spontaneous formation of filamentary structures through the aggregation of diffusing molecules.

Thin films of $Mn_{12}ac$ (the molecular dimensions are shown in Figure 3.45) on a Au(111) surface were prepared using Electrospray deposition (ESD) with coverages ranging from sub-monolayer to multilayers. Images of the adsorbed $Mn_{12}ac$ were acquired using an STM operating at room temperature under UHV conditions.
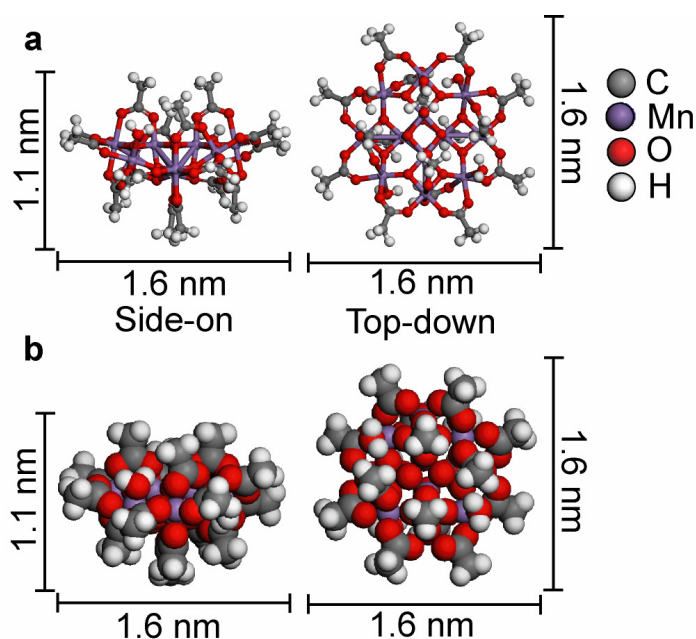
Figure 3.45. Chemical structure of $Mn_{12}ac$ showing the side-on and top-down views with the corresponding dimensions. (a) chemical structure, (b) space filling CPK model. Note the unsual anisotropic shape of the molecule.[106]

Figure 3.46a shows a large scale STM image of the surface following the deposition of a sub-monolayer of $Mn_{12}ac$ (~0.35 mL). A straightforward observation is that the molecules are mobile and diffuse on the surface readily after being adsorbed as their positions are non-random and they form complex aggregates in which meandering filamentary structures and small disordered clusters coexist. These features are somewhat reminiscent of the filamentary networks reported recently for planar organic molecules[103,104] which have been described as two-dimensional glasses.

From a simple consideration of the molecular hard sphere radius (Figure 3.46b) it might be expected that the $Mn_{12}ac$ molecules would be orientated so as to maximise contact area, potentially maximising vdW interactions with the substrate, giving rise to a circular cross section in STM images. However, as shown in the STM image of an isolated $Mn_{12}ac$ (Figure 3.46b) the orthogonal dimensions of the molecule, labelled r_1 and r_2, are not equal and the molecule is imaged with an ellipsoidal cross section. The average values of r_1 and r_2 for isolated molecules have been experimentally measured to be 1.6±0.4nm and 2.2±0.4nm respectively, with an aspect ratio of 1.4±0.2. The lateral dimensions of the $Mn_{12}ac$ as measured by STM are approximately 30% larger than the hard-sphere radius due to STM tip convolution. The average apparent-height of the molecules, 0.45 ±0.08 nm, is lower than the hard sphere dimension but this difference can be attributed to a lower local density of states associated with the $Mn_{12}ac$ as compared with the metallic Au surface.
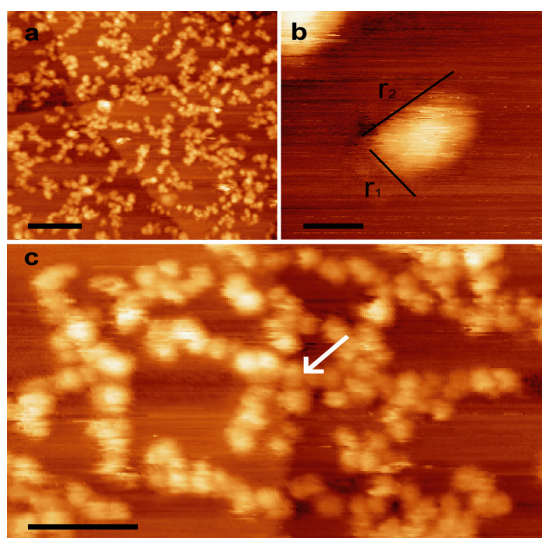
Figure 3.46. STM images of $Mn_{12}ac$ on Au(111). (a) Large scale STM image of the Au(111) surface after the UHV-ESD of ~0.35 mL of $Mn_{12}ac$ (V_{sample} = +1.80 V, I_{tunnel} = 0.03 nA). Filamentary structures are observed to run over the surface and are contiguous at step edges. Scale bar 20nm. (b) Close-up STM image of an isolated molecule (V_{sample} = +2.00 V, I_{tunnel} = 0.03 nA). The molecule displays an elliptical cross-section ($r_2 > r_1$). Scale bar 2nm. (c) STM image showing the internal structure of a molecular aggregate comprised of individual $Mn_{12}ac$ molecules (V_{sample} = +2.00 V, I_{tunnel} = 0.05 nA). Arrow indicates the position of the structure relative to a step edge. Scale bar 10nm.[106]

A striking feature of the molecular assemblies observed is the tendency of the $Mn_{12}ac$ molecules to self-assemble into meandering filamentary structures as depicted in Figure 3.46c. These structures are observed to run over step edges, giving rise to the large scale surface structure seen in Figure 3.46a. The formation of these structures is not associated with, and does not follow, the underlying herringbone reconstruction[105] of the Au(111) surface.
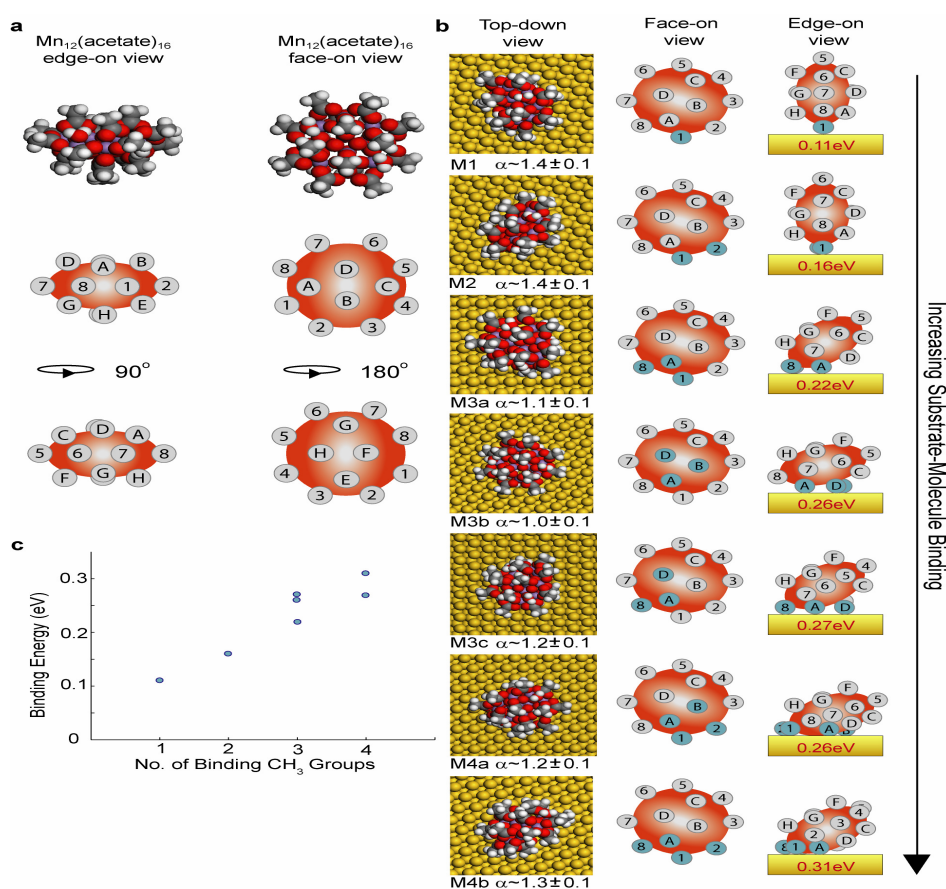
Figure 3.47. Calculated configuration of $Mn_{12}ac$ on Au(111). (a) CPK hard-sphere model of $Mn_{12}ac$ and schematic of the molecule with the CH_3 groups (grey circles) of the ligands labelled 1-8 and A-H with the $Mn_{12}O_{12}$ core represented as a red ellipsoid. (b) Top-down view of the states determined to be energy minima of the system by the MD quench simulation. The aspect ratio of each state α is shown in each case. The middle column is a schematic of a face-on view, with the CH_3 groups in contact with the Au surface highlighted as blue circles. The right hand column shows an edge-on view rotated by 90° compared to that of side 1, with the CH_3 groups in contact with the Au surface highlighted as blue circles. The states are shown in order of increasing bonding energy, M1 to M4b. (c) Binding energy of the $Mn_{12}ac$ to the Au surface as a function of the number of CH_3 groups in contact with the surface.[106]

The STM images raise questions concerning the orientation of $Mn_{12}ac$ molecules on the surface and the mechanism driving the self-assembly of these complex aggregates. Semi-empirical molecular dynamics (MD) simulations, performed by Dr. Alex Saywell, have been used to obtain information about the energetic states that an individual molecule deposited on to the Au(111) substrate may occupy. There are 16 CH_3 groups in total, eight of which lie around the circumference of the ellipsoid (labelled 1-8 in Figure 3.47), and four on both the top and bottom of the molecule (labelled A-D and E-H respectively). Molecular dynamics quench simulations were performed upon a single $Mn_{12}ac$ molecule on the Au(111) substrate.[106] The quench simulation allows geometry optimisation calculations to be performed using a variety of starting geometries determined by molecular dynamics. From the geometry optimised structures it is possible to identify several distinct local energy minima, each of which may be defined by the orientation of the CH_3 groups relative to the surface. The left hand column in Figure 3.47b shows a top-down view of the geometry optimised energy minima with the values for their aspect ratios. The middle column shows schematic representations of the molecule in which the CH_3 groups in contact with the Au(111) surface are highlighted for each orientation. The edge-on view in the right hand column describes the relative orientation of the molecules to the surface with the CH_3 groups in contact with the surface being highlighted in blue. States **M1** and **M2** (identified in Figure 3.47) correspond to energy minima where the molecule is positioned perpendicular to the gold surface, while in state **M3b** the molecule lies almost flat on the surface. For the lowest energy state (state **M4b**), the molecule is tilted so that four CH_3 groups are in contact with the surface.

The energies of the states have been plotted as a function of the number of CH_3 groups in contact with the surface (Figure 3.47c). The graph shows a linear trend which demonstrates that the binding energy of the molecule to the surface, and hence the molecular orientation, is determined by the number of CH_3 groups in contact with the Au(111) surface. State **M4b** has the greatest binding energy (0.31±0.02eV), and the geometry of this state gives a top-down aspect ratio of 1.3±0.1 which is in agreement with the value obtained from the STM images.
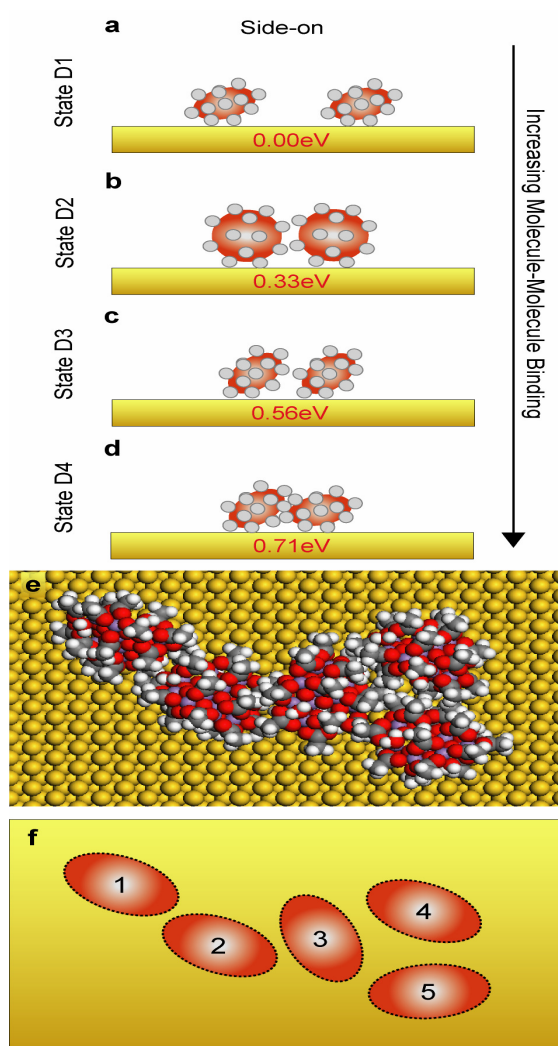
Figure 3.48. Calculated configurations of Mn₁₂ac pairs. (a)-(d) Schematics showing the energy minima of the molecule-molecule interaction between two molecules. (e) Final structure from a MD simulation of five Mn₁₂ac molecules on an Au(111) surface showing the formation of a meandering chain-like structure. (f) Schematic showing the positions of the five Mn₁₂ac molecules at the end of the MD simulation.[106]

The simulations also provide insight into the formation of the complex aggregates of $Mn_{12}ac$ molecules on the Au(111) surface. A quench simulation has been performed to determine the energy minima for a system containing two $Mn_{12}ac$ molecules absorbed on Au(111). The geometry of the four local energy minima states for two molecules is depicted in Figure 3.48a-d. For each state, the binding energy between the two molecules has been calculated. State **D1** defines a non-bonding configuration with no contact between the molecules while state **D2** shows an edge-to-edge configuration. States **D3** and **D4** show face-to-face configurations where the surface area between the two interacting molecules is maximised (the substrate interaction which is approximately equal for all pair configurations was included in the calculations but subtracted from the quoted values which thus correspond to intermolecular interactions). Importantly, the binding energy of state **D4** is considerably greater than that of state **D3** which results from the interdigitation of the methyl groups.

The determination of these states allows us to identify the anisotropy in the binding energy between pairs of molecules which manifests itself in the formation of the filamentary structures. Interestingly the two molecules in the most strongly bound pair arrangement (**D4**) adopt inequivalent surface configurations with, for example a difference in tilt angle of $\sim15^{o}$ as illustrated schematically in Figure 3.48. Consequently, a given molecule cannot maximise its pair-wise intermolecular interactions with more than one of its nearest neighbours. We may therefore expect a competition and interdependency between interactions when considering multiple nearest-neighbours. Overall, the molecular shape asymmetry is expected to lead to a complex intermolecular potential, which promotes an overall anisotropy through the face-to-face configuration, but has several local minima leading to large multiplicity

of quasi-degenerate configurations for an arrangement of many molecules. From this perspective, the $Mn_{12}ac$ morphology may be regarded as an analogue of networks recently described as glasses.[103,104]

Figure 3.48e shows the results of a MD simulation where the positions of five $Mn_{12}ac$ molecules on a Au(111) substrate have evolved over time. The resultant structure is a meandering quasi-1D arrangement of molecules similar to those observed in the STM images. Figure 3.48f shows a schematic of the final configuration with the molecules labelled 1 and 2 clearly adopting the state **D2** type of bonding configuration, while molecules 3, 4, and 5 adopt conformations similar to states **D3** and **D4**. It is important to note that the magnetic properties of $Mn_{12}ac$ are unlikely to be the driving force behind the formation of the observed structures. Hence, the MD simulations do not include any information about the magnetic interactions and the blocking temperature of $Mn_{12}ac$.
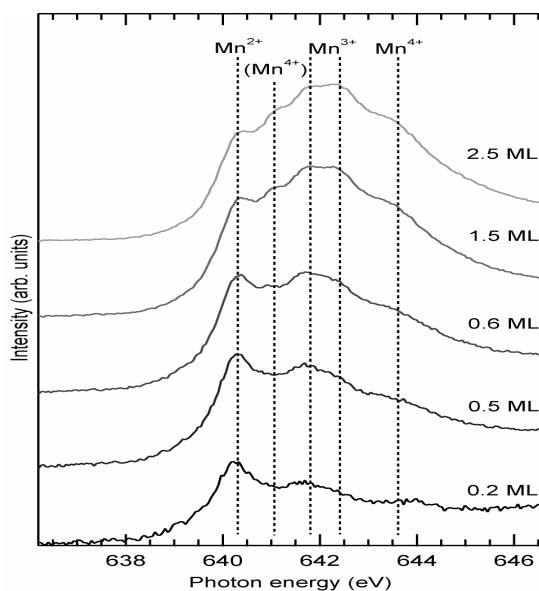
Figure 3.49. NEXAFS spectra measured at the Mn $2p$ adsorption edge (Mn L–edge) for a range of coverages comprised between 0.2 mL-2.5 mL. The photon energy was calibrated by measuring the energy separation of the Au $4f$ core-level photoemission peaks excited by 1st and 2nd order X-rays. The positions of the peaks corresponding to the presence of Mn^{2+}, Mn^{3+} and Mn^{4+} are labelled.[106]

The stability of $Mn_{12}ac$ during the deposition process was confirmed by near edge X-ray absorption fine structure (NEXAFS) measurements acquired at beamline D1011 of the MAX-Lab synchrotron radiation facility.[106] Figure 3.49 shows NEXAFS spectra taken at the $Mn2p$ adsorption edge for coverages between 0.2mL and 2.5mL which enable to identify the oxidation state of the manganese ions in the core of the molecule.

For multi-layer coverages the NEXAFS spectra are consistent with a mixture of Mn^{3+} and Mn^{4+} ions similar to that previously observed[53] for undamaged $Mn_{12}ac$ molecules. However for sub-monolayer coverages (0.2, 0.5, and 0.6mL), the spectra observed are consistent with a sample consisting predominantly of Mn ions in the +2 oxidation state. This analysis is based on a comparison with NEXAFS data acquired for a reference sample of $MnO^{53,107}$ which contains only Mn^{2+} ions and is characterised by a large peak in the NEXAFS spectra at ~640eV (labelled as Mn^{2+} in Figure 3.49).[53] It can therefore be concluded that the majority of Mn ions present are in a +2 oxidation state for $Mn_{12}ac$ deposited by UHV-ESD with sub-monolayer coverages. Similar to previous studies,[108] the growth of a peak corresponding to Mn^{2+} ions was observed over several hours for all coverages. This time dependent feature is however attributed to beam damage and is completely different to the peak observed previously corresponding to Mn^{2+} ions for sub-monolayer coverage. It is important to stress that this peak is not due to beam damage since all spectra shown have been acquired immediately after the initial exposure to the beam, before beam damage occurs. Indeed the features labelled Mn^{3+} (~642.0eV) and Mn^{4+} (643.5eV) in Figure 3.49 grow drastically as the coverage increases, confirming that the reduction to Mn^{+2} ions is a surface-mediated process. The mechanism for reduction may be due to direct charge transfer from the surface or arise from internal changes of the bonding within

the $Mn_{12}O_{12}$ core, possibly due to surface-induced modification or even loss of the attached H_2O or acetate ligands. A simple charge transfer from the surface would likely be associated with strong surface-core bonding which is in contradiction with the observed diffusivity of the $Mn_{12}ac$ molecules. The second hypothesis is therefore more likely. Modification of the peripheral ligation shell would naturally lead to corrections to our simple numerical model. Yet, the overall hypothesis that anisotropic interactions result from shape asymmetry are expected to remain valid. Overall, the expected oxidation states for an intact molecule are observed for multilayer coverage, confirming that the chemical properties of $Mn_{12}ac$ are unaffected by the UHV-ESD process.

The adsorbed $Mn_{12}ac$ may be induced to form structures with different order when deposited on a surface on which a hydrogen-bonded nanoporous network has been prepared. It has been previously shown by the Champness and Beton groups that nanoporous supramolecular templates can be formed on the Au(111) surface by the sequential deposition of PTCDI and melamine.[96] The pores within such a network have been shown to act as nanoscale traps for diffusing molecules[109] including, for low coverage, molecular species deposited by UHV-ESD. Figure 3.50a–c shows the structure of melamine, PTCDI and the hexagonal network respectively. The comparison of the hexagonal pore dimensions (width ~2.5nm) and those of the $Mn_{12}ac$ molecule leads us to expect that each pore would have the capacity to trap a single molecule. Figure 3.50d shows a Au(111) substrate which has been pre-patterned with a melamine/PTCDI hexagonal network and been exposed to a deposition of 0.05 monolayers $Mn_{12}ac$ using UHV-ESD. The positions of $Mn_{12}ac$ molecules held within a pore of this host/guest architecture are highlighted, and it can be seen that the resultant structure demonstrates a trapping of the molecules within the

pores. This shows that hydrogen-bonded supramolecular networks have the potential to trap $Mn_{12}ac$ deposited by UHV-ESD and locally inhibit the formation of filaments, such as those discussed above, or other molecular aggregates.

Figures 3.50e and 3.50f show close-up STM images of the hexagonal network containing two trapped $Mn_{12}ac$ molecules with the overlay in Figure 3.50f highlighting the positions of the network pores. A line profile (whose path is depicted in Figure 3.50f) shown in Figure 3.50g may be used to determine the periodicity of the hexagonal network and the position of the trapped $Mn_{12}ac$.
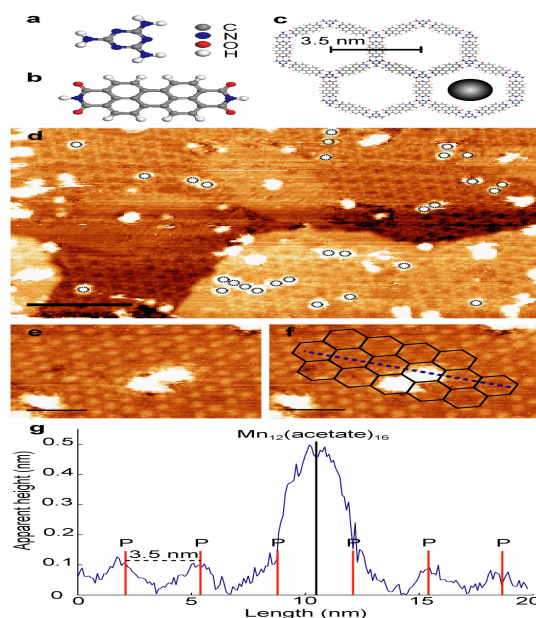
Figure 3.50. Chemical structures of (a) Melamine and (b) PTCDI (c) Structure of the self-assembled hexagonal network formed by the hydrogen bonding interactions between Melamine and PTCDI. The grey circle represents the size of a $Mn_{12}ac$ relative to the dimensions of the network. From geometric considerations one $Mn_{12}ac$ may be trapped within each pore. (d) STM image of the Au(111) surface pre-patterned with the melamine/PTCDI network prior to the UHV-ESD of $Mn_{12}ac$ (V_{sample} = +1.80 V, I_{tunnel} = 0.03 nA). The dashed black circles highlight $Mn_{12}ac$ trapped within a network pore. Scale bar 20nm. (e) Close-up STM image showing two $Mn_{12}ac$ molecules trapped within neighbouring network pores (V_{sample} = +1.80 V, I_{tunnel} = 0.03 nA). Scale bar 5nm. (f) STM image, from (e), with an overlay highlighting the position of the hexagonal network. Scale bar 5nm. (g) Line profile taken over a region of network containing one trapped $Mn_{12}ac$ molecule. The path of the line profile is shown in (f) and the positions of the PTCDI molecules are labelled P. The location of the trapped $Mn_{12}ac$ in the centre of the pore is marked.[106]

Interestingly there is an indication in this image that the occupancy of neighbouring host sites is slightly correlated. A similar effect for the capture of C_{60} dimers was reported previously by Staniec et al.[110] and attributed to a kinetic effect although an energetic origin is also possible for Mn_{12}ac.

In summary, this work demonstrates that molecules such as Mn_{12}ac can form complex aggregates when adsorbed at sub-monolayer coverages on a Au(111) surface. The growth of filamentary aggregates is due to an anisotropic intermolecular interaction arising directly from the asymmetric arrangement of the acetate ligands around the Mn_{12} core rather than from specific chemical interactions. The interlocking of these groups may be considered as a three dimensional analogue of the alkyl chain interdigitation as observed for planar molecules.[111] The growth of vapour deposited large molecules lacking a high degree of symmetry can give rise to highly complex structures which can be modelled using MD simulations.

It was also shown that the approach of supramolecular templating can influence the lateral organisation of the Mn_{12}ac molecules on surface. Indeed from the previous discussions regarding the molecular dimensions, intermolecular interactions leading to increased intermolecular separations together with the magnetic properties considerations of the various Mn_{12} derivatives synthesised over the course of this project, it is believed that these functionalised complexes would be extremely well suited for future UHV-ESD investigations on the Au(111) substrate as well as the PTCDI-melamine nanostructured template.

3.3 Conclusion

The work described throughout this third chapter is aimed at the synthesis of functionalised Mn_{12} SMMs for two-dimensional ordered assemblies on surfaces for potential high technology applications such as high-density data storage and quantum computing. Twelve functionalised Mn_{12} clusters possessing attractive peripheral ligation, seven of which are novel complexes, have been synthesised and successfully characterised by Infrared spectroscopy, MALDI-TOF mass spectrometry and elemental analysis. Each complex contains peripheral organic ligands which impart desirable properties with respect to solubility, molecular dimensions, intermolecular interactions and surface deposition.

It has been discovered that Mn_{12} clusters containing only rigid aromatic functionalities are found to crystallise easily whilst those containing long aliphatic alkyl chains (typically 4 carbon atoms or longer) have the likelihood of adopting disordered arrangements which strongly disturbs crystallisation. The incorporation of tert-butanoate but not adamantanecarboxylate ligands indicates the limit of steric bulk which can be accommodated around the Mn_{12} core.

The crystal structures of five of the complexes synthesised were solved and compared to evaluate the influence of the organic peripheral ligands on several factors such as the bond lengths of the $Mn_{12}O_{12}$ fragment, the molecular dimensions of the clusters, the intermolecular separation and the intermolecular interactions. It has been demonstrated, as anticipated, that the core structure remains unchanged upon ligand substitution which suggests that the magnetic properties of the clusters are conserved and should be very similar to one another.

Furthermore, it has been shown that increasing the size of the replacing carboxylate ligand increases the molecular dimensions of the complex which in turn enables to tailor the size of the molecule but also the intermolecular separation between them. Incorporating specific ligands can also give rise to intermolecular interactions such as π-π stacking and CH-π interactions capable of directing the arrangement of the clusters into preferential directions which in turn could prove to be an interesting feature for surface deposition purposes.

The magnetic properties were measured for complexes (2) and (4) in AC mode. Overall, complex (2) and complex (4) exhibit the expected magnetic properties commonly reported for SMMs belonging to the Mn_{12} family. The values found for the effective energy barriers, the blocking temperatures and the exponential pre-factors do not show unusual features. However, some discrepancies are still observed among the different clusters depending on the nature of the carboxylate ligands introduced around the magnetic core. Some recent studies have shown that these differences can be related to several factors such as the chemical and electronic structure of the ligands and the intramolecular exchange interactions between the metal centers within the complexes.[64] Dependence of the magnetic properties on the synthetic route employed, the solvents used, the type of sample studied (amorphous, crystalline, mixture of JT isomers, etc.) have also been established.[64-66]

The surface deposition work demonstrates that molecules such as $Mn_{12}ac$ can form complex aggregates when adsorbed at sub-monolayer coverages on a Au(111) surface. The growth of filamentary aggregates is due to an anisotropic intermolecular interaction arising directly from the asymmetric arrangement of the acetate ligands

around the Mn_{12} core rather than from specific chemical interactions. It was also shown that the approach of supramolecular templating can influence the lateral organisation of the Mn_{12}ac molecules on surface. The previous considerations regarding the molecular dimensions, intermolecular interactions leading to increased intermolecular separations together with the magnetic properties of the various Mn_{12} derivatives synthesised over the course of this project seem to indicate that these functionalised complexes would be extremely well suited for future UHV-ESD investigations on the Au(111) substrate as well as the PTCDI-melamine nanostructured template. It is anticipated that the combination of UHV-ESD and surface adsorption will find wide relevance for the controlled formation of nanostructured surfaces based not only Mn_{12}ac as considered here, but with many other large molecules.

3.4 Experimental

All reagents and solvents were purchased from Sigma Aldrich, Alfa Aesar, Fischer Scientific UK, and used without any further purification and all manipulations were performed under aerobic conditions unless otherwise stated. Elemental microanalyses were carried out by Stephen Boyer at the Microanalysis Service, London Metropolitan University, UK. Infrared spectra were measured as KBr discs using a Bruker Tensor 27 FT-IR spectrometer over the range 400-4000cm^{-1}. MALDI-TOF mass spectra were obtained using a Bruker Ultraflex MALDI TOF mass spectrometer. MALDI-TOF-MS samples were prepared by dissolution of the compounds in CH_2Cl_2 (10 μL) and then mixing this solution with a solution of the matrix DCTB (Trans-2-[3-(4-tert-butylphenyl)-2-methyl-2-propenylidone]-malononitrile) in MeCN (20 μL). A sample of the resulting solution (5 μL) was loaded onto a plate, the solvent was removed in air, and the sample transferred to the mass spectrometer for analysis. Electrospray ionisation mass spectra were collected using a microTOF mass spectrometer. ^{1}H NMR spectra were measured using a Bruker 400 MHz spectrometer.

Surface deposition studies

The experiments were carried out by the Beton group from the School of Physics and Astronomy at the University of Nottingham. Deposition of $Mn_{12}(acetate)_{16}$ and subsequent characterisation by STM were carried out using a UHV vacuum system with a base pressure of ~$5x10^{-11}$ Torr; separate chambers were used for deposition and characterisation. A 4 mm × 8 mm gold on mica substrate (thickness of 1500 Å; supplied commercially by Agilent) was loaded into the UHV system. The sample was cleaned by Ar ion sputtering (6 × 10^{-6} Torr, 0.7 keV, ~2 μA) and subsequent

annealing (~500 °C). Images of the surface were acquired using a scanning tunnelling microscope, housed within the UHV system, using electrochemically etched tungsten tips, and operating in constant current mode at room temperature. Images of the surface taken after the sputter-anneal cycle show the characteristic (22 × √3) herringbone reconstruction of the Au(111) surface.[103]

Using UHV-ESD $Mn_{12}(acetate)_{16}$, was transferred from a solution of methanol onto the Au(111) substrate. The UHV-ESD experimental set-up is described in detail elsewhere.[96,97] To summarise, a solution containing the molecules to be deposited is passed through a stainless steel emitter held at ~2 kV at a typical flow rate of 1 µL/min. This leads to the formation of a spray at atmospheric pressure outside the UHV system. The spray enters the UHV system via an aperture, passes through a series of differentially pumped chambers, and impinges upon the sample situated within a preparation chamber having a base pressure of 5×10^{-11} Torr. The pressure in the sample preparation chamber while open to the differential pumping system, but in the absence of spray, is ~2×10^{-8} Torr. During electrospray deposition, the pressure rises to ~4×10^{-8} Torr, with the additional pressure being due solely to the presence of the solvent molecules within the preparation chamber (ascertained by residual gas analysis).

Magnetic measurements

All magnetic data were obtained using a Quantum Design MPMS XL5 SQUID magnetometer. Pellet samples were carefully weighted and wrapped into Teflon with negligible diamagnetic contribution. AC measurements were performed in oscillating field of 3.5 Oe at frequencies 99.9, 498.7 and 999.9 Hz from 1.8 to 10 K for complexes (**2**) and (**4**). Measurements were repeated twice to ensure the results were

reproducible. Pascal's constants were used to estimate the diamagnetic corrections for each complex, which were substracted from the experimental susceptibilities to give the molar paramagnetic susceptibilities (χ_M). Direct current (DC) and alternating current (AC) magnetic data were recorded for **(12)**.

Crystallography

All single crystal X-ray experiments were performed on a Bruker SMART 1000 CCD or a Bruker SMART APEX CCD equipped with an Oxford Cryosystems open flow cryostat, [graphite monochromated Mo-Kα radiation (λ=0.71073 Å), ω scans]. Absorption corrections, if necessary, were applied by a semi-empirical approach. All of the single crystal structures were solved either by direct methods using SHELXS-97[112] or superflip,[113] all non-H atoms were located using subsequent difference-Fourier methods.[114] Unless otherwise stated, hydrogen atoms were placed in calculated positions and thereafter allowed to ride on their parent atoms. Additional restraints were placed on thermal and geometric parameters as required and appropriate. All graphical representations were generated using Mercury 1.4.1 (copyright CCDC 2001-2005).

For complex **(2)**, disorder was observed in the position of the phenyl ring of benzoate residue A. The occupancies of the two components were refined using free variables to have a sum of one with a value of 0.68(1) for the major component. The benzoic acid moiety 'O/X' which coordinates to Mn8 is disordered over two orientations. The occupancies of the two components were refined using a free variable giving a value of approximately 0.5 before being fixed exactly as such. The OH hydrogen atoms of neither of the components were observed in the electron difference map and were

omitted from the model. Charge balancing of the fragment indicated that this moiety is benzoic acid and not benzoate. Water moiety O102 with occupancy 0.5 is modelled as filling the coordination site at Mn8 when the benzoic acid carboxylic group is pointing away from the cluster. Water O102 and carboxylic acid oxygen O12O were constrained to have identical anisotropic displacement parameters (EADP). The hydrogen atoms of both water moieties were not observed in the electron density map and omitted from the model. The distance between C11X and C21X was constrained to have a value of 1.49Å (DFIX). Further components of disorder were indicated by the electron difference map but were weak and could not be modelled. A squeeze function was applied to the data to remove scattering contributions from two diffuse dichloromethane solvent molecules per asymmetric unit.

For complex **(3).3CH$_2$Cl$_2$**, the anisotropic displacement parameters of O103 (oxygen atom of one water ligand) have been restrained to behave isotropically (ISOR). The hydrogen atoms of the four water moieties were not observed in the difference map and were not included in the refinement. A squeeze function was applied to the data to remove scattering contributions from several disordered solvent residues. The largest void in the squeezed region contained 808 electrons, equating to approximately twenty additional dichloromethane molecules per unit cell.

For compound **(4)**, the crystal exhibited pseudo-merohedral twinning as described by twin law (100/0-10/-20-1). The phenyl-CH$_2$ and CH$_2$-CH$_3$ bond lengths of the ethyl groups were all constrained to have distances of 1.45 and 1.52 A respectively. The phenyl-CH$_3$ distances were all restrained to be the same. Due to weak data all the

methyl groups were modelled in a staggered conformation and the hydrogen atoms of the methanol molecules bound to the cluster could not be located.

For compound **(7).7CH$_2$Cl$_2$.4MeOH.H$_2$O**, the anisotropic displacement parameters of O1SS and C2SS (oxygen and carbon atoms of one methanol solvent molecule) have been restrained to behave isotropically (ISOR). The hydrogen atoms of the four methanol solvent molecules as well as those of the water solvent molecule were not observed in the difference map and were not included in the refinement. A squeeze function was applied to the data to remove scattering contributions from several disordered solvent residues. The largest void in the squeezed region contained 162 electrons, equating to approximately four additional dichloromethane molecules per unit cell.

For complex **(9).C$_6$H$_5$C$_6$H$_4$COOH**, disorder was observed in the conformation of the phenyl rings of one of the ligand (ligand N). The occupancies of the two orientations were refined using a free variable with the major component having an occupancy of 0.57(1). Disorder was also observed in the position of ligand L with the carboxylate group switching between bridging Mn6 and Mn9 or Mn6 and Mn9 (x+y, y-x+1,-z+2). The occupancies of the two positions were refined using a free variable before being fixed at the given value of 0.5. During the 50% percent of the time when the coordination sites on the two Mn9 atoms are not occupied by a carboxylate oxygen, the sites are occupied by water ligands O101 and O102.

An uncoordinated disordered biphenylcarboxylic acid molecule is centred on a special position such that the asymmetric unit contains one full occupancy phenyl ring and a half occupancy carboxylic acid group. The carboxylic acid group is placed in disorder

component part 2 so as not to clash with ligand L located in part 1. The hydrogen atoms for the water ligands and uncoordinated biphenyl carboxylic acid molecule were not observed in the electron density map and were not included in the refinement.

For complex (**12).2CH₃OH**, two partially occupied and badly disordered methanol molecules were removed using the PLATON SQUEEZE algorithm. This corresponds to two methanol molecules per complex, and is consistent with the electron count for each void volume supplied by the squeeze algorithm.

Synthesis

Synthesis of $[Mn_{12}O_{12}(CH_3CO_2)_{16}(H_2O)_4].2CH_3CO_2H.4H_2O$ (1)

In a typical procedure,[10] $Mn(CH_3CO_2)_2.4H_2O$ (4 g, 16.33mmol) was added to a 60% acetic acid solution (40mL) and the mixture was stirred until dissolution. Finely ground $KMnO_4$ (1 g, 6.33mmol) was then added in small aliquots over 2 min. The resulting mixture was stirred for approximately 1 min until all potassium permanganate was dissolved. The final solution was left to stand undisturbed at room temperature for 3 d. Black crystals obtained were filtered, copiously washed with acetone and dimethylformamide and dried under vacuum to yield $[Mn_{12}O_{12}(CH_3CO_2)_{16}(H_2O)_4].2CH_3CO_2H.4H_2O$ (2.32 g, 1.24mmol, 67%). FT-IR (KBr, cm^{-1}): 3426s (br), 2961m, 2926m, 2855m, 1418m, 1384s, 1095s, 543m. MALDI-TOF-MS (RN-m/z): 1795.6 $[Mn_{12}O_{12}(L)_{16}]^-$ L=CH_3CO_2; 1736.6 $[Mn_{12}O_{12}(L)_{15}]^-$; 1677.5 $[Mn_{12}O_{12}(L)_{14}]^-$; 1618.5 $[Mn_{12}O_{12}(L)_{13}]^-$. MALDI-TOF-MS (RP-m/z): 1736.6 $[Mn_{12}O_{12}(L)_{15}]^+$; 1677.5 $[Mn_{12}O_{12}(L)_{14}]^+$; 1618.5 $[Mn_{12}O_{12}(L)_{13}]^+$;

1560.6 $[Mn_{12}O_{12}(L)_{12}]^+$; 1501.6 $[Mn_{12}O_{12}(L)_{11}]^+$; 1442.5 $[Mn_{12}O_{12}(L)_{10}]^+$; 1383.6 $[Mn_{12}O_{12}(L)_9]^+$. Elemental Analysis (%) calculated for $C_{36}H_{72}Mn_{12}O_{56}$: C, 21.0; H, 3.5; found: C, 21.0; H, 3.5. The complex crystallises in the tetragonal space group *I*-4 with a= b= 17.192 Å, c= 12.314 Å, V=3639 Å^3.

Synthesis of $[Mn_{12}O_{12}(C_6H_5CO_2)_{16}(H_2O)_3(C_6H_5CO_2H)].C_6H_5CO_2H$ (2)

To a slurry of $Mn_{12}O_{12}(CH_3CO_2)_{16}(H_2O)_4$ (500 mg, 0.27mmol) in CH_2Cl_2 (70mL) was added benzoic acid (1.05 g, 8.64mmol). The mixture was stirred in a closed flask at room temperature overnight. The resulting solution was filtered and evaporated to dryness. To the residue was added toluene (60mL) and the solution was stirred for 15 min and evaporated to dryness to remove the released acetic acid as the toluene azeotrope. The addition and removal of toluene were repeated three times. To ensure full ligand substitution, the resulting dark brown powder was redissolved in CH_2Cl_2 (70mL) and further reacted with benzoic acid (1.05 g, 8.64mmol) at room temperature overnight. The resulting solution was filtered and evaporated to dryness and the residue was once again treated with three addition and removal cycles of toluene (60mL). The resultant dark brown powder was redissolved in CH_2Cl_2 before an equal volume of n-hexane was carefully layered on top and then left to stand undisturbed for several days at 12°C. Resulting dark brown crystals were then filtered, copiously washed with hexane and dried under vacuum (352 mg, 0.1mmol, 45%). Suitable crystals for XRD were obtained by carefully layering an equal volume of n-hexane on top of a saturated solution of the complex in CH_2Cl_2. FT-IR (KBr, cm^{-1}): 3425s (br), 3068w, 2962w, 2926w, 1702m, 1600m, 1558m, 1449m, 1418s, 1385m, 1260m, 1096s, 1072m, 1026m, 799m, 757w, 719s. MALDI-TOF-MS (RN-m/z): 2788.9 $[Mn_{12}O_{12}(L)_{16}]^-$ L=$C_6H_5CO_2$; 2667.7 $[Mn_{12}O_{12}(L)_{15}]^-$; 2546.1 $[Mn_{12}O_{12}(L)_{14}]^-$;

2425.6[$Mn_{12}O_{12}(L)_{13}$]$^-$. MALDI-TOF-MS (RP-m/z): 2668.0 [$Mn_{12}O_{12}(L)_{15}$]$^+$, 2546.8 [$Mn_{12}O_{12}(L)_{14}$]$^+$, 2425.6 [$Mn_{12}O_{12}(L)_{13}$]$^+$, 2305.0 [$Mn_{12}O_{12}(L)_{12}$]$^+$. Elemental Analysis (%) calculated for $Mn_{12}O_{12}(C_6H_5CO_2)_{16}(H_2O)_4$: C, 47.0; H, 3.1; found: C, 46.9; H, 3.2. The complex crystallises in the orthorhombic space group *Fdd*2 with a=31.120(1) Å, b=53.078(2) Å, c=17.4196(6) Å, V= 28774.0 (18) Å^3.

Synthesis of [$Mn_{12}O_{12}(CH_3$-p-$C_6H_4CO_2)_{16}(H_2O)_4$].$3CH_2Cl_2$ (3)

To a slurry of $Mn_{12}O_{12}(CH_3CO_2)_{16}(H_2O)_4$ (500 mg, 0.27mmol) in CH_2Cl_2 (70mL) was added p-toluic acid (1.16 g, 8.5mmol). The mixture was stirred in a closed flask at room temperature overnight. The resulting solution was filtered and evaporated to dryness. To the residue was added toluene (60mL) and the solution was stirred for 15 min and evaporated to dryness. The addition and removal of toluene were repeated three times. The overall reaction procedure and subsequent treatment were repeated once more. The resultant dark brown powder was redissolved in CH_2Cl_2, layered with an equal volume of n-hexane and left to stand undisturbed for several days at 6°C. Resulting dark brown crystals were then filtered, copiously washed with n-hexane and dried under vacuum (300 mg, 0.01mmol, 39%). FT-IR (KBr pellet, cm^{-1}): 2960w, 2922w, 1691m, 1589m, 1555m, 1509s, 1455vs, 1412s, 1213s, 1022m, 847m, 784vs, 712s, 626vs. MALDI-TOF-MS (RN-m/z): 3029 [$Mn_{12}O_{12}(L)_{16}$]$^-$ L=$CH_3C_6H_4CO_2$; 2893 [$Mn_{12}O_{12}(L)_{15}$]$^-$; 2758.5 [$Mn_{12}O_{12}(L)_{13}$]$^-$; 2621 [$Mn_{12}O_{12}(L)_{12}$]$^-$. Elemental Analysis (%) calculated for $Mn_{12}O_{12}(CH_3C_6H_4CO_2)_{16}(H_2O)_4$: C, 49.8; H, 3.9; found: C, 49.7; H, 3.7. Suitable crystals for XRD were obtained by layering carefully an equal volume of n-hexane on top of a saturated solution of the compound in CH_2Cl_2. The complex crystallizes in the triclinic space group *P*-1 with a= 18.305(5) Å, b=

19.413(5) Å, c= 24.574(6) Å, α= 74.1970(4), β=87.865(4), γ=85.738(4), V= 8378(4) Å^3.

Synthesis of [Mn$_{12}$O$_{12}$(CH$_3$CH$_2$C$_6$H$_4$CO$_2$)$_{16}$(CH$_3$OH)$_4$] (4)

To a slurry of Mn$_{12}$O$_{12}$(CH$_3$CO$_2$)$_{16}$(H$_2$O)$_4$ (500 mg, 0.27mmol) in CH$_2$Cl$_2$ (70mL) was added 4-ethylbenzoic acid (1.28 g, 8.57mmol). The mixture was stirred in a closed flask at room temperature overnight. The resulting solution was filtered and evaporated to dryness. To the residue was added toluene (60mL) and the solution was stirred for 15 min and evaporated to dryness. The addition and removal of toluene were repeated three times. The overall reaction procedure and subsequent treatment were repeated once more. The resultant dark brown powder was redissolved in CH$_2$Cl$_2$, layered with an equal volume of methanol and left to stand undisturbed for several days at 12°C. Resulting dark brown crystals were then filtered, copiously washed with methanol and dried under vacuum (460 mg, 0.14mmol, 51%). FT-IR (KBr, cm^{-1}): 3433s (br), 2960m, 2926m, 2876w, 1786w, 1714m, 1679m, 1433m, 1384s, 1351m, 1249m, 1153s (sh), 1084s, 799m, 739m, 554m, 462s. MALDI-TOF-MS (RN-m/z): 3238.9 [Mn$_{12}$O$_{12}$(L)$_{16}$]$^-$ L= CH$_3$CH$_2$C$_6$H$_4$CO$_2$, 3088.9 [Mn$_{12}$O$_{12}$(L)$_{15}$]$^-$, 2939.5 [Mn$_{12}$O$_{12}$(L)$_{14}$]$^-$, 2790.3 [Mn$_{12}$O$_{12}$(L)$_{13}$]$^-$. MALDI-TOF-MS (RP-m/z): 2939 [Mn$_{12}$O$_{12}$(L)$_{14}$]$^+$, 2791.6 [Mn$_{12}$O$_{12}$(L)$_{13}$]$^+$, 2642.8 [Mn$_{12}$O$_{12}$(L)$_{12}$]$^+$. Elemental Analysis (%) calculated for Mn$_{12}$O$_{12}$(CH$_3$CH$_2$C$_6$H$_4$CO$_2$)$_{16}$(MeOH)$_4$: C, 52.8 ; H, 4.8; found: C, 52.2; H, 4.6. Crystals suitable for XRD analysis were obtained by layering carefully an equal volume of methanol on top of a saturated solution of the compound in CH$_2$Cl$_2$. The complex crystallizes in the monoclinic space group *P2/c* with a= 20.184(6) Å b= 16.293(5) Å c= 30.918(7) Å, β=130.756(12), V= 7702 (4) Å^3.

Synthesis of [Mn$_{12}$O$_{12}$(CH$_3$CH$_2$CH$_2$-p-C$_6$H$_4$CO$_2$)$_{16}$(H$_2$O)$_4$] (5)

To a slurry of Mn$_{12}$O$_{12}$(CH$_3$CO$_2$)$_{16}$(H$_2$O)$_4$ (500 mg, 0.27mmol) in CH$_2$Cl$_2$ (70mL) was added 4-propylbenzoic acid (1.4 g, 8.57mmol). The mixture was stirred in a closed flask at room temperature overnight. The resulting solution was filtered and evaporated to dryness. To the residue was added toluene (60mL) and the solution was stirred for 15 min and evaporated to dryness. The addition and removal of toluene were repeated three times. The overall reaction procedure and subsequent treatment were repeated once more. The resultant dark brown powder was redissolved in CH$_2$Cl$_2$, layered with an equal volume of methanol and left to stand undisturbed for several days at 12°C. Resulting dark brown crystals obtained were then filtered, copiously washed with methanol and dried under vacuum (370 mg, 0.11mmol, 39%). Despite recurrent efforts, all the attempts of growing single crystals suitable for X-ray crystallography remained unsuccessful. FT-IR (KBr, cm^{-1}): 3425br, 3066w, 2959m, 2931m, 2871m, 1687m, 1610m, 1595m, 1553m, 1510m, 1420s, 1351m, 1093s, 797w, 769m, 473m. MALDI-TOF-MS (RN-m/z): 3463.1 [Mn$_{12}$O$_{12}$(L)$_{16}$]$^-$ L=CH$_3$CH$_2$CH$_2$-p-C$_6$H$_4$CO$_2$, 3300.1 [Mn$_{12}$O$_{12}$(L)$_{15}$]$^-$, 3138.4 [Mn$_{12}$O$_{12}$(L)$_{14}$]$^-$. MALDI-TOF-MS (RP-m/z): 3300.1 [Mn$_{12}$O$_{12}$(L)$_{15}$]$^+$, 3135.5 [Mn$_{12}$O$_{12}$(L)$_{14}$]$^+$. Elemental Analysis (%) calculated for Mn$_{12}$O$_{12}$(C$_6$H$_4$C$_3$H$_7$CO$_2$)$_{16}$(H$_2$O)$_4$: C, 54.4 ; H, 5.25; found: C, 54.45; H, 5.2.

Synthesis of [Mn$_{12}$O$_{12}$(CH$_3$CH$_2$CH$_2$CH$_2$–p-C$_6$H$_4$CO$_2$)$_{16}$(H$_2$O)$_4$] (6)

To a slurry of Mn$_{12}$O$_{12}$(CH$_3$CO$_2$)$_{16}$(H$_2$O)$_4$ (500 mg, 0.27mmol) in CH$_2$Cl$_2$ (70mL) was added 4-butylbenzoic acid (1.52 g, 8.57mmol). The mixture was stirred in a closed flask at room temperature overnight. The resulting solution was filtered and evaporated to dryness. To the residue was added toluene (60mL) and the solution was

stirred for 15 min and evaporated to dryness. The addition and removal of toluene were repeated three times. The overall reaction procedure and subsequent treatment were repeated once more. Numerous attempts at crystallisation were performed using layering techniques with various solvents and anti-solvents. Yet, all proved to be unsuccessful and consequently the following data correspond to the powder obtained (483 mg, 0.11mmol, 42%). FT-IR (KBr, cm^{-1}): 3441br, 3064w, 2957s, 2931s, 2859m, 2671w, 2556w, 2360w, 1690m, 1611m, 1587m, 1548m, 1509m, 1420s, 1384m, 1320m, 1294m, 1118m, 1020m, 947m, 855m, 763m, 703m, 624m, 549m. MALDI-TOF-MS (RN-m/z): 3686.5 [$Mn_{12}O_{12}(L)_{16}$]$^-$ L=$CH_3CH_2CH_2CH_2$–p-$C_6H_4CO_2$, 3509.1 [$Mn_{12}O_{12}(L)_{15}$]$^-$, 3331.6 [$Mn_{12}O_{12}(L)_{14}$]$^-$, 3154.6 [$Mn_{12}O_{12}(L)_{13}$]$^-$. MALDI-TOF-MS (RP-m/z): 3332.8 [$Mn_{12}O_{12}(L)_{14}$]$^+$, 3154.8 [$Mn_{12}O_{12}(L)_{13}$]$^+$.

Synthesis of [$Mn_{12}O_{12}((CH_3)_2C_6H_3CO_2)_{16}(CH_3OH)_4$]. 7$CH_2Cl_2$.4MeOH.$H_2O$ (7)

To a slurry of $Mn_{12}O_{12}(CH_3CO_2)_{16}(H_2O)_4$ (500 mg, 0.27mmol) in CH_2Cl_2 (70mL) was added 3,5-dimethylbenzoic acid (1.28 g, 8.6mmol). The mixture was stirred in a closed flask at room temperature overnight. The resulting solution was filtered and evaporated to dryness. To the residue was added toluene (60mL) and the solution was stirred for 15 min and evaporated to dryness. The addition and removal of toluene were repeated three times. The overall reaction procedure and subsequent treatment were repeated once more. The resultant dark brown powder was redissolved in CH_2Cl_2, layered with an equal volume of methanol and left to stand undisturbed for several days at 6°C. Resulting dark brown crystals were then filtered, copiously washed with methanol and dried under vacuum (348 mg, 0.1mmol, 40%). FT-IR (KBr pellet, cm^{-1}): 2918w, 1683vs, 1606s, 1528m, 1454m, 1412s, 1310vs, 1244vs, 1120m, 932s, 872m, 779m, 767s 726vs, 676vs, 613m. MALDI-TOF-MS (RN-m/z): 3238.4

$[Mn_{12}O_{12}(L)_{16}]^-$ L= $(CH_3)_2C_6H_3CO_2$; 3088.2 $[Mn_{12}O_{12}(L)_{15}]^-$; 2788 $[Mn_{12}O_{12}(L)_{14}]^-$.

Elemental Analysis (%) calculated for $Mn_{12}O_{12}((CH_3)_2C_6H_3CO_2)_{16}(CH_3OH)_4$: C, 52.8; H, 4.8; found: C, 52.4; H, 4.5. Suitable crystals for XRD were obtained by layering carefully an equal volume of methanol on top of a saturated solution of the compound in CH_2Cl_2. The complex crystallizes in the triclinic space group P-1 with a= 21.1503(10) Å, b= 22.2257(10) Å, c= 24.4386(11) Å, α= 89.7870(10), β=64.6330(10), γ=69.3710(10), V= 9566.5 (8) Å^3.

Synthesis of $[Mn_{12}O_{12}(C_{10}H_7CO_2)_{16}(H_2O)_4]$ (8)

The compound was synthesised as described previously[62] using slight modifications. 2-naphthoic acid (1.47 g, 8.57mmol) was added to a slurry of $Mn_{12}O_{12}(CH_3CO_2)_{16}(H_2O)_4$ (500 mg, 0.27mmol) in CH_2Cl_2 (70mL). The mixture was stirred in a closed flask at room temperature overnight. The resulting solution was filtered and evaporated to dryness. To the residue was added toluene (60mL) and the solution was stirred for 15 min and evaporated to dryness. The addition and removal of toluene were repeated three times. The overall reaction procedure and subsequent treatment with toluene were repeated once more. The resultant dark brown powder was redissolved in CH_2Cl_2, layered with an equal volume of n-hexane and left to stand undisturbed for several days at 12°C. Resulting dark brown crystals were then filtered, copiously washed with hexane and dried under vacuum (378 mg, 0.1mmol, 38%). The resulting crystals, issued from varied layering systems, were found to exhibit poor diffraction for X-ray diffraction analysis and thus no data was collected. FT-IR (KBr, cm^{-1}): 3442s (br), 2360m, 2341m, 1633m, 1602m, 1558m, 1384s, 1095s, 795m, 470m. MALDI-TOF-MS (RN-m/z): 3589.3 $[Mn_{12}O_{12}(L)_{16}]^-$ L=$C_{10}H_7CO_2$, 3417.7 $[Mn_{12}O_{12}(L)_{15}]^-$, 3246.5 $[Mn_{12}O_{12}(L)_{14}]^-$, 3071.3 $[Mn_{12}O_{12}(L)_{13}]$. Elemental Analysis

(%) calculated for $Mn_{12}O_{12}(C_{10}H_7CO_2)_{16}(H_2O)_4$: C, 57.7; H, 3.3; found: C, 57.9; H, 3.35.

Synthesis of $[Mn_{12}O_{12}(C_6H_5C_6H_4\text{-}p\text{-}CO_2)_{16}(H_2O)_4].C_6H_5C_6H_4COOH$ (9)

To a slurry of $Mn_{12}O_{12}(CH_3CO_2)_{16}(H_2O)_4$ (500 mg, 0.27mmol) in CH_2Cl_2 (70mL) was added 4-biphenylcarboxylic acid (0.85 g, 4.28mmol). The mixture was stirred in a closed flask at room temperature overnight. The resulting solution was filtered and evaporated to dryness. To the residue was added toluene (60mL) and the solution was stirred for 15 min and evaporated to dryness. The addition and removal of toluene were repeated three times. The overall reaction procedure and subsequent treatment were repeated once more. The resultant dark brown powder was redissolved in CH_2Cl_2, layered with an equal volume of n-hexane and left to stand undisturbed for several days at 6°C. Resulting dark brown crystals were then filtered, copiously washed with hexane and dried under vacuum (624 mg, 0.15mmol, 57%). FT-IR (KBr, cm^{-1}): 3443br, 3032w, 2362w, 1687m, 1609m, 1573m, 1541m, 1517m, 1449m, 1416s, 1181m, 1105m, 1008m, 861m, 791m, 751s, 697m, 546m, 528m. MALDI-TOF-MS (RN-m/z): 4005.4 $[Mn_{12}O_{12}(L)_{16}]^-$ $L=C_6H_5C_6H_4\text{-}p\text{-}CO_2$, 3808.2 $[Mn_{12}O_{12}(L)_{15}]^-$, 3611.6 $[Mn_{12}O_{12}(L)_{14}]^-$, 3414.3 $[Mn_{12}O_{12}(L)_{13}]^-$. Elemental Analysis (%) calculated for $Mn_{12}O_{12}(C_{12}H_9CO_2)_{16}(H_2O)_4$: C, 61.23 ; H, 3.76; found: C, 61.16 ; H, 3.65. Crystals suitable for XRD analysis were obtained by layering carefully an equal volume of hexane on top of a saturated solution of the compound in CH_2Cl_2. The complex crystallizes in the tetragonal space group *I*-42*d* with a=b= 20.593(3) Å, c= 64.577(16) Å, V= 27386 (9) $Å^3$.

Synthesis of [Mn$_{12}$O$_{12}$(CH$_3$(CH$_2$)$_7$CO$_2$)$_{16}$(H$_2$O)$_4$] (10)

To a slurry of Mn$_{12}$O$_{12}$(CH$_3$CO$_2$)$_{16}$(H$_2$O)$_4$ (500 mg, 0.27mmol) in CH$_2$Cl$_2$ (70mL) was added nonanoic acid (0.75mL, 4.28mmol). The mixture was stirred in a closed flask at room temperature overnight. The resulting solution was filtered and evaporation of the solvent yielded a brown oil. To the residue was added toluene (60mL) and the solution was stirred for 15 min and evaporated to give a brown oil. The addition and removal of toluene were repeated three times. The overall reaction procedure and subsequent treatment were repeated once more. No crystal could be obtained despite many layering attempts using diverse solvents. Therefore in an attempt to purify the resulting oil, the compound was dissolved in CH$_2$Cl$_2$ and the addition of n-hexane enabled the product to precipitate. The following data correspond to the dried precipitate obtained. FT-IR (KBr, cm^{-1}): 3443br, 2957s, 2925s, 2855s, 2359w, 1711w, 1581s (br), 1417s, 1385s, 1110mm, 606m, 467m. MALDI-TOF-MS (RN-m/z): 3367.0 [Mn$_{12}$O$_{12}$(L)$_{16}$]$^-$ L=C$_8$H$_{17}$CO$_2$, 3209.4 [Mn$_{12}$O$_{12}$(L)$_{15}$]$^-$, 3052.9 [Mn$_{12}$O$_{12}$(L)$_{14}$]$^-$. Elemental Analysis (%) calculated for Mn$_{12}$O$_{12}$(C$_8$H$_{17}$CO$_2$)$_{16}$(H$_2$O)$_4$: C, 50.29 ; H, 8.21; found: C, 50.35; H, 8.17.

Synthesis of [Mn$_{12}$O$_{12}$(CH$_3$CH$_2$CH$_2$CO$_2$)$_{16}$(H$_2$O)$_4$] (11)

To a slurry of Mn$_{12}$O$_{12}$(CH$_3$CO$_2$)$_{16}$(H$_2$O)$_4$ (500 mg, 0.27mmol) in CH$_2$Cl$_2$ (70mL) was added butyric acid (0.39mL, 4.28mmol). The mixture was stirred in a closed flask at room temperature overnight. The resulting solution was filtered and evaporation of the solvent yielded a brown oil. To the residue was added toluene (60mL) and the solution was stirred for 15 min and evaporated to give a brown oil. The addition and removal of toluene were repeated three times. The overall reaction procedure and subsequent treatment were repeated once more. The resultant oil was dried under

vacuum to afford a dark brown microcrystalline material. All the efforts made trying to grow crystals suitable for X-ray crystallography remained vain. FT-IR (KBr, cm^{-1}): 3431br, 2964s, 2934m, 2876m, 2284w, 1571s, 1418s, 1385m, 1316w, 1261w, 1098s, 799m, 555m, 465m. MALDI-TOF-MS (RN-m/z): 2244.3 $[Mn_{12}O_{12}(L)_{16}]^-$ L=$CH_3CH_2CH_2CO_2$, 2157.2 $[Mn_{12}O_{12}(L)_{15}]^-$, 2070.1 $[Mn_{12}O_{12}(L)_{14}]^-$. MALDI-TOF-MS (RP-m/z): 2081.1 $[Mn_{12}O_{12}(L)_{14}]^+$, 2006.1 $[Mn_{12}O_{12}(L)_{13}]^+$, 1918.9 $[Mn_{12}O_{12}(L)_{12}]^+$, 1832.1 $[Mn_{12}O_{12}(L)_{11}]^+$, 1745.1 $[Mn_{12}O_{12}(L)_{10}]^+$, 1658.05 $[Mn_{12}O_{12}(L)_9]^+$, 1571.3 $[Mn_{12}O_{12}(L)_8]^+$, 1484.4 $[Mn_{12}O_{12}(L)_7]^+$, 1397.56 $[Mn_{12}O_{12}(L)_6]^+$. Elemental Analysis (%) calculated for $Mn_{12}O_{12}(C_4H_7CO_2)_{16}(H_2O)_4$: C, 33.2 ; H, 5.2; found: C, 33.1 ; H, 5.3.

Synthesis of $[Mn_3O(O_2CC_{14}H_9)_6(CH_3OH)_3].2CH_3OH$ (12)

To a slurry of $Mn_{12}O_{12}(CH_3CO_2)_{16}(H_2O)_4$ (0.50 g, 0.27mmol) in dichloromethane (70mL) was added 9-anthracenecarboxylic acid (0.96 g, 4.32mmol). The reaction mixture was stirred at room temperature overnight and filtered to remove the unreacted starting material. The resulting dark brown solution was evaporated to dryness. The resulting powder was then redissolved in toluene (60mL) and evaporated to remove the released acetic acid as the toluene azeotrope. The addition and removal of toluene were performed two more times. To ensure full ligand substitution, the residue was redissolved in CH_2Cl_2 (70mL) and treated again with 9-anthracenecarboxylic acid (0.96 g, 4.32mmol). The solvent was removed under reduced pressure and three more cycles of addition and removal of toluene were performed. A nearly saturated solution of the complex in dichloromethane was prepared before methanol was layered on top. After 5 days at 6°C, dark brown crystals suitable for X-ray crystallography were obtained (86 mg, 0.05mmol, 20%).

FT-IR (KBr, cm^{-1}): 3432vs, 3053w, 2926w, 1945w, 1592s, 1487m, 1445m, 1426m, 1391m, 1320m, 1277m, 1089s (br), 888w, 866w, 846w, 797s, 734s, 665w, 637w, 599w, 559w, 462m. Elemental Analysis (%) calculated for $C_{93}H_{66}O_{16}Mn_3$: C, 69.6; H, 4.1. Found: C, 69.6; H, 3.9. The complex crystallizes in the trigonal space group R-3 with a=b= 18.9299(11) Å, c= 39.504(5) Å, γ=120°, V= 12259(4) Å^3.

Synthesis of [Mn$_{12}$O$_{12}$((CH$_3$)$_3$CCO$_2$)$_{16}$(H$_2$O)$_4$] (13)

The compound was synthesised as described previously[54] using slight modifications. To a slurry of $Mn_{12}O_{12}(CH_3CO_2)_{16}(H_2O)_4$ (1.5 g, 0.80mmol) in CH_2Cl_2 (210mL) was added pivalic acid (1.31 g, 12.85mmol). The mixture was stirred in a closed flask at room temperature overnight. The resulting solution was filtered and evaporated to dryness. To the residue was added toluene (180mL) and the solution was stirred for 15 min and evaporated to dryness. The addition and removal of toluene were repeated three times. The resultant dark brown powder was redissolved in CH_2Cl_2 (210mL) and to this solution was added pivalic acid (2.62 g, 25.7mmol). The subsequent mixture was stirred at room temperature overnight. The resulting solution was filtered and evaporated to dryness and the residue was once again treated with three addition and removal cycles of toluene (180mL) to yield [Mn$_{12}$O$_{12}$((CH$_3$)$_3$CCO$_2$)$_{16}$(H$_2$O)$_4$] as a dark brown crystalline solid (1 g, 0.4mmol, 50%). FT-IR (KBr, cm^{-1}): 3445br, 2963s, 2930m, 2874m, 2784m, 1703w, 1636m, 1589m, 1483s, 1426s, 1381m, 1261m, 1229m, 1093s (br), 877w, 801m, 620m, 463m. MALDI-TOF-MS (RN-m/z): 2384.5 [Mn$_{12}$O$_{12}$(L)$_{15}$]$^-$L=C$_4$H$_9$CO$_2$, 2282.1 [Mn$_{12}$O$_{12}$(L)$_{14}$]$^-$, 2181.5 [Mn$_{12}$O$_{12}$(L)$_{13}$]$^-$, 2080.2 [Mn$_{12}$O$_{12}$(L)$_{12}$]$^-$. MALDI-TOF-MS (RP-m/z): 2136.4 [Mn$_{12}$O$_{12}$(L)$_{13}$]$^+$, 2035 [Mn$_{12}$O$_{12}$(L)$_{12}$]$^+$, 1934.1 [Mn$_{12}$O$_{12}$(L)$_{12}$]$^+$, 1833.2 [Mn$_{12}$O$_{12}$(L)$_{11}$]$^+$, 1732.4 [Mn$_{12}$O$_{12}$(L)$_{10}$]$^+$, 1631.4 [Mn$_{12}$O$_{12}$(L)$_9$]$^+$, 1530.3 [Mn$_{12}$O$_{12}$(L)$_8$]$^+$, 1429.3

$[Mn_{12}O_{12}(L)_7]^+$, 1328.3 $[Mn_{12}O_{12}(L)_6]^+$. Elemental Analysis (%) calculated for $Mn_{12}O_{12}(C_4H_9CO_2)_{16}(H_2O)_4$: C, 37.8 ; H, 6.0; found: C, 37.9 ; H, 6.1.

Attempted synthesis of $[Mn_{12}O_{12}(C_{10}H_{15}CO_2)_{16}(H_2O)_4]$ (14)

- Method A

To a slurry of $Mn_{12}O_{12}(CH_3CO_2)_{16}(H_2O)_4$ (500 mg, 0.27mmol) in CH_2Cl_2 (70mL) was added 1-Adamantanecarboxylic acid (1.54 g, 8.57mmol). The mixture was stirred in a closed flask at room temperature overnight. The resulting solution was filtered and evaporated to dryness. To the residue was added toluene (60mL) and the solution was stirred for 15 min and evaporated to dryness. The addition and removal of toluene were repeated three times. The overall reaction procedure and subsequent treatment were repeated once more to yield a dark brown powder. Attempts to grow crystals by layering dissolving the compound in DCM and using MeOH, MeNO$_2$ and acetone as counter-solvents revealed to be unsuccessful.

- **Method B**

To a slurry of $Mn_{12}O_{12}((CH_3)_3CCO_2)_{16}(H_2O)_4$ **(13)** (500 mg, 0.27mmol) in CH_2Cl_2 (70mL) was added 1-Adamantanecarboxylic acid (0.78 g, 4.32mmol). The mixture was stirred in a closed flask at room temperature overnight. The resulting solution was filtered and evaporated to dryness. To the residue was added toluene (60mL) and the solution was stirred for 15 min and evaporated to dryness. The addition and removal of toluene were repeated three times. The overall reaction procedure and subsequent treatment were repeated once more to yield a dark brown powder. Attempts to grow crystals by layering dissolving the compound in DCM and using MeOH, MeNO$_2$ and acetone as counter-solvents proved to be unsuccessful. Characterisation of the crude

powder using MALDI-TOF-MS did not permit any clear identification of the powder obtained.

Synthesis of 1-Pyridylacylpyridinium Iodide (15)

The compound was synthesised as described previously[58,59] using slight modifications. To a solution of 2-acylpyridine (9.3mL, 82.6mmol) in pyridine (100mL) was added iodine (23 g, 90.6mmol). After being thoroughly degassed, the resulting mixture was heated to 100°C for 2h under nitrogen atmosphere. Upon cooling to room temperature, the mixture was filtered through a Buchner funnel and the black precipitate was copiously washed with diethyl ether and air-dried. The black solid was recrystallised from hot ethanol, filtered through a Buchner funnel and dried under vacuum to yield 1-pyridylacylpyridinium iodide as a black crystalline solid (25.7 g, 96 %). ^{1}H NMR (400 MHz, (CD$_3$)$_2$CO): δ ppm 6.82 (s, 2 H), 7.80 (ddd, J=6.78, 4.77, 2.13 Hz, 1 H), 8.04 - 8.18 (m, 2 H), 8.42 (t, J=7.15 Hz, 2 H), 8.84 (d, J=4.64 Hz, 1 H), 8.90 (t, J=7.84 Hz, 1 H), 9.29 (d, J=5.65 Hz, 2 H).

Synthesis of 5-Methyl-2,2'-bipyridine (16)

The compound was synthesised as described previously[58,59] using slight modifications. To a solution of 1-pyridylacylpyridinium iodide (12.5 g, 38.5mmol) in methanol (100mL) was added methacrolein (3.25mL, 39.5mmol) and ammonium acetate (14.8 g, 0.19 moles). The resulting mixture was heated to reflux point for 20h under nitrogen atmosphere. The mixture was allowed to cool to room temperature and the reaction was quenched with water (50mL). The organic product was extracted with n-hexane (5 x 20mL) and the combined organic layers were washed with water (2 x 50mL) and then dried over anhydrous magnesium sulfate. Evaporation of the

solvent yielded 5-methyl-2,2'-bipyridine as a yellow liquid (4.25 g, 25mmol, 65 %).

ESI-MS m/z: 171.1 [M+H]$^+$. ^{1}H NMR (400 MHz, CDCl$_3$): δ ppm 2.39 (s, 3 H), 7.25 - 7.31 (m, 1 H), 7.58 - 7.65 (m, 1 H), 7.80 (td, J=7.75, 1.75 Hz, 1 H), 8.29 (d, J=8.18 Hz, 1 H), 8.36 (dt, J=8.00, 0.97 Hz, 1 H), 8.51 (dd, J=1.46, 0.58 Hz, 1 H), 8.63 - 8.70 (m, 1 H). ^{13}C NMR (101 MHz, CDCl$_3$): δ ppm 18.29, 120.54, 120.73, 123.31, 133.36, 136.80, 137.40, 149.05, 149.57, 153.57, 156.23.

Synthesis of 2,2'-bipyridinyl-5-carboxylic acid (17)

5-methyl-2,2'-bipyridine (0.85 g, 5mmol), sodium hydroxide (600 mg, 15mmol) were dissolved in a ^{t}BuOH/water mixture (50mL). The temperature was set to 55°C and potassium permanganate (2.4 g, 15mmol) was added in small aliquots over the course of few hours. The mixture was left to react at 70°C overnight. The mixture was then heated at 90°C for several minutes and a few drops of ethanol were added to destroy the excess of KMnO$_4$. The resulting solution was filtered off to remove MnO$_2$, concentrated under reduced pressure and acidified with hydrochloric acid (pH=4) to get a white precipitate which was then washed with water, acetone and dried in air (0.56 g, 2.8mmol, 56%). ESI-MS m/z: 199.1 [M+H]$^+$; 223.0468 [M+Na]$^+$. ^{1}H NMR (400 MHz, (CD$_3$)$_2$SO$_2$): δ ppm 7.53 (ddd, J=7.53, 4.75, 1.17 Hz, 1 H), 8.00 (td, J=7.75, 1.90 Hz, 1 H), 8.42 (dd, J=8.33, 2.19 Hz, 1 H), 8.46 (dt, J=7.93, 1.00 Hz, 1 H), 8.52 (dd, J=8.26, 0.80 Hz, 1 H), 8.68 - 8.84 (m, 1 H), 9.17 (dd, J=2.19, 0.88 Hz, 1 H). ^{13}C NMR (101 MHz, (CD$_3$)$_2$SO$_2$): δ ppm 120.23, 121.26, 124.96, 126.52, 137.52, 138.22, 149.55, 150.14, 154.19, 158.39, 166.10. Elemental Analysis (%) calculated for C$_{11}$H$_8$N$_2$O$_2$: C, 65.99; H, 4.02; N, 13.99; Found: C, 65.99; H, 3.98; N, 13.88.

Attempted synthesis of [Mn$_{12}$O$_{12}$(C$_{10}$H$_7$N$_2$CO$_2$)$_{16}$(H$_2$O)$_4$] (18)

To a slurry of Mn$_{12}$O$_{12}$(CH$_3$CO$_2$)$_{16}$(H$_2$O)$_4$ (0.5 g, 0.27mmol) in CH$_2$Cl$_2$ (70mL) was added the previously synthesised 2,2'-bipyridinyl-5-carboxylic acid (0.86 g, 4.32mmol). The mixture was stirred in a closed flask at room temperature overnight. The resulting solution was filtered and evaporated to dryness. To the residue was added toluene (60mL) and the solution was stirred for 15 min and evaporated to dryness. The addition and removal of toluene were repeated three times. The resultant dark brown powder was redissolved in CH$_2$Cl$_2$ (70mL) and to this solution was added 2,2'-bipyridinyl-5-carboxylic acid (0.86 g, 4.32mmol). The subsequent mixture was stirred at room temperature overnight. The resulting solution was filtered and evaporated to dryness and the residue was once again treated with three addition and removal cycles of toluene (60mL) to yield a dark brown powder which proved to be insoluble in most organic solvent and therefore could not be purified or characterised.

Attempted synthesis of [Mn$_{12}$O$_{12}$(C$_5$H$_4$NCO$_2$)$_{16}$(H$_2$O)$_4$] (19)

- **Method A**

To a slurry of Mn$_{12}$O$_{12}$(CH$_3$CO$_2$)$_{16}$(H$_2$O)$_4$ (0.50 g, 0.27mmol) in CH$_2$Cl$_2$ (70mL) was added isonicotinic acid (1.06 g, 8.57mmol). The mixture was stirred in a closed flask at room temperature overnight. The resulting solution was filtered and evaporated to dryness. To the residue was added toluene (60mL) and the solution was stirred for 15 min and evaporated to dryness. The addition and removal of toluene were repeated three times. The brownish powder was redissolved in CH$_2$Cl$_2$ (70mL) and to this solution was added isonicotinic acid (1.06 g, 8.57mmol). The subsequent solution was stirred at room temperature overnight. The mixture was filtered and evaporated to dryness and the residue was once again treated with three addition and removal cycles

of toluene (60mL) to yield a brownish powder which could not be purified or characterised.

- **Method B**

To a slurry of $Mn_{12}O_{12}(CH_3CO_2)_{16}(H_2O)_4$ (0.50 g, 0.27mmol) in MeCN (70mL) was added isonicotinic acid (1.06 g, 8.57mmol). The mixture was stirred in a closed flask at room temperature overnight. The resulting solution was filtered and evaporated to dryness. To the residue was added toluene (60mL) and the solution was stirred for 15 min and evaporated to dryness. The addition and removal of toluene were repeated three times. The brownish powder was redissolved in MeCN (70mL) and to this solution was added isonicotinic acid (1.06 g, 8.57mmol). The subsequent solution was stirred at room temperature overnight. The mixture was filtered and evaporated to dryness and the residue was once again treated with three addition and removal cycles of toluene (60mL) to yield a brownish powder. Unfortunately, the resulting brownish powder was still insoluble in most organic solvents and consequently could not be purified by crystallisation despite several attempts or identified by the normal characterisation techniques.

3.5   References

1. J. Gomez-Segura, J. Veciana, D. Ruiz-Molina, *Chem. Commun.*, 2007, 3699

2. a. G. Christou, D. Gatteschi, D. N. Hendrickson, R. Sessoli, *MRS Bull.*, 2000, **25**, 66; b. D. Gatteschi, R. Sessoli, *Angew. Chem. Int. Ed.*, 2003, **42**, 268

3. a. R. Sessoli, D. Gatteschi, A. Caneschi, M. A. Novak, *Nature*, 1993, **365**, 141. b. R. Sessoli, H-K. Tsai, A. R. Schake, S. Wang, J. B. Vincent, K. Folting, D. Gatteschi, G. Christou, D. N. Hendrickson, *J. Am. Chem. Soc.*, 1993, **115**, 1804

4. C. Carbonera, I. Imaz, D. Maspoch, D. Ruiz-Molina, F. Luis, *Inorg. Chim. Acta,* 2008, 3951

5. D. Loss, D. P. DiVicenzo, G. Gunstein, *Phys B.*, 1993, **189**, 189

6. P. Gerbier, N. Domingo, J. Gomez-Segura, D. Ruiz-Molina, D. Amabilino, J. Tejada, B. Williamson, J. Veciana, *J. Mater. Chem.,* 2004, **14**, 2455

7. J. Vanslageren, http://www.imprs am.mpg.de/winterschool2008/vanslageren_stuttgart_2008.pdf, 2008

8. S. M. J. Aubin, Z. Sun, H. J. Eppley, E. M. Rumberger, I. A. Guzei, K. Folting, P. K. Gantzel, A. L. Rheingold, G. Christou, D. N. Hendrickson, *Inorg. Chem.*, 2001, **40**, 2127

9. T. Lis, *Acta Cryst.*, 1980, **B36**, 2042

10. J. M. North, *Ph.D. Thesis*, Florida State University, 2004

11. S. M. J. Aubin, Z. Sun, H. J. Eppley, E. M. Rumberger, I. A. Guzei, K. Folting, P. K. Gantzel, A. L. Rheingold, G. Christou, D. N. Hendrickson, *Polyhedron*, 2001, **20**, 1139

12. F. Pineider, M. Mannini, L. Sangregorio, L. Gorini L., R. Sessoli, *Inorg. Chimi. Acta*, 2008, **361,** 3944

13. L. Zobbi, M. Mannini, M. Pacchioni, G. Chastanet, D. Bonacchi, C. Zanardi, R. Biagi, U. Del Pennino, D. Gatteschi, A. Cornia, R. Sessoli, *Chem. Commun.*, 2005, **12**, 1640

14. C-D. Park, D-Y. Jung, *Bull. Korean Chem. Soc.*, 2001, **22**, 612

15. M. Soler, W. Wernsdorfer, Z. Sun, J. C. Huffman, D. N. Hendrickson, G. Christou, *Chem. Commun.*, 2003, **21**, 2672

16. N. E. Chakov, L. N. Zakharov, A. L. Rheingold, K. A. Abboud, G. Christou, *Inorg. Chem.*, 2005, **44**, 4555

17. W. Jeon, M. K. Jin, Y. Kim, D-Y. Jung, B. J. Suh, S. Yoon, *Bull. Korean Chem. Soc.*, 2004, **25**, 1036

18. A. Cornia, A. C. Fabretti, M. Pacchioni, L. Zobbi, D. Bonacchi, A. Caneschi, D. Gatteschi, R. Biagi, U. Del Pennino, V. De Renzi, L. Gurevisch, H. S. J. Van der Zant, *Angew. Chem. Int. Ed.*, 2003, **42**, 1645

19. M. Pacchioni, A. Cornia, A. C. Fabretti, L. Zobbi, D. Bonacchi, A. Caneschi, G. Chastanet, D. Gatteschi, R. Sessoli, *Chem. Commun.*, 2004, **21**, 2604

20. H. Miyasaka, R. Clerac, W. Wernsdorfer, L. Lecren, C. Bonhomme, K. Sugiura, M. A. Yamashita, *Angew. Chem. Int. Ed.,* 2004, **43**, 2801

21. S. M. J. Aubin, M. W. Wemple, D. M. Adams, H. L. Tsai, G. Christou, D. N. Hendrickson, *J. Am. Chem. Soc.*, 1996, **118**, 7746

22. E. K. Brechin, J. Yoo, J. C. Hoffman, D. N. Hendrickson, G. Christou, *Chem. Commun.*, 1999, **9**, 783

23. J. Yoo, E. K. Brechin, A. Yamaguchi, M. Nakano, J. C. Hoffman, A. L. Maniero, L. C. Brunel, K. Awaga, H. Ishimoto, G. Christou, D. N. Hendrickson, *Inorg. Chem.*, 2000, **39**, 3615

24. J. Yoo, A. Yamaguchi, M. Nakano, J. Krzystek, W. E. Streib, L. C. Brunel, H. Ishimoto, G. Christou, D. N. Hendrickson, *Inorg. Chem.*, 2001, **40**, 4604

25. E. Yang, N. Harden, W. Wernsdorfer, L. Zakharov, E. K. Brechin, A. L. Rheingold, G. Christou, D. N. Hendrickson, *Polyhedron,* 2003, **22**, 1857

26. L. M. Wittig, K. S. Murray, B. Moubaraki, S. R. Batten, L. Spiccia, K. J. Berry, *J. Chem. Soc. Dalton Trans.*, 2004, **7**, 1003

27. H. Andres, R. Basler, H.-U. Gudel, G. Aromi, G. Christou, H. Buttner, B. Ruffle, *J. Am. Chem. Soc.*, 2000, **122**, 12469

28. S. Hill, R. S. Edwards, N. Aliaga-Alcalde, G. Christou, *Science*, 2003, **302**, 1015

29. W. Wernsdorfer, N. Aliaga-Alcalde, D. N. Hendrickson, G. Christou, *Nature*, 2002, **416**, 406

30. C. J. Milios, C. P. Raptopoulou, A. Terzi, F. Lloret, R. Vicente, S. P. Perlepes, A. Escuer, *Angew. Chem. Int. Ed.,* 2003, **43**, 210

31. M. Murugesu, W. Wernsdorfer,K. A. Abboud, G. Christou, *Angew. Chem. Int. Ed.,* 2005, **44**, 892

32. E.K. Brechin, M. Soler, J. Davidson, D.N. Hendrickson, S. Parsons, G. Christou, Chem. Commun., 2002, **19**, 2252

33. D.J. Price, S.R. Batten, B. Moubaraki, K.S. Murray, *Chem. Commun.*, 2002, **7**, 762

34. P. King, W. Wernsdorfer, K.A. Abboud, G. Christou, *Inorg. Chem.*, 2004, **43**, 7315

35. M. Murugesu, J. Raftery, W. Wernsdorfer, G. Christou, E.K. Brechin, *Inorg. Chem.*, 2004, **43**, 4203

36. M. Murugesu, M. Habrych, W. Wernsdorfer, K.A. Abboud, G.Christou, *J. Am. Chem. Soc.*, 2004, **126**, 4766

37. L.F. Jones, G. Rajaraman, J. Brockman, M. Murugesu, E.C. Sanudo, J. Raftery, S.J. Teat, W. Wernsdorfer, G. Christou, E.K. Brechin, D. Collison, *Chem. Eur. J.*, 2004, **10**, 5180

38. M. Soler, E. Rumberger, K. Folting, D.N. Hendrickson, G. Christou, *Polyhedron,* 2001, **20**, 1365

39. M. Soler, W. Wernsdorfer, K. Folting, M. Pink, G. Christou, *J. Am. Chem. Soc.*, 2004, **126,** 2156

40. A. J. Tassiopoulos, A. Vinslave, W. Wernsdorfer, K.A. Abboud, G. Christou, *Angew. Chem. Int. Ed.*, 2004, **43**, 2117

41. L. Bogani, W. Wernsdorfer, *Nature*, 2008, **7**, 179

42. M. Burgert, S.Voss, S. Herr, M. Fonin, U. Groth, U. Rudiger, *J. Am. Chem. Soc.,* 2007, **129**, 14362

43. J. M. Lim, Y. Do, J. Kim, *Bull. Korean Chem. Soc.,* 2005, **26**, 1065

44. a. M. Clemente-Leon, H. Soyer, E. Coronado, C. Mingotaud, C. J. Gomez-Garcia, P. Delhaes, *Angew. Chem. Int. Ed.*, 1998, **37**, 2842. b. M. Clemente-Leon, E. Coronado, A. Soriano-Portillo, C. Mingotaud, J. M. Dominiguez-Vera, *Adv. Colloid Interface Sci.*, 2005, **116**, 193

45. J. Gomez-Segura, J. Veciana, D. Ruiz-Molina, *Chem. Commun.*, 2007, **36**, 3699

46. D. Gatteschi, L. Bogani, A. Cornia, M. Mannini, L. Sorace, R. Sessoli, *Solid State Sci.*, 2008, **12**, 1701

47. S. Voss, M. Fonin, U. Rudiger, M. Burgert, U. Groth, Y. S. Dedkov, *Phys. Rev. B*, 2007, **75**, 045107

48. M. Cavallini, F. Biscarini, J. Gomez-Segura, D. Ruiz-Molina, J. Veciana, *Nano Lett.*, 2003, **3**, 1527

49. M. Mannini, P. Sainctavit, R. Sessoli, R. Cartier dit Moulin, F. Pineider, M. A. Arrio, A. Cornia, D. Gatteschi, *Chem. Eur. J.*, 2008, **14**, 7530

50. Pennino Del U., V. De Renzi V., R. Biagi, V. Corradini, L. Zobbi, A. Cornia, D. Gatteschi, F. Bondino, E. Magnano, M. Zangrando, M. Zacchigna, A. Lichtenstein, D. W. Boukhvalov, *Surf. Sci.*, 2006, **600**, 4185

51. G. G. Condorelli, A. Motta, I. L. Fragala, F. Giannazzo, C. Raineri, A. Caneschi, D. Gatteschi, *Angew. Chem., Int. Ed.*, 2004, **43**, 4081

52. A. Naitabdi, J. P. Bucher, P. Gerbier, P. Rabu, M. Drillon, *Adv. Mater.*, 2005, **17**, 1612

53. S. Voss, M. Fonin, U. Rudiger, M. Burgert, U. Groth, Y. S. Dedkov, *Phys Rev.*, 2007, **B75**, 45102

54. P. Gerbier, D. Ruiz-Molina, N. Domingo, D. Amabilino, J. Vidal-Gancedo, J. Tejada, D. Hendrickson, J. Veciana , *Monat. fur Chem.*, 2003, **134**, 265

55. A. Cornia, A. C. Fabretti, R. Sessoli, L. Sorace, D. Gatteschi, A. L. Barra, C. Daiguebonne, T. Roisnel, *Acta Cryst.*, 2002, **C58**, m371

56. P. Gerbier, D. Ruiz-Molina, J. Gomez, K. Wurst, J. Veciana, *Polyhedron*, 2003, **22**, 1951

57. D. Ruiz-Molina, P. Gerbier, E. Rumberger, D. B. Amanilino, I. A. Guzei, K. Folting, J. C. Huffman, A. Rheingold, G. Christou, J. Veciana, D. Hendrickson, *J. Mater. Chem.*, 2002, **12**, 1152

58. E. Zysman-Colman, J. D. Slinker, J. B. Parker, G. G. Malliaras, S. Bernhard, *Chem. Mater.*, 2008, **20**, 388

59. C. W. Y. Chung, P. H. Toy, *J. Comb. Chem.*, 2007, **9**, 115

60. K. Awaga, K. Takeda, *Phys. Rev. B*, 1998, **57**, R11062

61. K. Awaga, Y. Suzuki, H. Hachisuka, K. Takeda, *J. Mater. Chem.*, 2006, **16**, 2516

62. G. Q Bian, T. Kuroda-Sowa, T. Nagomi, K. Sugimoto, M. Maekawa, M. Munakata, H. Miyasaka, M. Yamashita, *Bull. Chem. Soc. Jpn.,* 2005, **78**, 1032

63. M. Soler, W.Wernsdorfer, Zi Sun c, Daniel Ruiz, J. C. Huffman, D. N. Hendrickson, G. Christou, *Polyhedron*, 2003, **22**, 1783

64. D. W. Boukhvalov,V. V. Dobrovitski, P. Kogerler, M. Al-Saqer, M. I. Katsnelson, A. I. Lichtenstein, B. N. Harmon, *Inorg. Chem.*, 2010, **49**, 10902

65. C. Carbonera, F. Luis, J. Campo, J. Sánchez-Marcos, A. Camón, J. Chaboy, D. Ruiz-Molina, I. Imaz, J. van Slageren, S. Dengler, M. González, *Phys. Rev.*, 2010, **B 81**, 014427

66. S. Hill, M. Murugesu, G. Christou, *Phys. Rev.*, 2009, **B 80**, 174416

67. M. Viciano-Chumillas, S. Tanase, I. Mutikainen, U. Turpeinen, L. Jos de Jongh, J. Reedijk, *Inorg. Chem.*, 2008, **47**, 5919

68. J.B. Vincent, H.R. Chang, K. Folting, J.C. Huffman, G. Christou, D.N. Hendrickson, *J. Am. Chem. Soc.*, 1987, **109**, 5703

69. J. An, Z.D. Chen, J.A. Bian, X.L. Jin, S.X. Wang, G.X.; Xu, *Inorg. Chim. Acta*, 1999, **287**, 82

70. J. Li, S.M. Yang, F.X. Zhang, Z.X. Tang, S.L. Ma, Q.Z. Shi, Q.J. Wu, Z.X. Huang, *Inorg. Chim. Acta*, 1999, **294**, 109

71. S.G. Baca, H. Stoeckli-Evans, C. Ambrus, S.T. Malinovskii, I. Malaestean, N. Gerbeleu, S. Decurtins, *Polyhedron*, 2006, **25**, 3617

72. R. Inglis, S.M. Taylor, L.F. Jones, G.S. Papaefstathiou, S.P. Perlepes, S. Datta, S. Hill, W. Wernsdorfer, E.K. Brechin, *Dalton Trans*., 2009, 9157; R. Inglis, G.S. Papaefstathiou, W. Wernsdorfer, E.K. Brechin, *Aust. J. Chem*., 2009, **62**, 1108; C.-S. Liu, E.C. Sanudo, L.-F. Yan, Z. Chang, J.-J.Wang, T.-L. Hu, *Transition Met. Chem.*, 2009, **34**, 51; R. Inglis, L.F. Jones, K. Mason, A. Collins, S.A. Moggach,

S. Parsons, S.P. Perlepes, S. Datta, S. Hill, W. Wernsdorfer, E.K. Brechin, *Chem. Eur. J.*, 2008, **14**, 9117; C.-S. Liu, E.C. Sanudo, J.-J.Wang, Z. Chang, L.-F. Yan, X.-H. Bu, *Aust. J. Chem.*, 2008, **61**, 382; C.C. Beedle, C.J. Stephenson, K.J. Heroux, W. Wernsdorfer, D.N. Hendrickson, *Inorg. Chem.*, 2008, **47**, 10798

73. M. Nishio, *Cryst. Eng. Comm.*, 2004, **6**, 130

74. I. Dance, M. Scudder, *Cryst. Eng. Comm.*, 2009, **11**, 2233

75. L.M.Wittick, L.F.Jones, P.Jensen, B.Moubaraki, L.Spiccia, K.J.Berry, K.S.Murray, *Dalton Trans.*, 2006, 1534; P.M.T.Piggot, L.A.Hall, A.J.P.White, D.J.Williams, L.K.Thompson, *Inorg.Chem.*, 2004, **43**, 1167; X.-H. Bu, M.-L. Tong, Y.-B. Xie, J.-R. Li, H.-C. Chang, S. Kitagawa, J. Ribas, *Inorg.Chem.*, 2005, **44**, 9837

76. R.J. Cross, L.J. Farrugia, P.D. Newman, R.D. Peacock, D. Stirling, *Inorg.Chem.*, 1999, **38,** 1186; M.U. Triller, D. Pursche, W.-Y. Hsieh, V.L. Pecoraro, A. Rompel, B. Krebs, *Inorg.Chem.*, 2003, **42,** 6274

77. M.D. Godbole, O. Roubeau, R. Clerac, H. Kooijman, A.L. Spek, E. Bouwman *Chem.Commun.*, 2005*,* 3715; S. Konar, A. Clearfield, *Inorg.Chem.*, 2008, **47,** 3489

78. (a) G. Pourroy, E. Coronado, M. Drillon, R. Georges, *Chem. Phys.*, 1986, **104**, 73. (b) M. I. Belinski, *Mol. Phys.*, 1987, **60**, 793. (c) V. Papaefthymiou, J. J. Girerd, I. Moura, J. J. G. Moura, E. Munck, 1987, *J. Am. Chem. Soc.*, 1987, **109**, 4703. (d) C. J. Gomez-Garcia, E. Coronado, G. Pourroy, *J. Appl. Phys.*, 1990, **67**, 5992

79. H-B. Xu, B-W. Wang, F. Pan, Z-M. Wang, S. Gao, *Angew. Chem. Int. Ed.*, 2007, **46**, 7388

80. X. Song, P. Yang, X. Mei, L. Li, D. Liao, *Eur. J. Inorg. Chem.*, 2010, 1689

81. R. D. Cannon, R. P. White, *Prog. Inorg. Chem.*, 1988, **36**, 195

82. T. C. Stamatatos, D. Foguet-Albiol, S-C. Lee, C. C. Stoumpos, C. P. Raptopoulou, A. Terzis, W. Wernsdorfer, S. O. Hill, S. P. Perlepes, G. Christou, *J. Am. Chem. Soc.*, 2007, **129**, 9484

83. S. Phark, Z. G. Khim, B. J. Kim, B. J. Suh, S. Yoon, J. Kim, J. M. Lim, Y. Do, *Jpn. J. Appl. Phys. 1*, 2004, **43**, 8273

84. A. Naitabdi, J.-P. Bucher, P. Gerbier, P. Rabu, M. Drillon, *Adv. Mater.*, 2005, **17**, 1612

85. V. Corradini, U. del Pennino, R. Biagi, *V.* de Renzi, A. Gambardella,. G. C. Gazzadi, A. Candini, L. Zobbi, A. Cornia, *Surf. Sci.*, 2007, **601**, 2618

86. S. H. Phark, Z. G. Khim, J. M. Lim, J. Kim, S. Yoon, *J. Magn. Magn. Mater.*, 2007, **310**, E483

87. F. Pineider, M. Mannini, R. Sessoli, A. Caneschi, D. Barreca, L. Armelao, A. Cornia, E. Tondello, D. Gatteschi, *Langmuir*, 2007, **23**, 11836

88. E. Coronado, A. Forment-Aliaga, F. M. Romero, V. Corradini,. R. Biagi, V. De Renzi, A. Gambardella, U. del Pennino, Inorg. Chem., 2005, **44**, 7693

89. R. V. Martínez, F. García, R. García, E. Coronado, A. Forment-Aliaga, F. M. Romero, S. Tatay, Adv. Mater., 2007, **19**, 291

90. R. W. Saalfrank, A. Scheurer, I. Bernt, F. W. Heinemann, A. V. Postnikov, V. Schunemann, A. X. Trautwein, M. S. Alam, H. Rupp, P. Muller, *Dalton Trans.*, 2006, 2865

91. J. Means, R. Srivastava, V. Meenakshi, W. Teizer, H. Zhao, K. Dunbar, Al. A. Kolomenskii, and H. A. Schuessler, *J. Magn. Magn. Mater.*, 2004, **284**, 215

92. V. Meenakshi, W. Teizer, D. Naugle,. H. Zhao, K. Dunbar, *Solid State Commun.*, 2004, **132**, 471

93. R. Moroni, R. Buzio, A. Chincarini, U. Valbusa, F. B. de Mongeot, L. Bogani, A. Caneschi, R. Sessoli, L. Cavigli, M. Gurioli, *J. Mater. Chem.*, 2008, **18**, 5999

94. L. Vitali, S. Fabris, A. Mosca Conte, S. Brink, M. Ruben, S. Baroni, K. Kern, *Nano Lett.*, 2008, **8,** 3364

95. A. L. Barra, A. Caneschi, D. Gatteschi, D. P. Goldberg, R. Sessoli, *J. Solid State Chem.*, 1999, **145**, 484

96. A. Saywell, G. Magnano, C. J. Satterley, L. M. A. Perdigão, N. R. Champness, P. H. Beton, J. N. O'Shea, *J. Phys. Chem. C,* 2008, **112**, 7706

97. C. J. Satterley, L. M. A. Perdigao, A. Saywell, G. Magnano, A. Rienzo, L. C. Mayor, V. R. Dhanak, P. H. Beton, J. N. O'Shea, *Nanotechnology*, 2007, **18**, 455304

98. H. Suzuki, T. Yamada, T. Kamikado, Y. Okuno, S. Mashiko, *J. Phys. Chem. B*, 2005, **109**, 13296-13300

99. S. Rauschenbach, R. Vogelgesang, N. Malinowski, J. Gerlach, M. Benyoucef, G. Constantini, Z. Deng, N. Thontasen, K. Kern, *ACS Nano*, 2009, **3**, 2901

100. H. Tanaka, T. Kawai, *Nature Nanotech.*, 2009, **4**, 518

101. L. C. Mayor, J. B. Taylor, G. Magnano, A. Rienzo, C. J. Satterley, J. N. O'Shea, Joachim Schnadt, *J. Chem. Phys.*, 2008, **129**, 114701

102. J. E. Lyon, M. M. Beerbom, R. Schlaf, Y. Zhu, S. A. Jenekhe, *Appl. Phys. Lett.*, 2006, **88**, 222109

103. M. Marschall, J. Reichert, A. Weber-Bargioni, K. Seufert, W. Auwärter, S. Klyatskaya, G. Zappellaro, M. Ruben, J. V. Barth, *Nature Chem.*, 2010, **2**, 131

104. R. Otero, M. Lukas, R. E. A. Kelly, W. Xu, E. Lægsgaard, I. Stensgaard, L. N. Kantorovich, F. Besenbacher, *Science*, 2008, **319**, 312

105. J. V. Barth, H. Brune, G. Ertl, R. J. Behm, *Phys. Rev. B, 1990,* **42**, 9307

106. A. Saywell, G. Magnano, C. J. Satterley, L. M.A. Perdigão, A. J. Britton, N. Taleb, M. C. Giménez-López, N. R. Champness, J. N. O'Shea, P. H. Beton, *Nature Comm.*, 2010, 1, 75. See Sup. Info. for details on MD simulations and synchrotron based experiments.

107. P. Ghigna, A. Campana, A. Lascialfari, A. Caneschi, D. Gatteschi, A. Tagliaferri, F. Borgatti, *Phys. Rev. B*, 2001, **64**, 132413

108. S. Voss, M. Fonin, L. Burova, M. Burgert, Y. S. Dedkov, A. B. Preobrajenski, E. Goering, U. Groth, A. R. Kaul, U. Ruediger, *App. Phys. A*, 2009, **94**, 491

109. J. A. W. Elemans, S. B. Lei, S. De Feyter, *Angew. Chem. Int. Ed.*, 2009, **48**, 7298

110. P. A. Staniec, L. M. A. Perdigao, A. Saywell, N. R. Champness, P. H. Beton, *Chem. Phys. Chem.,* 2007, **8**, 2177

111. J. Adisoejoso, K. Tahara, S. Okuhata, S. Lei, T. Tobe, S. De Feyter, *Angew. Chem. Int. Ed.*, 2009, **48**, 7353

112. G. M. Sheldrick, *Acta. Crystallogr. Sect. A*, 1990, **46**, 467

113. L. Palatinus, G. Chapuis, J. Appl. Crystallogr., 2007, **40**, 786

114. G. M. Sheldrick, University of Göttingen, 1997

Appendix 1. Crystallographic data of structures discussed in Chapter 2

A1.1: Table of bond lengths [Å] and angles [°] for (8).

_____

C(11)-C(12)	1.397(2)
C(11)-C(16)	1.400(2)
C(11)-C(41)	1.483(2)
C(12)-C(13)	1.390(2)
C(12)-H(12)	0.9500
C(13)-C(14)	1.395(2)
C(13)-C(21)	1.495(2)
C(14)-C(15)	1.393(2)
C(14)-H(14)	0.9500
C(15)-C(16)	1.398(2)
C(15)-C(31)	1.486(2)
C(16)-H(16)	0.9500
C(21)-O(22)	1.207(2)
C(21)-O(23)	1.3271(19)
O(23)-H(23)	0.85(2)
C(31)-O(32)	1.2225(19)
C(31)-O(33)	1.3159(18)
O(33)-H(33)	0.94(2)
C(41)-C(43)#1	1.395(2)
C(41)-C(42)	1.395(2)
C(42)-C(43)	1.386(2)
C(42)-H(42)	0.9500
C(43)-C(41)#1	1.395(2)
C(43)-H(43)	0.9500
O(1)-C(2)	1.239(2)
C(2)-N(3)	1.325(2)
C(2)-H(2)	0.9500
N(3)-C(4)	1.453(2)
N(3)-C(5)	1.457(2)
C(4)-H(4A)	0.9800
C(4)-H(4B)	0.9800
C(4)-H(4C)	0.9800
C(5)-H(5A)	0.9800

C(5)-H(5B)	0.9800
C(5)-H(5C)	0.9800
C(12)-C(11)-C(16)	118.10(14)
C(12)-C(11)-C(41)	120.50(14)
C(16)-C(11)-C(41)	121.40(14)
C(13)-C(12)-C(11)	121.52(14)
C(13)-C(12)-H(12)	119.2
C(11)-C(12)-H(12)	119.2
C(12)-C(13)-C(14)	119.93(14)
C(12)-C(13)-C(21)	118.18(14)
C(14)-C(13)-C(21)	121.89(14)
C(15)-C(14)-C(13)	119.40(14)
C(15)-C(14)-H(14)	120.3
C(13)-C(14)-H(14)	120.3
C(14)-C(15)-C(16)	120.30(14)
C(14)-C(15)-C(31)	121.60(14)
C(16)-C(15)-C(31)	118.09(13)
C(15)-C(16)-C(11)	120.73(14)
C(15)-C(16)-H(16)	119.6
C(11)-C(16)-H(16)	119.6
O(22)-C(21)-O(23)	123.89(15)
O(22)-C(21)-C(13)	123.69(14)
O(23)-C(21)-C(13)	112.42(13)
C(21)-O(23)-H(23)	106.8(15)
O(32)-C(31)-O(33)	122.71(14)
O(32)-C(31)-C(15)	122.00(14)
O(33)-C(31)-C(15)	115.29(13)
C(31)-O(33)-H(33)	105.7(13)
C(43)#1-C(41)-C(42)	118.29(14)
C(43)#1-C(41)-C(11)	120.58(14)
C(42)-C(41)-C(11)	121.12(14)
C(43)-C(42)-C(41)	120.60(15)
C(43)-C(42)-H(42)	119.7
C(41)-C(42)-H(42)	119.7
C(42)-C(43)-C(41)#1	121.10(14)
C(42)-C(43)-H(43)	119.5
C(41)#1-C(43)-H(43)	119.5

O(1)-C(2)-N(3)	125.26(15)
O(1)-C(2)-H(2)	117.4
N(3)-C(2)-H(2)	117.4
C(2)-N(3)-C(4)	121.88(14)
C(2)-N(3)-C(5)	120.65(15)
C(4)-N(3)-C(5)	117.46(14)
N(3)-C(4)-H(4A)	109.5
N(3)-C(4)-H(4B)	109.5
H(4A)-C(4)-H(4B)	109.5
N(3)-C(4)-H(4C)	109.5
H(4A)-C(4)-H(4C)	109.5
H(4B)-C(4)-H(4C)	109.5
N(3)-C(5)-H(5A)	109.5
N(3)-C(5)-H(5B)	109.5
H(5A)-C(5)-H(5B)	109.5
N(3)-C(5)-H(5C)	109.5
H(5A)-C(5)-H(5C)	109.5
H(5B)-C(5)-H(5C)	109.5

_____

Symmetry transformations used to generate equivalent atoms:

#1 -x,-y+1,-z+1

A1.2: Table of torsion angles [°] for (8).

_____

C(16)-C(11)-C(12)-C(13)	-1.0(2)
C(41)-C(11)-C(12)-C(13)	178.51(14)
C(11)-C(12)-C(13)-C(14)	0.6(2)
C(11)-C(12)-C(13)-C(21)	-178.60(14)
C(12)-C(13)-C(14)-C(15)	0.1(2)
C(21)-C(13)-C(14)-C(15)	179.23(14)
C(13)-C(14)-C(15)-C(16)	-0.3(2)
C(13)-C(14)-C(15)-C(31)	-178.88(13)
C(14)-C(15)-C(16)-C(11)	-0.2(2)
C(31)-C(15)-C(16)-C(11)	178.46(14)
C(12)-C(11)-C(16)-C(15)	0.8(2)
C(41)-C(11)-C(16)-C(15)	-178.69(14)
C(12)-C(13)-C(21)-O(22)	-3.3(2)
C(14)-C(13)-C(21)-O(22)	177.58(15)
C(12)-C(13)-C(21)-O(23)	176.09(13)
C(14)-C(13)-C(21)-O(23)	-3.1(2)
C(14)-C(15)-C(31)-O(32)	178.16(14)
C(16)-C(15)-C(31)-O(32)	-0.5(2)
C(14)-C(15)-C(31)-O(33)	-2.1(2)
C(16)-C(15)-C(31)-O(33)	179.28(13)
C(12)-C(11)-C(41)-C(43)#1	-31.5(2)
C(16)-C(11)-C(41)-C(43)#1	147.99(15)
C(12)-C(11)-C(41)-C(42)	147.33(15)
C(16)-C(11)-C(41)-C(42)	-33.2(2)
C(43)#1-C(41)-C(42)-C(43)	1.1(2)
C(11)-C(41)-C(42)-C(43)	-177.81(14)
C(41)-C(42)-C(43)-C(41)#1	-1.1(3)
O(1)-C(2)-N(3)-C(4)	-1.6(2)
O(1)-C(2)-N(3)-C(5)	179.08(15)

_____

Symmetry transformations used to generate equivalent atoms:

#1 -x,-y+1,-z+1

A1.3: Table of bond lengths [Å] and angles [°] for (13).

_____

C(11)-C(12)	1.3933(18)
C(11)-C(16)	1.3963(17)
C(11)-C(41)	1.4841(16)
C(12)-C(13)	1.3943(17)
C(12)-H(12)	0.9500
C(13)-C(14)	1.3936(18)
C(13)-C(21)	1.4826(18)
C(21)-O(22)	1.2327(16)
C(21)-O(23)	1.3093(15)
O(23)-H(23)	0.8400
C(14)-C(15)	1.3879(19)
C(14)-H(14)	0.9500
C(15)-C(16)	1.3947(17)
C(15)-C(31)	1.4983(17)
C(31)-O(32)	1.2142(16)
C(31)-O(33)	1.3181(17)
O(33)-H(33)	0.8400
C(16)-H(16)	0.9500
C(41)-C(42)	1.3930(19)
C(41)-C(43)#1	1.4009(18)
C(42)-C(43)	1.3910(17)
C(42)-H(42)	0.9500
C(43)-O(44)	1.3753(16)
C(43)-C(41)#1	1.4009(18)
O(44)-C(45)	1.4226(15)
C(45)-C(51)	1.5084(18)
C(45)-H(45A)	0.9900
C(45)-H(45B)	0.9900
C(51)-C(56)	1.3919(19)
C(51)-C(52)	1.3924(18)
C(52)-C(53)	1.393(2)
C(52)-H(52)	0.9500
C(53)-C(54)	1.387(2)
C(53)-H(53)	0.9500
C(54)-C(55)	1.388(2)
C(54)-H(54)	0.9500
C(55)-C(56)	1.387(2)

C(55)-H(55)	0.9500
C(56)-H(56)	0.9500
O(1)-C(2)	1.2371(19)
N(3)-C(2)	1.3304(18)
N(3)-C(5)	1.448(2)
N(3)-C(4)	1.450(2)
C(2)-H(2)	0.9500
C(4)-H(4C)	0.9800
C(4)-H(4A)	0.9800
C(4)-H(4B)	0.9800
C(5)-H(5A)	0.9800
C(5)-H(5C)	0.9800
C(5)-H(5B)	0.9800
C(12)-C(11)-C(16)	118.29(11)
C(12)-C(11)-C(41)	121.16(11)
C(16)-C(11)-C(41)	120.55(11)
C(11)-C(12)-C(13)	120.94(12)
C(11)-C(12)-H(12)	119.5
C(13)-C(12)-H(12)	119.5
C(14)-C(13)-C(12)	120.30(12)
C(14)-C(13)-C(21)	122.19(11)
C(12)-C(13)-C(21)	117.47(11)
O(22)-C(21)-O(23)	123.82(12)
O(22)-C(21)-C(13)	121.14(12)
O(23)-C(21)-C(13)	115.03(11)
C(21)-O(23)-H(23)	109.5
C(15)-C(14)-C(13)	119.15(11)
C(15)-C(14)-H(14)	120.4
C(13)-C(14)-H(14)	120.4
C(14)-C(15)-C(16)	120.38(11)
C(14)-C(15)-C(31)	118.70(11)
C(16)-C(15)-C(31)	120.92(12)
O(32)-C(31)-O(33)	124.46(12)
O(32)-C(31)-C(15)	122.02(12)
O(33)-C(31)-C(15)	113.51(11)
C(31)-O(33)-H(33)	109.5
C(15)-C(16)-C(11)	120.90(12)

C(15)-C(16)-H(16)	119.5
C(11)-C(16)-H(16)	119.5
C(42)-C(41)-C(43)#1	118.97(11)
C(42)-C(41)-C(11)	119.52(11)
C(43)#1-C(41)-C(11)	121.52(12)
C(43)-C(42)-C(41)	121.02(12)
C(43)-C(42)-H(42)	119.5
C(41)-C(42)-H(42)	119.5
O(44)-C(43)-C(42)	123.51(12)
O(44)-C(43)-C(41)#1	116.43(11)
C(42)-C(43)-C(41)#1	120.02(12)
C(43)-O(44)-C(45)	117.48(10)
O(44)-C(45)-C(51)	108.94(10)
O(44)-C(45)-H(45A)	109.9
C(51)-C(45)-H(45A)	109.9
O(44)-C(45)-H(45B)	109.9
C(51)-C(45)-H(45B)	109.9
H(45A)-C(45)-H(45B)	108.3
C(56)-C(51)-C(52)	119.19(13)
C(56)-C(51)-C(45)	117.76(12)
C(52)-C(51)-C(45)	123.05(12)
C(51)-C(52)-C(53)	120.11(13)
C(51)-C(52)-H(52)	119.9
C(53)-C(52)-H(52)	119.9
C(54)-C(53)-C(52)	120.20(13)
C(54)-C(53)-H(53)	119.9
C(52)-C(53)-H(53)	119.9
C(53)-C(54)-C(55)	119.88(13)
C(53)-C(54)-H(54)	120.1
C(55)-C(54)-H(54)	120.1
C(56)-C(55)-C(54)	119.92(13)
C(56)-C(55)-H(55)	120.0
C(54)-C(55)-H(55)	120.0
C(55)-C(56)-C(51)	120.68(13)
C(55)-C(56)-H(56)	119.7
C(51)-C(56)-H(56)	119.7
C(2)-N(3)-C(5)	121.21(14)
C(2)-N(3)-C(4)	121.36(15)

C(5)-N(3)-C(4)	117.39(13)
O(1)-C(2)-N(3)	124.18(15)
O(1)-C(2)-H(2)	117.9
N(3)-C(2)-H(2)	117.9
N(3)-C(4)-H(4C)	109.5
N(3)-C(4)-H(4A)	109.5
H(4C)-C(4)-H(4A)	109.5
N(3)-C(4)-H(4B)	109.5
H(4C)-C(4)-H(4B)	109.5
H(4A)-C(4)-H(4B)	109.5
N(3)-C(5)-H(5A)	109.5
N(3)-C(5)-H(5C)	109.5
H(5A)-C(5)-H(5C)	109.5
N(3)-C(5)-H(5B)	109.5
H(5A)-C(5)-H(5B)	109.5
H(5C)-C(5)-H(5B)	109.5

_____

Symmetry transformations used to generate equivalent atoms:

#1 -x+1,-y+2,-z+2

A1.4 : Table of torsion angles [°] for (13).

_____

C(16)-C(11)-C(12)-C(13)	0.62(19)
C(41)-C(11)-C(12)-C(13)	179.77(12)
C(11)-C(12)-C(13)-C(14)	1.2(2)
C(11)-C(12)-C(13)-C(21)	-176.63(12)
C(14)-C(13)-C(21)-O(22)	179.61(13)
C(12)-C(13)-C(21)-O(22)	-2.6(2)
C(14)-C(13)-C(21)-O(23)	-1.05(19)
C(12)-C(13)-C(21)-O(23)	176.69(11)
C(12)-C(13)-C(14)-C(15)	-1.50(19)
C(21)-C(13)-C(14)-C(15)	176.18(12)
C(13)-C(14)-C(15)-C(16)	0.07(19)
C(13)-C(14)-C(15)-C(31)	179.45(12)
C(14)-C(15)-C(31)-O(32)	-1.4(2)
C(16)-C(15)-C(31)-O(32)	177.98(12)
C(14)-C(15)-C(31)-O(33)	178.84(12)
C(16)-C(15)-C(31)-O(33)	-1.78(19)
C(14)-C(15)-C(16)-C(11)	1.7(2)
C(31)-C(15)-C(16)-C(11)	-177.62(12)
C(12)-C(11)-C(16)-C(15)	-2.1(2)
C(41)-C(11)-C(16)-C(15)	178.79(12)
C(12)-C(11)-C(41)-C(42)	-132.78(14)
C(16)-C(11)-C(41)-C(42)	46.35(18)
C(12)-C(11)-C(41)-C(43)#1	47.70(18)
C(16)-C(11)-C(41)-C(43)#1	-133.18(14)
C(43)#1-C(41)-C(42)-C(43)	-0.1(2)
C(11)-C(41)-C(42)-C(43)	-179.68(12)
C(41)-C(42)-C(43)-O(44)	-177.38(12)
C(41)-C(42)-C(43)-C(41)#1	0.1(2)
C(42)-C(43)-O(44)-C(45)	-12.67(19)
C(41)#1-C(43)-O(44)-C(45)	169.73(11)
C(43)-O(44)-C(45)-C(51)	-172.79(11)
O(44)-C(45)-C(51)-C(56)	-172.72(11)
O(44)-C(45)-C(51)-C(52)	7.17(17)
C(56)-C(51)-C(52)-C(53)	0.22(19)
C(45)-C(51)-C(52)-C(53)	-179.67(12)
C(51)-C(52)-C(53)-C(54)	-0.7(2)

C(52)-C(53)-C(54)-C(55)	0.5(2)
C(53)-C(54)-C(55)-C(56)	0.0(2)
C(54)-C(55)-C(56)-C(51)	-0.5(2)
C(52)-C(51)-C(56)-C(55)	0.4(2)
C(45)-C(51)-C(56)-C(55)	-179.73(12)
C(5)-N(3)-C(2)-O(1)	-177.50(14)
C(4)-N(3)-C(2)-O(1)	0.3(3)

_____

Symmetry transformations used to generate equivalent atoms:

#1 -x+1,-y+2,-z+2

A1.5: Table of bond lengths [Å] and angles [°] for (19).

_____

Fe(1)-Cg1 Centroid of C(60)-C(64)	1.645
Fe(1)-Cg2 Cenroid of C(65)-C(69)	1.642
Fe(1)-C(60)	2.0441(19)
Fe(1)-C(61)	2.0438(19)
Fe(1)-C(62)	2.0482(19)
Fe(1)-C(63)	2.0449(19)
Fe(1)-C(64)	2.035(2)
Fe(1)-C(65)	2.039(2)
Fe(1)-C(66)	2.043(2)
Fe(1)-C(67)	2.044(2)
Fe(1)-C(68)	2.045(2)
Fe(1)-C(69)	2.042(2)
C(11)-C(12)	1.390(3)
C(11)-C(16)	1.395(3)
C(11)-C(41)	1.492(3)
C(12)-C(13)	1.401(3)
C(12)-H(12)	0.9500
C(13)-C(14)	1.388(3)
C(13)-C(21)	1.504(3)
C(13)-C(21')	1.548(15)
C(21)-O(22)	1.206(3)
C(21)-O(23)	1.333(3)
C(21')-O(22')	1.226(16)
C(21')-O(23)	1.334(15)
O(23)-C(24)	1.458(3)
C(24)-C(25)	1.478(4)
C(24)-H(24A)	0.9900
C(24)-H(24B)	0.9900
C(25)-H(25A)	0.9800
C(25)-H(25B)	0.9800
C(25)-H(25C)	0.9800
C(14)-C(15)	1.394(3)
C(14)-H(14)	0.9500
C(15)-C(16)	1.394(3)
C(15)-C(31)	1.496(3)
C(16)-H(16)	0.9500

C(31)-O(32)	1.204(2)
C(31)-O(33)	1.340(2)
O(33)-C(34)	1.452(2)
C(34)-C(35)	1.503(3)
C(34)-H(34A)	0.9900
C(34)-H(34B)	0.9900
C(35)-H(35A)	0.9800
C(35)-H(35B)	0.9800
C(35)-H(35C)	0.9800
C(41)-C(43)#1	1.386(3)
C(41)-C(42)	1.417(3)
C(42)-C(43)	1.403(3)
C(42)-C(51)	1.434(3)
C(43)-C(41)#1	1.386(3)
C(43)-H(43)	0.9500
C(51)-C(52)	1.196(3)
C(52)-C(60)	1.421(3)
C(60)-C(64)	1.438(3)
C(60)-C(61)	1.442(3)
C(61)-C(62)	1.425(3)
C(61)-H(61)	0.9500
C(62)-C(63)	1.421(3)
C(62)-H(62)	0.9500
C(63)-C(64)	1.421(3)
C(63)-H(63)	0.9500
C(64)-H(64)	0.9500
C(65)-C(66)	1.420(3)
C(65)-C(69)	1.430(3)
C(65)-H(65)	0.9500
C(66)-C(67)	1.422(3)
C(66)-H(66)	0.9500
C(67)-C(68)	1.422(3)
C(67)-H(67)	0.9500
C(68)-C(69)	1.424(3)
C(68)-H(68)	0.9500
C(69)-H(69)	0.9500
C(12)-C(11)-C(16)	119.33(18)

C(12)-C(11)-C(41)	120.57(18)
C(16)-C(11)-C(41)	120.08(18)
C(11)-C(12)-C(13)	120.35(19)
C(11)-C(12)-H(12)	119.8
C(13)-C(12)-H(12)	119.8
C(14)-C(13)-C(12)	120.30(19)
C(14)-C(13)-C(21)	121.91(19)
C(12)-C(13)-C(21)	117.63(19)
C(14)-C(13)-C(21')	118.4(8)
C(12)-C(13)-C(21')	115.6(6)
O(22)-C(21)-O(23)	124.1(2)
O(22)-C(21)-C(13)	124.3(2)
O(23)-C(21)-C(13)	111.61(19)
O(22')-C(21')-O(23)	120.8(14)
O(22')-C(21')-C(13)	130.0(14)
O(23)-C(21')-C(13)	108.9(10)
C(21)-O(23)-C(24)	114.96(19)
C(21')-O(23)-C(24)	120.9(8)
O(23)-C(24)-C(25)	108.2(2)
O(23)-C(24)-H(24A)	110.1
C(25)-C(24)-H(24A)	110.1
O(23)-C(24)-H(24B)	110.1
C(25)-C(24)-H(24B)	110.1
H(24A)-C(24)-H(24B)	108.4
C(24)-C(25)-H(25A)	109.5
C(24)-C(25)-H(25B)	109.5
H(25A)-C(25)-H(25B)	109.5
C(24)-C(25)-H(25C)	109.5
H(25A)-C(25)-H(25C)	109.5
H(25B)-C(25)-H(25C)	109.5
C(13)-C(14)-C(15)	119.28(18)
C(13)-C(14)-H(14)	120.4
C(15)-C(14)-H(14)	120.4
C(16)-C(15)-C(14)	120.51(18)
C(16)-C(15)-C(31)	121.11(18)
C(14)-C(15)-C(31)	118.38(17)
C(15)-C(16)-C(11)	120.21(18)
C(15)-C(16)-H(16)	119.9

C(11)-C(16)-H(16)	119.9
O(32)-C(31)-O(33)	123.90(19)
O(32)-C(31)-C(15)	124.07(19)
O(33)-C(31)-C(15)	112.03(17)
C(31)-O(33)-C(34)	115.45(16)
O(33)-C(34)-C(35)	107.55(17)
O(33)-C(34)-H(34A)	110.2
C(35)-C(34)-H(34A)	110.2
O(33)-C(34)-H(34B)	110.2
C(35)-C(34)-H(34B)	110.2
H(34A)-C(34)-H(34B)	108.5
C(34)-C(35)-H(35A)	109.5
C(34)-C(35)-H(35B)	109.5
H(35A)-C(35)-H(35B)	109.5
C(34)-C(35)-H(35C)	109.5
H(35A)-C(35)-H(35C)	109.5
H(35B)-C(35)-H(35C)	109.5
C(43)#1-C(41)-C(42)	118.71(17)
C(43)#1-C(41)-C(11)	120.71(17)
C(42)-C(41)-C(11)	120.58(17)
C(43)-C(42)-C(41)	119.39(17)
C(43)-C(42)-C(51)	119.94(17)
C(41)-C(42)-C(51)	120.65(17)
C(41)#1-C(43)-C(42)	121.84(17)
C(41)#1-C(43)-H(43)	119.1
C(42)-C(43)-H(43)	119.1
C(52)-C(51)-C(42)	177.4(2)
C(51)-C(52)-C(60)	176.3(2)
C(52)-C(60)-C(64)	125.85(18)
C(52)-C(60)-C(61)	126.54(17)
C(64)-C(60)-C(61)	107.57(16)
C(52)-C(60)-Fe(1)	128.71(14)
C(64)-C(60)-Fe(1)	69.02(11)
C(61)-C(60)-Fe(1)	69.33(11)
C(62)-C(61)-C(60)	107.59(17)
C(62)-C(61)-Fe(1)	69.78(11)
C(60)-C(61)-Fe(1)	69.35(11)
C(62)-C(61)-H(61)	126.2

C(60)-C(61)-H(61)	126.2
Fe(1)-C(61)-H(61)	126.2
C(63)-C(62)-C(61)	108.43(17)
C(63)-C(62)-Fe(1)	69.56(11)
C(61)-C(62)-Fe(1)	69.45(11)
C(63)-C(62)-H(62)	125.8
C(61)-C(62)-H(62)	125.8
Fe(1)-C(62)-H(62)	126.8
C(64)-C(63)-C(62)	108.57(17)
C(64)-C(63)-Fe(1)	69.25(11)
C(62)-C(63)-Fe(1)	69.80(11)
C(64)-C(63)-H(63)	125.7
C(62)-C(63)-H(63)	125.7
Fe(1)-C(63)-H(63)	126.8
C(63)-C(64)-C(60)	107.83(17)
C(63)-C(64)-Fe(1)	69.99(11)
C(60)-C(64)-Fe(1)	69.69(11)
C(63)-C(64)-H(64)	126.1
C(60)-C(64)-H(64)	126.1
Fe(1)-C(64)-H(64)	125.8
C(64)-Fe(1)-C(65)	123.14(9)
C(64)-Fe(1)-C(69)	105.35(8)
C(65)-Fe(1)-C(69)	41.02(8)
C(64)-Fe(1)-C(66)	161.04(9)
C(65)-Fe(1)-C(66)	40.71(9)
C(69)-Fe(1)-C(66)	68.61(9)
C(64)-Fe(1)-C(67)	155.61(9)
C(65)-Fe(1)-C(67)	68.70(9)
C(69)-Fe(1)-C(67)	68.63(9)
C(66)-Fe(1)-C(67)	40.73(9)
C(64)-Fe(1)-C(61)	69.48(8)
C(65)-Fe(1)-C(61)	121.60(8)
C(69)-Fe(1)-C(61)	156.65(8)
C(66)-Fe(1)-C(61)	108.54(9)
C(67)-Fe(1)-C(61)	125.31(9)
C(64)-Fe(1)-C(60)	41.29(8)
C(65)-Fe(1)-C(60)	106.74(8)
C(69)-Fe(1)-C(60)	119.92(8)

C(66)-Fe(1)-C(60)	124.85(9)
C(67)-Fe(1)-C(60)	162.28(9)
C(61)-Fe(1)-C(60)	41.32(7)
C(64)-Fe(1)-C(63)	40.76(8)
C(65)-Fe(1)-C(63)	159.99(9)
C(69)-Fe(1)-C(63)	122.95(9)
C(66)-Fe(1)-C(63)	157.53(9)
C(67)-Fe(1)-C(63)	121.36(9)
C(61)-Fe(1)-C(63)	68.77(8)
C(60)-Fe(1)-C(63)	68.82(8)
C(64)-Fe(1)-C(68)	119.43(9)
C(65)-Fe(1)-C(68)	68.80(9)
C(69)-Fe(1)-C(68)	40.79(8)
C(66)-Fe(1)-C(68)	68.50(9)
C(67)-Fe(1)-C(68)	40.70(9)
C(61)-Fe(1)-C(68)	161.65(8)
C(60)-Fe(1)-C(68)	155.32(8)
C(63)-Fe(1)-C(68)	106.65(9)
C(64)-Fe(1)-C(62)	68.83(8)
C(65)-Fe(1)-C(62)	157.76(9)
C(69)-Fe(1)-C(62)	160.34(8)
C(66)-Fe(1)-C(62)	122.76(9)
C(67)-Fe(1)-C(62)	108.49(8)
C(61)-Fe(1)-C(62)	40.77(8)
C(60)-Fe(1)-C(62)	68.87(7)
C(63)-Fe(1)-C(62)	40.64(8)
C(68)-Fe(1)-C(62)	124.40(8)
C(66)-C(65)-C(69)	107.77(19)
C(66)-C(65)-Fe(1)	69.77(12)
C(69)-C(65)-Fe(1)	69.58(12)
C(66)-C(65)-H(65)	126.1
C(69)-C(65)-H(65)	126.1
Fe(1)-C(65)-H(65)	126.1
C(65)-C(66)-C(67)	108.32(19)
C(65)-C(66)-Fe(1)	69.52(12)
C(67)-C(66)-Fe(1)	69.68(12)
C(65)-C(66)-H(66)	125.8
C(67)-C(66)-H(66)	125.8

Fe(1)-C(66)-H(66)	126.5
C(66)-C(67)-C(68)	107.99(19)
C(66)-C(67)-Fe(1)	69.59(12)
C(68)-C(67)-Fe(1)	69.71(12)
C(66)-C(67)-H(67)	126.0
C(68)-C(67)-H(67)	126.0
Fe(1)-C(67)-H(67)	126.3
C(67)-C(68)-C(69)	108.02(19)
C(67)-C(68)-Fe(1)	69.58(12)
C(69)-C(68)-Fe(1)	69.46(11)
C(67)-C(68)-H(68)	126.0
C(69)-C(68)-H(68)	126.0
Fe(1)-C(68)-H(68)	126.5
C(68)-C(69)-C(65)	107.90(19)
C(68)-C(69)-Fe(1)	69.75(11)
C(65)-C(69)-Fe(1)	69.40(11)
C(68)-C(69)-H(69)	126.0
C(65)-C(69)-H(69)	126.0
Fe(1)-C(69)-H(69)	126.4

_____

Symmetry transformations used to generate equivalent atoms:

#1 -x,y,-z+1/2

A1.6: Table of torsion angles [°] for (19).

_____

C(16)-C(11)-C(12)-C(13)	-0.2(3)
C(41)-C(11)-C(12)-C(13)	178.14(19)
C(11)-C(12)-C(13)-C(14)	1.3(3)
C(11)-C(12)-C(13)-C(21)	-174.1(2)
C(11)-C(12)-C(13)-C(21')	154.3(12)
C(14)-C(13)-C(21)-O(22)	-156.1(2)
C(12)-C(13)-C(21)-O(22)	19.3(4)
C(21')-C(13)-C(21)-O(22)	112.5(14)
C(14)-C(13)-C(21)-O(23)	23.8(3)
C(12)-C(13)-C(21)-O(23)	-160.9(2)
C(21')-C(13)-C(21)-O(23)	-67.7(13)
C(14)-C(13)-C(21')-O(22')	147(3)
C(12)-C(13)-C(21')-O(22')	-7(3)
C(21)-C(13)-C(21')-O(22')	-108(4)
C(14)-C(13)-C(21')-O(23)	-40(2)
C(12)-C(13)-C(21')-O(23)	166.4(12)
C(21)-C(13)-C(21')-O(23)	65.2(14)
O(22)-C(21)-O(23)-C(21')	-109.1(15)
C(13)-C(21)-O(23)-C(21')	71.0(14)
O(22)-C(21)-O(23)-C(24)	-0.1(4)
C(13)-C(21)-O(23)-C(24)	180.0(2)
O(22')-C(21')-O(23)-C(21)	110(3)
C(13)-C(21')-O(23)-C(21)	-64.5(13)
O(22')-C(21')-O(23)-C(24)	21(3)
C(13)-C(21')-O(23)-C(24)	-153.1(9)
C(21)-O(23)-C(24)-C(25)	-168.5(2)
C(21')-O(23)-C(24)-C(25)	-132.2(14)
C(12)-C(13)-C(14)-C(15)	-1.4(3)
C(21)-C(13)-C(14)-C(15)	173.8(2)
C(21')-C(13)-C(14)-C(15)	-153.7(11)
C(13)-C(14)-C(15)-C(16)	0.5(3)
C(13)-C(14)-C(15)-C(31)	-178.66(19)
C(14)-C(15)-C(16)-C(11)	0.5(3)
C(31)-C(15)-C(16)-C(11)	179.68(18)
C(12)-C(11)-C(16)-C(15)	-0.7(3)
C(41)-C(11)-C(16)-C(15)	-179.05(18)

C(16)-C(15)-C(31)-O(32)	175.2(2)
C(14)-C(15)-C(31)-O(32)	-5.6(3)
C(16)-C(15)-C(31)-O(33)	-4.9(3)
C(14)-C(15)-C(31)-O(33)	174.24(18)
O(32)-C(31)-O(33)-C(34)	-2.8(3)
C(15)-C(31)-O(33)-C(34)	177.34(17)
C(31)-O(33)-C(34)-C(35)	-173.26(18)
C(12)-C(11)-C(41)-C(43)#1	59.9(3)
C(16)-C(11)-C(41)-C(43)#1	-121.7(2)
C(12)-C(11)-C(41)-C(42)	-119.4(2)
C(16)-C(11)-C(41)-C(42)	58.9(3)
C(43)#1-C(41)-C(42)-C(43)	-2.5(3)
C(11)-C(41)-C(42)-C(43)	176.91(18)
C(43)#1-C(41)-C(42)-C(51)	179.17(18)
C(11)-C(41)-C(42)-C(51)	-1.4(3)
C(41)-C(42)-C(43)-C(41)#1	3.1(3)
C(51)-C(42)-C(43)-C(41)#1	-178.51(19)
C(52)-C(60)-C(61)-C(62)	176.93(19)
C(64)-C(60)-C(61)-C(62)	-0.9(2)
Fe(1)-C(60)-C(61)-C(62)	-59.54(13)
C(52)-C(60)-C(61)-Fe(1)	-123.5(2)
C(64)-C(60)-C(61)-Fe(1)	58.60(13)
C(60)-C(61)-C(62)-C(63)	0.5(2)
Fe(1)-C(61)-C(62)-C(63)	-58.80(14)
C(60)-C(61)-C(62)-Fe(1)	59.27(13)
C(61)-C(62)-C(63)-C(64)	0.2(2)
Fe(1)-C(62)-C(63)-C(64)	-58.55(13)
C(61)-C(62)-C(63)-Fe(1)	58.73(14)
C(62)-C(63)-C(64)-C(60)	-0.8(2)
Fe(1)-C(63)-C(64)-C(60)	-59.66(13)
C(62)-C(63)-C(64)-Fe(1)	58.89(14)
C(52)-C(60)-C(64)-C(63)	-176.84(18)
C(61)-C(60)-C(64)-C(63)	1.0(2)
Fe(1)-C(60)-C(64)-C(63)	59.84(13)
C(52)-C(60)-C(64)-Fe(1)	123.3(2)
C(61)-C(60)-C(64)-Fe(1)	-58.80(13)
C(63)-C(64)-Fe(1)-C(65)	164.01(12)
C(60)-C(64)-Fe(1)-C(65)	-77.16(13)

C(63)-C(64)-Fe(1)-C(69)	123.05(12)
C(60)-C(64)-Fe(1)-C(69)	-118.12(12)
C(63)-C(64)-Fe(1)-C(66)	-168.3(2)
C(60)-C(64)-Fe(1)-C(66)	-49.5(3)
C(63)-C(64)-Fe(1)-C(67)	51.1(2)
C(60)-C(64)-Fe(1)-C(67)	169.91(18)
C(63)-C(64)-Fe(1)-C(61)	-80.92(12)
C(60)-C(64)-Fe(1)-C(61)	37.92(11)
C(63)-C(64)-Fe(1)-C(60)	-118.83(16)
C(60)-C(64)-Fe(1)-C(63)	118.83(16)
C(63)-C(64)-Fe(1)-C(68)	81.34(14)
C(60)-C(64)-Fe(1)-C(68)	-159.83(11)
C(63)-C(64)-Fe(1)-C(62)	-37.16(12)
C(60)-C(64)-Fe(1)-C(62)	81.68(12)
C(62)-C(61)-Fe(1)-C(64)	81.00(13)
C(60)-C(61)-Fe(1)-C(64)	-37.89(11)
C(62)-C(61)-Fe(1)-C(65)	-161.93(12)
C(60)-C(61)-Fe(1)-C(65)	79.18(14)
C(62)-C(61)-Fe(1)-C(69)	162.1(2)
C(60)-C(61)-Fe(1)-C(69)	43.3(3)
C(62)-C(61)-Fe(1)-C(66)	-119.02(13)
C(60)-C(61)-Fe(1)-C(66)	122.10(12)
C(62)-C(61)-Fe(1)-C(67)	-76.91(15)
C(60)-C(61)-Fe(1)-C(67)	164.20(12)
C(62)-C(61)-Fe(1)-C(60)	118.88(17)
C(62)-C(61)-Fe(1)-C(63)	37.23(12)
C(60)-C(61)-Fe(1)-C(63)	-81.65(12)
C(62)-C(61)-Fe(1)-C(68)	-41.5(3)
C(60)-C(61)-Fe(1)-C(68)	-160.4(2)
C(60)-C(61)-Fe(1)-C(62)	-118.88(17)
C(52)-C(60)-Fe(1)-C(64)	-119.8(2)
C(61)-C(60)-Fe(1)-C(64)	119.36(16)
C(52)-C(60)-Fe(1)-C(65)	1.7(2)
C(64)-C(60)-Fe(1)-C(65)	121.51(12)
C(61)-C(60)-Fe(1)-C(65)	-119.12(12)
C(52)-C(60)-Fe(1)-C(69)	-40.9(2)
C(64)-C(60)-Fe(1)-C(69)	78.90(13)
C(61)-C(60)-Fe(1)-C(69)	-161.73(12)

C(52)-C(60)-Fe(1)-C(66)	42.7(2)
C(64)-C(60)-Fe(1)-C(66)	162.48(12)
C(61)-C(60)-Fe(1)-C(66)	-78.16(14)
C(52)-C(60)-Fe(1)-C(67)	74.0(3)
C(64)-C(60)-Fe(1)-C(67)	-166.2(3)
C(61)-C(60)-Fe(1)-C(67)	-46.9(3)
C(52)-C(60)-Fe(1)-C(61)	120.9(2)
C(64)-C(60)-Fe(1)-C(61)	-119.36(16)
C(52)-C(60)-Fe(1)-C(63)	-157.6(2)
C(64)-C(60)-Fe(1)-C(63)	-37.84(11)
C(61)-C(60)-Fe(1)-C(63)	81.53(12)
C(52)-C(60)-Fe(1)-C(68)	-73.8(3)
C(64)-C(60)-Fe(1)-C(68)	46.0(2)
C(61)-C(60)-Fe(1)-C(68)	165.36(18)
C(52)-C(60)-Fe(1)-C(62)	158.7(2)
C(64)-C(60)-Fe(1)-C(62)	-81.56(12)
C(61)-C(60)-Fe(1)-C(62)	37.81(12)
C(62)-C(63)-Fe(1)-C(64)	-120.15(17)
C(64)-C(63)-Fe(1)-C(65)	-42.4(3)
C(62)-C(63)-Fe(1)-C(65)	-162.5(2)
C(64)-C(63)-Fe(1)-C(69)	-74.41(14)
C(62)-C(63)-Fe(1)-C(69)	165.44(12)
C(64)-C(63)-Fe(1)-C(66)	170.1(2)
C(62)-C(63)-Fe(1)-C(66)	50.0(3)
C(64)-C(63)-Fe(1)-C(67)	-157.90(12)
C(62)-C(63)-Fe(1)-C(67)	81.95(14)
C(64)-C(63)-Fe(1)-C(61)	82.79(12)
C(62)-C(63)-Fe(1)-C(61)	-37.35(11)
C(64)-C(63)-Fe(1)-C(60)	38.32(12)
C(62)-C(63)-Fe(1)-C(60)	-81.83(12)
C(64)-C(63)-Fe(1)-C(68)	-116.01(12)
C(62)-C(63)-Fe(1)-C(68)	123.85(12)
C(64)-C(63)-Fe(1)-C(62)	120.15(17)
C(63)-C(62)-Fe(1)-C(64)	37.27(11)
C(61)-C(62)-Fe(1)-C(64)	-82.73(13)
C(63)-C(62)-Fe(1)-C(65)	164.3(2)
C(61)-C(62)-Fe(1)-C(65)	44.3(3)
C(63)-C(62)-Fe(1)-C(69)	-38.8(3)

C(61)-C(62)-Fe(1)-C(69)	-158.8(2)
C(63)-C(62)-Fe(1)-C(66)	-159.63(12)
C(61)-C(62)-Fe(1)-C(66)	80.37(14)
C(63)-C(62)-Fe(1)-C(67)	-116.94(12)
C(61)-C(62)-Fe(1)-C(67)	123.06(13)
C(63)-C(62)-Fe(1)-C(61)	120.00(17)
C(63)-C(62)-Fe(1)-C(60)	81.69(12)
C(61)-C(62)-Fe(1)-C(60)	-38.31(12)
C(61)-C(62)-Fe(1)-C(63)	-120.00(17)
C(63)-C(62)-Fe(1)-C(68)	-74.65(14)
C(61)-C(62)-Fe(1)-C(68)	165.35(12)
C(64)-Fe(1)-C(65)-C(66)	166.64(12)
C(69)-Fe(1)-C(65)-C(66)	-118.96(18)
C(67)-Fe(1)-C(65)-C(66)	-37.45(13)
C(61)-Fe(1)-C(65)-C(66)	81.79(15)
C(60)-Fe(1)-C(65)-C(66)	124.43(13)
C(63)-Fe(1)-C(65)-C(66)	-161.6(2)
C(68)-Fe(1)-C(65)-C(66)	-81.27(14)
C(62)-Fe(1)-C(65)-C(66)	49.4(3)
C(64)-Fe(1)-C(65)-C(69)	-74.40(15)
C(66)-Fe(1)-C(65)-C(69)	118.96(19)
C(67)-Fe(1)-C(65)-C(69)	81.51(14)
C(61)-Fe(1)-C(65)-C(69)	-159.24(12)
C(60)-Fe(1)-C(65)-C(69)	-116.61(13)
C(63)-Fe(1)-C(65)-C(69)	-42.7(3)
C(68)-Fe(1)-C(65)-C(69)	37.69(13)
C(62)-Fe(1)-C(65)-C(69)	168.40(19)
C(69)-C(65)-C(66)-C(67)	-0.4(2)
Fe(1)-C(65)-C(66)-C(67)	59.06(15)
C(69)-C(65)-C(66)-Fe(1)	-59.43(14)
C(64)-Fe(1)-C(66)-C(65)	-36.6(3)
C(69)-Fe(1)-C(66)-C(65)	38.07(13)
C(67)-Fe(1)-C(66)-C(65)	119.74(18)
C(61)-Fe(1)-C(66)-C(65)	-117.24(13)
C(60)-Fe(1)-C(66)-C(65)	-74.27(15)
C(63)-Fe(1)-C(66)-C(65)	163.6(2)
C(68)-Fe(1)-C(66)-C(65)	82.05(14)
C(62)-Fe(1)-C(66)-C(65)	-160.01(12)

C(64)-Fe(1)-C(66)-C(67)	-156.3(2)
C(65)-Fe(1)-C(66)-C(67)	-119.74(18)
C(69)-Fe(1)-C(66)-C(67)	-81.67(14)
C(61)-Fe(1)-C(66)-C(67)	123.02(13)
C(60)-Fe(1)-C(66)-C(67)	165.99(12)
C(63)-Fe(1)-C(66)-C(67)	43.9(3)
C(68)-Fe(1)-C(66)-C(67)	-37.69(13)
C(62)-Fe(1)-C(66)-C(67)	80.25(14)
C(65)-C(66)-C(67)-C(68)	0.4(2)
Fe(1)-C(66)-C(67)-C(68)	59.35(15)
C(65)-C(66)-C(67)-Fe(1)	-58.96(14)
C(64)-Fe(1)-C(67)-C(66)	161.57(19)
C(65)-Fe(1)-C(67)-C(66)	37.43(13)
C(69)-Fe(1)-C(67)-C(66)	81.62(14)
C(61)-Fe(1)-C(67)-C(66)	-76.97(15)
C(60)-Fe(1)-C(67)-C(66)	-40.8(3)
C(63)-Fe(1)-C(67)-C(66)	-161.93(13)
C(68)-Fe(1)-C(67)-C(66)	119.26(18)
C(62)-Fe(1)-C(67)-C(66)	-119.08(13)
C(64)-Fe(1)-C(67)-C(68)	42.3(3)
C(65)-Fe(1)-C(67)-C(68)	-81.83(14)
C(69)-Fe(1)-C(67)-C(68)	-37.64(13)
C(66)-Fe(1)-C(67)-C(68)	-119.26(18)
C(61)-Fe(1)-C(67)-C(68)	163.77(12)
C(60)-Fe(1)-C(67)-C(68)	-160.0(2)
C(63)-Fe(1)-C(67)-C(68)	78.81(15)
C(62)-Fe(1)-C(67)-C(68)	121.65(13)
C(66)-C(67)-C(68)-C(69)	-0.3(2)
Fe(1)-C(67)-C(68)-C(69)	59.01(14)
C(66)-C(67)-C(68)-Fe(1)	-59.27(15)
C(64)-Fe(1)-C(68)-C(67)	-161.39(13)
C(65)-Fe(1)-C(68)-C(67)	81.58(14)
C(69)-Fe(1)-C(68)-C(67)	119.47(19)
C(66)-Fe(1)-C(68)-C(67)	37.72(13)
C(61)-Fe(1)-C(68)-C(67)	-46.4(3)
C(60)-Fe(1)-C(68)-C(67)	165.58(18)
C(63)-Fe(1)-C(68)-C(67)	-119.04(13)
C(62)-Fe(1)-C(68)-C(67)	-78.08(15)

C(64)-Fe(1)-C(68)-C(69)	79.14(14)
C(65)-Fe(1)-C(68)-C(69)	-37.89(13)
C(66)-Fe(1)-C(68)-C(69)	-81.75(14)
C(67)-Fe(1)-C(68)-C(69)	-119.47(19)
C(61)-Fe(1)-C(68)-C(69)	-165.9(2)
C(60)-Fe(1)-C(68)-C(69)	46.1(2)
C(63)-Fe(1)-C(68)-C(69)	121.49(13)
C(62)-Fe(1)-C(68)-C(69)	162.45(13)
C(67)-C(68)-C(69)-C(65)	0.0(2)
Fe(1)-C(68)-C(69)-C(65)	59.12(14)
C(67)-C(68)-C(69)-Fe(1)	-59.09(14)
C(66)-C(65)-C(69)-C(68)	0.2(2)
Fe(1)-C(65)-C(69)-C(68)	-59.34(14)
C(66)-C(65)-C(69)-Fe(1)	59.55(14)
C(64)-Fe(1)-C(69)-C(68)	-117.50(13)
C(65)-Fe(1)-C(69)-C(68)	119.26(19)
C(66)-Fe(1)-C(69)-C(68)	81.46(14)
C(67)-Fe(1)-C(69)-C(68)	37.57(13)
C(61)-Fe(1)-C(69)-C(68)	168.84(19)
C(60)-Fe(1)-C(69)-C(68)	-159.68(12)
C(63)-Fe(1)-C(69)-C(68)	-76.79(15)
C(62)-Fe(1)-C(69)-C(68)	-47.7(3)
C(64)-Fe(1)-C(69)-C(65)	123.25(13)
C(66)-Fe(1)-C(69)-C(65)	-37.80(13)
C(67)-Fe(1)-C(69)-C(65)	-81.69(14)
C(61)-Fe(1)-C(69)-C(65)	49.6(3)
C(60)-Fe(1)-C(69)-C(65)	81.06(14)
C(63)-Fe(1)-C(69)-C(65)	163.95(12)
C(68)-Fe(1)-C(69)-C(65)	-119.26(19)
C(62)-Fe(1)-C(69)-C(65)	-166.9(2)

_____

Symmetry transformations used to generate equivalent atoms:

#1 -x,y,-z+1/2

Appendix 2. Crystallographic data summary of structures discussed in Chapter 3

A.2.1. Crystal data and structure refinement for (2)

Identification code	mnbzaq
Empirical formula	C130 H104 Cl8 Mn12 O51
Formula weight	3425.01
Temperature	150(2) K
Wavelength	0.71073 Å
Crystal system	Orthorhombic
Space group	Fdd2
Unit cell dimensions	$a = 31.1204(11)$ Å $\quad \alpha= 90°.$
	$b = 53.078(2)$ Å $\quad \beta= 90°.$
	$c = 17.4196(6)$ Å $\quad \gamma = 90°.$
Volume	28774.0(18) Å^3
Z	8
Density (calculated)	1.581 Mg/m^3
Absorption coefficient	1.248 mm^{-1}
F(000)	13824
Crystal size	0.57 x 0.15 x 0.13 mm^3
Theta range for data collection	2.02 to 27.52°.
Index ranges	-40<=h<=36, -68<=k<=68, -22<=l<=21
Reflections collected	63971
Independent reflections	16419 [R(int) = 0.0644]
Completeness to theta = 27.50°	100.0 %
Absorption correction	None
Refinement method	Full-matrix least-squares on F^2
Data / restraints / parameters	16419 / 2275 / 970
Goodness-of-fit on F^2	0.960
Final R indices [I>2sigma(I)]	R1 = 0.0506, wR2 = 0.1192
R indices (all data)	R1 = 0.0641, wR2 = 0.1237
Absolute structure parameter	0.002(14)
Largest diff. peak and hole	0.980 and -0.377 e.Å^{-3}

A.2.2. Crystal data and structure refinement for (3)

Identification code	mnsala
Empirical formula	C141 H148 Cl26 Mn12 O48
Formula weight	4191.57
Temperature	150(2) K
Wavelength	0.71073 Å
Crystal system	Triclinic
Space group	P-1
Unit cell dimensions	a = 18.305(5) Å α= 74.197(4)°.
	b = 19.413(5) Å β= 87.865(4)°.
	c = 24.574(6) Å γ = 85.738(4)°.
Volume	8378(4) Å^3
Z	2
Density (calculated)	1.662 Mg/m^3
Absorption coefficient	1.364 mm^{-1}
F(000)	4240
Crystal size	0.60 x 0.22 x 0.22 mm^3
Theta range for data collection	1.09 to 25.10°.
Index ranges	-21<=h<=21, -22<=k<=23, -29<=l<=28
Reflections collected	62235
Independent reflections	29672 [R(int) = 0.1348]
Completeness to theta = 25.10°	99.4 %
Absorption correction	Semi-empirical from equivalents
Max. and min. transmission	0.7452 and 0.3988
Refinement method	Full-matrix least-squares on F^2
Data / restraints / parameters	29672 / 5177 / 1584
Goodness-of-fit on F^2	0.770
Final R indices [I>2sigma(I)]	R1 = 0.1046, wR2 = 0.2425
R indices (all data)	R1 = 0.2405, wR2 = 0.2822
Largest diff. peak and hole	1.240 and -0.946 e.Å^{-3}

A.2.3. Crystal data and structure refinement for (4)

.

Identification code	mnetbz
Empirical formula	C148 H156 Mn12 O48
Formula weight	3362.01
Temperature	150(2) K
Wavelength	0.71073 Å
Crystal system	Monoclinic
Space group	P 2/c
Unit cell dimensions	a = 20.184(6) Å α= 90°.
	b = 16.293(5) Å β= 130.756(12)°.
	c = 30.918(7) Å γ = 90°.
Volume	7702(4) Å^3
Z	2
Density (calculated)	1.450 Mg/m^3
Absorption coefficient	1.028 mm^{-1}
F(000)	3456
Crystal size	0.37 x 0.26 x 0.17 mm^3
Theta range for data collection	2.01 to 25.10°.
Index ranges	-24<=h<=24, -17<=k<=17, -27<=l<=36
Reflections collected	26935
Independent reflections	12543 [R(int) = 0.132]
Completeness to theta = 25.10°	91.5 %
Absorption correction	Semi-empirical from equivalents
Max. and min. transmission	0.431 and 0.239
Refinement method	Full-matrix least-squares on F^2
Data / restraints / parameters	12543 / 1763 / 939
Goodness-of-fit on F^2	0.97
Final R indices [I>2sigma(I)]	R1 = 0.119, wR2 = 0.296
R indices (all data)	R1 = 0.246, wR2 = 0.370
Extinction coefficient	0.0011(5)
Largest diff. peak and hole	1.15 and -0.83 e.Å^{-3}

A.2.4. Crystal data and structure refinement for (7)

Identification code	mnsalb
Empirical formula	C159 H192 Cl14 Mn12 O53
Formula weight	4106.71
Temperature	150(2) K
Wavelength	0.71073 Å
Crystal system	Triclinic
Space group	P-1

Unit cell dimensions	a = 21.1503(10) Å	α = 89.7870(10)°.
	b = 22.2257(10) Å	β = 64.6330(10)°.
	c = 24.4386(11) Å	γ = 69.3710(10)°.

Volume	9566.5(8) Å^3
Z	2
Density (calculated)	1.426 Mg/m^3
Absorption coefficient	1.033 mm^{-1}
F(000)	4216
Crystal size	0.36 x 0.15 x 0.12 mm^3
Theta range for data collection	1.87 to 27.47°.
Index ranges	-27<=h<=26, -28<=k<=28, -31<=l<=31
Reflections collected	85543
Independent reflections	42960 [R(int) = 0.0331]
Completeness to theta = 27.47°	98.1 %
Absorption correction	Semi-empirical from equivalents
Max. and min. transmission	0.6468 and 0.5504
Refinement method	Full-matrix least-squares on F^2
Data / restraints / parameters	42960 / 5705 / 2140
Goodness-of-fit on F^2	1.044
Final R indices [I>2sigma(I)]	R1 = 0.0764, wR2 = 0.2087
R indices (all data)	R1 = 0.1010, wR2 = 0.2229
Largest diff. peak and hole	1.027 and -0.916 e.Å^{-3}

A.2.5. Crystal data and structure refinement for (9)

Identification code	mnoodp
Empirical formula	C234 H172 Mn12 O52
Formula weight	4475.00
Temperature	150(2) K
Wavelength	0.71073 Å
Crystal system	Tetragonal
Space group	I -4 2 d
Unit cell dimensions	a = 20.593(3) Å $\alpha = 90°$.
	b = 20.593(3) Å $\beta = 90°$.
	c = 64.577(16) Å $\gamma = 90°$.
Volume	27386(9) Å^3
Z	4
Density (calculated)	1.085 Mg/m^3
Absorption coefficient	0.595 mm^{-1}
F(000)	9168
Crystal size	0.66 x 0.50 x 0.45 mm^3
Theta range for data collection	2.08 to 27.50°.
Index ranges	-17<=h<=26, -26<=k<=26, -76<=l<=83
Reflections collected	101225
Independent reflections	15726 [R(int) = 0.083]
Completeness to theta = 27.50°	99.9 %
Absorption correction	Semi-empirical from equivalents
Max. and min. transmission	0.746 and 0.604
Refinement method	Full-matrix least-squares on F^2
Data / restraints / parameters	15726 / 1328 / 738
Goodness-of-fit on F^2	1.11
Final R indices [I>2sigma(I)]	R1 = 0.0856, wR2 = 0.257
R indices (all data)	R1 = 0.126, wR2 = 0.295
Absolute structure parameter	-0.02(3)
Largest diff. peak and hole	0.98 and -0.62 e.Å^{-3}

A.2.6. Crystal data and structure refinement for (12)

Identification code	mnoltb
Empirical formula	C95 H71 Mn3 O18
Formula weight	1665.34
Temperature	150(2) K
Wavelength	0.71073 Å
Crystal system	Trigonal
Space group	R -3
Unit cell dimensions	a = 18.9299(11) Å $\quad$ α= 90°.
	b = 18.9299(11) Å $\quad$ β= 90°.
	c = 39.504(5) Å $\quad$ γ = 120°.
Volume	12259.3(17) Å^3
Z	6
Density (calculated)	1.353 Mg/m^3
Absorption coefficient	0.528 mm^{-1}
F(000)	5160
Crystal size	0.21 x 0.17 x 0.13 mm^3
Theta range for data collection	2.15 to 27.51°.
Index ranges	-13<=h<=24, -24<=k<=24, -51<=l<=51
Reflections collected	25821
Independent reflections	6265 [R(int) = 0.0521]
Completeness to theta = 27.50°	99.9 %
Absorption correction	Semi-empirical from equivalents
Max. and min. transmission	0.934 and 0.840
Refinement method	Full-matrix least-squares on F^2
Data / restraints / parameters	6265 / 0 / 339
Goodness-of-fit on F^2	1.125
Final R indices [I>2sigma(I)]	R1 = 0.0891, wR2 = 0.1882
R indices (all data)	R1 = 0.1240, wR2 = 0.2057
Largest diff. peak and hole	0.697 and -0.408 e.Å^{-3}